Physik-Department der

Technischen Universität München
Lehrstuhl für Experimentalphysik 3

# Magnetic properties of low dimensional spin systems

Verena Sabine Kargl

Vollständiger Abdruck der von der Fakultät für Physik der Technischen Universität München zur Erlangung des akademischen Grades eines

Doktors der Naturwissenschaften (Dr. rer. nat.)

genehmigten Dissertation.

| | |
|---|---|
| Vorsitzender: | Univ.-Prof. Dr. W. Weise |
| Prüfer der Dissertation: | 1. Univ.-Prof. Dr. P. Böni<br>2. Univ.-Prof. (komm. L.) Dr. A. Meyer |

Die Dissertation wurde am 31.01.2006 bei der Technischen Universität München eingereicht und durch die Fakultät für Physik am 16.03.2006 angenommen.

# Contents

# Summary

This thesis studies the dimensional crossover from antiferromagnetic 3D order to 1D Heisenberg behavior of antiferromagnetic half odd integer spin chains upon changing the doping concentration in $Ca_{2+x}Y_{2-x}Cu_5O_{10}$ and increasing the temperature in $CsVBr_3$.

The crystal structure of the $S = 1/2$ cuprate compounds $Ca_{2+x}Y_{2-x}Cu_5O_{10}$ shows edge sharing $CuO_2$ chains. By means of hole doping in terms of increasing the Ca/Y ratio, the magnetic $Cu^{2+}$ ions are canceled out in the chains. Instead, the number of holes increases from zero in $Ca_2Y_2Cu_5O_{10}$ to 0.34 holes/Cu in $Ca_{0.83}CuO_2$ ($x = 2.15$), respectively. Dimerization of adjacent spins in the $CuO_2$ chains is favored with an increasing number of holes.
Neutron spectroscopy, susceptibility and specific heat measurements resolve complex magnetic properties that arise from a doping independent Néel state below $\sim 29$ K, disorder in the $CuO_2$ chains and 1D Heisenberg behavior. The order temperature and the magnetic moment of the 3D antiferromagnetic phase decrease from $\sim 29$ K to $\sim 12$ K and from $\sim 0.92\mu_B$ to $\sim 0.28\mu_B$ for the parent compound $Ca_2Y_2Cu_5O_{10}$ and $Ca_{0.83}CuO_2$, respectively. The collinear magnetic structure of samples with $0 \leq x \leq 1.5$ shows ferromagnetic exchange along the chain axis that changes to antiferromagnetic correlations for the doping concentration $x = 2.15$. The chain exchange is well understood within the $J_1$-$J_2$ model for edge sharing $CuO_2$ chains and classifies the chain behavior as frustrated with a doping independent antiferromagnetic next nearest neighboring spin interaction.
Hole doping lifts the frustration of nearest neighboring spins and leads to disorder in terms of a spin glass-like state in $Ca_{3.5}Y_{0.5}Cu_5O_{10}$. Higher doped samples $Ca_{3.5}Y_{0.5}Cu_5O_{10}$ and $Ca_{0.83}CuO_2$ show 1D Heisenberg behavior, where the magnetic intrachain exchange of $\sim 60$ K is almost spatially isotropic. The distance of two coupled spins corresponds to two times the copper distance along the chain yielding next nearest neighboring spin interaction.

Below its Néel temperature of 20.4 K the triangular antiferromagnet $CsVBr_3$ ($S = 3/2$) is characterized by a strong antiferromagnetic intrachain exchange along the crystallographic $c$ axis, weak interaction in the hexagonal basal plane and a XY-like anisotropy that forces spins in a 120° structure. Studying the spin wave energy gap at the magnetic zone center (0 0 3) in the paramagnetic phase resolves its upward renormalization upon increasing temperature. This unusual behavior contradicts the general belief of a gapless excitation spectrum for antiferromagnetic half odd integer spin chains. In contrast, the temperature evolution of the gap energy can be consistently described within the frame of a hexagonal Heisenberg model that emphasizes 3D magnetic correlations and neglects anisotropy.

# Chapter 1

# Introduction

Quantum phase transitions have been extensively studied over the last decades both from a theoretical and an experimental point of view. It is well known that a magnetic system can show a crossover from a long range ordered state to quasi 1D magnetic behavior or even high-$T_c$ superconductivity [1]. This drastic change in the spin correlations might be evoked by an external parameter that influences the spin system. Among those are for instance an external magnetic field, pressure that is applied to the system or doping of substitutes into the investigated compound. In this sense much attention was drawn to the investigation of charge doping into a Mott insulator that shows three dimensional antiferromagnetic order. By doping, lower Néel temperatures are achievable until long range order completely vanishes for a particular doping concentration. Instead, high-$T_c$ superconductivity or low dimensional magnetism appears to dominate microscopic and macroscopic properties. In particular, the discovery of high-$T_c$ superconductivity in $La_{2-x}Ba_xCuO_4$ by J. G. Bednorz and K. A. Müller [2] increased the attention given to transition metal oxides such as nickelates and cuprates as possible candidates exhibiting these kinds of generic phase diagrams.

## 1.1 Quasi 1D magnetism in cuprates

Among the transition metal oxides only cuprate compounds feature low dimensional magnetic properties. It is assumed that high-$T_c$ superconductivity and magnetic short range correlations are exclusively observed for one doping concentration. The existence of both phenomena are attributed to the exceptional crystal structure of copper oxides that favors well isolated Cu-O planes [3]. Between these planes e.g. alkaline earth elements, yttrium or lanthanum are localized that represent a reservoir for charge doping. For high-$T_c$ superconductors the four fold $CuO_4$ units in the Cu-O planes are typically arranged in a way that two of these share a corner. Magnetic exchange is mediated via the covalent 180° Cu-O-Cu bond. Furthermore, an angle of almost 90° can be found for the Cu-O-Cu bond yielding edge sharing $CuO_4$ units. High-$T_c$ superconductivity is only observed for the first type of assembling $CuO_4$ units, whereas low dimensional magnetism in terms of spin chains and spin ladders originate from both types of Cu-O-Cu bonding. Figure 1.1 illustrates both possibilities to assemble $CuO_4$ units. The spin quantum number of copper 1/2 yields either antiferromagnetic spin chains or ladders.

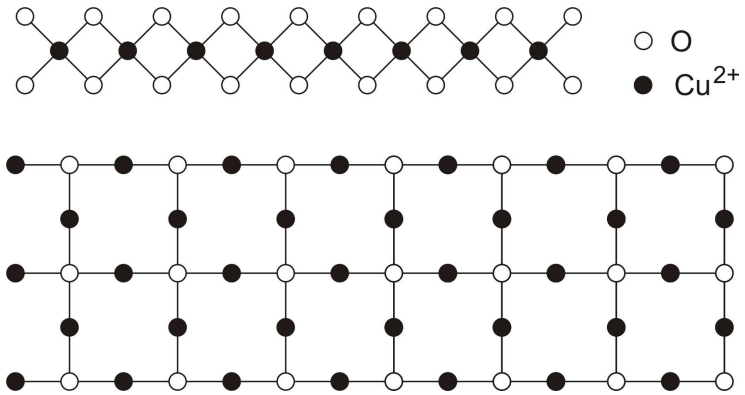


Figure 1.1: Illustration of an edge sharing $CuO_2$ chain (above) and a three-leg ladder (below). Here, $CuO_4$ units assemble in a corner sharing way with a bonding angle of 180°. Magnetic exchange is mediated along and perpendicular to the rungs of the ladder. In the limit of infinite legs the spin ladder approaches the conventional 2D magnet.

In general, a spin chain is characterized by one dimensionally coupled spins [4]. However, chains are locally separated from each other preventing magnetic exchange between them. The degree of freedom for the spins can vary between Ising, XY and three dimensional Heisenberg behavior. Ladder systems of variable width are formed of parallelly arranged spin chains that show an equivalent magnitude of the exchange measured along the chains as well as along the rungs. The number of legs might vary from two for a simple two-leg ladder to higher values for a $n$-leg ladder. In the limit of infinite number of chains the ladder system approaches the conventional two dimensional magnet.

Much effort was put into theoretically describing the ground state properties as well as those of the excited spin system of the antiferromagnetic $S = 1/2$ and $S = 1$ spin chains and the $S = 1/2$ ladders. For an overview of these systems refer to [5, 6] and citations therein. All of these spin systems show properties of pure quantum mechanical origin, whereas those exhibiting 2D or 3D magnetic correlations still behave classically. True magnetic order is expected to occur at temperatures that are low compared to the energy of the system. In case of the antiferromagnetic $S = 1/2$ chain this happens only at zero Kelvin [7]. Moreover, collective dynamics of these highly correlated electron systems are extraordinary in the sense that magnetic properties are only observed for one dimensional order and show no equivalent for 2D or 3D order. For instance, only spin 1/2 chains exhibit a gapless excitation spectrum. Based on this finding it is assumed that all antiferromagnetic half integer spin chains feature equivalent characteristics in their ground state properties and their excitation spectrum. In contrast, Haldane predicted for integer spin chains a finite spin gap between the ground state and the first excited energy level [8]. The transition from a single chain to the two dimensional magnet whose magnetic structure is formed of numerous coupled spin chains or ladders amplifies the unusual properties. It has turned out that the ground state properties of ladders crucially depend on their width. An odd number of legs are expected to behave in analogy to antiferromagnetic spin 1/2 chains. The excitation spectrum is gapless and spin correlations fall off with a power law of the site separation of spins. An even-leg ladder shows short range order at low temperatures. Excited $S = 1$ states are separated from the ground state by a finite energy gap and the spin correlation exponentially decreases with the site distance.

In order to verify these theoretical approaches, neutron scattering turned out to be a

valuable tool. It offers the possibility to directly probe on interatomic length scales characteristic properties of a sample such as the excitation spectrum and the density of states. In this sense, numerous experiments were carried out on cuprate compounds or materials with spin 1/2. For instance, the 3D antiferromagnet $KCuF_3$ shows the spinon continuum[1] of an antiferromagnetic spin 1/2 chain [9]. $(VO)_2P_2O_7$, $SrCuO_3$ and $La_2Cu_2O_5$ are experimentally proven as realizations of two-leg ladders with spin 1/2 [10, 11, 12]. In contrast, $Sr_2Cu_3O_5$ exhibits properties of a three-leg ladder ($S=1/2$) [13]. The widely known 'phone-number' compound $(Sr,Ca)_{14}Cu_{24}O_{42}$ features characteristics of both the antiferromagnetic spin chain and a two-leg ladder [11]. Its complex crystal structure of corner sharing ladders and edge sharing $CuO_2$ chains turned it difficult to distinguish between both types of $CuO_4$ assemblies [14, 15, 16, 17]. Besides low dimensional magnetism high-$T_c$ superconductivity was found in $Sr_{0.4}Ca_{13.6}Cu_{24}O_{42}$ under an applied pressure of 5 GPa [18]. When doping the two-leg ladders with holes, singlets that are formed along the rungs of the ladder are broken up. Non magnetic $Cu^{3+}$ pair along the rungs and it is believed this tendency provokes superconductivity.
Another remarkable phenomenon of pure quantum mechanical origin is found in the cuprate $CuGeO_3$ that is formed of $GeO_2$ tetrahedrons and edge sharing $CuO_2$ chains [19]. It exhibits a spin-Peierls transition around 14 K, where a spin gap opens up in the dispersion. Above this transition temperature the uniform $CuO_2$ chains exhibit isotropic exchange and the excitation spectrum is gapless. Owing to a magnetoelastic coupling between lattice vibrations and the electronic structure the lattice distorts, i.e. the exchange measured along the chain now depends on the spin distance. The uniform chain dimerizes in terms of singlet formation and a spin gap occurs in the spin-Peierls phase. Besides this cuprate organic molecules like $MEM(TCNQ)_2$ [20] or the compound $\alpha$'-$NaV_2O_5$ [21] show a spin-Peierls transition below their transition temperatures of 18 K and 34 K, respectively.

## 1.2 Outline of this thesis

In this thesis we focus on two examples of quasi one dimensional systems that are studied by means of bulk measurements and/or neutron spectroscopy. We chose the cuprate compounds $Ca_{2+x}Y_{2-x}Cu_5O_{10}$ whose crystal structure shows edge sharing $CuO_2$ chains. Antiferromagnetic 1D Heisenberg behavior is expected to occur upon increasing the Ca/Y ratio from $x=0$ to 2. Dilution of the magnetic chains of undoped $Ca_2Y_2Cu_5O_{10}$ leads to dimerization[2]. Our study is devoted to the evolution of both the magnetic long and short range behavior with respect to charge doping by holes. Experimental findings are analyzed for the antiferromagnetic 1D Heisenberg chain with alternating exchange and the 3D antiferromagnetic phase that coexist depending on temperature and doping concentration. Susceptibility and specific heat measurements demonstrate for higher doped compounds quasi 1D properties originating from the 1D Heisenberg chain. Although doping leads to a dilution of the magnetic chains, the long range order does not vanish. The quasi 1D behavior is close to that of the uniform chain. In order to probe the excitation spectrum of these samples, inelastic neutron scattering experiments were performed. Besides triple axis spectrometers that allow for probing a particular $(\mathbf{Q},\omega)$ point in reciprocal space,

[1] The gapless excitation spectrum of the antiferromagnetic $S=1/2$ Heisenberg chain is called the spinon continuum. Spinons are the elementary excitation particles with $S=1/2$.

[2] Dimerization describes the coupling of two neighboring spins, when the magnetic exchange in the chain is not spatially uniform.

we used a time of flight instrument. It provides access to the inelastic coherent scattering function. Based on the observed spin dynamics we characterized the different phases with respect to the doping concentration $x$. In agreement with bulk measurements we observe in $Ca_2Y_2Cu_5O_{10}$ spin wave dynamics that arise from the antiferromagnetic Néel state. Moreover, we found evidence of a spin glass phase in $Ca_{3.5}Y_{0.5}Cu_5O_{10}$. A highly doped compound $Ca_{0.83}CuO_2$, that corresponds to the doping concentration $x = 2.15$, can be characterized in terms of 1D Heisenberg behavior. Singlet formation between next nearest neighboring spins is observed. In order to adhere experimental findings to theory, we calculated for this sample the structure factor and the scattering law based on the model of dimerized chains.
During this work polycrystalline samples were used. Owing to the synthesis conditions with an oxygen pressure of more than 200 bar and a reaction temperature of $\sim 1100$ K no single crystals were at our disposal.

Besides cuprate systems, the class of $ABX_3$ compounds[3] are expected to show quasi 1D magnetic properties in terms of antiferromagnetic spin chains. In these systems the temperature serves as external parameter provoking quasi 1D chain behavior. It originates from antiferromagnetically coupled $B$ ions that run along one crystallographic direction. With increasing temperature the weaker interchain coupling of adjacent chains is expected to be destroyed. Only the stronger intrachain correlations should dominate the dynamical behavior in the paramagnetic regime. Below the order temperature these samples exhibit various ground states depending on the kind of anisotropy and the strength of their exchange parallel and perpendicular to the chain direction. In this thesis we investigated the compound $CsVBr_3$ that is characterized as a triangular frustrated antiferromagnet, when 3D order sets in. Although the spin quantum number 3/2 does not yield properties of the antiferromagnetic $S = 1/2$ chain, we probe general aspects of antiferromagnetic spin chains with a half odd integer spin value. It is assumed that in contrast to the Haldane conjecture for integer spin chains the excitation spectrum of these chains is gapless. We clearly show that in the paramagnetic phase the observed degenerate in-plane dispersion branches[4] feature an excitation gap. In addition, we found an unusual upward renormalization of the gap energy with temperature. Comparing these findings to other members of the $ABX_3$ family such as $CsMnBr_3$ ($S = 5/2$) and $CsNiCl_3$ ($S = 1$) elucidates that this behavior appears to be independently of the spin quantum number a general feature of the paramagnetic spin dynamics of these three compounds. A recent theoretical approach that emphasizes 3D magnetic correlations without anisotropy explains the observed spin dynamics in the disordered phase. This appears to question the model character of $CsVBr_3$ and its related representatives of the $ABX_3$ class for studying quasi 1D behavior.

The outline of this thesis is as follows: chapter 2 will provide an overview of theoretical results in the field of quasi one dimensional magnetism for antiferromagnetic $S = 1/2$ and $S = 1$ spin chains. We explain the model of the antiferromagnetic $S = 1/2$ alternating Heisenberg chain that describes dimerization between neighboring spins. In addition, im-

[3] $ABX_3$ compounds are formed of an alkali metal $A$, a 3d transition metal $B$ and an halide $X$. A general description of $ABX_3$ compounds is presented in chapter 2.5.

[4] $CsVBr_3$ shows three magnon branches: the optic out-of-plane branch, the acoustic and the optic in-plane modes.

portant aspects of the two model systems $Ca_{2+x}Y_{2-x}Cu_5O_{10}$ and $CsVBr_3$ are presented. The complex magnetic order in copper oxide compounds and $CsVBr_3$ require various experimental methods to elucidate their inherent properties. Chapter 3 is devoted to these experimental techniques applied to resolve the magnetic behavior of both systems. Among those are macroscopic bulk measurements, such as D.C./A.C. magnetization and specific heat, as well as neutron spectroscopy that probes microscopic properties of the samples.

In sequence, the investigation of the magnetic behavior of $Ca_{2+x}Y_{2-x}Cu_5O_{10}$ samples is presented in chapter 4, that is followed by the results of the study on $CsVBr_3$ (see chapter 5). Chapter 4.1 reports on the sample synthesis, the chemical characterization and the nuclear structure of the $Ca_{2+x}Y_{2-x}Cu_5O_{10}$ compounds. Afterwards, we present macroscopic and microscopic investigations of $Ca_{2+x}Y_{2-x}Cu_5O_{10}$. We will focus on the low dimensional behavior of the compound series that is revealed by susceptibility and specific heat measurements (see chapter 4.2 and 4.3). Furthermore, results of the magnetic structure in the long range ordered state are presented in chapter 4.4 that were obtained by neutron diffraction. Chapter 4.5 summarizes data of the dynamical behavior of the compound series with doping. We will show that the spin dynamics of the undoped parent compound $Ca_2Y_2Cu_5O_{10}$ is understood in terms of spin waves. $Ca_{3.5}Y_{0.5}Cu_5O_{10}$ provides evidence of a spin glass phase below $\sim 17\,\mathrm{K}$. The highly doped compound $Ca_{0.83}CuO_2$ ($x = 2.15$) is characterized as model of the 1D Heisenberg chain. We found the dimer extent to be compatible with the next nearest copper distance. Finally, in chapter 4.6 the obtained data are discussed in comparison to literature. In particular, we will construct a phase diagram of $Ca_{2+x}Y_{2-x}Cu_5O_{10}$ with respect to the Ca/Y ratio and explain the effect of dimerization of the $CuO_2$ chains within competing nearest and next nearest neighbor interactions.

Chapter 5 reports on the investigation of the triangular antiferromagnet $CsVBr_3$. We present an introduction to its 3D behavior below the Néel temperature of $\sim 20.4\,\mathrm{K}$ (see chapter 5.1 and 5.2). Moreover, inelastic neutron scattering data of the paramagnetic phase of this sample are shown (chapter 5.3) and discussed within the framework of conventional linear spin wave theory, dipolar exchange and a recently developed theoretical approach describing one dimensional behavior in $ABX_3$ compounds (see chapter 5.4). We further compare $CsVBr_3$ to the structural related compounds $CsMnBr_3$ and $CsNiCl_3$.

Chapter 6 concludes important aspects of this thesis work.

Detailed mathematical calculations of the dynamical behavior of $Ca_{2+x}Y_{2-x}Cu_5O_{10}$ samples are presented in appendix A and B. The first one covers a brief introduction to linear spin wave theory that was applied to calculate the 3D dispersion of $Ca_2Y_2Cu_5O_{10}$ in a semi classical approach. The second appendix summarizes the powder averaged structure factor and scattering law of dimerized chains. These calculations apply for $Ca_{0.83}CuO_2$.

The model of the damped harmonic oscillator is illustrated in appendix C. Based on the time dependence of the equation of motion for the damped harmonic oscillator we derive the scattering law in the frequency domain. This formula is used for fitting purposes of $CsVBr_3$ data.

# Chapter 2

# Theory - antiferromagnetic Heisenberg spin chains

*This chapter serves as introduction to antiferromagnetic spin chains with integer and half integer spin value. We chronologically arrange major steps in theory and collect the most important characteristics of both systems. The interested reader is referred to references given in the text and citations therein. Chapter 2.2 explains the model system of the antiferromagnetic spin 1/2 Heisenberg chain with alternating exchange to which this thesis work is devoted. Thermodynamical properties of the 1D Heisenberg chain are discussed in chapter 2.3. Finally, it is briefly noted why the investigated compounds* $Ca_{2+x}Y_{2-x}Cu_5O_{10}$ *and* $CsVBr_3$ *are recognized as model systems for the antiferromagnetic* $S = 1/2$ *chain (see chapter 2.4 and 2.5).*

## 2.1 General properties

For theory, solving the one dimensional antiferromagnetic quantum chains for $S = 1$ and $S = 1/2$ was a challenge ever since the first exact solution by Bethe in 1931 [7]. Based on the Hamiltonian for nearest neighbor coupling between spins $\hat{\mathbf{S}}_i$ and $\hat{\mathbf{S}}_{i+1}$

$$H = J \sum_i \hat{\mathbf{S}}_i \hat{\mathbf{S}}_{i+1} \,, \tag{2.1}$$

the ground state properties of the antiferromagnetic spin 1/2 Heisenberg chain and its massless excitations are explained. $\hat{\mathbf{S}}_i$ denotes the spin operator of the spin system and $J$ the exchange constant measured along the chain. Within the chain the magnetic correlation with respect to the left and right neighbor of one particular spin is isotropic (see Figure 2.1). The obtained dispersion relation $\omega \propto \sin(Q)$ is periodic over the Brillouin zone with $Q$ representing the wavevector and $\omega$ the energy of excited states. The non symmetry breaking ground state of the chain was found to consist of singlets with $S = 0$. Excitations from the ground state in terms of threefold degenerate triplets describe the lowest lying excited states. They are pictured as movable domain walls[1] called spinons that can be continuously excited from the ground state without a finite energy gap at the zone center. Des Cloiseaux and Pearson [22] derived the dispersion of the lowest lying

[1] A domain wall denotes the boundary between two domains with different spin alignment. In case of the well known Bloch wall the two adjacent domains feature antiferromagnetic spin coupling. Within the wall the spin is rotating by 180° to compromise for the opposite spin orientation.

excitations $\epsilon_l = \frac{\pi}{2} J \left|\sin\left(Q\right)\right|$ which they interpreted as bosons ($S=1$). Today it is well understood that the basic excitations have fermionic character [23]. The gapless excitation spectrum, the spinon continuum, consists of elementary particles with $S=1/2$ that can couple to pairs with the energy $\epsilon(Q) = \epsilon_1(Q_1) + \epsilon_2(Q_2)$. Based on the numerical Müller ansatz [24] the upper boundary of the spinon continuum $\epsilon_u = \pi J \left|\sin\left(Q/2\right)\right|$ was found. Figure 2.2 (a) illustrates the excitation spectrum of the antiferromagnetic $S=1/2$ spin chain. It was further found that in the quasi ordered Kosterlitz-Thouless phase [25] the spin-spin correlation function falls off with the power of the distance $r$ of two spins [26]

$$\left\langle \hat{S}_0^\alpha \hat{S}_r^\beta \right\rangle \propto (-1)^r \delta^{\alpha\beta} \frac{\sqrt{\ln r}}{r} \,. \tag{2.2}$$

$\hat{S}^\alpha$ denotes the $\alpha$ coordinate of the spin operator with $\alpha,\, \beta \in \{x, y, z\}$. True order only holds at zero temperature, where no thermal fluctuations are present. It is commonly accepted that all half odd integer spin chains feature gapless excitations [4].

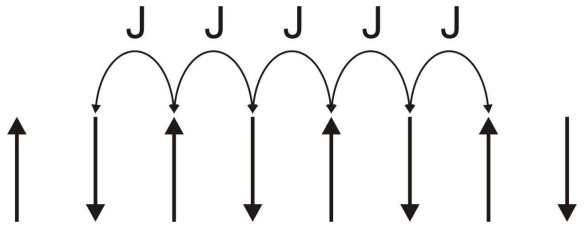


Figure 2.1: Scheme of the antiferromagnetic uniform spin 1/2 chain with a spatially isotropic exchange $J$ between left and right neighboring spins.

Haldane investigated the properties of the $S=1$ spin chain [8]. His most striking result was that the ground state of the spin 1 chain is highly correlated. A finite spin gap of $\Delta \simeq 0.4J$ separates the ground state energy from the lowest excitations. The latter are interpreted as massive $S=1$ particles that are threefold degenerate. Visualized as domain walls they are expected to disturb the hidden order in the Haldane phase of the antiferromagnetic spin 1 chain [27] by moving through the chain. At early stages argued these predictions are now widely accepted and contributions were made in terms of the excitation spectrum for the antiferromagnetic spin 1 chain [28]. It follows the relation $\omega = \sqrt{v \sin^2\left(Q\right) + \Delta^2}$ with the effective spin velocity $v$ and the energy gap $\Delta$. The correlation was found to fall off exponentially with the site separation $r$

$$\left\langle \hat{S}_0^\alpha \hat{S}_r^\beta \right\rangle \propto (-1)^r \delta^{\alpha\beta} \frac{\exp\left\{-r/\xi\right\}}{\sqrt{r}} \,, \tag{2.3}$$

where $\xi$ denotes the correlation length. Higher integer spin quantum numbers yield a decrease in the gap energy with $\Delta \propto JS \exp\left\{-\pi S\right\}$ [29], attributing the $S=1$ case to a purely quantum mechanical origin.

In contrast, linear spin wave theory describes the excitation spectrum of a long range ordered spin system that allows for three dimensional magnetic correlations. This approach was developed around 1950 with major contributions by Anderson [30]. Within this framework magnons were introduced as quasi particles of an excitation wave moving through the lattice. Ferromagnetic and antiferromagnetic correlations between spins yield a dispersion relation $\hbar\omega(\mathbf{Q})$ that is proportional to $Q^2$ and $Q$ at the magnetic zone center,

respectively. From the beginning it was obvious that the restriction of an antiferromagnetic 3D Hamiltonian to the 1D case did not correspond to the antiferromagnetic uniform chain. Excitations of the long range ordered Néel state that arises from two sublattice magnetizations of opposite spin value are only twofold degenerate. Obeying Bose statistics they bear the spin quantum number one. The dispersion relation of these states only holds in the reduced Brillouin zone, as antiferromagnetic order yields a doubling of the unit cell extension. For a mathematical introduction to linear spin wave theory refer to appendix A.1.

## 2.2 Alternating exchange in the $S = 1/2$ spin chain

As soon as the exchange constant between the left ($J_1$) and right ($J_2$) neighbor spin differs, preferred magnetic correlations based on

$$H = \sum_i \left( J_1 \hat{\mathbf{S}}_{2i} \hat{\mathbf{S}}_{2i-1} + J_2 \hat{\mathbf{S}}_{2i} \hat{\mathbf{S}}_{2i+1} \right) = J \sum_i \left( \hat{\mathbf{S}}_{2i} \hat{\mathbf{S}}_{2i-1} + \alpha \hat{\mathbf{S}}_{2i} \hat{\mathbf{S}}_{2i+1} \right) \tag{2.4}$$

are introduced in the uniform antiferromagnetic $S = 1/2$ chain. Here, $J_2 = \alpha J$ is reduced in strength compared to $J_1 = J$. The alternation parameter $\alpha$ is a measure of the magnetic exchange to the adjacent left and right spin with $0 \leq \alpha \leq 1$. A modification in the spatially isotropic exchange of the uniform chain may be evoked by changing the coupling distance of magnetic ions or the relative strength of $J$ and $\alpha J$. Dimerization of spins within an uniform chain leads to a modification of the excitation spectrum. Bougourzi and coworkers [31], Barnes and coworkers [32, 33], Harris and coworkers [34] and Uhrig and Schulz [35] exactly and numerically solved the ground state and the low lying excitations for this model, respectively. Uhrig and Schulz used a different convention for the Hamiltonian for dimerized chains (here given in the limit of nearest neighbor interaction)

$$H = \tilde{J} \sum_i \left( 1 + (-1)^i \delta \right) \hat{\mathbf{S}}_i \hat{\mathbf{S}}_{i+1} = J \sum_i \left( \hat{\mathbf{S}}_{2i} \hat{\mathbf{S}}_{2i-1} + \lambda \hat{\mathbf{S}}_{2i} \hat{\mathbf{S}}_{2i+1} \right) , \tag{2.5}$$

where $\delta$ denotes the alternation parameter of the coupling of a particular spin with respect to the left and right neighbor. Note the relations $\alpha = \lambda = (1 - \delta)/(1 + \delta)$ and $\tilde{J} = J(1 + \delta) = J(1 + \alpha)/2$. $\delta = 0$ ($\alpha = 1$) represents the limit of the uniform chain, whereas $\delta = 1$ ($\alpha = 0$) defines spin singlets without coupling to one of its neighboring dimers.

The gapless spinon continuum changes to a magnon mode and the n-magnon continua for $0 < \alpha < 1$. The lower boundary of the continuum develops a dispersion that is separated from the ground state by a gap $\Delta < J$ at $Q = 0$ and $\pi$. This magnon branch accounts for the lowest lying excitations with $S = \pm 1$ and 0. Furthermore, the remaining n-continuous excitation bands are themselves separated from the triplet branch by a gap of the order of $n\Delta$ at $Q$ equal to zero and $\pi$. In the limit of a chain with isolated dimers the discrete energy levels are infinitively degenerate with energies $J$, $2J$, $3J$, .... Figure 2.2 illustrates the excitation spectrum of the antiferromagnetic spin 1/2 chain. Decrease in the alternation parameter $\alpha$ yields the formation of dimers, i.e. coupled spins that interact with the exchange parameter $J$.

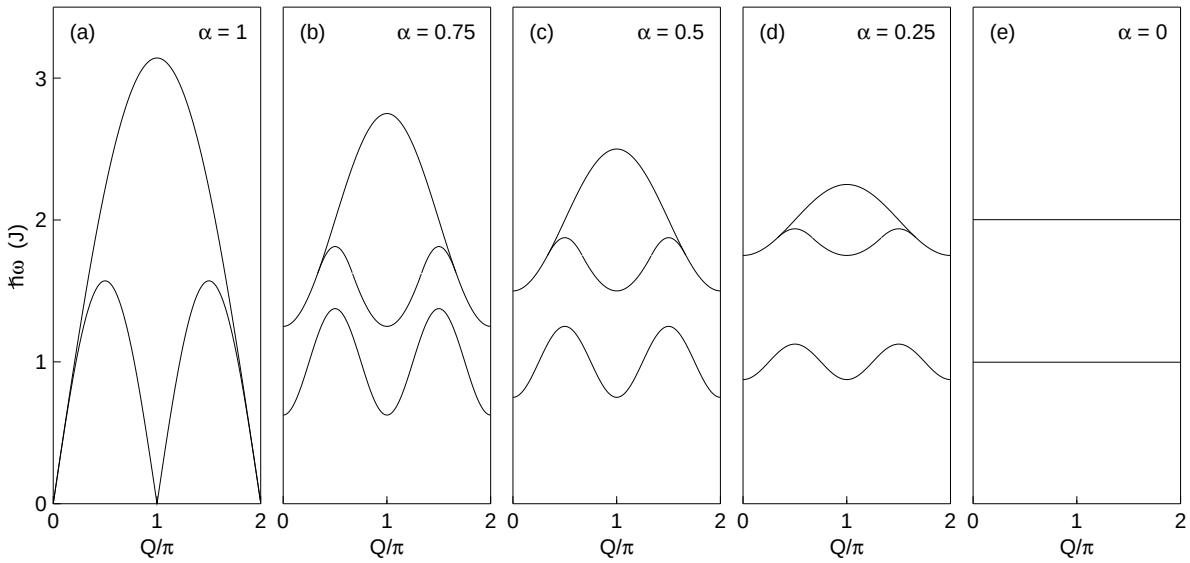


Figure 2.2: Excitation spectrum of the (a) uniform chain ($\alpha = 1$) that evolves with dimerization ($0 \leq \alpha < 1$). (b) to (d) illustrate how the gapless spinon continuum changes to the triplet and the first magnon continuum for $\alpha$ equal to 0.75, 0.5 and 0.25. (e) The solid lines correspond to the discrete excitation levels for a chain with isolated dimers ($\alpha = 0$). The excitation spectra are sketched based on [22, 24, 31, 32, 33, 34, 35].

## 2.3 Thermodynamical properties of the alternating $S = 1/2$ chain

Thermodynamical properties of the antiferromagnetic spin 1/2 Heisenberg chain are deduced from the internal energy $U$ of the spin system. $U$ is assumed to behave power law like and proportional to $ANJ\,(k_BT/J)^{\gamma}$, where T denotes the temperature, $J$ the magnetic exchange between adjacent spins and $N$ the number of spins [36]. The constants $\gamma$ and $A$ are equal to $\sim 2.06$ and $\sim 0.175$, respectively. Numerical approximation in the limit of infinite spins yields the desired quantities such as susceptibility and specific heat. For a broad overview of thermodynamical behavior of low dimensional systems refer to Jongh and Miedema [37].

The susceptibility of the uniform chain is obtained by Bonner and Fisher [36] using finite chain calculations (see dashed line in Figure 2.3). It displays a rounded maximum at $k_BT/J \simeq 0.641$ of the absolute height $\chi_{max}J/(g^2\beta^2) \simeq 0.149$. $k_B$ denotes the Boltzmann constant, $g$ the paramagnetic Landé factor and $\beta = 1/(k_BT)$ the inverse temperature. The energy scale of the system is approximately defined by the temperature, where the maximum occurs. Upon approaching zero temperature, the susceptibility yields a finite value. The energy of the lowest lying excitations is infinitely close to the ground state energy. Thus, even in the limit $T \to 0$ these excitations are populated visualized in a finite value of $\chi(T = 0)$. Results given by Eggert and coworkers [38] and Frischmuth and coworkers [39] agree well with the study of Bonner and Fisher. When $\alpha$ is less than one, an energy gap opens up between the ground state and the density of lowest lying excitations. Susceptibility exponentially vanishes with the strength of the energy gap $\Delta$, when the temperature reduces to zero. Bulaevskiĭ [40] and Bonner and coworkers [41] calculated

the behavior of $\chi(T)$ for $0 < \alpha < 1$ using Hartree-Fox approximation. Numerical results in the dimer limit are given by Barnes and Riera [42].

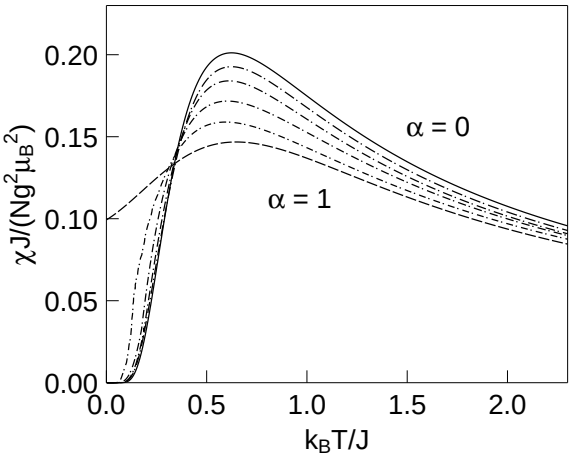


Figure 2.3: Reduced susceptibility of the alternating Heisenberg spin chain. The solid line, the dashed line and the dot-dashed lines indicate the susceptibility of the purely dimerized spin chain ($\alpha = 0$), of the uniform spin chain ($\alpha = 1$) and of the alternating spin chain model ($\alpha = 0.2$, 0.4, 0.6 and 0.8), respectively. Taken from [38, 39, 40, 41].

Numerical approximations of the theoretical curves for $\chi(T)$ depending on the alternation $\alpha$ were obtained by investigating model systems. Notice, that the following formulas follow the convention of the magnetic exchange $J$ as introduced in Eq. (2.1) and Eq. (2.4). Estes and coworkers [43] fitted the Bonner-Fisher results for susceptibility of Dihalobis(thiazole)copper(II) complexes yielding the closed form for the uniform chain (*uni*)

$$\chi_{uni} = \frac{N_{uni} g^2 \mu_B^2}{k_B T} \frac{0.25 + 0.07498x + 0.07524x^2}{1 + 0.99310x + 0.17214x^2 + 0.75783x^3} \,. \tag{2.6}$$

Here, $x$ denotes the reduced interaction exchange $J/(k_B T)$, $N_{uni}$ the number of magnetic spins in units of the Avogadro number $N_A$, $g$ the Landé factor and $\mu_B$ the Bohr magneton. Susceptibility of the alternating Heisenberg chain (*ahc*) was derived by Hall and coworkers [44] analyzing data of various organic compounds in terms of

$$\chi_{ahc} = \frac{N_{ahc} g^2 \mu_B^2}{k_B T} \frac{A + Bx + Cx^2}{1 + Dx + Ex^2 + Fx^3} \,. \tag{2.7}$$

Similarly to Eq. (2.6), $N_{ahc}$ denotes the number of magnetic spins contributing to the magnetic response of the sample and $x$ the reduced magnetic exchange $J/(k_B T)$. The constants $A$, $B$, ... $F$ are numerically determined and depend up to the fourth order on $\alpha$. Susceptibility of a chain with isolated dimers ($\alpha = 0$) was obtained by Matsuda and Katsumata [45] and Carter and coworkers [46] for the spin chain/ladder compound $Sr_{14}Cu_{24}O_{41}$ and doped compositions of $(La,Sr,Ca)_{14}Cu_{24}O_{41}$, respectively. With $N_d$ denoting the number of involved magnetic spins that equals twice the number of formed dimers in the chain, susceptibility reads

$$\chi_d = \frac{N_d g^2 \mu_B^2}{k_B T} \frac{1}{3 + \exp\left(J/k_B T\right)} \,. \tag{2.8}$$

Specific heat of an antiferromagnetic spin 1/2 Heisenberg chain features a characteristic behavior that distinguishes at first glance from that of a dimerized chain. For comparison of the corresponding curves see Figure 2.4. The low temperature limit ($T \lesssim 0.4\, J/k_B$) of

the uniform antiferromagnetic chain is given by the linear approximation of Takeda and coworkers [47] according to

$$C(T)_{uni} = \frac{2N_{uni}k_B^2 T}{3J}\,, \tag{2.9}$$

where $N_{uni}$ denotes the number of magnetic spins in units of the Avogadro constant and $J$ the antiferromagnetic exchange. This result is compatible with the numerical Bonner-Fisher approximation [36] yielding the constant of proportionality equal to 2/3 instead of $\simeq 0.7$. At intermediate temperatures ($0.4\,J/k_B \lesssim T \lesssim 0.75\,J/k_B$ ) specific heat features a broad maximum of the height $C_{max}/(Nk_B) \simeq 0.35$ at the temperature $k_B T_{max}/J \simeq 0.481$. In the dimer approximation specific heat reads

$$C(T)_d = \frac{3}{2}N_d \left(\frac{J}{T}\right)^2 \frac{\exp\left(-J/T\right)}{\left(1+3\exp\left(-J/T\right)\right)} \tag{2.10}$$

with the number of dimerized $Cu^{2+}$ spins $N_d$. This value equals twice the number of formed dimers in the chain. Comparable with the behavior of susceptibility for a dimerized chain specific heat exponentially falls off with the exchange parameter $J$ measured along the chain in the limit $T \to 0$. The finite energy gap between the ground state and the density of the lowest lying excitations requires thermal energy to overcome this energy barrier.

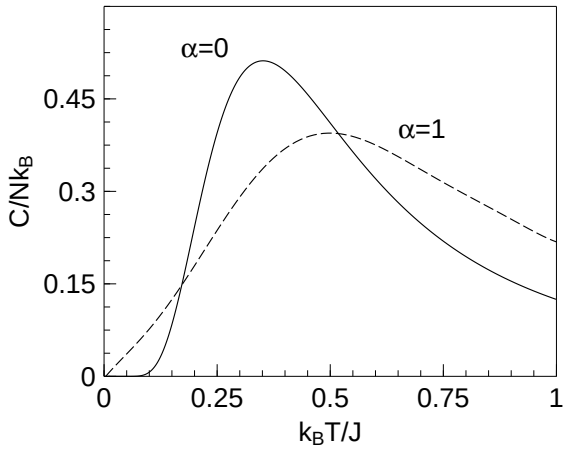


Figure 2.4: Specific heat of the alternating $S = 1/2$ antiferromagnetic Heisenberg chain. The solid line indicates the chain with isolated dimers ($\alpha = 0$) and the dashed line the uniform chain ($\alpha = 1$). Taken from [36, 37].

## 2.4 Model system $Ca_{2+x}Y_{2-x}Cu_5O_{10}$

The crossover from long range order to antiferromagnetic 1D Heisenberg behavior can be evoked by an external parameter that influences the spin system. In order to illustrate this effect, this thesis work will focus on the cuprate oxide compounds $Ca_{2+x}Y_{2-x}Cu_5O_{10}$. The electronic configuration of the magnetic $Cu^{2+}$ ions yields a spin quantum number of 1/2. Charge doping into $CuO_2$ chains serves as decisive parameter that should lead to quasi 1D magnetic behavior in terms of the alternating 1D Heisenberg chain.

The compound series is structurally related to the $NaCuO_2$ type of materials [48]. Early investigations of the parent compound[2] $Ca_2Y_2Cu_5O_{10}$ revealed that the monoclinic crystal

[2]The parent compound of an at least binary alloy, e.g. $A_{1-x}B_x$, represents the undoped sample $A_1$, where the doping concentration of the substitute $x$ equals zero.

structure exhibits $CuO_2$ chains of edge sharing $CuO_4$ square units [49, 50]. The bonding angle of the Cu-O-Cu exchange path is almost 90°. The $CuO_2$ chains are separated by planes bearing Ca and Y atoms. Within the chains chemical bonding is mediated by a hybridization of the $3d_{x^2-y^2}$ Cu orbital and the $2p_{x,y}$ orbitals of the oxygen ions. Each copper donates two holes to close-by oxygens forming a covalent bond. Owing to the bonding angle, two hybrid orbitals at the site of one oxygen ion are almost orthogonal to each other.

It is known that the magnetic exchange of the edge sharing $CuO_2$ chain follows the Hamiltonian

$$H = \sum_i \left( J_1 \hat{\mathbf{S}}_i \hat{\mathbf{S}}_{i+1} + J_2 \hat{\mathbf{S}}_i \hat{\mathbf{S}}_{i+2} \right) , \tag{2.11}$$

where $J_1$ describes nearest neighbor and $J_2$ next nearest neighbor interaction between spins $\hat{\mathbf{S}}_i$, $\hat{\mathbf{S}}_{i+1}$ and $\hat{\mathbf{S}}_i$, $\hat{\mathbf{S}}_{i+2}$ [51]. In contrast, Eq. (2.4) accounts for the alternating Heisenberg chain with not spatially uniform nearest neighbor interaction. The correlation $J_1$ mediates the superexchange along the Cu-O-Cu path. Its sign and magnitude follows the Anderson-Kanamori-Goodenough rules [52, 53, 54] and depends on the orthogonality of the two hybrid orbitals, i.e. on the Cu-O-Cu bonding angle $\theta$. In case of $\theta = 90°$, these orbitals do not overlap yielding ferromagnetic coupling of the holes due to Hund's rule. Around 95° the nearest neighbor exchange vanishes, whereas $\theta > 95°$ evokes antiferromagnetic correlations. In the overlapping hybrid orbitals Pauli's principle forces antiferromagnetic hole pairing. The antiferromagnetic next nearest neighbor exchange $J_2$ along the Cu-O-O-Cu path is almost $\theta$ independent for $80° \leq \theta \leq 100°$. Respecting the Cu-O distance along the exchange path its magnitude is of the order of $\sim 75\,\mathrm{K}$. Moreover, the magnetic order of the chains crucially depends on $\theta$, i.e. the ratio of $J_2/|J_1|$ and vary e.g. between frustrated chains, a ferromagnetic phase or the resonating valence bond state [55, 56, 57, 58, 59]. Figure 2.5 illustrates the competing magnetic exchanges of the edge sharing $CuO_2$ chain.

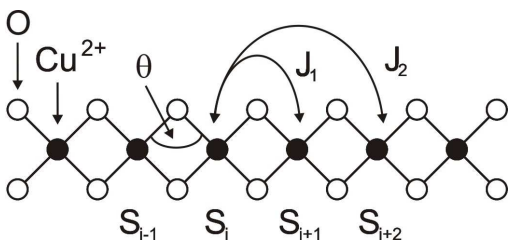


Figure 2.5: Scheme of the $J_1$-$J_2$ model for the edge sharing $CuO_2$ chain. The magnetic exchange to the nearest neighboring spin $J_1$ differs from that to the next nearest neighboring spin $J_2$. While $J_2$ is antiferromagnetic and $\theta$ independent, $J_1$ depends on the Cu-O-Cu angle and changes its sign from ferromagnetic to antiferromagnetic exchange around 95°.

While increasing the Ca/Y ratio in the compound series, holes are introduced into the spin system. These are strongly bound to the central $Cu^{2+}$ ion of the $CuO_4$ square and the chains turn diluted. The effective Hamiltonian of the single-band Hubbard model in the limit of a large on-site repulsion at the Cu site applies for describing the motion of these holes [60]. Spins of $Cu^{2+}$ ions are canceled out and nonmagnetic units ($S = 0$) are created. These Zhang-Rice singlets consist of a nonmagnetic $Cu^{3+}$ and four oxygen ions. As they repel each other, they are assumed to be homogeneously distributed in the spin chain. Magnetic exchange via the Cu-O-Cu bond is reduced. Consequently, dimerization occurs owing to interaction of magnetic Cu spins whose strength depends on the exchange

path and the relative magnitude of $J_1$ and $J_2$. Figure 2.6 illustrates both the uniform and the dimerized antiferromagnetic copper oxide spin chain.

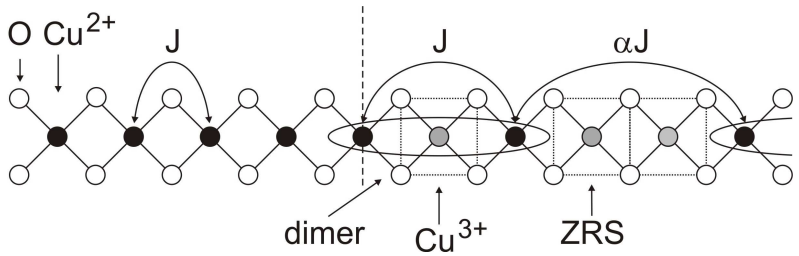


Figure 2.6: Scheme of an antiferromagnetic spin 1/2 Heisenberg spin chain. The left hand part displays the uniform spin chain with an isotropic exchange $J$ between one spin and its left and right neighbor. Superexchange mediates the coupling via a Cu-O-Cu bond. The right hand part of the spin chain illustrates the effect of dimerization. Nonmagnetic $CuO_4$ units that bear one $Cu^{3+}$ and four oxygen ions changes the isotropic magnetic exchange between spins ($J$ and $\alpha J$) and lead to a preferred bonding in the chain. These units are called Zhang-Rice singlets (ZRS).

Hole doping of $Ca_{2+x}Y_{2-x}Cu_5O_{10}$, i.e. diluting the $CuO_2$ spin chains, increases the formal copper valence from 2+ to 2.4+ for $Ca_2Y_2Cu_5O_{10}$ and $Ca_4Cu_5O_{10}$, respectively. Table 2.1 collects the formal Cu valence of selected $Ca_{2+x}Y_{2-x}Cu_5O_{10}$ samples that are investigated in this study. We obtained these values considering charge balance of a compound, where the valence of Ca, Y and O ions are +2, +3 and -2. For instance, the formal valence per one copper ion of $Ca_2Y_2Cu_5O_{10}$ is calculated to be $|(2\cdot 2+3\cdot 2-2\cdot 10)/5| = 10/5 = 2$. In addition, the hole and spin density are noted that are derived from the valence. Besides the stoichiometric compound $Ca_4Cu_5O_{10}$ higher doped concentrations of the compound series exist. In this thesis results are presented for $Ca_{4.15}Cu_5O_{10}$. In literature this compound is referred to as $Ca_{0.83}CuO_2$ and we will adhere to this convention. When showing concentration dependent properties of the compound series, the concentration of this sample is called $x = 2.15$.

| Sample | Concentration $x$ | Cu-valence | Holes/Cu | $N$ |
|---|---|---|---|---|
| $Ca_2Y_2Cu_5O_{10}$ | 0 | 2 | 0 | 1 |
| $Ca_{2.5}Y_{1.5}Cu_5O_{10}$ | 0.5 | 2.1 | 0.1 | 0.9 |
| $Ca_3Y_1Cu_5O_{10}$ | 1 | 2.2 | 0.2 | 0.8 |
| $Ca_{3.5}Y_{0.5}Cu_5O_{10}$ | 1.5 | 2.3 | 0.3 | 0.7 |
| $Ca_4Cu_5O_{10}$ | 2 | 2.4 | 0.4 | 0.6 |
| $Ca_{0.83}CuO_2$ | 2.15 | 2.34 | 0.34 | 0.66 |

Table 2.1: Formal copper valence, number of holes and number of magnetic spins $N$ in units of the Avogadro number $N_A$ that depend on the doping concentration $x$. The values are calculated based on the stoichiometric composition of each sample. Upon charge doping the Cu valence and the number of holes per copper increases, whereas the number of spins in turn decreases.

The first successful synthesis of various doping concentrations of the compound series was achieved by Hayashi and coworkers [61] in 1996 using high pressure oxygen annealing. Electrical transport measurements characterized these polycrystalline samples to be electrically insulating. Susceptibility showed for all samples in the doping range of $0 \leq x \leq 2$

antiferromagnetic three dimensional order. The Néel temperature decreases with increasing Ca/Y ratio yielding $\sim 28\,\mathrm{K}$ for the parent compound and 16 K for $Ca_3Y_1Cu_5O_{10}$. Moreover, Susceptibility data of samples with $x \leq 1$ were interpreted as a complex behavior of antiferromagnetic 3D order superimposed to 1D antiferromagnetic spin chain behavior. The concentration $x \sim 1.5$ was characterized as the critical doping point, where a dimensional crossover from long range to short range behavior occurs. In $Ca_4Cu_5O_{10}$ only short range order in terms of the antiferromagnetic 1D Heisenberg chain was found. Chabot and coworkers [62] derived from susceptibility and specific heat that the magnetic order in $Ca_{2+x}Y_{2-x}Cu_5O_{10}$ is of long range order type for small doping concentrations. Around $x \sim 1$ one dimensional chain behavior shall exist evolving into the formation of clusters. Neutron diffraction of the parent compound revealed ferromagnetic correlations along the chain direction [63, 64]. This was confirmed by measuring the spin wave dispersion in the Néel state [65, 66]. Highly doped $Ca_{0.83}CuO_2$ revealed antiferromagnetic exchange along the chain [67].

This study focuses on the one dimensional properties of the compound series. In particular, we discuss the model of the antiferromagnetic 1D Heisenberg chain for these systems. In addition, we will investigate the effect of hole doping into the $CuO_2$ chains in terms of dimerization of neighboring spins.

## 2.5 Model system $CsVBr_3$

Besides charge doping temperature serves as effective parameter that induces low dimensional order into a magnetic system. In this sense we will focus on the $ABX_3$ compound $CsVBr_3$ that is expected to feature antiferromagnetic spin chain behavior above its Néel temperature [68].

In general, $ABX_3$ systems are formed of a single charged alkali metal ($A$), a 3d transition ion of double charge ($B$) and a halide anion ($X$). The magnetic ions are arranged in one dimensional chains favoring 1D behavior [68]. It has turned out that the magnetic exchange between spins along the chain is approximately three orders of magnitude higher than the interchain coupling. Furthermore, anisotropy found in these kind of systems varies from easy-axis to easy-plane anisotropy. It is of the same order as the interchain exchange. Magnetic correlations in the paramagnetic phase are thus dominated by the intrachain exchange, as temperature destroys the interchain exchange.

In particular, the $ABX_3$ compound $CsVBr_3$ belongs to the hexagonal space group [69]. Vanadium ions are located at the corners of the nuclear unit cell. The chains of $S = 3/2$ spins run along the $c$ axis, i.e. perpendicular to the basal plane. The compound is characterized as a triangular frustrated spin system below its Néel temperature of 20.4 K. Antiferromagnetic exchange is found along the $c$ axis and within the basal plane. Dipolar exchange gives raise to an $XY$-like anisotropy, that forces spins within the hexagonal plane. In the ordered phase the ratio of the intrachain to the interchain exchange yields $\sim 1012$. It is expected that the interchain exchange is destroyed upon increasing temperature. In the paramagnetic phase the strong intrachain exchange dominates the spin dynamics, which turns $CsVBr_3$ into an ideal candidate for studying low dimensional spin dynamics. Moreover, the temperature dependence of susceptibility, measured in a tem-

perature range from 1 K to 400 K, follows the antiferromagnetic 1D Heisenberg model [70].

From a theoretical point of view the comparison of different $ABX_3$ compounds that differ in the strength of the magnetic exchange, the anisotropy or the spin quantum number addresses general aspects of antiferromagnetic integer and half odd integer spin chains. Based on the gapless spinon continuum of the antiferromagnetic $S = 1/2$ chain it is commonly accepted that the dispersion of all half odd integer spin chains is gapless. In contrast, as predicted by Haldane, spin dynamics of integer spin chains feature the Haldane gap. The quasi 1D system $CsVBr_3$ approaches the quantum chain with its spin number 3/2. We will test the assumption of a gapless excitation spectrum in this compound.

# Chapter 3

# Experimental Methods

*Chapter 3 introduces the experimental methods that were applied to elucidate the magnetic behavior of quasi 1D $Ca_{2+x}Y_{2-x}Cu_5O_{10}$ and $CsVBr_3$. Besides macroscopic measurement techniques that probe the thermodynamical behavior of samples neutron scattering allows the investigation of the static and dynamic order on interatomic length scales.*

## 3.1 Bulk investigations

The first characterization of a sample is usually done by X-ray diffraction, in order to determine the crystal structure. The existence of magnetic order in the sample and macroscopic properties such as susceptibility and heat capacity are probed by bulk measurements. During this thesis a conventional calorimeter (Physical Property Measurement System, PPMS, by Quantum Design, Inc.) was employed [71]. The basic unit supplies a cryostat with superconducting coils next to the sample chamber (see Figure 3.1). These coils provide a stable external magnetic field up to $\pm 9\,\mathrm{T}$. Next to them a set of pick-up coils are placed for measuring the magnetic response of the sample by detecting the induced voltage when the sample is transported through the pick-up coils. Various supplementary measurement options can be installed into the sample chamber allowing for the investigations of magnetic phenomena such as static and dynamic susceptibility or magnetic phase transitions.

### 3.1.1 Magnetization

Both the D.C. and A.C. magnetization measurement technique are based on the principle of inductive magnetometry. The magnetic response of the sample is determined by voltage changes induced in the pick-up coils according to Faraday's law. The accuracy of both options depends on the measured quantity and vary from $3 \cdot 10^{-5}\,\mathrm{emu}$ to $1 \cdot 10^{-8}\,\mathrm{emu}$ for D.C. and A.C. magnetization, respectively. The D.C. technique determines the magnetization $M(T, H)$ of the sample that is proportional to the susceptibility $\chi(T, H)$, while A.C. magnetization probes its derivative. The latter technique is thus more sensitive towards small changes of $M(T, H)$.

During D.C. measurements a sample that is premagnetized by the time-constant external field $H$ moves through the cylindrical detection coils and induces a voltage. The amplitude of this signal is proportional to the speed of the sample ($\sim 100\,\mathrm{cm/s}$) during

the extraction. The voltage is proportional to the rate of the change of the magnetic flux through them, i.e. the voltage profile is the time derivative of the net flux through the coils. The sample moment is obtained by numerically integrating the voltage profile and fitting the known waveform for a dipole moving through the detection coils to the resulting data. Using this technique the susceptibility of the sample $\chi(T) = M(T)/H$ is deduced.

In A.C. measurements a small drive field with frequency $\omega$ is used that can be superimposed to an external D.C. field. It causes a time-dependent moment in the sample. The field of the time-dependent moment induces a current in the pick-up coils allowing measurements without sample motion. The derivative of the magnetization $\chi_{\text{A.C.}} = dM(T)/dH$ is thus extracted from the sample. At high frequencies the A.C. moment of the sample does not follow the D.C. magnetization curve owing to dynamic effects in the sample (the A.C. susceptibility is often known as the dynamic susceptibility). The magnetization of the sample may lag behind the drive field and therefore yields two quantities, the magnitude of the susceptibility and the phase shift via $\chi_{\text{A.C.}} = \chi' + i\chi''$, where $\chi'$ represents the real part of the dynamical susceptibility. The imaginary part $\chi''$ has a character of an absorption coefficient. The angle $\varphi = \arctan(\chi''/\chi')$ describes a phase lag of the magnetization behind the external field H.


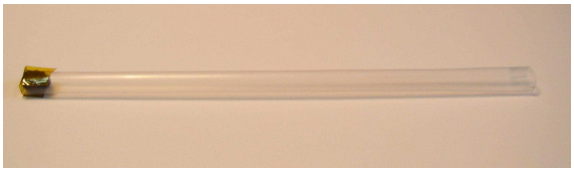

Figure 3.1: Left figure: The Physical Property Measurement System (PPMS, Quantum Design, Inc.) allows for a temperature range of 1.8 K to 400 K with an external vertical field from zero Tesla to $\pm 9$ T. Figure above: straw sample holder, in which a solid or powder sample is placed and that would be loaded into the sample chamber.

During an experiment powder or solid samples were mounted into a straw sample holder (see Figure 3.1). The end of the sample holder is closed using Kapton tape. After inserting the sample holder into the cryostat chamber, the sample center with respect to the magnetic signal is placed to be in the middle of the coils.

### 3.1.2 Heat capacity

Using the heat capacity option of the PPMS specific heat of a sample is measured by the relaxation technique [72]. A heater attached to the sapphire sample platform of the sample holder induces a constant heat pulse in the sample whose relaxation to the equilibrium temperature of the sample holder is measured (see Figure 3.2). The applied fitting algorithm results in the sample heat capacity $C_P(T) = (dQ/dT)_P$ at constant pressure $P$ at zero or applied external field, respectively. Here, $Q$ denotes the applied energy to the system in terms of thermal heat. In order to maintain a defined equilibrium pressure, the sample space is evacuated. The sample holder wires connecting the outer frame and the sapphire platform are calibrated in each magnetic field below a temperature of 20 K, since a Shottky anomaly of the wire material yields changes in the signal of up to the order of two. Thermal contact between the sample and the sample platform is provided by a thermal joint compound whose contribution to the sample specific heat has to be calibrated for each sample in every measured field.

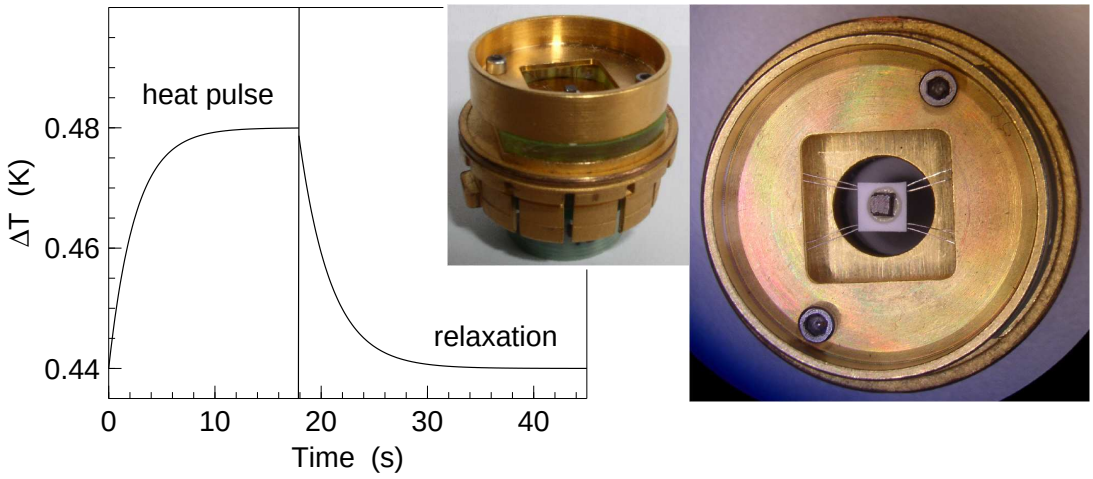


Figure 3.2: Scheme of the specific heat measurement principle. Side and top view of the sample holder. A sapphire platform is hold by eight wires that are used for the measurement of the time relaxation of the sample temperature to the platform temperature after having applied a heat pulse. The sample is attached to the platform by a thermal joint compound providing a thermal coupling of the sample to the platform.

## 3.2 Neutron scattering

Neutron spectroscopy is particular valuable for investigating microscopic structural and dynamical properties of polycrystalline and single crystalline ordered systems. For a detailed overview of this technique refer to [73, 74, 75, 76].

Neutrons directly interact with the nuclei of atoms in the target. Moreover, although uncharged, neutrons bear a magnetic moment $\boldsymbol{\mu_n}$ with spin 1/2 yielding an interaction with unpaired electrons of the target atoms. During the scattering process microscopic nuclear and magnetic properties of the target are simultaneously probed.

The scattering event is characterized by the change of the momentum and energy of the

scatterer and the target. Neutrons with a defined incident wavevector $\mathbf{k}$ and energy $E$ that are monochromatized from a white beam with an Maxwellian distribution scatter on the sample. This yields a changed wavenumber $\mathbf{k}'$ and energy $E'$ of the neutron. The sample that was initially in the state $\lambda$ and is transfered to its scattered state $\lambda'$ gains or looses the momentum transfer $\mathbf{Q} = \mathbf{k} - \mathbf{k}'$ and energy $\hbar\omega = E - E' = \hbar^2 \left(k^2 - k'^2\right)/(2m) = E_{\lambda'} - E_\lambda$ where $m$ denotes the neutron mass (see Figure 3.3). Elastic scattering is defined by no energy exchange between probe and target ($k = k'$) that leads to Bragg's law $Q = G = 2\pi/d$. Here, $\mathbf{G}$ denotes a reciprocal lattice vector on the Ewald sphere that is equivalent to the scattering vector and $d$ the corresponding interplanar spacing. Inelastic scattering results in a change of the sample and the neutron energy with the scattering vector $\mathbf{Q} = \mathbf{G} \pm \mathbf{q}$. In this notation $\mathbf{q}$ refers to the reduced scattering vector in the first Brillouin zone.

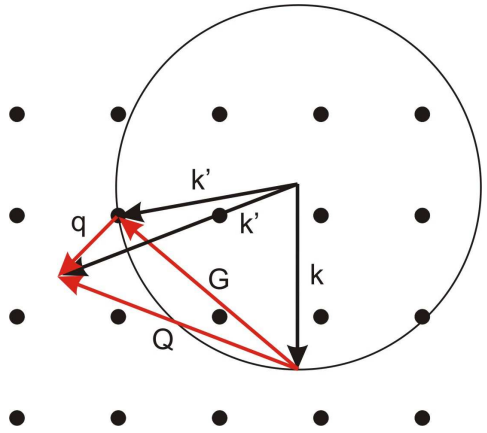


Figure 3.3: Scheme of the two dimensional reciprocal space of a square lattice. The elastic scattering geometry is defined by $\mathbf{Q} = \mathbf{G} = \mathbf{k} - \mathbf{k}'$. $\mathbf{k}$, $\mathbf{k}'$ and $\mathbf{Q}$ denote the incident/final neutron wavevector and the scattering vector. During an inelastic scattering event the momentum conservation $\mathbf{Q} = \mathbf{G} \pm \mathbf{q} = \mathbf{k}' - \mathbf{k}$ applies, where $\mathbf{q}$ represents the reduced scattering vector in the first Brillouin zone.

Respecting Fermi's Golden Rule as well as the energy conservation for the scattering process the number of neutrons, scattered at the potential $V$ per time interval into an angular region $d\Omega$ and energy interval $[E', E' + dE]$ and normalized to the incoming flux, are given by the partial differential cross section

$$\left(\frac{d^2\sigma}{d\Omega dE'}\right)_{\mathbf{k},\lambda\to\mathbf{k}',\lambda'} = \frac{k'}{k}\left(\frac{m}{2\pi\hbar^2}\right)^2 \left|\left\langle \mathbf{k}'\lambda'|\hat{V}|\mathbf{k}\lambda\right\rangle\right|^2 \delta(E_\lambda - E_{\lambda'} + E + E'). \tag{3.1}$$

Assuming the scattering potential weak and only of short range order compared to the neutron wavelength the evaluation of the matrix element is equivalent to the first Born approximation with plane waves for the incident and final neutron states. The measured partial differential cross section includes the ensemble average over all incident and final states of the target weighted by $p_\lambda = \exp\left(-E_\lambda\beta\right)/Z$, where $Z = \sum_\lambda \exp\left(-E_\lambda\beta\right)$ denotes the partition function and $\beta = (k_B T)^{-1}$ the inverse temperature.
The double differential cross section can be split into a coherent and incoherent part, respectively. For the first kind of scattering interference effects between different atoms lead to a distinct $\mathbf{Q}$ dependence, whereas for incoherent scattering the random distribution of the deviations of the scattering lengths from their mean value owing to fluctuations, isotope mixtures or lattice defects give raise to $\mathbf{Q}$ independent scattering.

Further evaluation of the double differential cross section yields the scattering function $S(\mathbf{Q}, \omega)$ via

$$\frac{d^2\sigma}{d\Omega dE'} \propto \frac{k'}{k} S(\mathbf{Q}, \omega)\,. \tag{3.2}$$

This quantity accounts for the sample response during an experiment and has to be calculated for each type of scattering potential. In the following section important equations for the scattering function used in this thesis shall be briefly derived, with emphasis on magnetic scattering. A more profound explanation of selected expressions are provided in the corresponding chapters of this work, where the data analysis is noted.

### 3.2.1 Coherent nuclear and magnetic scattering

For nuclear scattering the Fermi pseudo-potential

$$\hat{V}(\mathbf{r}) = \frac{2\pi\hbar^2}{m} \sum_j b_j \delta(\mathbf{r} - \mathbf{R}_j) \tag{3.3}$$

describes the interaction between scattered neutrons and different scattering centers (nucleus $j$ with scattering length $b_j$) at position $\mathbf{R}_j$ in the sample. Elastic scattering probed in a diffraction experiment only yields response at reciprocal lattice vectors $\mathbf{G}$. Considering the corresponding differential cross section

$$\left.\frac{d\sigma}{d\Omega}\right|_{coh}^{el,\,N} = \int_0^\infty \frac{d^2\sigma}{d\Omega dE'} dE' = N\frac{(2\pi)^3}{v_o} \sum_{\mathbf{G}} \delta(\mathbf{Q} - \mathbf{G}) |F_N(\mathbf{G})|^2 e^{-2W} \tag{3.4}$$

the nuclear structure factor $F_N(\mathbf{G}) = \sum_j b_j e^{i\mathbf{G}\cdot\mathbf{d_j}}$ accounts for the scattering intensity at the reciprocal lattice point $\mathbf{G}$. It results from all atoms $j$ in the unit cell at position $\mathbf{d}_j$ ($1 \leq j \leq N$). Temperature dependent displacement $\mathbf{u}$ of the atoms from their mean position are comprised in the Debye-Waller factor $e^{-2W}$ with $W = \frac{1}{2}\langle(\mathbf{Q}\cdot\mathbf{u})^2\rangle$. The quantity $v_0$ denotes the volume of the investigated nuclear unit cell.
The inelastic scattering function is related to the imaginary part of the dynamical susceptibility $\chi''(\mathbf{Q},\omega)$ by the fluctuation-dissipation theorem

$$S(\mathbf{Q},\omega) = (n(\omega)+1)\chi''(\mathbf{Q},\omega) \tag{3.5}$$

with $n(\omega) = (e^{\hbar\omega\beta} - 1)^{-1}$ denoting the Bose function. Note the asymmetry of the scattering function, known as the principle of detailed balance $S(-\mathbf{Q},-\omega) = e^{-\hbar\omega\beta} S(\mathbf{Q},\omega)$, putting an increased statistical weight on the the particle creation than on the particle annihilation process. Accounting for the nuclear dissipative part of the linear response various models can be used, among those such of the damped harmonic oscillator (see appendix C). The latter usually describes the lineshape of the scattering function in the frequency domain.

Magnetic scattering occurs owing to the interaction of the magnetic dipole moment of the neutron $\boldsymbol{\mu}_n = -\gamma\mu_N\boldsymbol{\sigma}$ with the moment of unpaired electrons $\boldsymbol{\mu}_e = -2\mu_B\mathbf{s}$ in the target. The quantity $\gamma = 1.913$ defines the gyromagnetic ratio, $\mu_N$ and $\mu_B$ denote the nuclear and Bohr magneton, $\boldsymbol{\sigma} = 2\mathbf{s}/\hbar$ the Pauli spin operator and $\mathbf{s}$ the spin angular momentum operator. The scattering potential $V_M(R)$ at the position $\mathbf{R}$ arises from the electron dipole moment $\boldsymbol{\mu}_e$ and the motion of the electron of momentum $\mathbf{p}$

$$\begin{aligned} V_M(\mathbf{R}) &= V_S(\mathbf{R}) + V_L(\mathbf{R}) \\ &= -\mu_N\mu_B\frac{\mu_0}{4\pi}\boldsymbol{\sigma}\left(\nabla\times\left(\frac{\mathbf{s}\times\hat{\mathbf{R}}}{R^2}\right) + \frac{1}{\hbar}\frac{\mathbf{p}\times\hat{\mathbf{R}}}{R^2}\right), \end{aligned} \tag{3.6}$$

where $\hat{\mathbf{R}}$ denotes the unit vector in $\mathbf{R}$ direction.
Evaluating the matrix element $\langle \mathbf{k}'\lambda'\sigma'|V_m|\mathbf{k}\lambda\sigma\rangle$ for the wave vector dependence $\mathbf{k}$ yields $\langle \lambda'\sigma'|\sigma \cdot \mathbf{S}_\perp|\lambda\sigma\rangle$. Here, the magnetic interaction vector $\mathbf{S}_\perp$ is introduced

$$\mathbf{S}_\perp = \hat{\mathbf{Q}} \times (\mathbf{S} \times \hat{\mathbf{Q}}) = \mathbf{S} - \hat{\mathbf{Q}}(\hat{\mathbf{Q}} \cdot \mathbf{S}) \,, \tag{3.7}$$

where $\hat{\mathbf{Q}}$ is the unit vector of the scattering vector.
To derive the magnetic coherent double differential cross section, we have to consider the the magnetic scattering amplitude that is given by

$$p = \left(\frac{\gamma r_0}{2}\right) g f(\mathbf{Q}) \,. \tag{3.8}$$

Here, $r_0$ represents the classical electron radius, $g$ the Landé splitting factor with respect to the electron configuration of the magnetic atom in the target and $f(\mathbf{Q})$ the magnetic form factor. The latter is defined as the Fourier transformation of the normalized distribution of the magnetization density operator $\mathbf{M}(\mathbf{r})$ of the particular atom

$$f(\mathbf{Q}) = \frac{\left\langle \lambda \left| \int \mathbf{M}(\mathbf{r}) e^{i\mathbf{Q}\cdot\mathbf{r}} d\mathbf{r} \right| \lambda \right\rangle}{\left\langle \lambda \left| \int \mathbf{M}(\mathbf{r}) d\mathbf{r} \right| \lambda \right\rangle} \,. \tag{3.9}$$

$\mathbf{M}(\mathbf{r})$ comprises both the spin and orbital part of the magnetization density assumed as delta function at the particular spin positions for the spin contribution and the line integral of the orbital current density, respectively. The magnetic scattering amplitude $p$ is of the order of the nuclear scattering length $b$.
The coherent double differential cross section for magnetic scattering thus reads

$$\left.\frac{d^2\sigma}{d\Omega dE'}\right|_{coh} = N e^{-2W} p^2 \frac{k'}{k} \sum_{\alpha\beta} \left(\delta_{\alpha\beta} - \hat{Q}_\alpha \hat{Q}_\beta\right) S^{\alpha\beta}(\mathbf{Q},\omega) \,, \tag{3.10}$$

where $\alpha$ and $\beta$ denote the Cartesian coordinates $x$, $y$ and $z$. The factor

$$\sum_{\alpha\beta} (\delta_{\alpha\beta} - \hat{Q}_\alpha \hat{Q}_\beta) \tag{3.11}$$

is often called the selection rule for magnetic scattering. Only fluctuations perpendicular to the scattering vector contribute to the magnetic cross section. The response function

$$S^{\alpha\beta}(\mathbf{Q},\omega) = \frac{1}{2\pi} \int_{-\infty}^{\infty} dt\, e^{-i\omega t} \sum_l e^{i\mathbf{Q}\mathbf{r}_l} \left\langle S_0^\alpha(0) S_l^\beta(t) \right\rangle \tag{3.12}$$

is the time and space Fourier transformed quantity of the spin pair correlation function $\left\langle S_0^\alpha(0) S_l^\beta(t) \right\rangle$ and explains the interference between a spin at the position $\mathbf{r}_0 = 0$ and time equal to zero to other spins $l$ at the position $\mathbf{r}_l$ at time $t > 0$.
According to elastic nuclear scattering the elastic magnetic coherent cross section is defined by

$$\left.\frac{d\sigma}{d\Omega}\right|_{coh}^{el,\,M} = N_M \frac{(2\pi)^3}{v_M} \sum_{\mathbf{G}_M} \delta(\mathbf{Q} - \mathbf{G}_M) |F_M(\mathbf{G}_M)|^2 e^{-2W} \,, \tag{3.13}$$

where $\mathbf{G}_M$ describes a magnetic reciprocal vector, $v_M$ the volume of the magnetic unit cell and $N_M$ the number of atoms in the unit cell. The magnetic structure factor $F_M(\mathbf{G}_M) = \sum_j p_j \mathbf{S}_{\perp j} e^{i\mathbf{G}_M \cdot \mathbf{d}_j}$ defines the amplitude of magnetic scattering at $\mathbf{G}_M$ to which the different magnetic atoms in the unit cell contribute.

### 3.2.2 Triple axis and time of flight spectroscopy

Two different types of spectrometers apply for measuring inelastic response of a target. The first type of instruments is a triple axis spectrometer (TAS, see Figure 3.4) that is based on the principle of B. N. Brockhouse. During a scan one particular point ($\mathbf{Q}$,$\omega$) is probed. Using a time of flight (tof) spectrometer a broad ($\mathbf{Q}, \omega$) space is instantaneously reached. In the following important aspects of both principles will be briefly presented, beginning with the TAS principle.

Out of a primarily collimated white neutron beam with a Maxwellian distribution a certain wavelength $\lambda$ is selected by a crystal monochromator (lattice spacing $d$). Bragg's law $2d \sin(\theta_M) = n\lambda$ defines the desired wavelength $\lambda$ from the incoming wavevector $\mathbf{k} = 2\pi/\lambda$. $2\theta_M$ defines the scattering angle of the neutrons on the monochromator crystal. Common monochromator materials are pyrolytic graphite (PG(002)), Heusler alloys (Heusler(111)) or copper crystals (Cu(111)). Higher orders of the incoming beam are effectively reduced by inserting a filter (beryllium or graphite) providing resonance absorption for certain neutron energies. The scattered neutrons will reach the sample after further collimation. Energy exchange with the sample modifies the wavevector of the scattered neutrons to $\mathbf{k}'$ (scattering angle $2\theta_S$). Though neutrons are scattered into a solid angle $d\Omega = 2\theta_S 2\Phi$ only neutrons in the scattering plane (defined by the scattering angle) are counted by the detector. Before reaching the detector neutrons scatter on the analyzer crystal (similar materials compared to the monochromator, scattering angle $2\theta_A$) with possible collimation before and after the analyzer. The final neutron energy is thus again defined by Bragg's law. The detector itself consists of a $^3$He beam tube counting arriving neutrons. In order to normalize for the incoming neutrons, a monitor is installed before the monochromator.

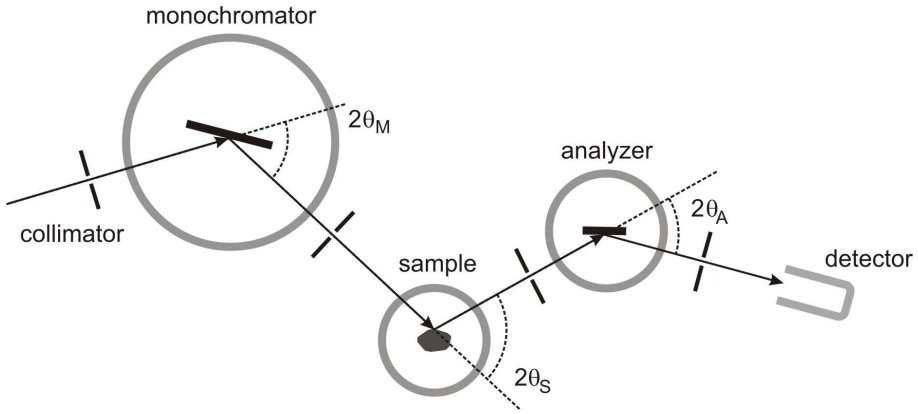


Figure 3.4: Scheme of a triple axis spectrometer in W configuration. The energy and momentum change of the sample is given by three axis (monochromator, sample and analyzer) with its corresponding scattering angles $2\theta_M$, $2\theta_S$ and $2\theta_A$.

The TAS instrument can be operated in two different modii. Using a fixed final energy the final wavevector $\mathbf{k}'$ of the scattered neutrons is kept constant, whereas the scattering vector $\mathbf{Q}$ and the incoming wavevector $\mathbf{k}$ vary. Keeping the incident energy of the neutrons constant defines the sample energy and momentum transfer by changing the scattering vector $\mathbf{Q}$ and the final wavevector $\mathbf{k}'$. Here, $k'^3/\tan\theta_A$ has be multiplied to the

measured intensity to obtain the true partial differential cross section. This geometrical factor accounts for the dependence of the energy resolution on the final wavevector.
In order to account for the probability that a neutron in a scattering process at ($\mathbf{Q}_0$,$\omega_0$) is detected within a particular deviation $\Delta\omega$ and $\Delta\mathbf{Q}$ from this point, the four dimensional resolution function $R(\mathbf{Q}-\mathbf{Q}_0, \omega-\omega_0)$ has to be included. It describes the reduced detection probability with respect to Gaussian angular distributions of a finite collimation and the mosaic spread of the monochromator, sample and analyzer crystal [77, 78]. Moreover, the curvature of the monochromator and analyzer, the sample geometry as well as the spatial configuration of the instrument set-up can be considered for the resolution function [79]. The measured intensity is proportional to the convolution of the partial differential cross section with the resolution function.

A complimentary technique to triple axis spectroscopy makes use of a time of flight instrument. For this purpose a pulsed neutron beam is required. Whereas a spallation source already provides time separated neutrons, the continuous flux of a reactor has to be interrupted with a defined frequency. The primary spectrometer provides the pulse sequence of neutrons obtained by a chopper system. The wavelength selection of the neutrons is achieved by either using the latter or by monochromator crystals according to Bragg's law. A suppressor chopper that rotates at a fraction of the frequency of the previous choppers allows for the possibility to cancel out additional neutron pulses. In case of a crystal monochromated spectrometer higher orders of $\lambda$ shall be suppressed by a Beryllium filter. Directly in front of the sample chamber a monitor is installed in order to normalize for the incoming neutron flux. The secondary spectrometer allows for determining both the momentum transfer $Q$ of the scattered neutrons at the sample site as well as their energy transfer $\hbar\omega$. It consists of a detector box equipped with detector banks in various heights at the distance $L$ from the sample site. The distance $L$ defines the flightpath. Typically an angular range $2\theta$ from $\sim 15^\circ$ to $\sim 120^\circ$ is covered with $^3$He beam tubes. Ideally, the whole flightpath of the neutron is purged with helium or argon, in order to avoid diffuse scattering on molecules in air.
The momentum transfer of the neutron is given by the angle $2\theta$ between the incoming and outgoing wavevector via $Q^2 = k^2 + k'^2 - 2kk'\cos\theta$. The energy transfer to the sample is obtained as the difference of the initial energy of the neutron compared to the scattered neutron using the energy-wavelength dependence $E \propto 1/\lambda^2$. Using the de-Broglie relation $\lambda = 3956/v$ the wavelength is determined by the non relativistic neutron velocity $v = L/t$. $t$ denotes the time that a neutron needs passing from the sample to the detector.

### 3.2.3 Reduction of time of flight data

We introduce to the raw data reduction of time of flight data by explaining the necessary correction factors that have to be applied to the measured intensity $I(2\theta, tof)$ [80]. Important quantities of neutron scattering such as the scattering law and the resolution function are related to $I(2\theta, tof)$.

We recall the relation between the scattering law $S(\mathbf{Q},\omega)$ and the partial differential cross section $d^2\sigma/(d\Omega dE')$

$$\frac{d^2\sigma}{d\Omega dE'} \propto \frac{k'}{k} S(\mathbf{Q},\omega)\,, \tag{3.14}$$

where $\mathbf{Q} = \mathbf{k} - \mathbf{k}'$ denotes the scattering vector, $E' = E - \hbar\omega$ the final neutron energy and $d\Omega$ the solid angle, to which neutrons scatter. Separating coherent from incoherent scattering $S(\mathbf{Q}, \omega)$ reads

$$S(\mathbf{Q}, \omega) = \frac{\sigma_{inc}}{4\pi} S_{inc}(\mathbf{Q}, \omega) + \frac{\sigma_{coh}}{4\pi} S_{coh}(\mathbf{Q}, \omega) \tag{3.15}$$

with the weighting factor $\sigma_{inc}$ and $\sigma_{coh}$ that denote the total coherent and incoherent cross section, respectively. The measured intensity $I(\mathbf{Q}, \omega)$ is the convolution of the partial differential cross section and the resolution function $R(\mathbf{Q} - \mathbf{Q}', \omega - \omega')$

$$I(\mathbf{Q}, \omega) \propto \int d\omega' d\mathbf{Q}' S(\mathbf{Q}', \omega') R(\mathbf{Q} - \mathbf{Q}', \omega - \omega') \tag{3.16}$$

respecting the wavevector and energy broadening of the measured $(\mathbf{Q}, \omega)$-point.

During a time of flight experiment data are simultaneously obtained for an angular range $2\theta_{i_{min}} \leq 2\theta_i \leq 2\theta_{i_{max}}$ $(i \in [i_{min}, i_{max}])$. For each angle $2\theta_i$ the measured intensity $I(2\theta, tof)$ depends on time of flight $tof$ measured in units of time/length. $tof$ is related to the time $t$ neutrons need to cover the flight path $L$ and thus the neutron energy $E = m/(2tof^2)$. Here, $m$ denotes the neutron mass. Elastically scattered neutrons arrive at the detector at time $tof_{el}$ that is defined by the incident neutron energy $E$. An inelastic scattering event of a neutron yields a modified neutron velocity and consequently a shift of the arriving time at the detector compared to elastically scattered neutrons. The measurement process is continuous in time and is realized by equidistant time channels.

When deducing the scattering law based on the measured intensity $I(2\theta, tof)$, important aspects have to be paid attention to. The scattering law depends on the norm of the scattering vector $\mathbf{Q}$, since the accessible $(Q,\omega)$ space is defined by $Q = \sqrt{k^2 + k'^2 - 2kk' \cos\theta}$. The resolution function defined in the $(2\theta,\omega)$ space is thus a function of the energy transfer for a constant scattering angle. The observed intensity yields a broadening in $\omega$. Several correction factors are applied to $I(2\theta, tof)$ for deducing $S(Q, \omega)$ that will be presented in the following. Among those are the normalization of the measured intensity to the incoming neutron flux $\Phi$, the correction for different detector efficiencies and the self absorption of both the sample and its surrounding container. Moreover, interpolation to constant wavenumbers has to be considered.

The measured intensity $I(2\theta, tof)$ counts the number of neutrons $N$ being detected with a probability $p_i$ at a particular scattering angle $2\theta_i$ within a time interval $\Delta t_i$ and the solid angle $\Delta\Omega_i$

$$N_i = p_i A_S \Phi \Delta t_i I(2\theta, tof) \Delta\Omega_i \,. \tag{3.17}$$

$A_S$ denotes the illuminated area of the sample and $\Delta t_i$ the detection time that is divided into a certain number of time channels of equidistant width. Normalization of the detector counting rate to that of the monitor $N_M$,

$$N_M = p_M A_M \Phi \Delta t_i \,, \tag{3.18}$$

yields the quantity $\tilde{N}$ with

$$\tilde{N} = \frac{p_i A_S}{p_M A_M} I(2\theta, tof) \Delta\Omega_i \,. \tag{3.19}$$

$A_M$ and $p_M$ defines the monitor area and the monitor efficiency, respectively. $\tilde{N}$ turns independent of the incoming neutron flux and the measured time.
Correcting this quantity for the monitor normalized number of neutrons scattered on the standard sample vanadium that was measured in equal experimental conditions compared to the sample results in $\tilde{I}(2\theta, tof)$. We obtain the sample intensity that is corrected for the efficiency of each detector.
Figure 3.5 (a) shows typical sample and empty can data depending on $tof$ for one scattering angle $2\theta_i$ that are corrected for the monitor counts and vanadium. Figure 3.5 (b) depicts the corresponding vanadium data that are summed over the elastic line. This plot illustrates different detector efficiencies for each scattering angle $2\theta_i$. The two observed peaks originate from scattering on the aluminum sample holder.

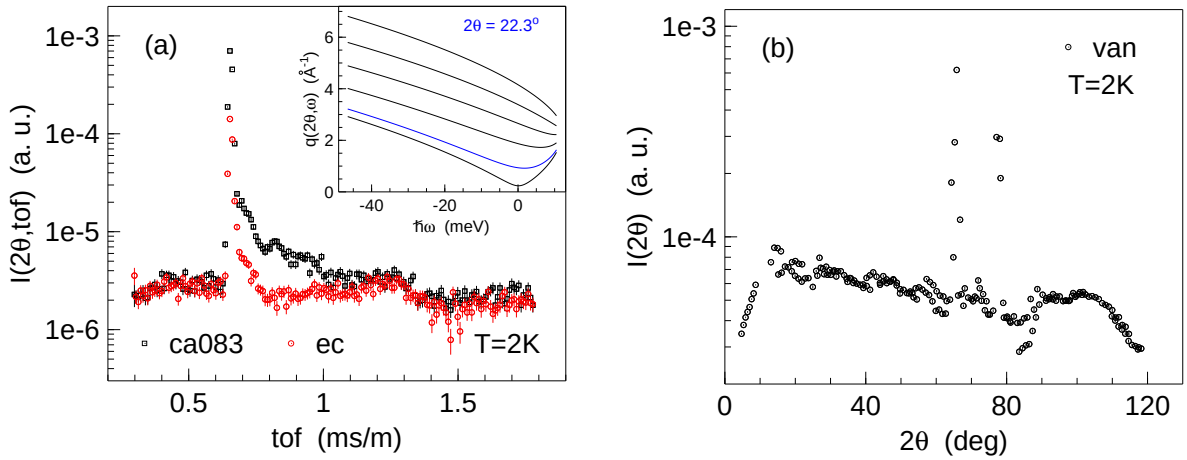


Figure 3.5: $Ca_{0.83}CuO_2$ (ca083), vanadium (van) and empty can (ec) data measured on IN4 with an incident wavelength of 2.6 Å at 2 K. (a) Sample and empty can data are obtained at $2\theta = 22.3°$ (summed over ten detector angles and three time channels). Both data sets are normalized to the monitor and vanadium. The inset illustrates the accessible $(Q, \omega)$ space. (b) Vanadium data summed over the elastic line. The two Bragg reflections originate from scattering on the aluminum sample container.

Further transfer of $\tilde{I}(2\theta, tof)$ to $\tilde{I}(2\theta, \omega)$ considers a factor $tof^4$ that results from the relation

$$\frac{d^2\sigma}{d\Omega dE'} \propto \frac{d^2\sigma}{d\Omega dtof}\left|\frac{dtof}{dE'}\right| \propto \frac{d^2\sigma}{d\Omega dtof}\left|tof^3\right| \tag{3.20}$$

and $k' \propto 1/tof$. This factor turns evident at $\omega > 0$ (neutron energy loss). A proper subtraction of the instrumental background at small $tof$ reduces the effect before converting the monitor and vanadium normalized data to $\tilde{I}(2\theta, \omega)$ (see Figure 3.6 (a)).
Considering absorption effects on the sample and the sample container during the scattering process a simple subtraction of the container signal from the combined sample and container signal does not hold. Two absorption factors have to calculated accounting for both contributions depending on the chosen sample geometry [81]. The scattering function of the sample $S(2\theta, \omega)$ is thus related to the combined sample and empty can intensity $\tilde{I}_{S,C}(2\theta, \omega)$ and the empty can intensity $\tilde{I}_C(2\theta, \omega)$

$$S(2\theta, \omega) = \frac{1}{A_S(\theta, \omega)}\tilde{I}_{S,C}(2\theta, \omega) - \frac{A_{rel}(2\theta, \omega)}{A_S(\theta, \omega)}\tilde{I}_C(2\theta, \omega)\,, \tag{3.21}$$

where $A_S(2\theta,\omega)$ denotes the absorption coefficient for a scattering process of a neutron on the sample and its absorption while passing the latter. $A_{rel}(2\theta,\omega) = A_C(2\theta,\omega)/A_S(2\theta,\omega)$ is defined as the relative absorption between scattering on the container and scattering on the sample, respectively. For all time of flight experiments performed during this thesis a hollow cylinder with an annular sample geometry was chosen. In this case the angular dependence of $A_i(2\theta,\omega)$ ($i \in \{A,C\}$) is almost negligible, whereas a clear energy dependence is observed. $\omega > 0$ corresponding to neutron energy loss processes yields a decrease of both absorption coefficients. The strength of this effect depends on the accessible energy transfer and is more pronounced for larger $\omega$. Figure 3.6 (b) displays the absorption coefficient $A_s(2\theta,\omega)$ of $Ca_{0.83}CuO_2$ at 2.6 Å.

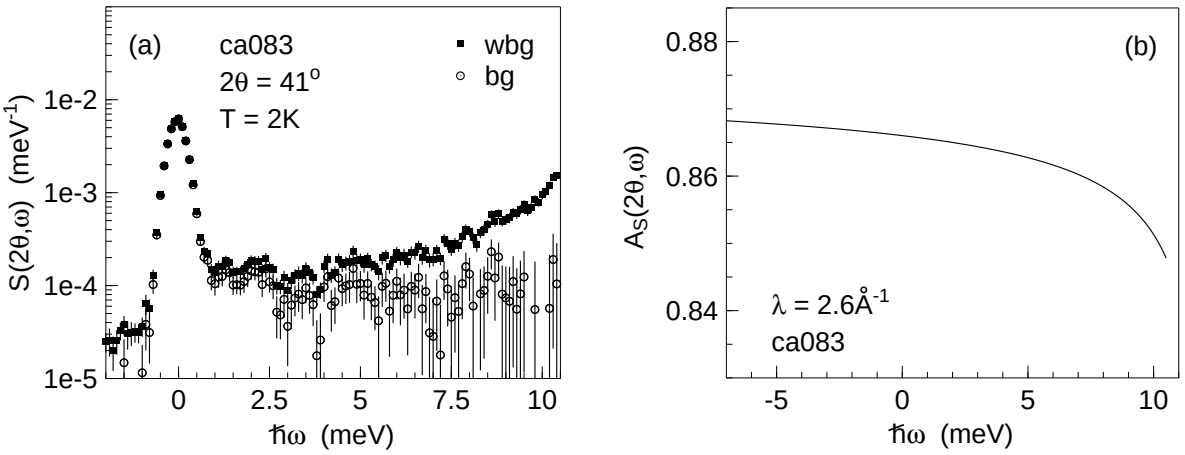


Figure 3.6: Data of $Ca_{0.83}CuO_2$ (ca083) measured on IN4 with an incident wavelength of 2.6 Å at 2 K. (a) $S(2\theta,\omega)$ not corrected/corrected (wbg/bg) for the instrumental background in $tof$, respectively. The measured data are shown on a constant energy grid. (b) Self absorption factor $A_S(2\theta,\omega)$ of $Ca_{0.83}CuO_2$.

Interpolation to constant wavenumbers $Q$ yields the desired quantity $S(Q,\omega)$, where the nonlinear relation between $Q$ and the incoming and outgoing wavevector are taken into account.
Weighting $S(Q,\omega)$ with the detailed balance factor results in the symmetric scattering function. This correction is indispensable for low temperatures or large energy transfer. Obtaining the scattering function in absolute units the difference between the scattering power of the sample and the used vanadium has to be considered by a $Q$ independent factor.

### 3.2.4 Neutron scattering experiments

During this thesis work the compound series $Ca_{2+x}Y_{2-x}Cu_5O_{10}$ and the triangular frustrated antiferromagnet $CsVBr_3$ were studied by means of neutron spectroscopy, in oder to elucidate their quasi 1D magnetic behavior. Elastic and inelastic neutron scattering experiments were performed at the Forschungsreaktor München II (FRM II, Germany), Institut Laue-Langevin (ILL, France), the NIST Center for Neutron Research (NCNR, USA) and Paul Scherrer Institut (PSI, Switzerland). Table 3.1 provides an overview of the investigations contributing to this thesis.

For all experiments at the ILL, NIST and PSI orange cryostats were employed providing

a temperature range from 1.8 K to 300 K and a temperature stability of $\sim 0.1$ K. At the FRM II closed cycle refrigerators were used allowing for the temperature range of 3.5 K to 300 K and a temperature stability of better than 0.2 K.

$Ca_{2+x}Y_{2-x}Cu_5O_{10}$ samples were finely grounded and densely filled into vanadium or aluminum sample holders under helium atmosphere. $CsVBr_3$ was sticked into its sample holder using glue. The particular sample geometry of each experiment will be described in the experimental part of this thesis. Furthermore, necessary experimental details of each experiment are noted later.

| Sample | Static order | Dynamics |
|---|---|---|
| $Ca_2Y_2Cu_5O_{10}$ | DMC, SPODI, TASP | TASP, SPINS |
| $Ca_{2.5}Y_{1.5}Cu_5O_{10}$ | DMC, SPODI, TASP | - |
| $Ca_3Y_1Cu_5O_{10}$ | DMC, HRPT | - |
| $Ca_{3.1}Y_{0.9}Cu_5O_{10}$ | DMC | - |
| $Ca_{3.2}Y_{0.8}Cu_5O_{10}$ | DMC, HRPT | - |
| $Ca_{3.5}Y_{0.5}Cu_5O_{10}$ | HRPT | PANDA |
| $Ca_{0.83}CuO_2$ | D20, HRPT | IN3, IN4 |
| $CsVBr_3$ | - | TASP |

Table 3.1: Overview of the neutron scattering investigations performed on instruments of the FRM II, ILL, NIST and PSI for $Ca_{2+x}Y_{2-x}Cu_5O_{10}$ compounds and $CsVBr_3$. The instrumental set-up and the particular sample geometry is noted in the corresponding chapter.

# Chapter 4

# Quasi 1D behavior in $Ca_{2+x}Y_{2-x}Cu_5O_{10}$

*Literature reports a complex magnetic behavior of $Ca_{2+x}Y_{2-x}Cu_5O_{10}$ samples. To resolve this, we used various experimental techniques such as susceptibility and specific heat measurements as well as elastic and inelastic neutron spectroscopy. This chapter reports the experimental findings of these measurements. We introduce general properties of the compound series (see chapter 4.1) and present experimental findings (see chapter 4.2 to chapter 4.5). Finally, the obtained results are discussed with respect to other $CuO_2$ chain compounds (see chapter 4.6).*
*For clarity, each section of this chapter will contain a short summery.*

## 4.1 Sample preparation and characterization

This section is devoted to the sample preparation process of polycrystalline $Ca_{2+x}Y_{2-x}Cu_5O_{10}$ compounds and the analysis of their chemical composition (see chapter 4.1.1 and 4.1.2). Chapter 4.1.3 introduces the crystal structure of the investigated compound series. Electron paramagnetic resonance measurements were performed to define the Landé splitting factor $g$ that is used for data analyzing of susceptibility measurements (see chapter 4.1.4).

### 4.1.1 High pressure oxygen annealing

The sample synthesis of copper oxide compounds $Ca_{2+x}Y_{2-x}Cu_5O_{10}$ simultaneously enforces experimental conditions of temperatures of about $\sim 1100\,K$ and an oxygen pressure at the synthesis volume of higher than 200 bar. Single crystals of such materials are synthesized using a mirror furnace offering these requirements. During this work only powder samples were used.

$Ca_{2+x}Y_{2-x}Cu_5O_{10}$ samples with stoichiometric concentrations of $0 \leq x \leq 2.15$ were synthesized by a solid state reaction from the precursor materials $CaO/CaCO_3$, CuO and $Y_2O_3$[61]. The parent compound, undoped $Ca_2Y_2Cu_5O_{10}$, was prepared at 1000 K and ambient pressure based on CuO, $Y_2O_3$ and $CaCO_3$ (each material 99.999 %, Alfa Aesar). Doped samples ($0< x \leq 1.5$) were obtained from CuO (99.995 %, Alfa Aesar), $Y_2O_3$ (99.995 %, Alfa Aesar) and CaO (99.9 %, Alfa Aesar). During the synthesis the reaction

temperature and the oxgen pressure was about $\sim 1100\,\mathrm{K}$ and $\sim 200\,\mathrm{bar}$, respectively. For highly doped $Ca_{0.83}CuO_2$ CuO and CaO was used at similar experimental conditions compared to the synthesis of less doped samples. Substituting CaO for $CaCO_3$ during the synthesis of doped samples prevents the decomposition of $CaCO_3$ and CuO into $CO_2$ in the closed volume of the oven.

In order to prove the sample quality, we performed susceptibility measurements after the sample synthesis. Doped samples with $1 \leq x \leq 1.5$ provided evidence of a not totally completed sample synthesis reaction in terms of a too low D.C. magnetization signal compared to literature [61, 62]. Moreover, the second order phase transition from the paramagnetic to the Néel state that is visible in specific heat appeared very broad. A second annealing was performed, where the samples were reground, again pressed into pellets and heated in similar conditions compared to the first reaction. During this synthesis the oxygen pressure was increased yielding a higher sample homogeneity owing to an increased oxygen penetration of the samples.

Experimental conditions of the synthesis reaction of doped samples required a sample preparation in collaboration with Dr. S. Kazakov and Dr. J. Karpinski of the Laboratory for Solid State Physics, Eidgenössische Technische Hochschule, Switzerland. We synthesized the parent compound $Ca_2Y_2Cu_5O_{10}$ at the Walter Meissner Institute for low temperature physics, Munich, using the technical equipment of the crystal growth laboratory. Table 4.1 provides an overview of the available samples obtained during this thesis.

| Sample composition | Precursor material | T (K) | P (bar) | Time (h) |
|---|---|---|---|---|
| $Ca_2Y_2Cu_5O_{10}$ | CuO, $Y_2O_3$, $CaCO_3$ | 1000 | ambient | 36 |
| $Ca_{2.5}Y_{1.5}Cu_5O_{10}$ | CuO, $Y_2O_3$, CaO | 1100 | 200 | 20 |
| $Ca_{2.75}Y_{1.25}Cu_5O_{10}$ | CuO, $Y_2O_3$, CaO | 1100 | 200 | 20 |
| $Ca_{2.9}Y_{1.1}Cu_5O_{10}$ | CuO, $Y_2O_3$, CaO | 1100 | 200 | 20 |
| $Ca_3Y_1Cu_5O_{10}$ | CuO, $Y_2O_3$, CaO | 1100 | 500 | 20 |
| $Ca_{3.1}Y_{0.9}Cu_5O_{10}$ | CuO, $Y_2O_3$, CaO | 1100 | 500 | 20 |
| $Ca_{3.2}Y_{0.8}Cu_5O_{10}$ | CuO, $Y_2O_3$, CaO | 1100 | 450 | 45 |
| $Ca_{3.5}Y_{0.5}Cu_5O_{10}$ | CuO, $Y_2O_3$, CaO | 1100 | 530 | 50 |
| $Ca_{0.83}CuO_2$ | CuO, CaO | 1050 | 200 | 36 |

Table 4.1: Stoichiometric compositions, precursor materials and reaction conditions (temperature, oxygen pressure and time) of $Ca_{2+x}Y_{2-x}Cu_5O_{10}$ samples. The parent compound $Ca_2Y_2Cu_5O_{10}$ was synthesized at the Walter Meissner Institute, doped samples at the Eidgenössische Technische Hochschule, Switzerland.

In the following, the steps for synthesizing $\sim 15\,\mathrm{g}$ undoped $Ca_2Y_2Cu_5O_{10}$ is described in detail, which is representative for the synthesis of all $Ca_{2+x}Y_{2-x}Cu_5O_{10}$ samples.
Based on the reaction equation

$$Y_2O_3 + 2CaCO_3 + 5CuO \rightarrow Ca_2Y_2Cu_5O_{10} + 2CO_2 \tag{4.1}$$

$Y_2O_3$, CuO and $CaCO_3$ were separately annealed for 6 h at 740 °C, 6 h at 650° and 4 h at 500 °C, respectively. Afterwards, the dry powder were homogeneously mixed under

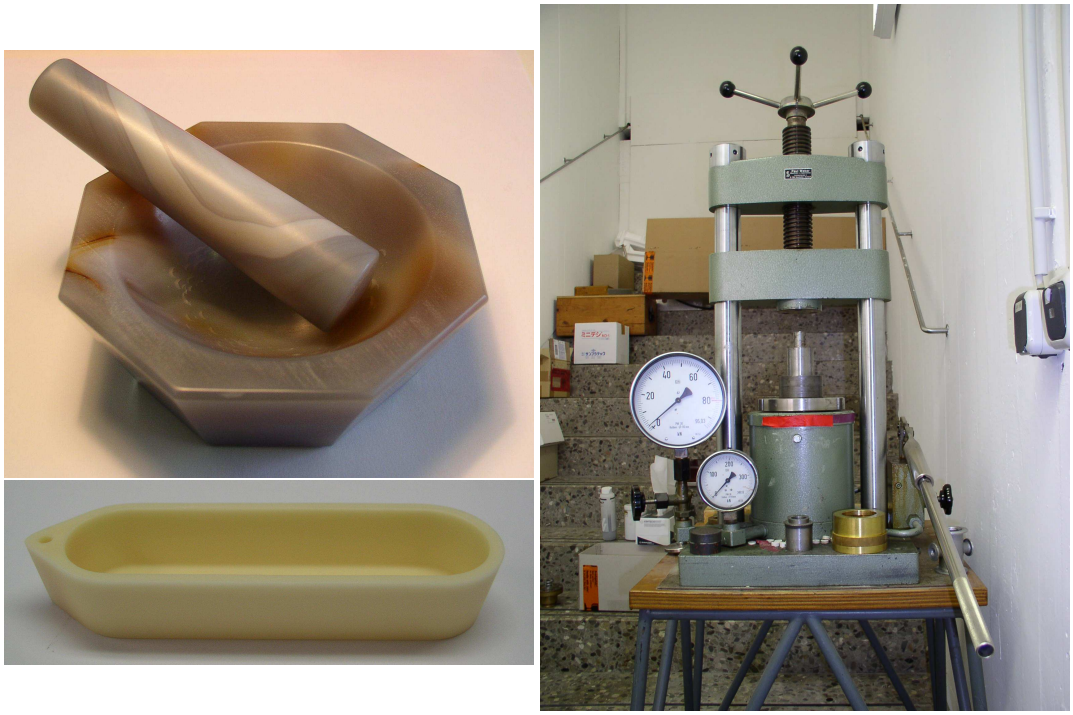

Figure 4.1: Technical equipment that was used during the sample synthesis process at the Walter Meissner Institute. Left figure: Mortar with basin and crucible for grinding the components into fine powder and heating up the pellets in the oven. Right figure: Moulding press for pressing the loose powder into pellets.

consideration of their required amount for 15 g sample mass (4.6040 g of $Y_2O_3$, 4.0814 g of $CaCO_3$ and 8.1093 g of CuO). The mixture was reheated at 900° in an $Al_2O_3$ crucible for 12 h in air atmosphere. The powder was again ground and pressed into 12 pellets (diameter $\sim$1 cm, height of each pellet $\sim$0.3 cm) and reheated at 950 °C for 10 h. Two times the pellets were reground and again pelletized. Each time the sample pellets were held at 1000 °C for 24 h and 36 h, respectively. During the heating and cooling procedure a temperature ramp of 100°/h was used. The sample synthesis was performed using a conventional oven (LH 30/14 by Nabertherm GmbH, Lilienthal). Figure 4.1 illustrates the used eqipment during the sample synthesis.

### 4.1.2 Sample stoichiometry

The magnetic behavior of $Ca_{2+x}Y_{2-x}Cu_5O_{10}$ is decisively influenced by the composition of the investigated sample. Deviations from the stoichiometric concentrations of the oxygen content and the calcium, copper and rare earth concentrations in terms of site vacancies or an additional amount of one particular ion will result in lattice distortions. In particular, it was shown for $Ca_{0.83}CuO_2$ that a small increase of the oxygen concentration yields a lower copper valency [82]. The number of magnetic copper ions within the chain increases and the degree of dimerization becomes less. The variation of the element concentrations are easily observed in bulk properties such as resistance, magnetization and specific heat.

We chose two approaches to verify the quality of the synthesized samples with respect to their element concentrations. The oxygen content was determined by Dr. E. Pomjakushina (Chemistry Department of the Paul Scherrer Institut, Switzerland) using iodometric titration [83]. The method of induced coupled plasma optical emission spectroscopy (ICP-OES) was applied to determine the stoichiometric concentration of yttrium, copper and calcium. The measurements were performed by S. Buchheit at the Radiochemistry Department of the Ludwigs-Maximilians-Universität München, Germany. Table 4.2 shows the results of both investigations.

| Nominal stoichiometry | Ca (p.f.u.) | Y (p.f.u.) | Cu (p.f.u.) | O (p.f.u.) |
|---|---|---|---|---|
| $Ca_2Y_2Cu_5O_{10}$ | 2.00(7) | 1.92(1) | 4.80(2) | 9.98 |
| $Ca_{2.9}Y_{1.1}Cu_5O_{10}$ | not performed | not performed | not performed | 10.00 |
| $Ca_3Y_1Cu_5O_{10}$ | 3.00(1) | 0.85(0.3) | 4.74(2) | 10.08 |
| $Ca_{3.2}Y_{0.8}Cu_5O_{10}$ | 3.20(1) | 0.78(0.3) | 4.93(2) | 10.02 |
| $Ca_{3.5}Y_{0.5}Cu_5O_{10}$ | 3.50((1) | 0.49(0.2) | 5.00(0.2) | 9.96 |
| $Ca_{0.83}CuO_2$ | 0.830(2) | - | 0.996(4) | 2.026 |

Table 4.2: Chemical analysis of synthesized $Ca_{2+x}Y_{2-x}Cu_5O_{10}$ samples. The element concentrations are given per formula unit (p.f.u.). Ca, Y, Cu concentrations were determined by means of ICP-OES, the oxygen content by iodometric titration. The error of the oxygen concentration is better than 0.2 % of the absolute value.

Almost all samples show a Cu deficiency of 3 % that may origin from Cu evaporation during the heating procedure. However, no evidence of this effect was found during the sample preparation and no compensation of the lost material was possible.

### 4.1.3 Crystal structure

The layered crystal structure of the compounds $Ca_{2+x}Y_{2-x}Cu_5O_{10}$ is closely related to the phases $NaCuO_2$ [84] and $CaCuO_2$ [85]. These samples feature edge sharing planar $CuO_2$ chains that are separated by planes with either alkali or rare earth ions [49, 50]. The copper oxide chains reside on an orthorhombic face centered sublattice that belongs to the space group Fmmm. The approximate lattice constants are $a \simeq 2.8\,\text{Å}$, $b \simeq 6.3\,\text{Å}$ and $c \simeq 10.6\,\text{Å}$. The $CuO_2$ chains run along the $a$ direction and are stacked along the two perpendicular directions. It is further known that the Ca/Y ions form an orthorhombic C centered sublattice, where the unit cell parameters are $a \simeq 3.4\,\text{Å}$, $b \simeq 6.3\,\text{Å}$ and $c \simeq 5.3\,\text{Å}$. A mismatch of five copper ions to four Ca/Y ions along the $a$ direction yields an incommensurate structure. In order to account for this modulation in the compounds, two approaches can be used: a large monoclinic unit cell and a superstructure.

Within the superstructure approach the strong nuclear satellite reflections in a diffraction pattern are indexed as $(h - \delta a,\, k,\, l \pm \delta c)$ based on the $CuO_2$ subcell. The coefficients $1/\delta a$ and $1/\delta c$ are of the order of five and four and strongly depend on the Ca/Y ratio. Raising $x$ leads to an increase in the factor $1/\delta a$ from five to six and an increase in $1/\delta c$ from four to five. The propagation vector $[\delta a\, 0\, \delta c]$ describes the satellite reflections of the modulated superstructure.
The second approach employs the monoclinic space group $P2_1/c$, where the volume of the unit cell is about $1000\,\text{Å}^3$. The lattice parameters $\tilde{a}$, $\tilde{b}$ and $\tilde{c}$ are equal to $a/\delta a \simeq 14.2\,\text{Å}$, $b \simeq 6.3\,\text{Å}$ and $c/\sin\beta \simeq 15.5\,\text{Å}$, respectively. The angle between the $\tilde{a}$ and $\tilde{c}$ direction satisfies the relation $\beta \simeq 180° - \arctan\left((\delta a \cdot c)/((1 - \delta c) \cdot a)\right)$ and is of the order of 135°. One chemical unit cell comprises 16 Ca/Y ions, 20 copper ions and 40 oxygen ions. Figure 4.2 illustrates the crystal structure of $Ca_{2+x}Y_{2-x}Cu_5O_{10}$ compounds.

### 4.1.4 Landé splitting factor $g$

Considering Eq. (2.6) to Eq. (2.8) (see chapter 2.3) the Landé factor $g$ significantly influences the multi parameter fit function of susceptibility that contains $g$, the number of magnetic spins $N$, the alternating parameter $\alpha$ and the exchange $J$ as free parameters. We used electron paramagnetic resonance (EPR) to determine the effective $g$-factor of $Ca_{2+x}Y_{2-x}Cu_5O_{10}$ samples. For an overview of this technique refer to [86].

During an EPR experiment the sample is exposed to an external magnetic field $B$ and irradiated by a microwave with frequency $\nu$. Owing to the Zeeman splitting the two energy levels $W_{M_s}$

$$E = g\mu_B B_{res} M_s \tag{4.2}$$

are non degenerate, where $M_s = \pm 1/2$ denotes the projection of the electron spin. Resonant absorption between the two levels is observed, when the energy difference $\Delta E$ between both non degenerate states and the energy of the external field $B_{res}$

$$\Delta E = h\nu = g\mu_B B_{res} \tag{4.3}$$

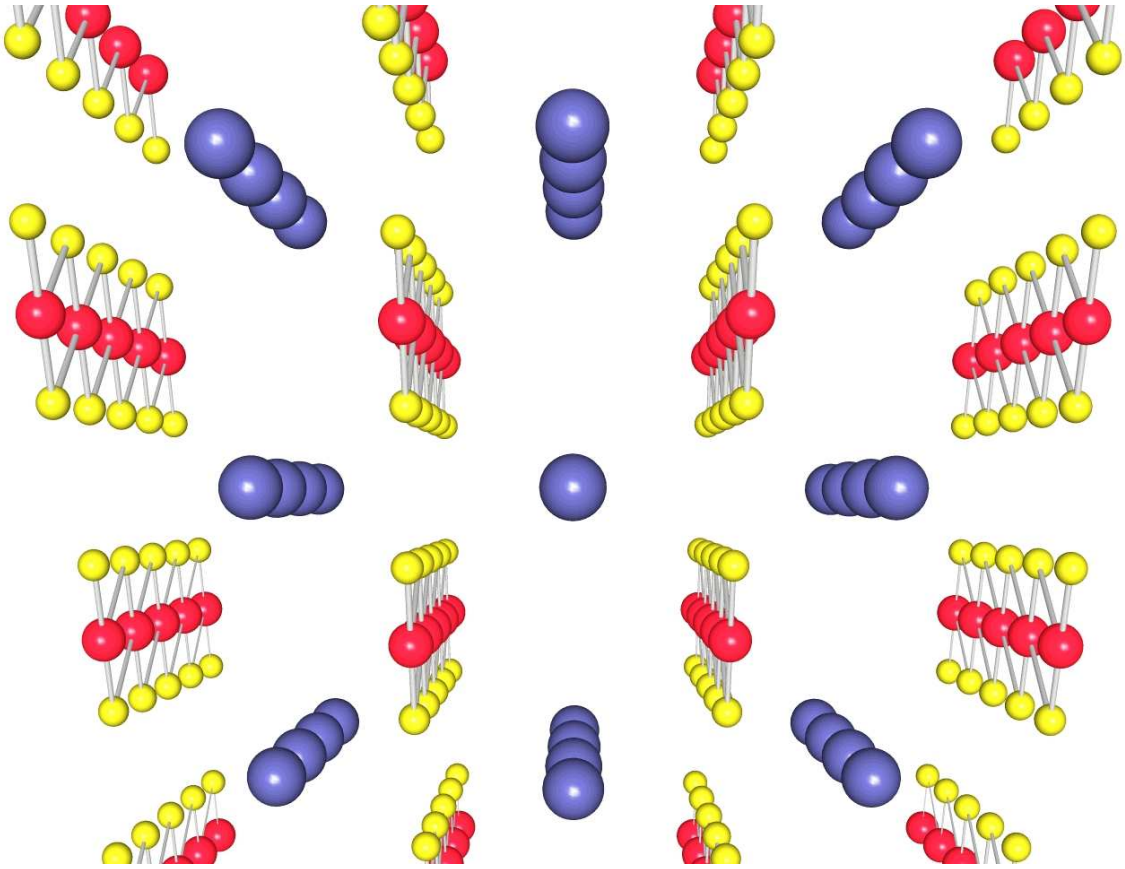

Figure 4.2: Crystal structure of the copper oxide compounds $Ca_{2+x}Y_{2-x}Cu_5O_{10}$. View along the $a$ axis, where $b$ runs horizontally and $c$ vertically. Copper ions are sketched in red color, oxide ions in yellow color and Ca/Y in blue color. The copper oxide chains are formed along the $a$ axis.

coincide. Usually, the frequency is kept constant in the experiment and the field is scanned.

EPR experiments were performed at the Physik Department E17, Technische Universität München, on a Brucker Elexsys 580 Spectrometer that is equipped with an ESP 380-1010 microwave bridge and operates in the X band (microwave frequency 9.5 GHz). $Ca_2Y_2Cu_5O_{10}$, $Ca_3Y_1Cu_5O_{10}$, $Ca_{3.5}Y_{0.5}Cu_5O_{10}$ and $Ca_{0.83}CuO_2$ were measured above its 3D order temperature up to 300 K.

Figure 4.3 (a) displays the first derivative of the obtained reflection signal. The resonant field $B_{res}$ that corresponds to the absorption from the lower energy state to the higher one is derived from the first derivative of the signal. Since the lineshape of the actual resonant absorption peak is almost symmetric, the position of the maximum of that peak corresponds to the value for zero intensity of the first derivative. The lineshape of the absorption peak further implies a maximum and a minimum of the first derivative at an equidistant position from the center field $B_{res}$. We obtained $B_{res}$ by determining the fields corresponding to the maximum and minimum of the first derivative. The resonant field is given by the half distance of the minimum and maximum position of the measured curve.

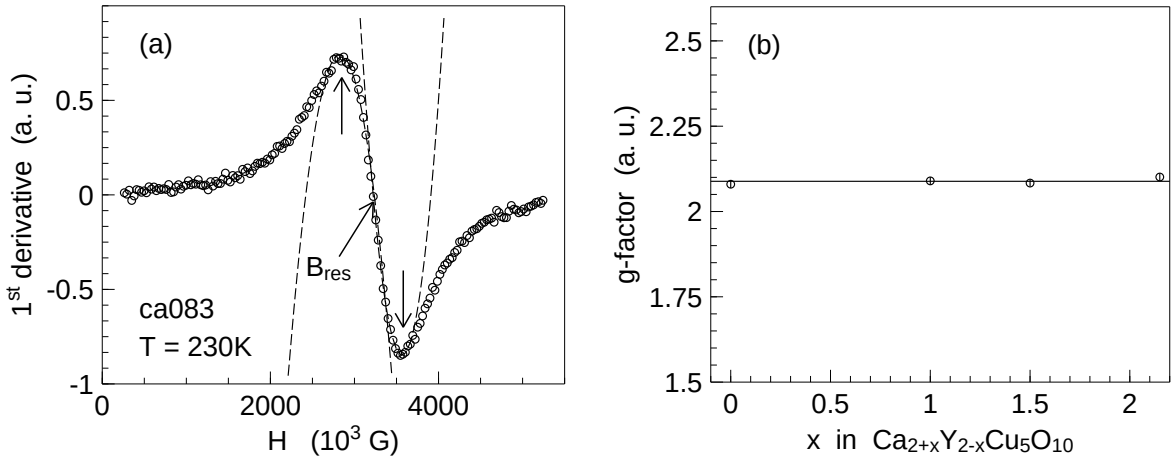


Figure 4.3: Electron paramagnetic resonance measurement of $Ca_{2+x}Y_{2-x}Cu_5O_{10}$. (a) First derivative of the resonance absorption measured at 230 K for $Ca_{0.83}CuO_2$ (ca083). (b) Concentration dependence of the $g$-factor in $Ca_{2+x}Y_{2-x}Cu_5O_{10}$.

Data evaluation yields a temperature and concentration independent $g$-factor for the investigated samples of the compound series (see Figure 4.3 (b)). Table 4.3 collects the results of the Landé factor for $x = 0$, 1, 1.5 and $Ca_{0.83}CuO_2$, respectively. The obtained experimental values agree well with literature values of similar $S = 1/2$ systems such as $Ca_{0.85}CuO_2$ [87] and $Sr_{0.73}CuO_2$ [88]. Both samples exhibit a Landé factor of 2.08.

| | Landé factor $g$ |
|---|---|
| $Ca_2Y_2Cu_5O_{10}$ | 2.08(1) |
| $Ca_3Y_1Cu_5O_{10}$ | 2.09(1) |
| $Ca_{3.5}Y_{0.5}Cu_5O_{10}$ | 2.08(1) |
| $Ca_{0.83}CuO_2$ | 2.10(1) |

Table 4.3: Landé factor $g$ of particular $Ca_{2+x}Y_{2-x}Cu_5O_{10}$ samples that were determined by means of electron paramagnetic resonance. The obtained values are both temperature and concentration independent in the investigated temperature range.

## 4.2 Magnetization study

This section reports the investigation of magnetic order in $Ca_{2+x}Y_{2-x}Cu_5O_{10}$ by means of D.C. and A.C. magnetization measurements. The first part is devoted to the observation of a complex magnetic phase diagram in terms of 3D antiferromagnetic phase, disorder and 1D Heisenberg behavior in higher doped samples (see chapter 4.2.1). Analyzing the high temperature data by means of the Curie Weiss law shows that hole doping effectively reduces the magnetic $Cu^{2+}$ ions in the chain (see chapter 4.2.2). Susceptibility data at low and medium temperatures are discussed within the frame of the alternating 1D Heisenberg chain model (chapter 4.2.3).

We measured D.C. and A.C. magnetization for $Ca_{2+x}Y_{2-x}Cu_5O_{10}$ samples with $0 \leq x \leq 2.15$ in the temperature range of 1.9 K to 300 K. D.C. measurements were performed in an external field between 0.1 T to 9 T, in order distinguish between long range order and short range correlations. Between 1.9 K and 70 K the samples were measured in 0.4 K steps. Above 70 K the difference between two data points was extended to 0.8 K. For illustration purposes all data are displayed in a semilogarithmic plot with 70 to 100 points per decade. Besides the temperature dependence at constant fields, data were obtained probing the field dependence at fixed temperatures.

Solid pieces of each sample were mounted into straw sample holders that were closed with Kapton tapes at the sample end. Both the straw and the tape provide a diamagnetic contribution to the sample signal that might even mask the latter one. Experimentally ascertained, these two additives strongly depend on the used sample holder and may vary in strength. Avoiding uncertainties for data analysis the sample volume to which the magnetic response is proportional was adjusted in such a way that the diamagnetic part of the sample environment represents even in the paramagnetic regime only 1 % of the overall obtained signal. Furthermore, error bars of the D.C. and A.C. magnetization are drastically reduced compared to the first measurements of both quantities. Figure 4.4 illustrates the absolute D.C. magnetization signal of the straw sample holder in 1 T in comparison to data of $Ca_{0.83}CuO_2$.

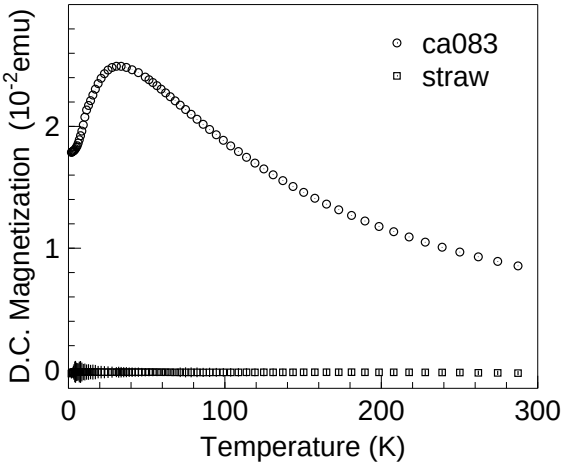


Figure 4.4: D.C. magnetization of the empty sample holder (straw) and of the combined sample holder and $Ca_{0.83}CuO_2$ (ca083) in 1 T. The diamagnetic contribution of the straw and the Kapton tape differ by 2 orders of magnitude from the overall sample and sample holder signal. The accuracy of D.C. measurements is of the order of $3 \cdot 10^{-5}$ emu. This kind of sample holder was used for D.C. and A.C. magnetization measurements.

Depending on the sample density the investigated pieces weight between $\sim 150$ mg and $\sim 400$ mg. In order to further exclude inhomogeneities of each sample during the data analysis process, we measured at least two pieces of each sample.

### 4.2.1 Magnetic phases

Figure 4.5 (a) and (b) displays the susceptibility of $Ca_2Y_2Cu_5O_{10}$ and $Ca_3Y_1Cu_5O_{10}$ in units of emu/mole, respectively. The data are obtained by means of D.C. magnetization measurements in an external field of 1 T.

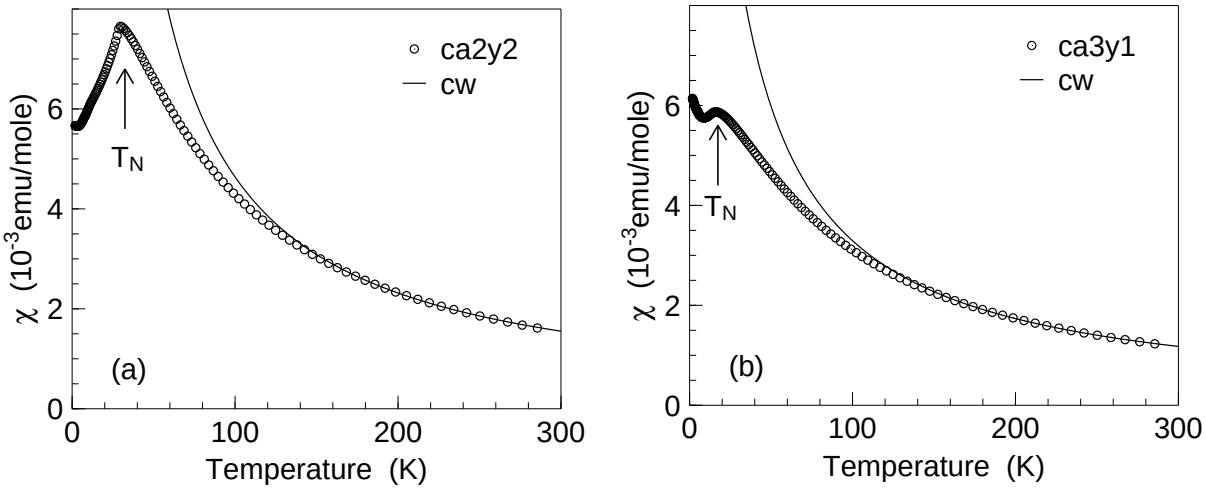


Figure 4.5: Susceptibility of (a) $Ca_2Y_2Cu_5O_{10}$ (ca2y2) and (b) $Ca_3Y_1Cu_5O_{10}$ (ca3y1), measured in 1 T. Upon doping, the antiferromagnetic phase transition temperature $T_N$ decreases. Below 7 K, $\chi(T)$ increases in magnitude, what is attributed to antiferromagnetic correlations. The solid lines indicate a fit using the Curie Weiss law (cw, see chapter 4.2.2).

The parent compound exhibits typical signs of an antiferromagnetic phase transition around $\sim 30$ K. Susceptibility increases up to a maximum and again decreases upon lowering the temperature. At the lowest experimentally accessible temperature $\chi(T)$ yields a constant value of $\sim 5.7 \cdot 10^{-3}$ emu/mole. Single crystal data of a conventional 3D antiferromagnetic system show $\chi_{\parallel}(T) \to 0$ for $T \to 0$ or exhibit a constant value below $\chi_{max}(T_N)$. This low temperature behavior depends on the applied magnetic field that is either orientated parallel to the sample magnetization $M(T)$ or perpendicular to it. In contrast, a 3D ferromagnetic phase is characterized by an increase of the susceptibility $\chi(T \to 0)$ until the spontaneous magnetization saturates.
Further $Ca^{2+}$ doping leads to a decrease in the absolute value of susceptibility. Moreover, the second order phase transition shifts to lower temperatures. $Ca_3Y_1Cu_5O_{10}$ shows an order temperature of $\sim 20$ K. The transition changes from a sharp feature for $\chi(T)$ to a broad maximum. Below 7 K susceptibility continuously increases in this compound. This feature is an overall signature of the investigated samples with the doping concentration $0.75 \leq x \leq 1.5$. We do not observe a saturation of $\chi(T)$ within the highest applied field of 9 T for $T \to 0$.
Figure 4.6 (a) displays the susceptibility of $Ca_{3.5}Y_{0.5}Cu_5O_{10}$. Th signal increases upon decreasing temperature. Around 12 K the slope of $\chi(T)$ changes. We observe below this temperature antiferromagnetic correlations that are revealed by a linear fit to the inverse susceptibility (see inset of Figure 4.6 (a)). This low temperature antiferromagnetic phase might mask the long range order temperature that is visible in less doped samples.
In $Ca_{0.83}CuO_2$ the absolute signal of the susceptibility further decreases compared to $Ca_{3.5}Y_{0.5}Cu_5O_{10}$ (see Figure 4.6 (b)). It shows signatures of the antiferromagnetic 1D

Heisenberg chain in terms of a very broad rounded maximum around $\sim 33\,\mathrm{K}$ and a constant value for $T \to 0$. Around $\sim 12\,\mathrm{K}$ $\chi(T)$ exhibits a change in its slope. Upon increasing field, susceptibility data clearly shows an increase in $\chi(T)$ with decreasing $T$ (see inset of Figure 4.6 (b)). This feature is attributed to a magnetic phase transition. Based on the position of the rounded maximum in the curve the magnetic exchange $J$ measured along the chain is estimated to be $J/k_B \simeq T_{max}/0.641 \simeq 55\,\mathrm{K}$ (see chapter 2.3).

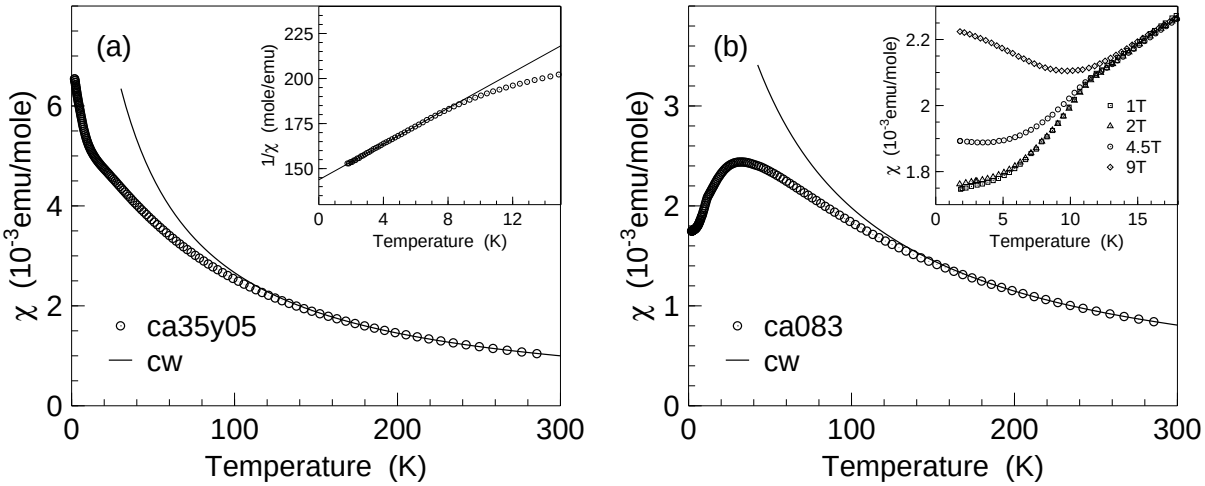


Figure 4.6: Susceptibility of (a) $Ca_{3.5}Y_{0.5}Cu_5O_{10}$ (ca35y05) and (b) $Ca_{0.83}CuO_2$ (ca083), measured in 1 T. The susceptibility of $Ca_{3.5}Y_{0.5}Cu_5O_{10}$ features a change in its slope around 12 K. Below this temperature $1/\chi(T)$ reveals antiferromagnetic correlations (see inset in plot (a)). The susceptibility of highly doped $Ca_{0.83}CuO_2$ resembles that of the 1D Heisenberg chain. The inset in plot (b) enlarges the low temperature behavior of $\chi(T)$ for the applied fields of 1 T, 2 T, 4.5 T and 9 T. We note a magnetic phase transition around 12 K. The solid lines indicate a fit using the Curie Weiss law (cw, see chapter 4.2.2).

The low temperature increase in doped samples might be a sign of disorder that leads to a spin glass state. Both D.C. and A.C. magnetization should reveal a distinct behavior for such a magnetic state. Zero field cooled and non zero field cooled susceptibility usually show a significant change that starts around the spin glass temperature. This feature originates from an increased spin orientation with respect to the field, when cooling in an external field. However, we do not observe a change within these two quantities for all samples. We further investigated the frequency dependent A.C. magnetization that should feature a shift of the real part of $\chi(T)$ to higher temperatures when increasing the applied frequency [89]. In agreement with zero field and non zero field cooled D.C. magnetization no frequency dependence of the signal is visible between 10 Hz up to 1 kHz.

In order to support the results of the low temperature magnetic behavior around the phase transition temperature, we obtained $M(H)$ for temperatures $T < T_N$, $T \sim T_N$ and $T > T_N$. Figure 4.7 displays the field dependence of the D.C. magnetization in units of $\mu_B$/Cu at various temperatures for $Ca_2Y_2Cu_5O_{10}$, $Ca_3Y_1Cu_5O_{10}$, $Ca_{3.5}Y_{0.5}Cu_5O_{10}$ and $Ca_{0.83}CuO_2$. We notice a decreasing signal upon raising the doping concentration $x$. Furthermore, the shown magnetization curves feature a linear behavior of $M(H)$ up to 9 T in the investigated temperature range. $Ca_{3.5}Y_{0.5}Cu_5O_{10}$ shows a deviation from this linear behavior starting around 4.5 T.

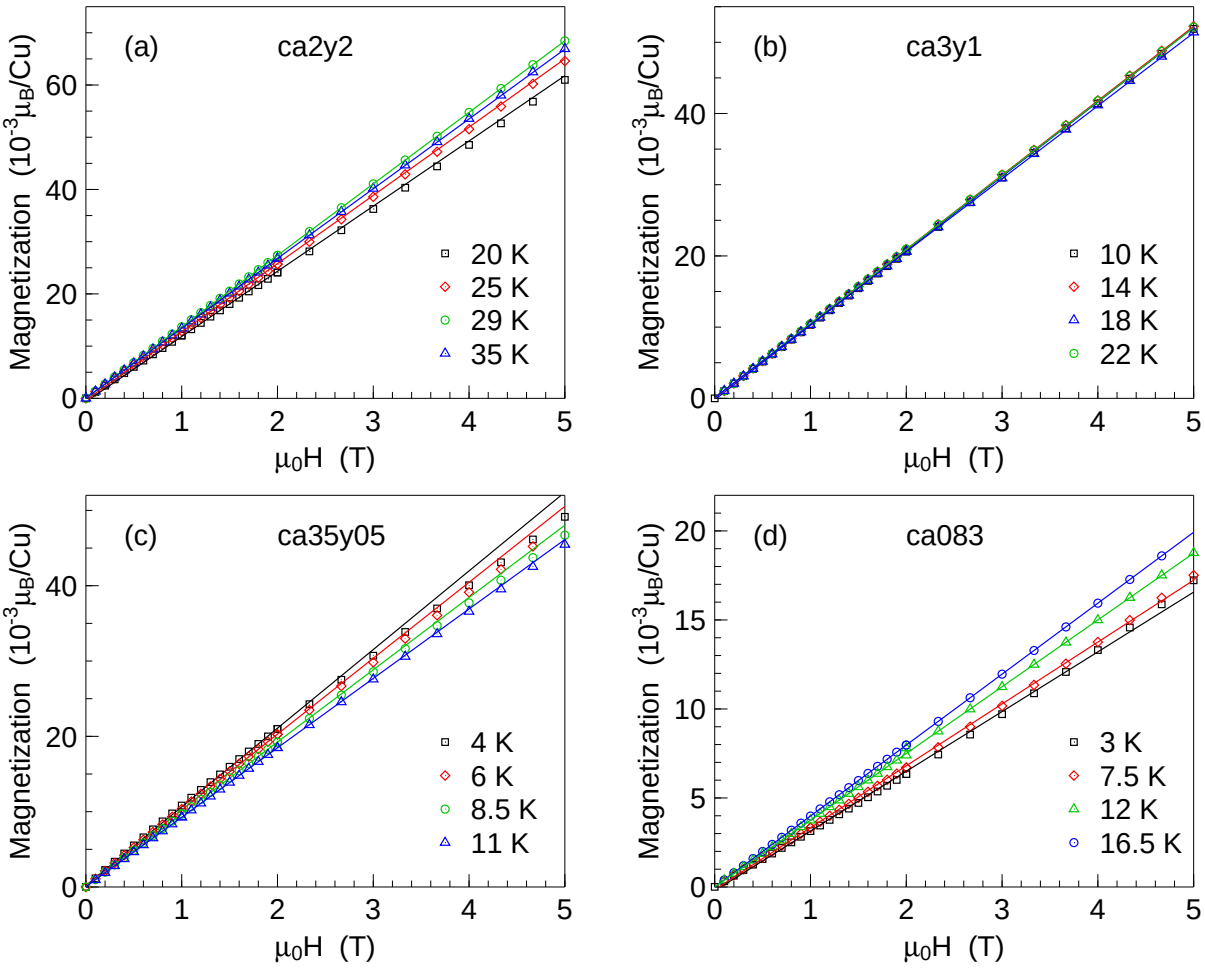


Figure 4.7: Field dependence of the D.C. magnetization of (a) $Ca_2Y_2Cu_5O_{10}$ (ca2y2), (b) $Ca_3Y_1Cu_5O_{10}$ (ca3y1), (c) $Ca_{3.5}Y_{0.5}Cu_5O_{10}$ (ca35y05) and (d) $Ca_{0.83}CuO_2$ (ca083) in units of $\mu_B$/Cu for temperatures $T < T_N$ up to $T > T_N$. The solid lines display linear fits to the experimental data. Increasing the Ca/Y ratio leads to a smaller absolute value of the magnetization. We observe a linear dependence of the magnetization on the applied field up to 9 T. Only $Ca_{3.5}Y_{0.5}Cu_5O_{10}$ features deviations from this linear behavior around 4.5 T.

$Ca_{3.5}Y_{0.5}Cu_5O_{10}$ shows a deviation from this linear behavior starting around 4.5 T.

### 4.2.2 Curie Weiss behavior in the paramagnetic regime

The paramagnetic phase of a magnetic system is characterized by thermal induced spin fluctuations. Long range order is destroyed and only short range correlations dominate the magnetic response. In this sense, high temperature susceptibility data are described using the Curie Weiss law [90]

$$\chi_{cw} = \frac{N_{cw} g^2 \mu_B^2 S(S+1)}{3k_B(T-\theta_{cw})} \tag{4.4}$$

for free $Cu^{2+}$ spins ($S = 1/2$). $N_{cw}$ denotes the number of magnetic copper ions that contribute to the signal. We use a $g$-factor equal to 2.09 for all samples that was determined by EPR measurements (see chapter 4.1.4)[1]. $\mu_B$ denotes the Bohr magneton and $k_B$ the Boltzmann constant. The Curie Weiss temperature $\theta_{cw}$ distinguishes between ferromagnetic and antiferromagnetic correlations in the paramagnetic regime for values $\theta_{cw} > 0$ and $\theta_{cw} < 0$, respectively. The fit range was estimated from the inverse susceptibility. Within the Curie Weiss approach, $\chi^{-1}(T)$ follows a linear behavior with $\chi^{-1}(T) \propto T - \theta_{cw}$. The interpolation of the inverse susceptibility to $\chi^{-1}(\theta_{cw}) = 0$ served as start parameter for the Curie Weiss temperature during the fitting process. Examples of Curie Weiss fits to the susceptibility of the $Ca_{2+x}Y_{2-x}Cu_5O_{10}$ samples are indicated by the solid lines in Figure 4.5 (a), (b), Figure 4.6 (a) and (b).

Table 4.4 collects the fit results for the number of copper spins participating in the magnetic signal. For comparison, the expected numbers of magnetic copper ions are provided which are derived from the copper valence. We note that for $0 \leq x \leq 1.5$ $N_{cw}$ is by 10 % larger compared to the number of magnetic spins in each sample based on the stoichiometric formula. $Ca_{0.83}CuO_2$ almost exactly exhibits the expected spin density of magnetic $Cu^{2+}$ based on the sample valence. Hole doping into the $CuO_2$ chains effectively cancels out magnetic $Cu^{2+}$ spins. Holes, i. e. non magnetic $Cu^{3+}$, transform $CuO_4$ units into Zhang-Rice singlets that induces singlet pairing of neighboring spins [5].

| $x$ | 0 | 0.75 | 1 | 1.2 | 1.5 | 2.15 |
|---|---|---|---|---|---|---|
| $N$ | 1 | 0.85 | 0.8 | 0.76 | 0.7 | 0.66 |
| $N_{cw}$ | 1.10(1) | 0.98(2) | 0.89(1) | 0.86(1) | 0.78(1) | 0.67(1) |

Table 4.4: Number of free spins $N_{cw}$ per formula unit obtained by a Curie Weiss fit to the susceptibility of $Ca_{2+x}Y_{2-x}Cu_5O_{10}$ samples. For comparison, the expected number of magnetic spins $N$ based on the copper valence are noted.

The obtained Curie Weiss temperature $\theta_{cw}$ indicates the magnetic correlations in the investigated temperature range (see Figure 4.8). The parent compound exhibits a small ferromagnetic contribution, which is in agreement with susceptibility measurements from

[1] We note that most of the susceptibility studies of $Ca_{2+x}Y_{2-x}Cu_5O_{10}$ use a $g$-value that is derived from a fit of the Curie Weiss law in the paramagnetic phase, where the number of magnetic ions is set to unity for $Ca_2Y_2Cu_5O_{10}$. The obtained values vary from 2.1 to 2.24 [61, 62, 91] and significantly change fitting parameters of the alternating chain model.

literature [63]. Hole doping decreases the Curie Weiss temperature $\theta_{cw}$ that indicates strong antiferromagnetic correlations in the disordered phase.

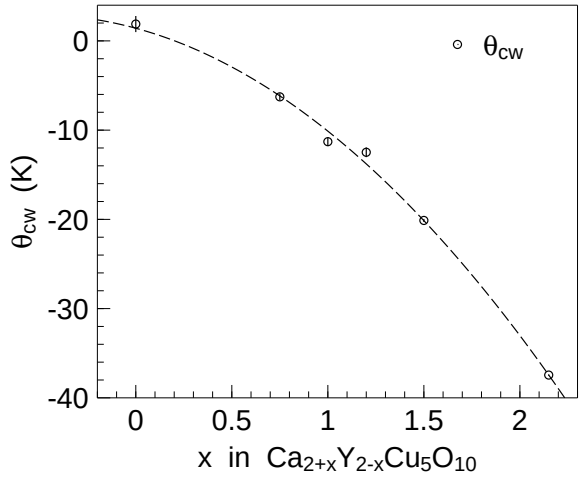


Figure 4.8: Curie Weiss temperature $\theta_{cw}$ of $Ca_{2+x}Y_{2-x}Cu_5O_{10}$ samples. $\theta_{cw}$ is obtained from a fit to the susceptibility in a temperature range of $\sim 170\,\mathrm{K}$ to $290\,\mathrm{K}$. The dashed line is a guide to the eye. A negative Curie Weiss temperature indicates antiferromagnetic correlations in the investigated temperature range, whereas $\theta_{cw} > 0$ yields ferromagnetic exchange. Upon increasing the Ca/Y ratio, magnetic correlations are antiferromagnetic and increase in strength.

### 4.2.3 1D Heisenberg behavior

At first sight analyzing the susceptibility of the parent compound and slightly doped $Ca_{2.75}Y_{1.25}Cu_5O_{10}$ in terms of 1D Heisenberg chains is at odds with the data. The antiferromagnetic transition clearly dominates the magnetic signal and turns it impossible to decompose $\chi(T)$ into different processes. Moreover, assuming for all $Ca_{2+x}Y_{2-x}Cu_5O_{10}$ samples the magnetic exchange $J \sim 55\,\mathrm{K}$ of $Ca_{0.83}CuO_2$ as the overall energy scale of the chain contribution a Néel temperature of $30\,\mathrm{K}$ of $Ca_2Y_2Cu_5O_{10}$ definitively masks the quasi 1D term.

Susceptibility of medium doped samples ($x = 1$, 1.2 and 1.5) exhibits an increase at lowest temperatures that shifts to $10\,\mathrm{K}$ in $Ca_{3.5}Y_{0.5}Cu_5O_{10}$. Furthermore, the prominent transition from the paramagnetic to the Néel state becomes less pronounced compared to lower doped samples. Fitting the data below $10\,\mathrm{K}$ by means of the Curie Weiss law reveals antiferromagnetic correlations. We thus assume three contributions for $\chi(T)$,

$$\chi(T) = \chi_0 + \chi_{cw}(T) + \chi_{ahc}(T)\,, \tag{4.5}$$

that superpose in the investigated temperature range. $\chi_{cw}(T)$ and $\chi_{ahc}(T)$ denote the Curie Weiss term (see Eq. (4.4)) and the contribution of the alternating Heisenberg chain (see Eq. (2.7)), respectively. $\chi_0$ represents temperature independent bulk diamagnetic and Van Vleck contributions. During data analysis this quantity was treated as fitting parameter. We reduce the number of free parameters in the fitting equation by fixing $g$ to 2.09 and setting the total spin density $N = N_{cw} + N_{ahc}$ to the expected value from the sample valence. The Curie Weiss temperature $\theta_{cw}$ of the low temperature antiferromagnetic phase was determined from the fit of a straight line to the linear behavior of the inverse susceptibility $\chi^{-1}(T)$. We kept $\theta_{cw}$ fixed to these values for each sample. The number of spins of the Curie Weiss term and the 1D Heisenberg chain contribution as well as the energy scale $J$ of the chain were treated as free parameters. We thus fitted the data in the limit of the antiferromagnetic chain with isolated dimers ($\alpha = 0$), the semi dimerized chain ($\alpha = 0.5$) and the uniform chain ($\alpha = 1$).

Data fitting only yields a reasonable description of $\chi(T)$ for $Ca_{3.5}Y_{0.5}Cu_5O_{10}$, while for samples with $x = 1$ and 1.2 the lineshape cannot be matched. We attribute the observed deviations of the fit from the data to the dominant long range ordered phase that stills significantly contributes to the total susceptibility. Figure 4.9 displays the fit of Eq. (4.5) to the data. The black solid, the red dashed and the blue dotted line indicate the fits for $\alpha = 1$, 0.5 and 0. As illustrated in the inset of this plot, all fits with the chosen values for $\alpha$ deviate from the experimental data at low temperature. In the high temperature range all curves describe the data equally well.

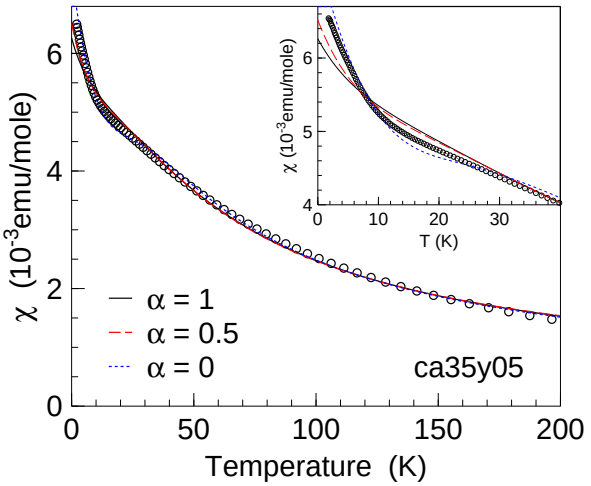


Figure 4.9: Susceptibility of $Ca_{3.5}Y_{0.5}Cu_5O_{10}$ (ca35y05). The black solid, the red dashed and the blue dotted line indicate a fit of Eq. (4.5) to the data in case of the uniform chain, the semi dimerized chain and the chain with isolated dimers. During fitting the data the Curie Weiss temperature $\theta_{cw}$ of the low temperature contribution, the Landé factor $g$ and the total number of magnetic spins $N = N_{cw} + N_{ahc}$ was kept constant. At high temperature the data are equally well described independently of $\alpha$. Below 30 K the agreement between the data and the fits does not favor a particular value for $\alpha$ (see inset).

Table 4.5 collects the results obtained by a fit to the measured data of $Ca_{3.5}Y_{0.5}Cu_5O_{10}$. The number of magnetic copper spins $N_{ahc}$ that contribute to the spin chain behavior varies between $\sim 0.23$ and $\sim 0.35$ for the chain with isolated dimers ($\alpha = 0$) and the uniform chain, respectively. On average, the 1D Heisenberg chain term contributes $\sim 35\,\%$ to the total susceptibility. The energy scale of the exchange $J$ yields values between $\sim 50$ K and $\sim 70$ K.

| | $\alpha = 0$ | $\alpha = 0.5$ | $\alpha = 1$ |
|---|---|---|---|
| $N_{ahc}$ | 0.23(2) | 0.22(4) | 0.34(8) |
| $J/k_B$ (K) | 71(7) | 71(17) | 48(10) |
| $N_{cw}$ | 0.47(2) | 0.48(4) | 0.36(8) |
| $\lvert\theta_{cw}\rvert$ (K) | 28.95(3) | 28.95(3) | 28.95(3) |
| $\chi_0$ (emu/mole) | $2.5(4)\cdot 10^{-4}$ | $2.9(9)\cdot 10^{-4}$ | $2.7(9)\cdot 10^{-4}$ |

Table 4.5: Fit parameters of the alternating Heisenberg chain model to the susceptibility of $Ca_{3.5}Y_{0.5}Cu_5O_{10}$. During the fit $\theta_{cw}$, the total number of spins $N$ and the alternating parameter $\alpha$ was kept fixed.

The susceptibility of $Ca_{0.83}CuO_2$ resembles the susceptibility of the uniform Heisenberg chain. Since no Curie Weiss contribution is observed at low temperatures, we will use

$$\chi(T) = \chi_0 + \chi_{1D}(T)\,, \tag{4.6}$$

where $\chi_0$ represents the temperature independent contribution (see above) and $\chi_{1D}(T)$ the 1D Heisenberg term. In a first approach the approximation of Bonner and Fischer for the uniform chain is used ($\alpha = 1$, see Eq. (2.6)). Furthermore, the alternating Heisenberg

chain is used as fitting function. Table 4.6 summarizes the fit results of both approaches. The spin density $N_{1D}$ contributing to the 1D Heisenberg term deviates from both the number of spins deduced from the Curie Weiss fit and from the value that is expected from the formal copper valence.

We further consider a 3D coupling of the isolated chains that was successfully included into the 1D Heisenberg chain model to describe the susceptibility of $Ca_{0.83}CuO_{2+\delta}$ [82]. Schulz [92] used a mean field treatment of loosely coupled chains in terms of the Hamiltonian

$$H = J \sum_i \left( \hat{\mathbf{S}}_{2i} \hat{\mathbf{S}}_{2i-1} + \alpha \hat{\mathbf{S}}_{2i} \hat{\mathbf{S}}_{2i+1} \right) + J_\perp \sum_{i,\boldsymbol{\delta}} \hat{\mathbf{S}}_{2i} \hat{\mathbf{S}}_{2i+\boldsymbol{\delta}} \tag{4.7}$$

to account for an exchange $J_\perp$ perpendicular to the chain direction. In agreement with the earlier introduced convention $J$ denotes the magnetic exchange parallel to the chain. The summation over the nearest neighbor spins perpendicular to the chain is indicated by $\boldsymbol{\delta}$. Schulz further derived an expression for $J_\perp$ using the long range order temperature $T_N$ and the exchange $J$ along the chains to be

$$J_\perp = \frac{k_B T_N}{4A(\ln(\Lambda J/(k_B T_N)))^{1/2}} \,. \tag{4.8}$$

Here, $A$ and $\Lambda$ are numerically determined to be 0.32 and 5.8. Based on the uniform chain model we calculated $J_\perp$ to be 5.1 K. In a first order approach the transverse exchange is introduced into the closed form of the analytical approximation of Eq. (2.7) as the Curie Weiss temperature $\theta_{CW}$ is introduced in Eq. (4.4). In this sense, the energy of the exchange measured parallel to the chain is rescaled by $J_\perp$. We expect the introduction of the transverse exchange into the chain model accompanied by an increase in the number of magnetic spins within the chain. Moreover, the transverse interaction influences the intrachain coupling and a preferential dimerization is evoked.

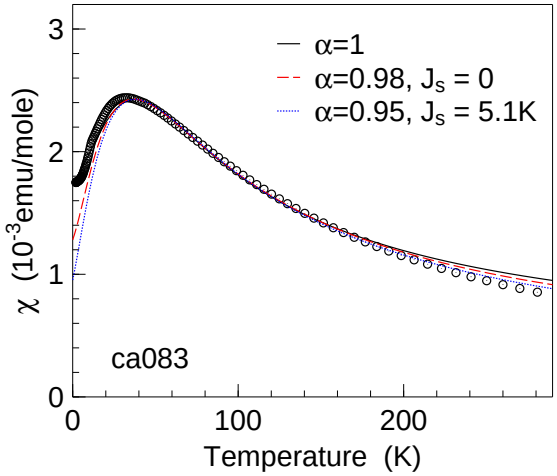


Figure 4.10: Susceptibility of $Ca_{0.83}CuO_2$ (ca083). The black solid line represent a fit to the data based on the uniform chain approximation of Bonner and Fischer. The red dashed and the blue dotted line indicate the fit using the 1D Heisenberg chain model without and with a transverse exchange between the chains. We observe over a large temperature range an agreement between the 1D Heisenberg chain model and the data.

Table 4.6 summarizes the obtained fit results for the Bonner Fisher approximation and the alternating Heisenberg chain using $J_\perp = 0$ K and $J_\perp = 5.1$ K, respectively. The black solid, the red dashed and the blue dotted line in Figure 4.10 display the corresponding fits to the data. All curves reproduce well the data within a broad temperature range of 35 K to 200 K. Above 200 K the model of loosely coupled chains describes the data best. We

remind of the restriction of $\chi_{ahc}$ to temperatures $T \gtrsim 0.5J$ to understand the deviation of the fits from the experimental data below 35 K. We observe both an increase in $N_{1D}$ and $J$ and a decrease of the alternating parameter $\alpha$ upon introducing an transverse interaction of the chains.

| $\alpha$ | $N_{1D}$ | $J/k_B$ (K) | $J_\perp/k_B$ (K) | $\chi_0$ (emu/mole) |
|---|---|---|---|---|
| 1 | 0.51(3) | 58(2) | - | $3.1(7)\cdot 10^{-4}$ |
| 0.98(1) | 0.55(2) | 59(1) | - | $2.1(4)\cdot 10^{-4}$ |
| 0.95(1) | 0.58(2) | 66(1) | 5.1 | $1.4(4)\cdot 10^{-5}$ |

Table 4.6: Fit results of $Ca_{0.83}CuO_2$ based on the model of the uniform ($\alpha = 1$) and the alternating 1D Heisenberg chain with a transverse interaction $J_\perp$. $N_{1D}$ denotes the number of magnetic spins in the chain, $J$ the exchange measured along the chain and $\chi_0$ the temperature independent diamagnetic and Van Vleck contribution.

Based on Eq. (4.7) Schulz estimated the staggered magnetization that depends on the intrachain and the interchain exchange. Applying this model to $Ca_{0.83}CuO_2$ the ordered moment is estimated to be

$$m_0 \simeq 1.017\mu_B\sqrt{J_\perp/J} \simeq 0.28\mu_B\,. \tag{4.9}$$

Here, we used the values for $J$ and $J_\perp$ as displayed in Table 4.6.

In summary, susceptibility measurements of $Ca_{2+x}Y_{2-x}Cu_5O_{10}$ compounds show that the compound series exhibit a long range ordered state below $\sim 29$ K. This 3D antiferromagnetic phase diminishes with doping, however, it does not vanish. Despite a dilution of 0.33 holes/Cu the highly doped sample $Ca_{0.83}CuO_2$ still exhibits a Néel state. Its order temperature is reduced by a factor of 2.5 compared to the parent compound.
Low and medium doped compounds with $0.75 \leq x \leq 1.5$ show an increase in susceptibility below $\sim 10$ K. A Curie Weiss fit to the data resolves antiferromagnetic correlations, whose contribution to the total susceptibility increases with doping. The origin of the term might be explained by magnetic impurities, that only contribute at low temperatures to the overall signal. However, since we observe a concentration dependence of the Curie Weiss temperature and of its weight to the total signal, this explanation is most unlikely. One apt to think that this term results from the $CuO_2$ chains. Upon doping, disorder in terms of holes are introduced into the chains. Amazingly, this Curie Weiss term vanishes upon further $Ca^{2+}$ increase and does not lead to a spin glass state in $Ca_{0.83}CuO_2$, but a 3D antiferromagnetic ground state. This argument can be judged as a precursor of a change in the magnetic properties of $Ca_{2+x}Y_{2-x}Cu_5O_{10}$ between $x = 1.5$ and 2.15.
We only observe 1D Heisenberg behavior in higher doped samples. In contrast to the clear 1D behavior of $Ca_{0.83}CuO_2$, $\chi(T)$ of $Ca_{3.5}Y_{0.5}Cu_5O_{10}$ features the large Curie Weiss term that prevents a definite determination of the alternating parameter and the chain exchange. We observe values of $J$ between $\sim 48$ K and $\sim 70$ K in case of the uniform and the dimerized chain model. The highly doped compound shows an $\alpha$ value close to the uniform chain. The exchange measured along the chain is of the order of 60 K.
Susceptibility data of $Ca_{2+x}Y_{2-x}Cu_5O_{10}$ above 170 K show that hole doping in terms of increasing the Ca/Y ratio effectively reduces the number of magnetic $Cu^{2+}$ ions in

the chains. In addition, the positive Curie Weiss temperature of the parent compound indicates that the dominant correlation within the $CuO_2$ chains is ferromagnetic. Obviously, this sample might not be an example of the 1D antiferromagnetic Heisenberg chain. Higher doped samples exhibits antiferromagnetic interactions. Assuming a ferromagnetically coupled spin chain, dilution of the spin chain provokes antiferromagnetically coupled spins.

## 4.3 Specific heat study

By means of specific heat measurements we resolve the 3D order temperature (see chapter 4.3.1) and analyze data of higher doped compounds in terms of the antiferromagnetic uniform Heisenberg chain (see chapter 4.3.2).

Specific heat was measured for $Ca_{2+x}Y_{2-x}Cu_5O_{10}$ samples in the temperature range of 2 K to 300 K without external field. Furthermore, we investigated the field dependence of the second order phase transition temperature with respect to the applied field up to 9 T. Below $\sim$40 K temperature steps were chosen to be about 0.05 K. This coincides with the temperature accuracy of the PPMS specific heat option. Owing to long measurement times beyond the phase transition temperature we used a logarithmic temperature scale. Each obtained data point was measured two to four times, in order to decrease the error bars of $C(T)$. We performed field dependent calibration measurements for the wire resistances of the sample holder platform. In addition, the specific heat contribution of the used amount of the thermal joint compound was calibrated before each sample measurement.
During the first measurements the vacuum grease Apiezon N (Quantum Design, Inc.) was used by default as thermal joint compound in the temperature range of 2 K to 320 K [93]. However, we observed disadvantages of the grease in terms of its random distribution on the sample platform wires, when heating up the sample platform. This effect may short-circuit the platform wires that are attached to the sample platform and falsify the obtained sample specific heat values. Avoiding a very time consuming cleaning process after each sample measurement, we further employed the silicone oil based Wakefield compound 120-2 (Wakefield Thermal Solutions, Inc.) as thermal coupling in the temperature range of 2 K to 320 K. Besides a very easy experimental handling, it offers the advantage of a factor of two to three less in its specific heat contribution below 50 K compared to the Apiezon N grease. In addition to the literature provided calibration of the specific heat of the Wakefield compound 120-2 for 2 K to 40 K and 20 K to 100 K [94, 95], the calibration was extended to the temperature range of 100 K to 320 K using a polynomial function. With respect to the instrumental options of applying the heat pulse the best experimental parameters were determined providing the highest accuracy for the reported specific heat curve of the standard sample silver [96, 97].
The mass of the investigated samples varied between 12 mg to 25 mg. In order to increase the thermal coupling of the sample to the thermal joint compound, the polycrystalline samples were polished by hand.

### 4.3.1 Phase transition temperature

Susceptibility measurements of undoped and low doped $Ca_{2+x}Y_{2-x}Cu_5O_{10}$ samples already provide evidence of a long range ordered state below $\sim 30$ K. Upon doping up to the concentration $x = 1.5$, the visible peak in $\chi(T)$ broadens and is masked by antiferromagnetic correlations at low temperatures. Only $Ca_{0.83}CuO_2$ that is doped with 0.3 holes/Cu features again a phase transition to a long range ordered state. It is worth noting this result, as the diluted $CuO_2$ chains of this compound show an antiferromagnetic coupling to adjacent chains. A Néel phase coexists with short range correlations that originate from the 1D spin chain behavior. In the following, we investigate the long range ordered state that can be observed by specific heat measurements.

Figure 4.11 (a) displays the temperature dependence of $C(T)/T$ of the parent compound in units of J/(mole K$^2$) per Cu ion. In agreement with all doped samples C(T) yields a room temperature value of $C(T)$ between 20 J/(mole K) to 25 J/(mole K). This value approximately coincides with the Dulong-Petit[2] value of the specific heat at high temperatures. Around $\sim 29$ K specific heat significantly increases and features a $\lambda$-type anomaly. This temperature corresponds to the maximum in susceptibility and is a clear sign of a second order phase transition. In contrast, the $\lambda$ anomaly resulting from a lattice distortion increases more pronounced within a much smaller temperature range. At low temperature the signal tends to zero.

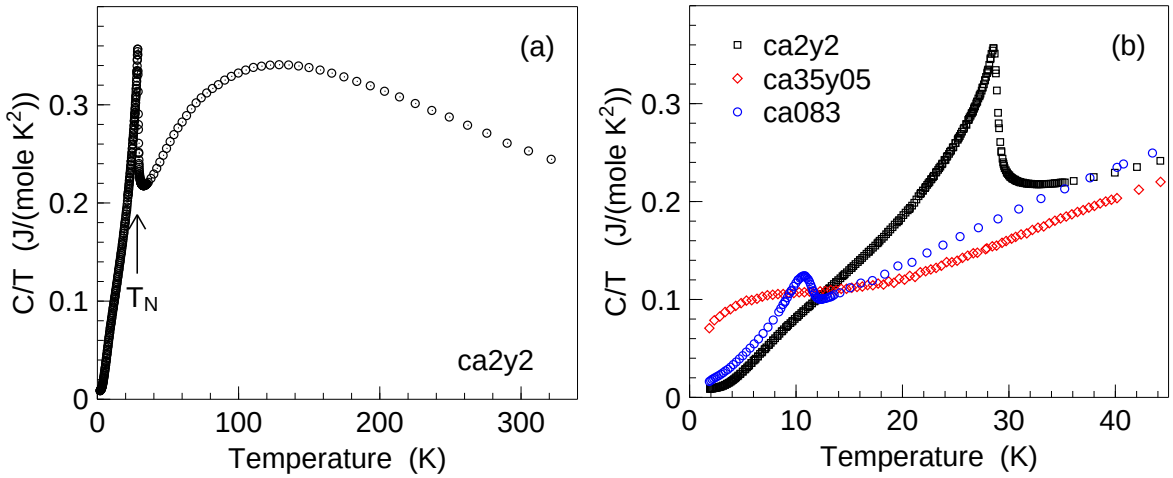


Figure 4.11: $C(T)/T$ per Cu of polycrystalline $Ca_{2+x}Y_{2-x}Cu_5O_{10}$ samples for (a) $Ca_2Y_2Cu_5O_{10}$ (ca2y2) and (b) $Ca_2Y_2Cu_5O_{10}$ (ca2y2), $Ca_{3.5}Y_{0.5}Cu_5O_{10}$ (ca35y05) and $Ca_{0.83}CuO_2$ (ca083). Data were obtained without external field. The inflection point of $C(T)/T$ that corresponds to the minimum in the first derivative yields the order temperature.

Upon doping, the $\lambda$ anomaly shifts to lower temperatures as it was already observed in susceptibility. Moreover, the phase transition broadens and at $x = 1.5$, only a broad plateau is observable (see Figure 4.11 (b)). Similarly, $C(T \to 2\,\mathrm{K})/T$ significantly increases up to 0.07 J/(mole K$^2$) in $Ca_{3.5}Y_{0.5}Cu_5O_{10}$ compared to 0.009 J/(mole K$^2$) in $Ca_2Y_2Cu_5O_{10}$. Highly doped $Ca_{0.83}CuO_2$ features a $\lambda$ anomaly around 12 K that coincides with the kink in $\chi(T)$.

[2]The Dulong-Petit approximation of specific heat holds at high temperatures, where $C(T) \to 3N_A k_B$ applies [90].

The temperature of the second order phase transition is given by the inflection point in the $\lambda$ anomaly of the temperature normalized specific heat [98]. This coincides with the minimum of the first derivative of $C(T)/T$. Undoped and less doped samples clearly exhibit a sharp minimum yielding a well defined transition temperature. We account for the broadening of the transition at medium doped samples by fitting a Gaussian function to the first derivative. The lineshape of this function reproduces the data better than e.g. a parabola. The error bar is given as the full width half maximum of the Gaussian peak. As $Ca_{3.5}Y_{0.5}Cu_5O_{10}$ exhibits a broad plateau in $C(T)/T$ no clear sign of a minimum can be observed in the derivative. Table 4.7 collects the transition temperatures of the investigated samples.
The field dependence of the transition temperature was probed for $H = 0\,\mathrm{T}$ up to $9\,\mathrm{T}$. No sample features a broadening of the $\lambda$ anomaly or a change in $T_N$. We conclude that the magnetic field does not influence the phase diagram of the compounds $Ca_{2+x}Y_{2-x}Cu_5O_{10}$ for the investigated fields.

| | $T_N$ (K) |
|---|---|
| $Ca_2Y_2Cu_5O_{10}$ | 28.8(2) |
| $Ca_{2.5}Y_{1.5}Cu_5O_{10}$ | 26.3(9) |
| $Ca_{2.75}Y_{1.25}Cu_5O_{10}$ | 25.7(11) |
| $Ca_3Y_1Cu_5O_{10}$ | 18.5(12) |
| $Ca_{3.2}Y_{0.8}2Cu_5O_{10}$ | 16.4(26) |
| $Ca_{3.5}Y_{0.5}Cu_5O_{10}$ | - |
| $Ca_{0.83}CuO_2$ | 11.5(3) |

Table 4.7: Phase transition temperature $T_N$ of $Ca_{2+x}Y_{2-x}Cu_5O_{10}$ obtained from specific heat measurements without applied field. The transition temperature is deduced from the inflection point in $C(T)/T$. Larger error bars of $T_N$ for medium doped samples account for the broadening of the $\lambda$ anomaly. Specific heat of $Ca_{3.5}Y_{0.5}Cu_5O_{10}$ features a broad plateau without any phase transition.

### 4.3.2 1D Heisenberg behavior

In order to elucidate the 1D Heisenberg behavior of $Ca_{2+x}Y_{2-x}Cu_5O_{10}$ samples, the obtained specific heat was fitted by

$$C(T) = C_{lat}(T) + C_{mag}(T)\,, \tag{4.10}$$

with $C_{lat}(T)$ and $C_{mag}(T)$ denoting the phonon and the magnetic contribution to the specific heat. The magnetic term is given by Eq. (2.9) and Eq. (2.10) in case of the uniform and the solely dimerized Heisenberg chain, where $C_{mag}(T)$ is proportional to $T$ and $\exp\left(J/(k_BT)\right)$, respectively. In case of the uniform chain the linear approximation holds for $k_BT \lesssim 0.4J$ that corresponds for $J \simeq 60\,\mathrm{K}$[3] to a temperature of $\sim 24\,\mathrm{K}$.

The lattice contribution $C_{lat}(T)$ was fitted based on the Debye approximation of specific heat at low temperatures with $C_{lat}(T) = \beta T^3$. Here, the constant $\beta$ is given by [90]

$$\beta \simeq \frac{12\pi^4}{5} N_A k_B \left(\frac{1}{\theta_D}\right)^3 \simeq 234 N_A k_B \left(\frac{1}{\theta_D}\right)^3 . \tag{4.11}$$

with the Debye temperature $\theta_D$. This kind of modeling the phonon term is valid up to temperatures of $\simeq 0.2\,\theta_D$. For fitting reasons an empirical term $\gamma T^5$ was further included

[3]The value for the magnetic exchange $J$ is chosen in agreement with fit results for susceptibility.

in the phonon part $C_{lat}(T)$. We note the Debye temperatures of calcium, yttrium and copper to be 230 K, 280 K and 343 K [90]. This corresponds to a maximum fitting range up to $\sim$70 K and to $\beta$ values between 0.16 mJ/(mole K$^4$) and 0.05 mJ/(mole K$^4$).

By fitting experimental data in the temperature range of $T_N \lesssim T \lesssim 0.2\,\theta_D$, values for the number of magnetic spins $N$, the intrachain exchange $J$ and the lattice contribution constants $\beta$ and $\gamma$ are derived. However, data fitting converges neither for the model of the uniform chain nor the chain with isolated dimers with reasonable fitting parameters. We thus limit the number of magnetic ions contributing to $C_{mag}(T)$ to its expected value from the copper valence and show consistency with the exchange parameters derived from susceptibility measurements.

In a first approach, we use the 1D uniform Heisenberg chain as the magnetic contribution to the specific heat. Similarly to susceptibility, only higher doped samples are described with reasonable parameters in the proper fit range. Table 4.8 summarizes the derived parameters for $Ca_{3.5}Y_{0.5}Cu_5O_{10}$ and $Ca_{0.83}CuO_2$. Since the Debye temperatures shows similar values to $\theta_D$ of the pure sample elements, the phonon contribution is reasonably approximated. Figure 4.12 displays fits to specific heat data of $Ca_{3.5}Y_{0.5}Cu_5O_{10}$ and $Ca_{0.83}CuO_2$ using the uniform Heisenberg chain (black solid lines). The magnetic term $C_{mag}(T)/T$ (red dashed line) of the investigated samples follows a temperature independent value above the phase transition. This is compatible with the uniform chain behavior. The blue dotted lines indicate the lattice contribution to the total specific heat.

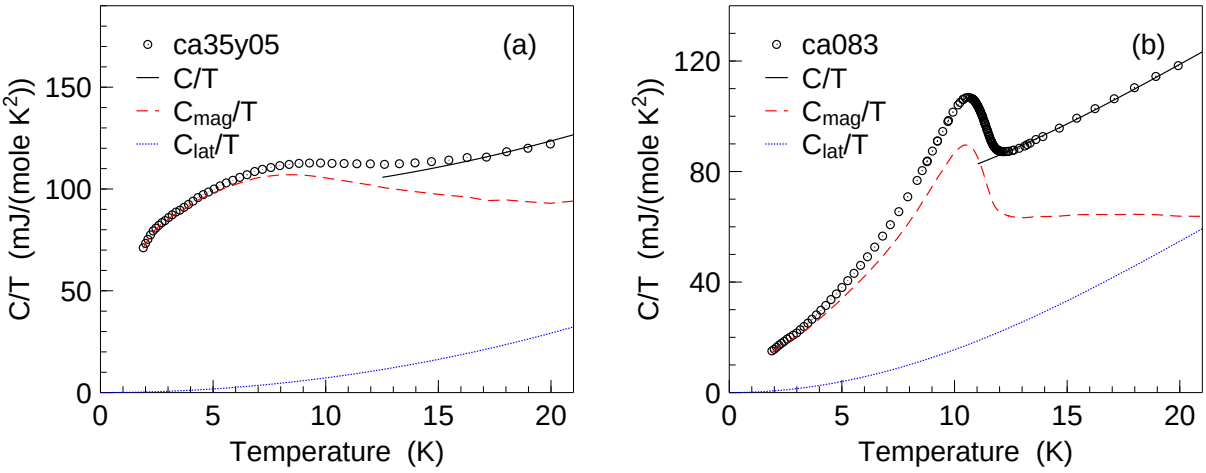


Figure 4.12: $C(T)/T$ of (a) $Ca_{3.5}Y_{0.5}Cu_5O_{10}$ (ca35y05) and (b) $Ca_{0.83}CuO_2$ (ca083). The black solid lines represent the fits of Eq. (4.10) using the uniform Heisenberg chain approach for the magnetic term. The red dashed lines display the magnetic specific heat term $C_{mag}(T)/T$ that yields a temperature independent value. The lattice contribution $C_{lat}(T)$ is indicated by the blue dotted lines.

Fitting specific heat in terms of a chain with isolated dimers does not describe the lineshape of $C(T)$ for any investigated sample. Here, we used the low temperature Debye approximation for the lattice contribution as start parameters for $\beta$ and $\gamma$. It follows, that only antiferromagnetic 1D Heisenberg behavior of the uniform chain or slightly dimerized chains can be observed in higher doped samples of $Ca_{2+x}Y_{2-x}Cu_5O_{10}$.

| | $N$ | $J/k_B$ (K) | $\beta$ (mJ/(mole K$^4$)) | $\theta_D$ (K) | $\gamma$ (mJ/(mole K$^6$)) |
|---|---|---|---|---|---|
| $Ca_{3.5}Y_{0.5}Cu_5O_{10}$ | 0.7 | 41(1) | 0.072(6) | 300 | $2.7(40)\cdot10^{-6}$ |
| $Ca_{0.83}CuO_2$ | 0.66 | 58(1) | 0.161(4) | 229 | $-6.1(4)\cdot10^{-5}$ |

Table 4.8: Fitting parameters of the uniform chain model to specific heat of $Ca_{3.5}Y_{0.5}Cu_5O_{10}$ and $Ca_{0.83}CuO_2$: number of $Cu^{2+}$ ions $N$, intrachain exchange $J$, lattice contribution constant $\beta$, Debye temperature $\theta_D$ and lattice contribution constant $\gamma$. The error of $\theta_D$ is less than 1 K.

Specific heat of $Ca_{2+x}Y_{2-x}Cu_5O_{10}$ samples agrees well with susceptibility measurements and reveal both 3D order that coexists with 1D Heisenberg behavior at higher doped samples. The order temperature decreases from $\sim 29$ K to $\sim 12$ K for $Ca_{2+x}Y_{2-x}Cu_5O_{10}$ and $Ca_{0.83}CuO_2$, respectively.
For $Ca_{3.5}Y_{0.5}Cu_5O_{10}$ and $Ca_{0.83}CuO_2$ the data can be consistently described with the model of the uniform Heisenberg spin chain. The extracted value of the intrachain exchange $J \simeq 41$ K of $Ca_{3.5}Y_{0.5}Cu_5O_{10}$ approximately coincides with that of susceptibility measurements for the $\alpha = 1$ approach. The value of the magnetic correlation $J$ that was found for $Ca_{0.83}CuO_2$ is in best agreement with those of susceptibility measurements.
We observe an increase of $C(T \to 0)$ for medium doped samples. This feature might be correlated to the low temperature Curie Weiss type term in susceptibility that was attributed to disorder of the $CuO_2$ chains. However, a profound explanation of this feature requires a measurement techniques that microscopically probes magnetic properties in these samples. We expect, that $Ca_{3.5}Y_{0.5}Cu_5O_{10}$ represents the best candidate for such an investigation, since the behavior of $\chi(T)$ and $C(T)$ is most pronounced compared to less doped samples.

## 4.4 Neutron diffraction study

Bulk measurements elucidated a magnetic phase transition from a paramagnetic to an antiferromagnetic state for $Ca_{2+x}Y_{2-x}Cu_5O_{10}$ samples. The concentration dependent study of the ordered magnetic structure by means of elastic neutron scattering reveals the sign of the magnetic exchange along the chain direction as well as the value of the Cu-O-Cu bonding angle (see chapter 4.4.2). These results represent the key in understanding the adaptability of the antiferromagnetic 1D Heisenberg behavior within the frame of the $J_1$-$J_2$ model of edge sharing $CuO_2$ chains. Furthermore, investigating the sublattice magnetization of $Ca_2Y_2Cu_5O_{10}$ and $Ca_{2.5}Y_{1.5}Cu_5O_{10}$ resolves the magnetic character of the phase transition (see chapter 4.4.3).

### 4.4.1 Experimental details and data analysis

In order to determine the magnetic structure, we performed experiments on the diffractometers DMC and HPRT (PSI), D20 (ILL) and SPODI (FRM II) for numerous $Ca_{2+x}Y_{2-x}Cu_5O_{10}$ samples. Table 4.9 provides an overview of the investigated samples, the wavelength $\lambda$ and the diameter $d$ of the vanadium sample holder for each experiment. Besides a low temperature pattern data were collected at an elevated temperature

above the order temperature. The value of $T_N$ was estimated from specific heat measurements (see Table 4.7). Furthermore, the sublattice magnetization of $Ca_2Y_2Cu_5O_{10}$ and $Ca_{2.5}Y_{1.5}Cu_5O_{10}$ were probed on the cold triple axis spectrometer TASP, PSI (80'-80'-sample-80', fixed final wavevector $k' = 1.97\,\text{Å}$, aluminum sample holder).

| | $x$ | $\lambda$ (Å) | $d$ (mm) |
|---|---|---|---|
| DMC | $0 \leq x \leq 1.2$ | 2.56 | 7 |
| HRPT | $1 \leq x \leq 2.15$ | 1.89 | 7 |
| SPODI | 0, 0.5 | 1.54 | 8 |
| D20 | 2.15 | 1.89 | 10 |

Table 4.9: Overview of the performed experiments at the PSI, FRM II and ILL, in order to elucidate the magnetic structure of $Ca_{2+x}Y_{2-x}Cu_5O_{10}$ in the ordered phase. For each spectrometer the investigated samples, the wavelength $\lambda$ and the diameter $d$ of the vanadium sample holders are mentioned.

Owing to the importance of these results numerous neutron diffraction experiments were performed. The cold powder diffractometer DMC provides access to an $Q$ range of $0.5\,\text{Å}^{-1}$ to $3.5\,\text{Å}^{-1}$. The low background level shall help to elucidate weak magnetic Bragg reflections in a first test experiment after the sample synthesis. The powder diffractometers HRPT and SPODI allow the investigation of the magnetic structure of $Ca_{2+x}Y_{2-x}Cu_5O_{10}$ samples within a reasonable $Q$ range up to $7\,\text{Å}^{-1}$. The high intensity diffractometer D20 offers a neutron flux of $\sim 10^7\,\text{n}/(\text{s}\,\text{cm}^2)$ at the sample site. We probed the magnetic order of highly doped $Ca_{0.83}CuO_2$, as a magnetic moment of only $0.28\,\mu_B$ is expected from the intrachain and the interchain exchange values (see chapter 4.2.3). The measurement of the sublattice magnetization offers a direct means to probe the temperature dependence of the order parameter around $T_N$. The observed second order phase transition can be unambiguously attributed to the magnetic order, as for instance a lattice distortion also yields a diverging heat capacity signal at its transition temperature.

Fine polycrystalline powder was sealed under helium into vanadium sample holders. Expecting from the moment of free copper spins a magnetic moment of less than $1\,\mu_B$, the material of the sample holder appeared to be a crucial point during the experiment. The ratio $R$ of the incoherent background level of the sample holder to that of the sample itself [99]

$$R = \frac{\sigma_{sh}}{\sigma_s} \cdot \frac{n_{sh}}{n_s} \cdot \frac{2\Delta R}{R} \tag{4.12}$$

correspond to 1.3 and 0.002 for vanadium and aluminum, respectively. Here, $\sigma_{sh}$ and $\sigma_s$ denote the incoherent cross section per atom of the sample holder and the sample. The average incoherent cross section of $Ca_{2+x}Y_{2-x}Cu_5O_{10}$ samples is calculated to be $\simeq 0.2\,\text{barn}$. The atomic concentration of both the sample holder and the sample, $n_{sh}$ and $n_s$, is approximately of the order of one. The wall thickness $\Delta R$ and the radius of the sample holder $R$ are assumed to be equal to 0.1 mm and 4 mm for both materials. Aluminum sample holders shall only little contribute to the overall background level. Besides the sample holder the sample itself and the cryostat may significantly add to the incoherent background. The chemical composition of the sample in terms of site vacancies or distributions of different elements at the same site might play an important role. A test experiment elucidated a similar background level for a vanadium and an aluminum sample holder (see Figure 4.13). As aluminum coherently contributes to the measured signal, only vanadium samples holders were used for the investigation of the magnetic structure.

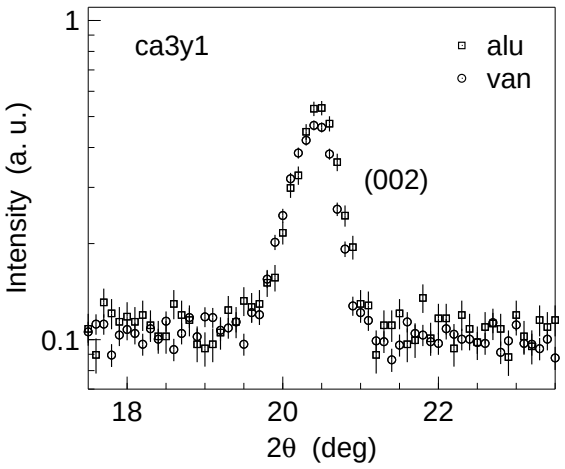


Figure 4.13: Part of the diffraction pattern of $Ca_3Y_1Cu_5O_{10}$ (ca3y1), measured on HRPT, PSI, with an aluminum (alu) and vanadium (van) sample holder of equivalent dimensions. The intensity of both data sets is normalized with respect to the monitor. The Bragg reflection (0 0 2) originates from the nuclear pattern. The incoherent background for both sample holders coincide. Thus, the sample itself or the sample environment dominates the background level, which might originate from the chemical composition of the sample in terms of site vacancies or element distributions on equivalent sample sites.

For data analyzing we reconsider the general expressions of the partial cross sections for coherent nuclear and magnetic scattering presented in chapter 3.2.1. For coherent nuclear Bragg scattering the intensity of a powder peak with the Miller indices $(h\,k\,l)$ is given by [74]

$$\left.\frac{d\sigma}{d\Omega}\right|_{coh}^{el,\,N} = \mathcal{C}\cdot|F_N(\mathbf{G})|^2\, m_{hkl} e^{-2W}\mathcal{P}(\theta)\,\mathcal{A}(\theta)\,. \tag{4.13}$$

The constant $\mathcal{C}$ comprises the details of the instrumental configuration as well as those of the sample itself. The quantity $F_N(\mathbf{G})$ represents the nuclear structure factor of the reciprocal lattice vector $\mathbf{G}$

$$F_N(\mathbf{G}) = \sum_j c_j b_j e^{i\mathbf{G}\cdot\mathbf{d}_j} \tag{4.14}$$

that is summed over all atoms $j$ $(1 \leq j \leq N_N)$ with their occupancy $o_j$ and scattering length $b_j$ in the nuclear unit cell. The vector $\mathbf{d}_j$ describes the copper atom position in real space. $m_{hkl}$ denotes the multiplicity of the reflection $(h\,k\,l)$ [100], $e^{-2W}$ the Debye Waller factor and $\mathcal{P}(\theta) = 1/\left(\sin(\theta)\sin(2\theta)\right)$ the phase space factor for the scattering angle $\theta$ depending on a cylindric sample geometry. The factor $\mathcal{A}(\theta)$ accounts for the absorption of neutrons that depends on the scattering angle $\theta$ and the cylindric sample geometry [101]. The cross section for coherent magnetic elastic scatting

$$\left.\frac{d\sigma}{d\Omega}\right|_{coh}^{el,\,M} = \mathcal{C}\cdot(\gamma r_0)^2\left\langle\mu_z^2\right\rangle|f(\mathbf{Q})|^2(1-\langle\hat{Q}_z^2\rangle)\,|F_M(\mathbf{G}_M)|^2\, m_{hkl} e^{-2W}\mathcal{P}(\theta)\mathcal{A}(\theta) \tag{4.15}$$

defines the integrated intensity of a magnetic reflection $(h\,k\,l)$, where the neutron electron dipole coupling constant $-\gamma r_0$ equals to $-0.539\cdot10^{-12}$ cm. $\langle\mu_z\rangle$ denotes the thermal average of the $z$-component of the magnetic moment in units of Bohr magnetons $\mu_B$. The magnetic form factor $f(\mathbf{Q})$ is the Fourier transform of the magnetization density operator in a single atom [102]. It is calculated within the diploe approximation for the $Cu^{2+}$ electronic configuration $3d^9$. The factor $1-\langle Q_z^2\rangle = 1-\langle\cos^2\alpha\rangle$ arises from the selection rule for magnetic scattering. The intensity of a powder peak depends on the relative orientation of the unit vector direction of the moment with respect to the unit scattering vector $\hat{Q}_z$. $\alpha$ denotes the angle between these two quantities. For powder data this factor has to be summed over all equivalent reflections $(h\,k\,l)$ contributing to one lattice spacing

$d_{hkl}$. In case of an orthorhombic lattice $1 - \langle Q_z^2 \rangle$ corresponds to [103]

$$1 - \langle Q_z^2 \rangle = 1 - \left( (ha^\star)^2 \cos^2 \phi_a + (kb^\star)^2 \cos^2 \phi_b + (lc^\star)^2 \cos^2 \phi_c)^2 \right) \cdot \frac{d^2}{4\pi^2} \,, \tag{4.16}$$

where $a^\star$, $b^\star$ and $c^\star$ denotes the lattice constants of the unit cell in reciprocal space, $d$ the lattice spacing in real space and $\phi_i$ the angle between the magnetic moment and the crystallographic $a$, $b$ or $c$ axis. The magnetic structure factor $F_M(\mathbf{G}_M)$ of a magnetic reciprocal lattice vector is determined according to Eq. (4.14) with $b_j = 1$ and $N_M$ equals to the number of magnetic atoms in the cell.

We used the Rietveld refinement program Fullprof [104], the structure analysis program Modi [105] and the crystallographic programs Supercell [106] and Ball & Sticks [107] for determining the magnetic unit cell as well the propagation vectors of the incommensurable nuclear structure. In particular, Fullprof was used to define the lattice parameters and to model the magnetic intensity with respect to the spin orientation. Furthermore, the magnetic and nuclear intensities of particular Bragg reflections were independently calculated. The magnetic moment was estimated based on the given formula Eq. (4.13) to Eq. (4.15), where the Debye Waller factor was set to unity.

### 4.4.2 Antiferromagnetic Néel state

Figure 4.14 shows the magnetic relevant $CuO_2$ subcell that belongs to the orthorhombic F centered space group (No. 69 [102]). Copper and oxygen ions are sketched in red and yellow color, respectively. $CuO_2$ chains run along the $a$ direction and are stacked along the $c$ direction. Within the asymmetric unit cell copper and oxygen hold the 4a and 16m position with the fractional coordinates $(\mathrm{x}, \mathrm{y}, \mathrm{z}) = (0, 0, 0)$ and $(0, \sim 0.05, \sim 0.6)$, respectively [85, 108]. Ca and Y atoms are assumed to be stoichiometrically distributed on the 16l position with $(\sim 0.4, 0.25, 0.25)$.

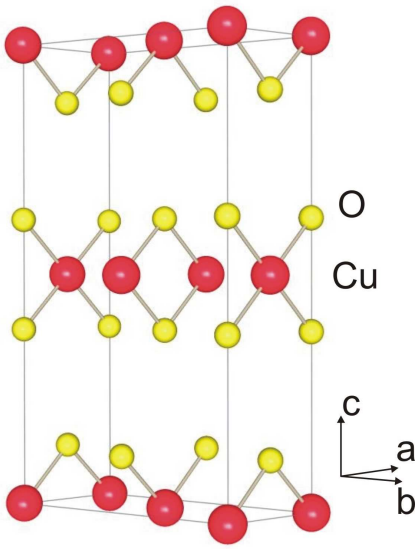


Figure 4.14: Scheme of the face centered orthorhombic $CuO_2$ subcell of the $Ca_{2+x}Y_{2-x}Cu_5O_{10}$ compounds. The lattice parameters are $a \simeq 2.8$ Å, $b \simeq 6.3$ Å and $c \simeq 10.6$ Å. Respecting the unit cell dimensions, the Cu-O-Cu exchange path along the $a$ axis is preferred. Thus, edge sharing $CuO_2$ chains formed by $CuO_4$ units run along the $a$ axis and are stacked along the $c$ axis.

During the Rietveld refinement of the lattice constants the occupancies of each sample is

adjusted to its chemical formula. We account for the incommensurate structure by using a second face centered phase with a propagation vector as described in chapter 4.1.3. This phase was treated in the powder matching mode of Fullprof.
The lattice constants of the $CuO_2$ cell are shown in Figure 4.15. The values are obtained for the 2 K data and are on average $a \simeq 2.80$ Å, $b \simeq 6.25$ Å and $c \simeq 10.575$ Å. Within the error bars we do not observe a significant change of them with respect to the pattern above $T_N$. Increasing the Ca/Y ratio leads to smaller lattice constants along the $a$ and $c$ direction. In contrast, the lattice spacing along the $b$ direction increases with raising $x$. Substituting yttrium with an ion radius of 212 pm by calcium with an ion radius of 194 pm, smaller atoms are inserted in the structure. This might explain the concentration dependent change of the lattice constants. Both the value of the lattice constants and their evolution with $x$ is in agreement with the first synthesized samples of Hayashi and coworkers [61].

According to Mizuno and coworkers [51] the angle $\theta$ of the Cu-O-Cu bond sensitively determines, whether ferromagnetic or antiferromagnetic exchange is found between nearest neighbor spins of the $CuO_2$ chain (see chapter 2.4). We remind that around 95° the nearest neighbor exchange $J_1$ changes its sign from ferromagnetic to antiferromagnetic interaction. The next nearest antiferromagnetic exchange $J_2$ does not change upon increasing $\theta$. Table 4.10 summarizes the obtained bonding angles for the investigated samples. The observed value of $\theta$ of the undoped and the highly doped compound agree well with those obtained by Fong and coworkers [63] and Meijer and coworkers [82]. For samples with a doping concentration $0 \leq x \leq 1.5$ the Cu-O-Cu angle $\theta$ increases from 92.1(2)° to 94.0(2)°, respectively. We thus expect ferromagnetic nearest neighbor exchange along the chain that decreases in strength. The highly doped compound shall feature antiferromagnetic nearest neighbor and next nearest neighbor interaction. In this way, a change of the magnetic exchange along the $a$ axis is expected.

| | $\theta$ (deg) |
|---|---|
| $Ca_2Y_2Cu_5O_{10}$ | 92.1(2) |
| $Ca_{2.5}Y_{1.5}Cu_5O_{10}$ | 92.8(2) |
| $Ca_3Y_1Cu_5O_{10}$ | 92.6(1) |
| $Ca_{3.2}Y_{0.8}Cu_5O_{10}$ | 92.8(2) |
| $Ca_{3.5}Y_{0.5}Cu_5O_{10}$ | 94.0(2) |
| $Ca_{0.83}CuO_2$ | 95.6(2) |

Table 4.10: Cu-O-Cu bonding angle $\theta$ of $Ca_{2+x}Y_{2-x}Cu_5O_{10}$ samples along the chain axis. With increasing Ca/Y ratio the bonding angle increases. The nearest neighbor interaction $J_1$ along the chain changes its sign from ferromagnetic to antiferromagnetic correlations around 95°.

In order to determine the magnetic structure of $Ca_{2+x}Y_{2-x}Cu_5O_{10}$ samples, we collect all magnetic reflections that are visible in the difference pattern of obtained data below and above the order temperature $T_N$. For $0 \leq x \leq 1.5$ samples only Bragg reflections with even-even-odd and odd-odd-even Miller indices are observed that correspond to the propagation vector [0 0 1] [102]. We conclude that ferromagnetic $ab$ planes are antiferromagnetically stacked along the $c$ axis. In agreement with the allowed Shubnikov groups representation analysis for the Fmmm space group with the propagation vector $k = [0\,0\,1]$ and the Cu-position $(0, 0, 0)$ shows that there are three possible antiferromagnetic solutions that correspond to the $\tau_3$, $\tau_5$ and $\tau_7$ irreducible representations with the spin direction along $a$, $b$ or $c$-axis respectively [105, 109]. The observation of the most

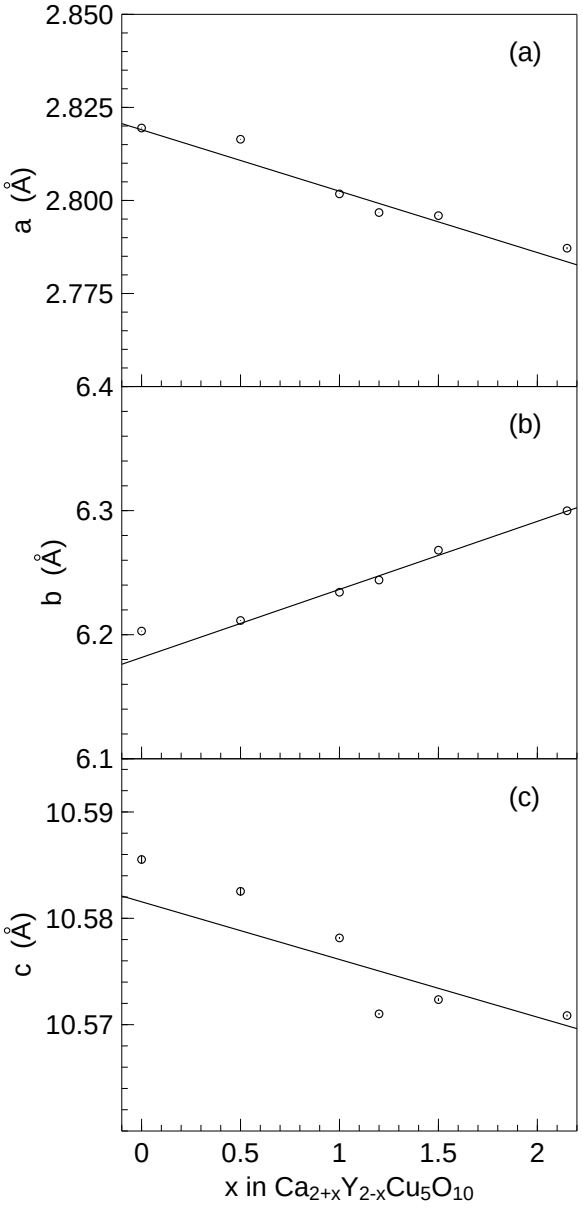


Figure 4.15: Lattice constants of the face centered orthorhombic Fmmm $CuO_2$ subcell of $Ca_{2+x}Y_{2-x}Cu_5O_{10}$ along the (a) $a$, (b) $b$ and (c) $c$ direction. Increasing the Ca/Y ratio leads to an increase in $b$, while $a$ and $c$ decrease. These results coincide with Hayashi and coworkers [61].

prominent magnetic Bragg reflection (0 0 1) excludes the spin orientation parallel to the $c$ axis. Modeling the spin direction with respect to the $a$ and $b$ axis will reveal the magnetic structure.

In a first approach a diffraction experiment on the cold powder diffractometer DMC was performed for samples with $0 \leq x \leq 1.2$. This experiment provides an accessible $Q$-range of 0.51 Å$^{-1}$ to 3.5 Å$^{-1}$. Only few magnetic reflections indexed as (0 0 1) corresponding to $\sim$0.59 Å$^{-1}$, (0 0 3) ($\sim$1.8 Å$^{-1}$) and the double peak formation (0 2 3)/(1 1 2) ($\sim$2.7 Å$^{-1}$) were observed. Owing to the magnetic form factor the peak intensities strongly decrease with higher scattering angles. In comparison to the integrated intensity of the most prominent peak (0 0 1), all other peak areas are smaller by a factor of 25. Figure 4.16 displays the ratios of the integrated intensities (0 0 3)/(0 0 1) and (0 2 3) + (1 1 2)/(0 0 1) of these reflections. For comparison, data of $Ca_2Y_2Cu_5O_{10}$ obtained by the studies of Fong and coworkers [63] and Matsuda and coworkers [64] are included in the figure. Changing the doping concentration $x$ yields constant peak ratios. Furthermore, both literature values coincide with this study. This is the first indication for minor or no modifications of the magnetic structure with doping in this particular concentration range. Respecting the powder averaged selection rule (see Eq. (4.16)) the spin orientation of the collinear antiferromagnetic structure cannot be derived from peaks such as (0 0 $l$).

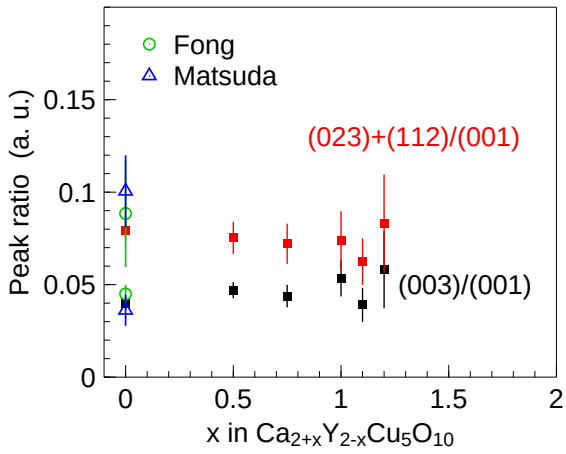


Figure 4.16: Ratios of the magnetic reflections (0 0 3) and (0 2 3) + (1 1 2) to (0 0 1) in the doping range $0 \leq x \leq 1.2$. Larger error bars account at higher $x$ for a weaker magnetic signal. For comparison the corresponding values for $Ca_2Y_2Cu_5O_{10}$ obtained by the work of Fong and coworkers [63] and Matsuda and coworkers [64] are indicated. Since we observe constant ratios of the magnetic Bragg reflections, we conclude that the magnetic structure does not significantly change compared to that of the parent compound.

Data collected at the HRPT (PSI) and SPODI (FRM II) offers an $Q$ range up to of $\sim$6.5 Å$^{-1}$ and 7 Å$^{-1}$. Figure 4.17 displays how modeling the magnetic structure with the magnetic moment parallel to the $a$ and to the $b$ direction appears for $Ca_3Y_1Cu_5O_{10}$. Obviously, the model with the magnetization $m$ parallel to $b$ agrees better with the given data. This plot is representative for all samples with $0 \leq x \leq 1.5$. In order to verify this result for all investigated samples, we calculated the magnetic intensities with $m \parallel a$ and $m \parallel b$ using Eq. (4.15) and (4.16). Table 4.11 summarizes the values of the calculated magnetic intensities for sample with $x$ equal to 0, 0.5, 1, 1.2 and 1.5. Moreover, the observed integrated intensities are provided that were determined by means of Gaussian functions to the magnetic Bragg reflections of the difference pattern. For comparison, all values are normalized in such a way that the integrated intensity of the (0 0 1) Bragg reflection equals to 100. The error bars of the observed peak areas account for the small peak intensities. Furthermore, strong nuclear reflections superimpose on the magnetic pattern, where the scattering angle of nuclear and magnetic reflections coincide. This is the case

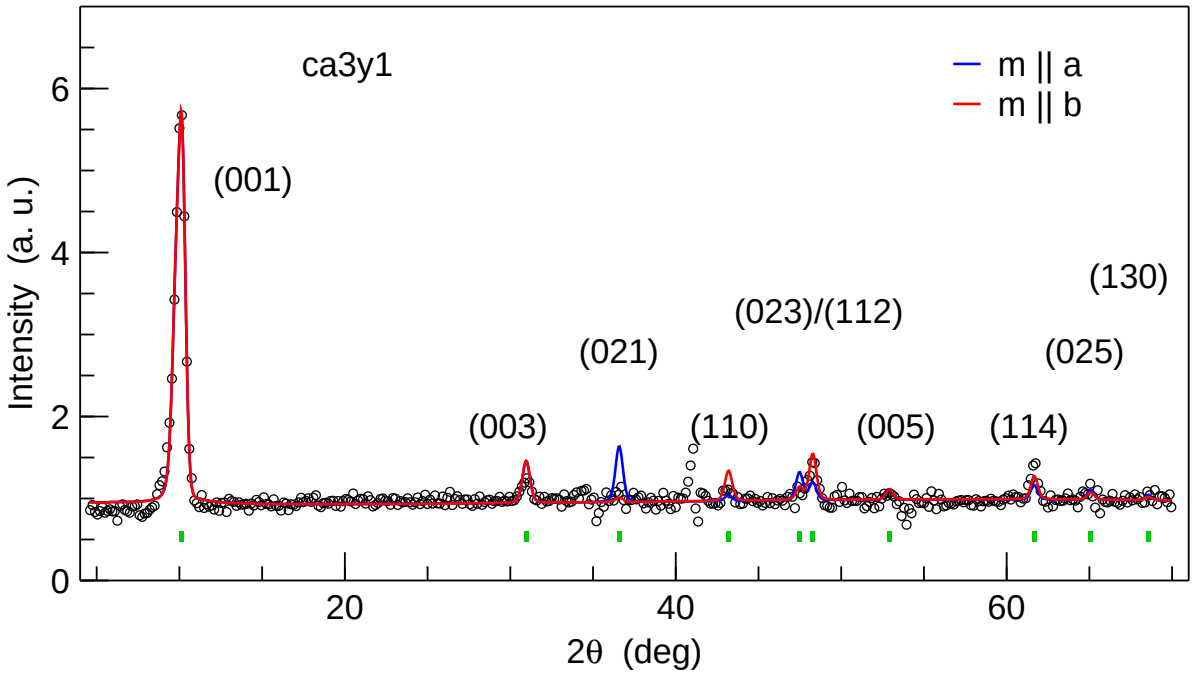


Figure 4.17: Difference pattern of $Ca_3Y_1Cu_5O_{10}$ (ca3y1), obtained on HRPT (PSI) with an incident wavelength of 1.89 Å. For illustration purposes, the error bars of the data are removed (approximately the symbol size). The solid blue and red line display the calculated intensity profile, where the magnetization is fixed parallel to the $a$ and $b$ axis, respectively. The green ticks indicate the positions of the magnetic Bragg reflections. The corresponding Miller indices are displayed above the peak position except for (0 0 1).

| | $(h\,k\,l)$ | $\lvert Q\rvert$ (Å$^{-1}$) | Data | $m \parallel a$ | $m \parallel b$ |
|---|---|---|---|---|---|
| $Ca_2Y_2Cu_5O_{10}$ | (0 0 1) | 0.59 | 100(1) | 100 | 100 |
| | (0 0 3) | 1.78 | 4.7(6) | 8.1 | 8.1 |
| | (0 2 1) | 2.10 | 1.4(9) | 10.0 | 0.8 |
| | (1 1 0) | 2.46 | 4.0(7) | 1.1 | 5.3 |
| | (0 2 3)/(1 1 2) | 2.70/2.72 | 11(1) | 4.6/2.9 | 2.0/7.6 |
| | (1 1 4) | 3.41 | 6.4(1) | 2.1 | 3.3 |
| $Ca_{2.5}Y_{1.5}Cu_5O_{10}$ | (0 0 1) | 0.59 | 100(2) | 100 | 100 |
| | (0 0 3) | 1.78 | 6(1) | 8.1 | 8.1 |
| | (0 2 1) | 2.10 | 1.3(9) | 10.1 | 0.8 |
| | (1 1 0) | 2.46 | 2.8(2) | 1.1 | 5.3 |
| | (0 2 3)/(1 1 2) | 2.70/2.72 | 9(2) | 4.6/2.9 | 2.0/7.6 |
| | (0 0 5) | 2.97 | 2(1) | 1.6 | 1.6 |
| | (1 1 4) | 3.41 | 6(2) | 2.1 | 3.3 |
| $Ca_3Y_1Cu_5O_{10}$ | (0 0 1) | 0.59 | 100(1) | 100 | 100 |
| | (0 0 3) | 1.78 | 5.0(6) | 8.2 | 8.2 |
| | (0 2 3)/(1 1 2) | 2.70/2.72 | 8.6(7) | 4.8/2.9 | 2.1/7.8 |
| | (1 1 4) | 3.77 | 6.7(5) | 2.2 | 3.5 |
| $Ca_{3.2}Y_{0.8}Cu_5O_{10}$ | (0 0 1) | 0.59 | 100(1) | 100 | 100 |
| | (0 0 3) | 1.78 | 4(1) | 8.2 | 8.2 |
| | (0 2 3)/(1 1 2) | 2.70/2.72 | 9(2) | 4.8/2.9 | 2.1/7.8 |
| | (1 1 4) | 3.77 | 8(1) | 2.2 | 3.5 |
| $Ca_{3.5}Y_{0.5}Cu_5O_{10}$ | (0 0 1) | 0.59 | 100(5) | 100 | 100 |

Table 4.11: Integrated intensities of the observed magnetic Bragg reflections for $Ca_{2+x}Y_{2-x}Cu_5O_{10}$ samples. For comparison, both the calculated and the observed intensities are normalized in such as way that the peak area of the (001) reflections is equal to 100. The peak area of the (001) reflection is by a factor of 25 larger compared to the integrated intensity of all other reflections. The magnetic structure factor $F_M(\mathbf{G}_M)$ is calculated based on Eq. (4.14). The multiplicities $m_{hkl}$ are defined with respect to the space group [100].

for all reflections except the (0 0 1) and (0 0 3) peak position. Data analysis thus becomes difficult in terms of residuals of those peaks that are of the order of the weak magnetic peaks. We still observe that a better agreement between the data and the calculated models is given for the spin orientation parallel to the $b$ direction.

Specific heat of the highly doped compound $Ca_{0.83}CuO_2$ indicates a phase transition from the paramagnetic to a 3D ordered phase [82]. Diffraction experiments on HRPT (PSI) and D20 (ILL) both provide evidence of long range order in terms of a magnetic Bragg reflection close to the strong nuclear one (0 0 2) (see Figure 4.18). Within the given magnetic $CuO_2$ subcell the observed peak can be indexed as $(\frac{1}{2}\,0\,1)$. This finding suggests a doubling of the magnetic unit cell along $a$ compared to less doped samples. Antiferromagnetic exchange is observed along the $a$ and the $c$ axis. No further magnetic Bragg reflections were observed in both experiments. This is understandable, since the estimated magnetic moment of this sample is only $\simeq 0.28\mu_B$. This peak was not observed for $Ca_{3.5}Y_{0.5}Cu_5O_{10}$. We conclude that the magnetic structure of the 3D antiferromagnetic Néel state for $Ca_{2+x}Y_{2-x}Cu_5O_{10}$ samples with $0 \leq x \leq 1.5$ differs from that of $Ca_{0.83}CuO_2$.

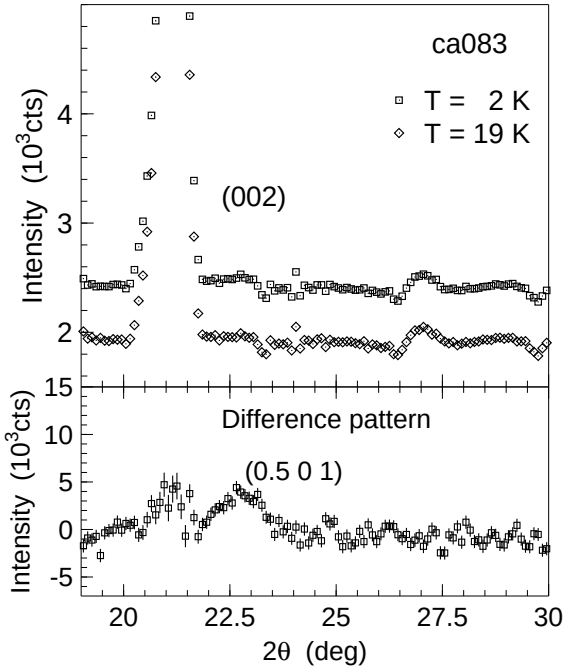


Figure 4.18: Neutron diffraction pattern of $Ca_{0.83}CuO_2$ (ca083) between 19° and 30° measured above and below the order temperature. The data are obtained on D20 with an incident wavelength of $\lambda = 1.89$ Å. The high temperature data are offset for clarity. The difference pattern are shown below the spectra: Besides the residuals of the strong nuclear (002) reflection ($\sim 21°$) the magnetic reflection $(\frac{1}{2}\,0\,1)$ around 23° is observable.

In order to calculate the magnetic moment $\mu$, we extracted the instrumental constant $\mathcal{C}$ for each sample using the (1 1 3), (1 1 5), (1 3 3) and (1 3 5) nuclear reflections. These Bragg peaks are well isolated from other nuclear and magnetic Bragg reflections. Within the asymmetric unit cell they originate from the magnetic CuO sublattice with almost no contributions of Ca/Y sites. In order to further exclude uncertainties with respect to the spin orientation and the statistical data quality, only the (0 0 1) magnetic reflection was used for calculating $\mu$. Table 4.12 provides an overview of the concentration dependence of the calculated magnetic moments in units of $\mu_B$. As already expected from the decreasing integrated intensity of the most prominent (0 0 1) reflection, an increase in the Ca/Y ratio leads to a decrease of the magnetic moment from $0.92(1)\,\mu_B$ to $0.22(6)\,\mu_B$ for $Ca_2Y_2Cu_5O_{10}$ and $Ca_{3.5}Y_{0.5}Cu_5O_{10}$, respectively. The magnetic moment of the parent

compound coincides with the moment of $1\,\mu_B$ of the free copper ion. In addition, this value agrees well with the magnetic moment deduced by Fong and coworkers [63] and Matsuda and coworkers [64] for a powder sample and a single crystal.

| | $\mu$ ($\mu_B$) |
|---|---|
| $Ca_2Y_2Cu_5O_{10}$ | 0.92(1) |
| $Ca_{2.5}Y_{1.5}Cu_5O_{10}$ | 0.81(1) |
| $Ca_3Y_1Cu_5O_{10}$ | 0.49(1) |
| $Ca_{3.2}Y_{0.8}Cu_5O_{10}$ | 0.31(1) |
| $Ca_{3.5}Y_{0.5}Cu_5O_{10}$ | 0.22(6) |
| $Ca_{0.83}CuO_2$ | 0.28 |

Table 4.12: Magnetic moment of $Ca_{2+x}Y_{2-x}Cu_5O_{10}$ samples in units of Bohr magneton $\mu_B$. The value of the magnetic moment in undoped compound $Ca_2Y_2Cu_5O_{10}$ agrees well with literature [63, 64] and coincides with the moment $1\,\mu_B$ of a free copper ion. Upon doping, we notice a decrease in the magnetic moment. The magnetic moment of $Ca_{0.83}CuO_2$ was estimated from susceptibility measurements (see chapter 4.2.3).

### 4.4.3 Sublattice magnetization

The sublattice magnetization $M(T)$ proves whether the second order phase transition that is observed in susceptibility and specific heat measurements is attributed to magnetic order. It is derived as the square root of the temperature dependence of the integrated intensity of a magnetic reflection. The Neél temperature is determined by least square fitting using the scaling law [4]

$$M(T) \sim \left(\frac{T_N - T}{T_N}\right)^{\beta} \tag{4.17}$$

in the temperature range of $0.8T_N \leq T \leq T_N$. The quantity $\beta$ denotes the critical exponent that classifies the universality calls of the investigated sample.

We probed the sublattice magnetization of $Ca_2Y_2Cu_5O_{10}$ and $Ca_{2.5}Y_{1.5}Cu_5O_{10}$ on TASP (PSI) using the most prominent (0 0 1) magnetic peak. Figure 4.19 (a) illustrates the (0 0 1) reflection at four temperatures obtained for $Ca_{2.5}Y_{1.5}Cu_5O_{10}$. We observe that the amplitude of the reflection is decreasing with temperature. Above the order temperature the antiferromagnetic reflection vanishes. The solid lines are fits to the data using a Gaussian function with a constant background. Figure 4.19 (b) displays the temperature dependence of the square root of the integrated intensity of the (0 0 1) reflection for both samples. In order to match the absolute value of the integrated intensity, the presented data are normalized using the Bloch $T^{3/2}$ theorem for $T \to 0$[4]. Data evaluation based on Eq. (4.17) yields an order temperature of 28.6(1) K and 26.2(2) as well as the critical exponents $\beta = 0.31(2)$ and 0.42(6) for $x = 0$ and 0.5, respectively.
Within the error bars the first exponent is compatible with Ising behavior, whereas the latter one corresponds to the $\beta$ value of 3D Heisenberg behavior[5] [110]. We notice that we expect from the magnetic structure analysis Heisenberg behavior with an easy-axis anisotropy for the spin degree of freedom. The latter accounts for the spin orientation

[4]The Bloch $T^{3/2}$ theorem describes the spontaneous magnetization $M(T)$ within one domain, where $M(T)/M(T=0) \propto 1 - aT^{3/2}$ [4].

[5]For Ising, XY and Heisenbeg behavior $\beta$ is equal to 0.326, 0.346 and 0.367 [110].

parallel to the $b$ axis. The value of the extracted critical exponent is highly sensitive towards the number of measured points within the fitting range. In case of the parent compound the estimated order temperature $T_N$ coincide with the values that were obtained by Fong and coworkers [63] and Matsuda and coworkers [64]. Furthermore, $T_N$ shows consistency with the values deduced from specific heat measurements (see chapter 4.3.1).

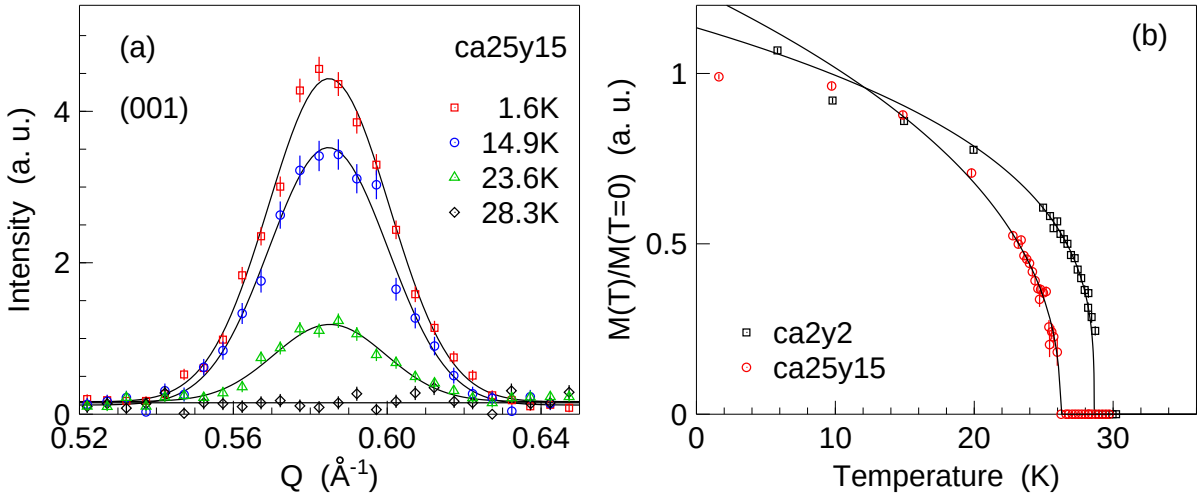


Figure 4.19: (a) Intensity of the (0 0 1) magnetic reflection at various temperatures obtained in $Ca_{2.5}Y_{1.5}Cu_5O_{10}$ (ca25y15). The solid lines display fits to the data using a Gaussian function. (b) Sublattice magnetization $M(T)$ of $Ca_2Y_2Cu_5O_{10}$ (ca2y2) and $Ca_{2.5}Y_{1.5}Cu_5O_{10}$ (ca25y15). The data are scaled respecting the Bloch $T^{3/2}$ theorem at low temperatures. The error bars of the integrated intensities are smaller than the data symbols.

In summary, neutron diffraction elucidates the Cu-O-Cu angle along the chain direction as well as the magnetic structure in the ordered phase. For a doping concentration of $0 \leq x \leq 1.5$ the magnetic structure is described as collinear with ferromagnetic $ab$ planes that are antiferromagnetically stacked along $c$. The spin orientation is found to be parallel to the $b$ direction. Only for the highly doped sample the observed $(\frac{1}{2}\,0\,1)$ reflection indicates a change in the chain correlation.
As $Ca_2Y_2Cu_5O_{10}$ features a Cu-O-Cu angle $\theta = 92°$, theory predicts competing strong ferromagnetic nearest neighbor exchange and weaker antiferromagnetic next nearest neighbor correlations along the chain [51]. The structure analysis resolved an effective ferromagnetic chain exchange. This result excludes the parent compound as realization of the antiferromagnetic $S = 1/2$ Heisenberg chain. In contrast, the highly doped compound exhibits antiferromagnetic exchange along the chain with a Cu-O-Cu angle of 95.5° turning this sample into an ideal candidate for studying 1D behavior of the antiferromagnetic spin chain by means of inelastic neutron spectroscopy.

## 4.5 Spin dynamics

This section reports inelastic neutron scattering experiments of three members of the quasi 1D compound series $Ca_{2+x}Y_{2-x}Cu_5O_{10}$. We focused on the undoped parent com-

pound whose low temperature spin dynamics are understood by linear spin wave theory (see chapter 4.5.1). Furthermore, the investigation of the medium doped compound $Ca_{3.5}Y_{0.5}Cu_5O_{10}$ provides evidence of a spin glass state below $\sim 17\,\mathrm{K}$ (see chapter 4.5.2). The 1D Heisenberg behavior of the highly doped compound $Ca_{0.83}CuO_2$ reveals an intradimer extent of next nearest neighboring copper ions (see chapter 4.5.3).

### 4.5.1 3D antiferromagnet $Ca_2Y_2Cu_5O_{10}$

Previous experiments of undoped $Ca_2Y_2Cu_5O_{10}$ resolve a 3D antiferromagnetic state below $\sim 29\,\mathrm{K}$. The analysis of its ordered magnetic structure elucidated ferromagnetic exchange within the *ab* plane and antiferromagnetic correlations perpendicular to this plane. One expects the dynamical behavior below $T_N$ to be dominated by a spin wave with these type of magnetic interactions.

In order to obtain the magnon dispersion relation $\hbar\omega(\mathbf{q})$ all possible interactions within the magnetic unit cell have to be considered. Figure 4.20 displays the appropriate model based on the derived magnetic structure of the parent compound. Within each magnetic unit cell we observe ferromagnetic interaction along the *a*, *b* and thus along the $[\frac{1}{2}\,\frac{1}{2}\,0]$ direction. Along the *c* direction we observe antiferromagnetic correlations, i.e. the spins along the $[\frac{1}{2}\,0\,\frac{1}{2}]$ and $[\frac{3}{2}\,0\,\frac{1}{2}]$ direction show antiferromagnetic correlations, whereas along $[0\,0\,1]$ spins are ferromagnetically coupled. An easy-axis anisotropy term is expected, since the spins are oriented parallel to the *b* axis.

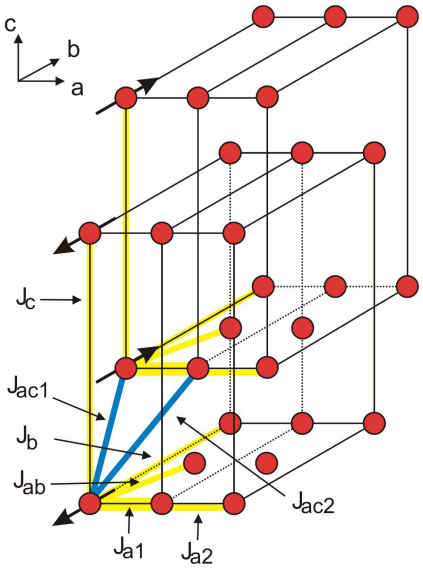


Figure 4.20: Model to obtain the magnon dispersion relation $\hbar\omega(\mathbf{q})$ of $Ca_2Y_2Cu_5O_{10}$. Copper ions (sketched in red color) are located at the corner of the orthorhombic unit cell as well as on each face side. Within one magnetic unit cell ferromagnetic exchange is found along the $[1\,0\,0]$ and $[0\,1\,0]$ direction. Thus, the magnetic correlations in the *ab* plane are also ferromagnetic. Two magnetic unit cells are antiferromagnetically coupled along the $[\frac{1}{2}\,0\,\frac{1}{2}]$ and $[\frac{3}{2}\,0\,\frac{1}{2}]$ direction. The exchange along $[0\,0\,1]$ is ferromagnetic. $J_i$ denotes the particular magnetic exchange, where the index $i$ is chosen with respect to the direction of the correlation between the copper ions.

The dispersion relation is calculated based on the Hamiltonian

$$H = \sum_{ij} J_{ij}\hat{\mathbf{S}}_i\hat{\mathbf{S}}_j + \sum_{ij} \tilde{J}_{ij}\hat{S}_i^z\hat{S}_j^z\,, \tag{4.18}$$

where $J_{ij}$ and $\tilde{J}_{ij}$ denote the Heisenberg exchange and the anisotropy parameter between spins $i$ and $j$, respectively. $\hat{\mathbf{S}}_i$ represent the spin operator of the spin $i$. The summation is carried out over nearest and next nearest neighbor spins in all crystallographic directions. We only consider magnetic correlations between spins within the largest distance of the

magnetic unit cell in real space. Linear spin wave theory yields the dispersion relation

$$\begin{aligned}\hbar\omega(\mathbf{q}) &= \Big[\Big(2J_{a1}(\cos(q_a a)-1)+2J_{a2}(\cos(2q_a a)-1)+2J_b(\cos(q_b b)-1)\\ &\quad +2J_c(\cos(q_c c)-1)+4J_{ab}(\cos(\tfrac{q_a a}{2})cos(\tfrac{q_b b}{2})-1)+4J_{ac1}+4J_{ac2}\\ &\quad -D\Big)^2-\Big(4J_{ac1}\cos(\tfrac{q_a a}{2})\cos(\tfrac{q_c c}{2})+4J_{ac2}\cos(\tfrac{3q_a a}{2})\cos(\tfrac{q_c c}{2})\Big)^2\Big]^{\frac{1}{2}} \quad (4.19)\end{aligned}$$

where the anisotropy $D$ is defined by $D=-2\tilde{J}_{a1}-2\tilde{J}_{a2}-2\tilde{J}_b-2\tilde{J}_c-4\tilde{J}_{ab}+4\tilde{J}_{ac1}+4\tilde{J}_{ac2}$. The quantities $q_a$, $q_b$ and $q_c$ represent the reduced scattering vector $q_x$ in units of $2\pi/x$ ($x\in\{a,b,c\}$) that transforms to the reciprocal lattice units via $\xi=q_x x/(2\pi)$. The exchange constants $J_i$ denote the magnetic correlations, where the index $i$ corresponds to the particular direction between two spins. The detailed mathematical derivation of the dispersion relation is presented in appendix A.2

Matsuda and coworkers performed an inelastic neutron scattering study on single crystal $Ca_2Y_2Cu_5O_{10}$ below $T_N$ [65]. Table 4.13 summarizes the fitted exchange and anisotropy parameters of the spin wave dispersion Eq. (4.19). The exchange $J_{ac2}$ was fixed to $J_{ac1}/2$ during the fit. Furthermore, next nearest neighbor correlations along the $c$ axis do not contribute to the observed excitation spectrum and were set to zero. Within the $J_1$-$J_2$ model for edge sharing $CuO_2$ chains the magnetic exchange along the chain axis should arise from ferromagnetic nearest neighbor and antiferromagnetic next nearest neighbor interaction, where $|J_1|>J_2$ is expected [51]. Lacking data points at the zone boundary along [1 0 0] the low energy dispersion is equally described using an approach with an effective ferromagnetic interaction and an approach with $J_{a1}$ and $J_{a2}$.

| | Cu position | $J_i$ (meV) |
|---|---|---|
| $2J_{a1}$ | $(a\,0\,0)$ | -6.9(1)/-8(1) |
| $2J_{a2}$ | $(2a\,0\,0)$ | 0/0.4(3) |
| $2J_b$ | $(0\,b\,0)$ | -0.061(6) |
| $2J_{ab}$ | $(\frac{1}{2}a\,\frac{1}{2}b\,0)$ | -0.030(3) |
| $2J_c$ | $(0\,0\,c)$ | 0 |
| $2J_{ac1}$ | $(\frac{1}{2}a\,0\,\frac{1}{2}c)$ | 1.494(3) |
| $2J_{ac2}$ | $(\frac{3}{2}a\,0\,\frac{1}{2}c)$ | 0.747 |
| $D_{ab}$ | $(a\,b\,0)$ | -0.399(1) |
| $D_{ac}$ | $(a\,0\,c)$ | -0.262(3) |

Table 4.13: Exchange $J_i$ of single crystal $Ca_2Y_2Cu_5O_{10}$ between the Cu ion at (0 0 0) and the corresponding counterpart in real space and anisotropy $D$ [65]. $J_i<0$ and $J_i>0$ account for ferromagnetic and antiferromagnetic interaction, respectively. Next nearest interaction along the $a$ and $c$ axis does not contribute to the spin wave dispersion. The single ion anisotropy $D_i$ was treated as fitting parameter, thus two terms are necessary to describe the dispersion relation along the axes of the magnetic unit cell.

Figure 4.21 displays the spin wave dispersion of the parent compound along the $[a\,0\,0]$, $[0\,b\,0]$ and $[0\,0\,c]$ direction of the magnetic unit cell. The three branches are indicated by the black, red and blue solid line, where the fit with $J_{a2}=0$ and $J_{a2}\neq 0$ are indicated by the dashed and solid line, respectively. Respecting the absolute value of the exchange constants we expect the maximum of the dispersion corresponding to $\omega(\mathbf{q})\parallel a$. The spin wave dispersion along the chain axis yields $\sim 20$ meV at the Brillouin zone boundary, while the maximum in energy transfer along $c$ is only about 5 meV at the zone boundary. Along the $b$ direction the dispersion is almost flat. Owing to the easy-axis anisotropy that forces spins parallel to the $b$ axis, we observe a spin gap of the order of 1.5 meV to 2 meV in all three crystallographic directions.

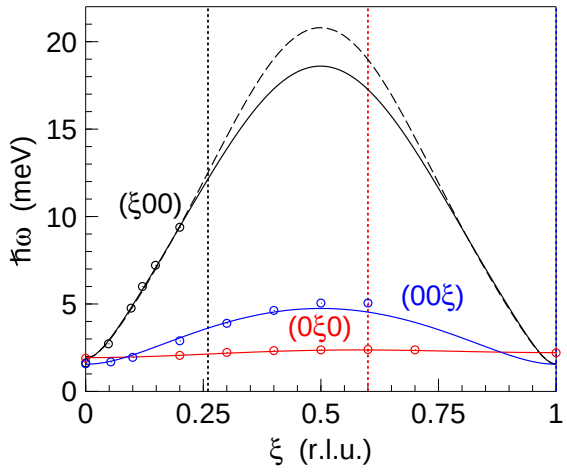


Figure 4.21: Dispersion relation of $Ca_2Y_2Cu_5O_{10}$ along the $[a\,0\,0]$, $[0\,b\,0]$ and $[0\,0\,c]$ direction in reciprocal lattice units (sketched in black, red and blue color). The solid black and the dashed black curve correspond to the exchange values $J_{a2} = 0$ and $J_{a2} \neq 0$. Data points are taken from [65]. A spin gap is present in the spin wave dispersion that originates from the spin orientation along the $b$ direction of the magnetic unit cell. As the lattice constants of the magnetic unit cell differ, the distance to the next Brillouin zone center along $a$, $b$ and $c$ corresponds to $2.24\,\text{Å}^{-1}$, $0.99\,\text{Å}^{-1}$ and $0.59\,\text{Å}^{-1}$, respectively. The dashed vertical lines indicate $Q = 0.59\,\text{Å}^{-1}$ for each crystallographic direction.

A powder sample limits the possibility to obtain a wavevector dependent dispersion relation $\hbar\omega(\mathbf{q})$. We thus restricted our investigation to the wavevector $Q = 0.59\,\text{Å}^{-1}$ that corresponds to the most intense magnetic Bragg reflection (001). Within the orthorhombic unit cell this $Q$ value coincides with $\xi \simeq 0.26$ r.l.u. along the $a$ axis, $\xi \simeq 0.6$ r.l.u. along $b$ and the magnetic zone center of the next Brillouin zone along the $c$ direction. Owing to the dispersion relation of $Ca_2Y_2Cu_5O_{10}$ the energy dependence of the excitation spectrum features a spin gap of $\sim 1.8$ meV. In a very naive picture, one apt to think that constant $Q$ scans in a powder sample cut through the dispersion branches along the crystallographic axis. We expect defined excitation energies of $\sim 1.8$ meV, $\sim 2$ meV and $\sim 12$ meV for the corresponding $q_x$ values along the $c$, $b$ and $a$ direction.

In order to elucidate the magnon dispersion of polycrystalline $Ca_2Y_2Cu_5O_{10}$, we performed a neutron scattering experiment on the cold triple axis spectrometer NG-5 (SPINS, NIST). The instrument was operated in the fixed final energy mode ($E' = 5$ meV) with the horizontally focusing analyzer (HFA) and the collimation 80'-sample-radial collimator-HFA. Owing to the focusing condition the measured intensity is increased compared to a flat analyzer (FA) at the expense of the $Q$ resolution. Raising energy transfer $\hbar\omega$ yields smaller scattering angles $\theta_S$. Around 3 meV the instrumental background drastically increases, which results from an instrumental set-up close to the direct beam. Furthermore, an experiment was carried out on the cold triple axis spectrometer TASP (PSI). During this experiment a fixed final energy of 8 meV and the instrumental set-up 80'-sample-80'-FA-80' was employed.

Figure 4.22 (a) depicts the observed 2 K excitation spectrum at $Q = 0.59\,\text{Å}^{-1}$ on NG-5. We clearly observe the energy gap of 1.5 meV to 2 meV in the excitation spectrum. By means of constant energy scans at $\hbar\omega = 1$ meV and 2 meV the gaped dispersion was approved (data are not shown). Owing to the decreasing scattering angle with raising energy transfer, the background significantly increases at energy transfers beyond 3 meV. Figure 4.22 (b) displays the equivalent spectrum measured on TASP with a flat analyzer. Two excitation peaks are observed around 2 meV and 3.9 meV. The solid line is a guide to

the eye using three Gaussian functions with a constant background for the quasielastic contribution and the two inelastic peaks. We remind the dispersion $\hbar\omega$ of single crystal $Ca_2Y_2Cu_5O_{10}$. We expect scattering between 2 meV and 5 meV, since a powder average over all **Q** directions has to be carried out. Measurements above the order temperature show that these excitations vanish. The magnetic signal thus originates from a spin wave excitation.

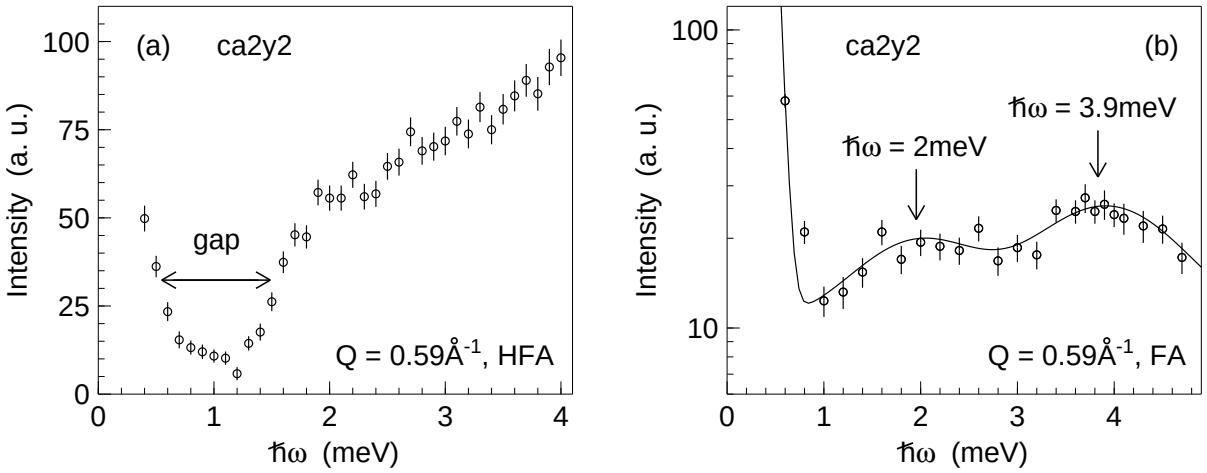


Figure 4.22: Excitation spectra of $Ca_2Y_2Cu_5O_{10}$ (ca2y2). Constant $Q$ scans at 0.59 $Å^{-1}$ are measured on (a) NG-5 (Spins, NIST) with an horizontally focused analyzer (HFA) and (b) TASP (PSI) using a flat analyzer (FA). (a) A spin gap of $\sim 1.8$ meV is visible in the dispersion that originates from the easy-axis anisotropy in this sample. The focusing condition increases the intensity at the expense of the $Q$ resolution. (b) Using a set-up with a flat analyzer reveals two distinct excitation peaks around 2 meV and 3.9 meV. The solid line is a guide to the eye.

The investigation of the polycrystalline sample confirmed the significant feature of the low energy dispersion of $Ca_2Y_2Cu_5O_{10}$: a spin gap that originates from an easy-axis anisotropy. This results is compatible with the dispersion relation of a single crystal of undoped $Ca_{2+x}Y_{2-x}Cu_5O_{10}$ and our magnetic structure study (see chapter 4.4). At this point it might be possible to calculate the powder averaged magnetic cross section for coherent scattering based on the derived exchange parameters of Matsuda and coworkers [65] for this particular $Q$ value (see e.g. Lovesey [75]). However, due to the complex dispersion relation the numerical very demanding calculation will not be done in this thesis work. In particular, only the lineshape at low energies can be compared to the experimental data. No further information about the high energy excitation spectra can be deduced in terms of the importance of the antiferromagnetic next nearest interaction along the frustrated $CuO_2$ chain.

### 4.5.2 Spin glass state in $Ca_{3.5}Y_{0.5}Cu_5O_{10}$

Bulk measurements provided evidence of a disordered state in $Ca_{3.5}Y_{0.5}Cu_5O_{10}$ below $\sim 10$ K. Susceptibility shows an increase, where the magnetic correlations are of antiferromagnetic type. In addition, specific heat elucidates a broad plateau yielding a constant value for $T \to 0$. To determine the low temperature phase in this sample, we performed a neutron scattering study on the cold triple axis spectrometer PANDA (FRM II) using the fixed final energies $E' = 4.7$ meV, 8.0 meV and 14.7 meV. For the last two final energies

a pyrolytic graphite filter was installed before the analyzer, whereas for measurements with 4.7 meV a cooled beryllium filter was used. The primary collimation was fixed to 60' during the experiment and the monochromator remained vertically focusing. Inelastic measurements made use of a slit with the dimensions 4 cm × 3 cm (height × width) located before the detector. During elastic measurements this slit was replaced by one that offered the similar height and does not horizontally restrict the beam.

Probing whether a spin glass-like state is present in $Ca_{3.5}Y_{0.5}Cu_5O_{10}$, an elastic neutron scattering study of the most intense magnetic Bragg reflection (0 0 1) was performed using two different instrumental energy resolutions. Neutrons with a final energy 4.7 meV show an energy resolution of ∼0.2 meV, whereas those with 14.7 meV probe fluctuations in the range of $\Delta(\hbar\omega) \sim 0.9$ meV.

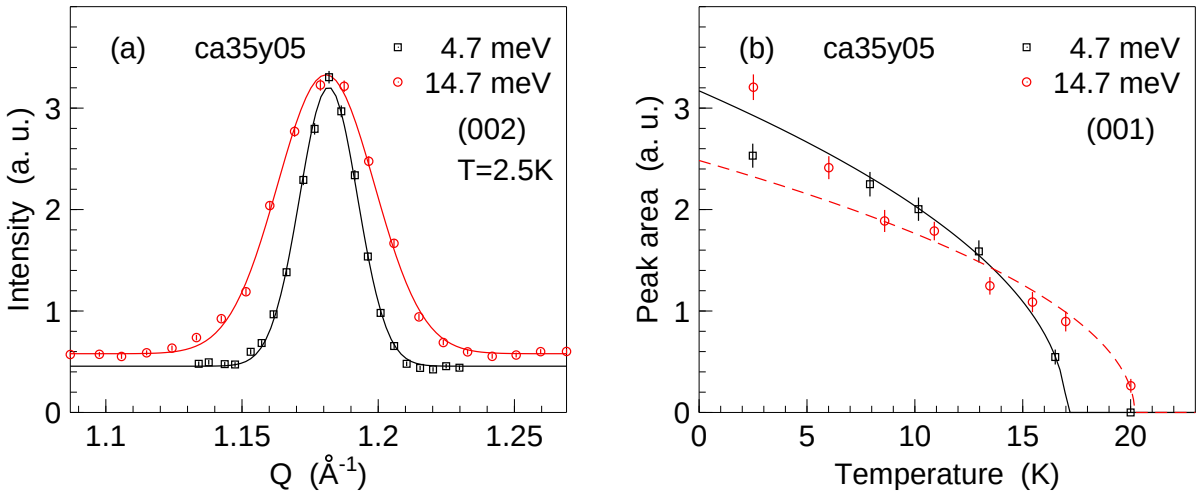


Figure 4.23: Comparison between data obtained with $E' = 4.7$ meV and 14.7 meV for $Ca_{3.5}Y_{0.5}Cu_5O_{10}$ (ca35y05). (a) The nuclear (0 0 2) reflection exhibits a different linewidth with respect to the instrumental resolution. The displayed data are normalized to the absolute amplitude of each other. (b) Background subtracted integrated intensity of the most intense magnetic Bragg peak (0 0 1). The data are normalized using the integrated intensity of the nuclear (002) reflection at 2.5 K.

Figure 4.23 (a) depicts the nuclear (0 0 2) Bragg reflection measured with these two energy resolution. For comparison, the shown data are normalized to match the amplitude of both peaks. The temperature dependence of the background subtracted integrated intensity of the (0 0 1) reflection is displayed in Figure 4.23 (b). The obtained peak areas are normalized with respect to the peak areas of the (0 0 2) reflection that were measured at 2.5 K for both energy resolutions. We observe a resolution dependent decrease in the integrated intensity of the (0 0 1) reflection. The broader resolution yields a higher order temperature ($T > 20$ K), when spin fluctuations are slowed down. 4.7 meV data reveal at ∼17 K the absence of the (0 0 1) reflection.

The dependence of the critical temperature on the instrumental resolution is considered as a typical sign of a spin glass. Spins are correlated within domains of a certain extent. Increasing temperature yields a decreasing correlation length on which spins fluctuate. Measuring the (0 0 1) reflection with a lower resolution probes a smaller correlation length

compared to data obtained with a smaller linewidth. Thus, we observe still fluctuations at an elevated temperature.

This result coincides with literature for a single crystal $Ca_{3.5}Y_{0.5}Cu_5O_{10}$ sample that exhibits a spin glass-like phase below 15 K [66, 91]. This phase was elucidated both by means of susceptibility measurements and inelastic neutron scattering. It was found that the spin glass state originates from magnetic spins that are coupled along the $a$ axis. The spin glass temperature that was observed by neutron scattering is a factor of two higher compared to that of susceptibility measurements.

### 4.5.3 1D Heisenberg behavior in $Ca_{0.83}CuO_2$

Susceptibility and specific heat measurements show evidence of 1D Heisenberg behavior in $Ca_{0.83}CuO_2$, where $\alpha$ was found to be close to the uniform chain and the exchange $J \sim 60\,\mathrm{K}$ (see chapter 4.2 to 4.3). The number of magnetic spins almost coincides with the expected value of 2/3. Although the $CuO_2$ chains in this sample are diluted by 33 %, we observe a long range ordered state below 12 K. Neutron diffraction elucidated antiferromagnetic correlations along the chain direction. Owing to these findings the dynamical behavior of highly doped $Ca_{0.83}CuO_2$ shall be dominated by quasi 1D properties. In the following, we investigate the structure factor and the scattering law $S(Q,\omega)$ for this sample. Both quantities behave in a typical way in case of the antiferromagnetic Heisenberg spin chain with alternating exchange.

Data were collected on the triple axis spectrometer IN3 and the thermal time of flight instrument IN4 that are installed at ILL. Both offer the possibility to instantaneously probe the excitation spectrum for a broad $(Q,\omega)$ range.
The spectrometer IN3 is equipped with a multi detector allowing the investigation of an elastic $Q$ range of $0.3\,\mathrm{Å}^{-1}$ to $3.9\,\mathrm{Å}^{-1}$. During the experiment the fixed final energy $E' = 31.16\,\mathrm{meV}$ and a collimation of 60' between the monochromator and the sample were chosen. $Ca_{0.83}CuO_2$ and the aluminum empty can was measured for both 2 K and 20 K. The sample was mounted into a cylindric aluminum sample holder with an diameter of $\sim 1\,\mathrm{cm}$. Correcting for the different detector efficiencies required the measurement of a vanadium sample.
Furthermore, an experiment was performed on IN4 that offers detectors within the angular range of $2.4° \leq 2\theta \leq 120°$. The chosen incident energies of 67.5 meV and 16.1 meV allows for an elastic $Q$ range of $0.2\,\mathrm{Å}^{-1} \leq Q \leq 9.7\,\mathrm{Å}^{-1}$ and $0.1\,\mathrm{Å}^{-1} \leq Q \leq 4.8\,\mathrm{Å}^{-1}$, respectively. The maximum in the accessible energy transfer range varied from $\sim 60\,\mathrm{meV}$ and 15 meV (neutron energy loss). We measured vanadium, the polycrystalline sample and the empty can in the temperature range of 2 K up to 80 K. The aluminum cylinder with an outer and inner diameter of 20 mm and 19 mm provided an annular hollow geometry. The wall thickness of the outer and the inner container was chosen to be 0.5 mm and 0.4 mm, respectively. With a mass of 6.4 g the transmission of the sample was about 94 %. Absorption effects of the aluminum can leads to a transmission factor of about 98%. The obtained data are analyzed as described in chapter 3.2.3.

Excitations of the dimerized antiferromagnetic spin 1/2 chain features a characteristic structure factor. $S(Q)$ of coupled dimers reveals typical distances of two coupled spins

within one dimer: the intradimer distance $d$ [32, 111, 112, 113]. This quantity corresponds to the first maximum in the structure factor. Moreover, the structure factor is almost insensitive towards the coupling between dimers, i.e. the alternating parameter $\alpha$. The interdimer distances $b$ (the distance between two dimers) give raise to small modulations of the amplitude of the structure factor. However, the position of the maxima and minima in the structure factor are unaffected.
The mathematical derivation of the powder averaged structure factor $S(Q)$ in $\mathcal{O}(\alpha)$ is presented in appendix B.1. We use the analytical expression of $S(\mathbf{Q})$ that is obtained by Barnes and coworkers [32]. The spherical integrated structure factor results in

$$S(Q)/|f(\mathbf{Q})|^2 = 1 - \frac{\sin(Qd)}{Qd} + \frac{\alpha}{2}\Big(\frac{\sin(Qb)}{Qb} - \frac{\sin(Q(d-b))}{2Q(d-b)} - \frac{\sin(2Q(b+d))}{2Q(d+b)}\Big), \quad (4.20)$$

where $d$ and $b$ denotes the intradimer and the interdimer distance, respectively. The form factor $f(\mathbf{Q})$ corrects for a decreasing intensity upon increasing wavevector $\mathbf{Q}$. In order to obtain the quantity $d$ from a fit to the experimental data, we use a constant background that accounts for incoherent scattering contributions. Fits on an extended $Q$ range included a phonon term $\propto Q^2$ and results in compatible results for the intradimer distance $d$.

Figure 4.24 (a) to (d) depict $S(Q)$ that is obtained by the experiments on IN3 and IN4 ($E = 16.1\,\mathrm{meV}$). The presented data at 2 K and a higher temperature above $T_N$ are inelastically summed over a broad energy range. We estimated this energy range reasonably large enough based on the exchange value $J$ that was revealed by susceptibility measurements for $Ca_{0.83}CuO_2$. For all plots data points at low $Q$ are removed, as in case of the IN3 experiments these data points correspond to a instrumental geometry near the direct beam. For IN4, the background of the small angle detectors are increased compared to detectors installed at higher scattering angles.
The structure factor clearly displays a broad maximum around $0.7\,\text{Å}^{-1}$. In a first approach we restricted the fit to the model of isolated dimers ($\alpha = 0$) in a $Q$ range up to $\sim 2.5\,\text{Å}^{-1}$. Above this $Q$ value phonon scattering contributes to the signal. Moreover, the magnetic form factor of $Cu^{2+}$ is already decreased by 30 % around $2.5\,\text{Å}^{-1}$. The intradimer distance measured on IN3 turns out to be 6.1(1) Å and 5.8(2) Å at 2 K and 20 K, respectively. In agreement, fits to the IN4 data yield values of 5.4(1) Å and 5.7(1) Å for 2 K and 25 K. The low statistics of the data prevent from extracting the interdimer distance. When restricting $\alpha$ equal to one, the deduced interdimer distance $b$ strongly depends on the starting parameters.

Both experiments consistently reveal a maximum in the structure factor around $0.7\,\text{Å}^{-1}$. This corresponds to the distance of two spins of about 5.7 Å in real space. Considering the distance of two copper atoms along the chain direction $a$ of 2.8 Å the intradimer distance is about twice this value. This result is understood within the frame of the $J_1$-$J_2$ model for a Cu-O-Cu angle of 95.5°, as the stronger magnetic exchange arises from the antiferromagnetic next nearest neighbor interaction [51]. The equivalent results for data below and above the Néel temperature demonstrate that the dynamical behavior of $Ca_{0.83}CuO_2$ follows the 1D Heisenberg model for antiferromagnetic spin chains. No ambiguity arises from the coexisting Néel state, since the long range antiferromagnetic order only sets in below 12 K. Although the interdimer distance cannot be revealed by the experimental

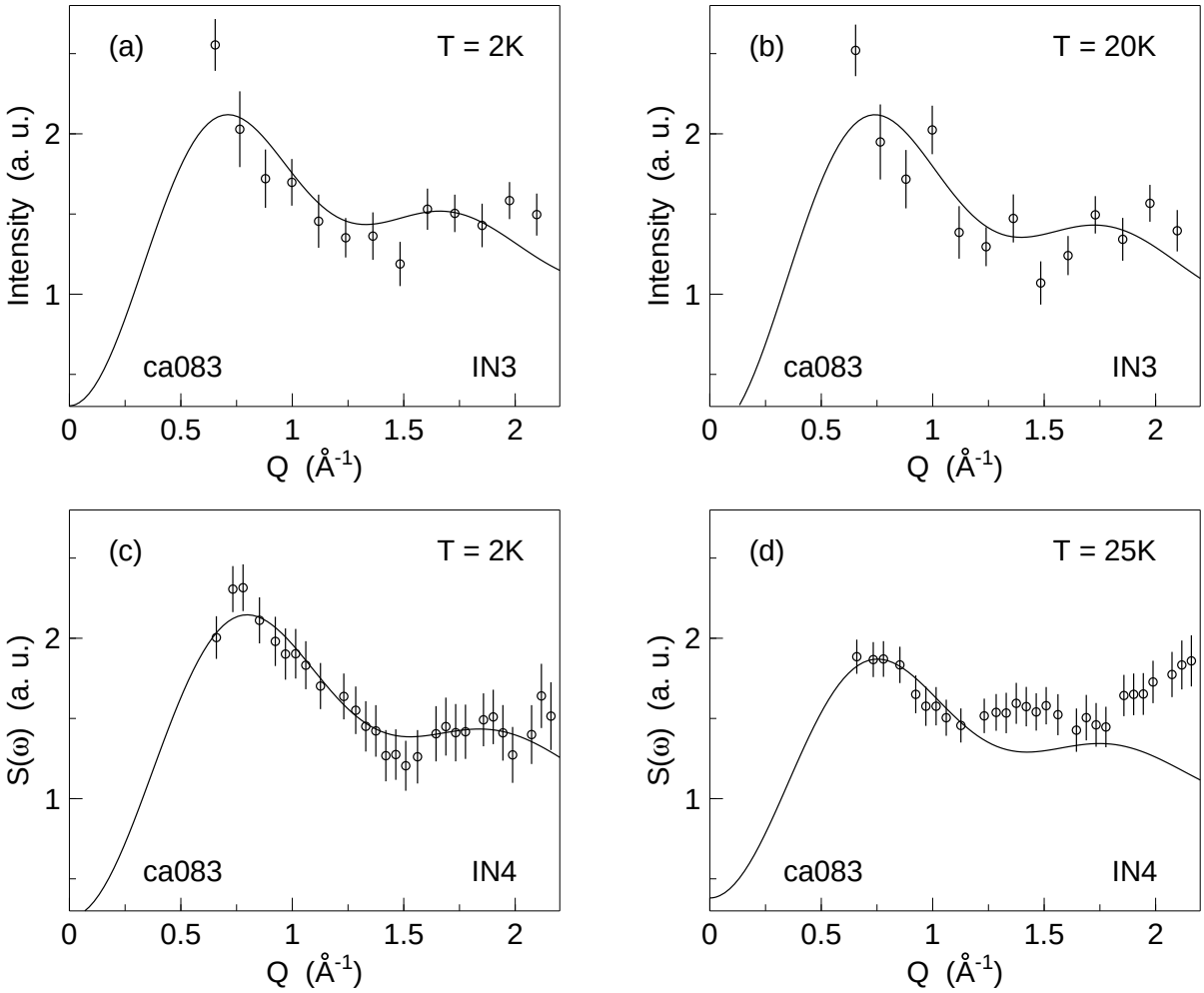


Figure 4.24: Structure factor $S(Q)$ of $Ca_{0.83}CuO_2$ (ca083), obtained from experiments on the spectro- meters IN3 and IN4 ($E' = 16.1\,\mathrm{meV}$) for two temperatures. The shown data are summed over the energy range $4\,\mathrm{meV} \leq \hbar\omega \leq 12\,\mathrm{meV}$ and $4\,\mathrm{meV} \leq \hbar\omega \leq 8\,\mathrm{meV}$, respectively. In case of IN3 data, points at low $Q$ are removed that corresponds to a instrumental geometry close to the direct beam. For IN4 plots, points of the low angle detectors are removed, as their instrumental background is increased compared to detectors at higher scattering angles. Raising intensity above $2\,\mathrm{Å}^{-1}$ is attributed to phonon scattering. The solid lines represent fits of the structure factor for $\alpha = 0$. We observe for the IN3 data at the two temperatures an overall agreement between both data and the fit. The discrepancy between the 2 K and 25 K data of IN4 starting around $1.2\,\mathrm{Å}^{-1}$ is attributed to increased phonon scattering with respect to the elevated temperature.

data, we expect this value to be three times the copper distance 8.4 Å. It corresponds to the length of the unit cell of the alternating chain [32]. In contrast, the unit cell length of the spatially uniform chain yields the distance between two adjacent spins $d$.

We now consider the scattering law $S(Q,\omega)$ that is composed of two terms

$$S(Q,\omega) = S_{mag}(Q,\omega) + S_{cont}(Q,\omega)\,. \tag{4.21}$$

The first contribution $S_{mag}(Q,\omega)$ describes the spectral density that arises from the triplet excitations. To obtain the scattering law, we make use of the conventional approach $S(Q,\omega) \propto S(q)\cdot g(\omega)$, where $S(q)$ denotes the instantaneous spin-spin correlation function and $g(\omega)$ the density of states function [114]. While $S(q)$ is given by Uhrig and Schulz [35], $g(\omega)$ is obtained using the approach $g(\omega) = |d(\hbar\omega(q))/dq|^{-1}$. The dispersion relation $\hbar\omega(q)$ is given up to the order $\mathcal{O}(\alpha)$, $\mathcal{O}(\alpha^3)$ and $\mathcal{O}(\alpha^5)$ by Uhrig and Schulz [35], Harris and coworkers [34] and Barnes and coworkers [32], respectively. Within the $\mathcal{O}(\alpha)$ approach of Uhrig and Schulz scattering occurs in the energy range of $1-\alpha/2 \lesssim \hbar\omega/\tilde{J} \lesssim 1+\alpha/2$ with the two Van Hove singularities at the energy band edges $\hbar\omega/\tilde{J} \simeq 1\pm\alpha/2$. We remind the relation between the exchange $J$ and $\tilde{J}$ to be $\tilde{J} = J(1+\alpha)/2$ (see chapter 2.2).
The quantity $S_{cont}(Q,\omega)$ originates from scattering on the magnon continuum. Uhrig and Schulz [35] numerically calculated the spectral density of this term by means of random phase transition. This approach is only valid in the limit of weakly coupled dimers such as the spin-Peierls compound $CuGeO_3$ or - as we have seen - the copper oxide system $Ca_{0.83}CuO_2$. The $Q$ integrated scattering law $\int S_{cont}(Q,\omega)dQ$ of the continuum features a large scattering intensity within the energy interval $2-\alpha \lesssim \hbar\omega/\tilde{J} \lesssim 2+\alpha$. Around the energy $\hbar\omega/\tilde{J} \simeq 2-\alpha/2$ we observe a significant maximum in $S(\omega)$. A detailed mathematical presentation of the scattering law is given in appendix B.2.

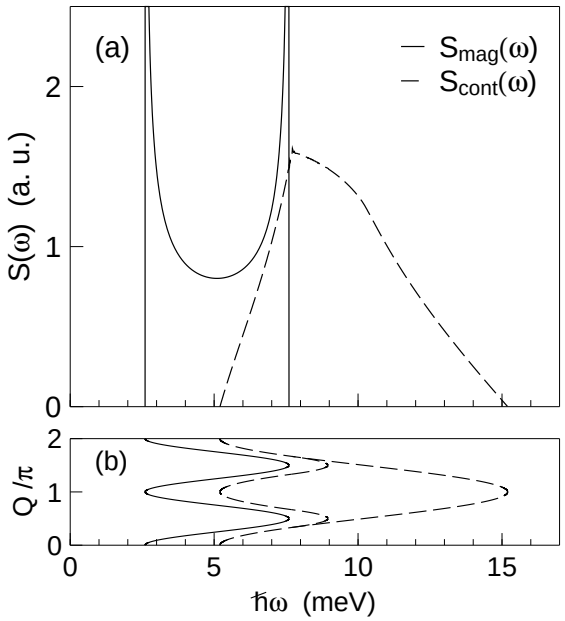


Figure 4.25: (a) Scattering intensity $S(\omega)$, integrated over the Brillouin zone. The solid and the dashed line display the magnon and the continuum contribution to $S(\omega)$, respectively. Both curves are calculated with the parameters $J = 5.1\,\mathrm{meV}$ and $\alpha = 0.98$ based on the model of for weakly coupled dimers [35]. The scattering intensity that results from the magnon band displays two sharp Van Hove singularities around $\hbar\omega \simeq J(1\pm\alpha/2)$. (b) For comparison, the dispersion relation of the triplet excitations (solid line) and the magnon continuum (dashed lines) are indicated [32, 35]).

Figure 4.25 (a) illustrates the calculated scattering intensity $S(\omega)$ that we expect for a magnetic exchange $J \simeq 60\,\mathrm{K} \simeq 5.1\,\mathrm{meV}$ and the alternating parameter $\alpha = 0.98$. The $Q$

integration was carried out numerically over the Brillouin zone. For comparison, the dispersion relation $\hbar\omega(q)$ is shown below the scattering intensity in Figure 4.25 (b). Converting the magnitude of the magnetic correlation $J$ to $\tilde{J}$ does not change the energy scale of the scattering law, as for the given $\alpha$ both parameters are nearly equivalent.

The measured intensity is obtained by a convolution of $S(\omega)$ with the instrumental resolution. Considering a constant energy resolution in terms of a Gaussian function with 1.4 meV full width half maximum (FWHM) broadens the calculated $S(\omega)$ in such a way that the Van Hove singularities at $\hbar\omega/\tilde{J} \simeq 1 \pm \alpha/2$ of the triplet excitations shift to higher and lower energy transfers, respectively. Moreover, the sharp maximum of the continuum states turns more smoother. This energy resolution is compatible with the quasielastic energy resolution measured on IN3 and that on IN4 with an incident energy of 16.1 meV. For an energy resolution of 3.4 meV FWHM that correspond to the 1.1 Å measurement on IN4 the significant features of the triplet and the continuum density of states vanishes into one broad peak.

To extract the magnetic scattering intensity from the nuclear one, a non magnetic reference compound is usually used [115]. In such a sample the magnetic ion is replaced by a nonmagnetic one that features an equivalent electron valence and a similar ion radius. The measured excitation spectrum is purely credited to the nuclear scattering. In case of $Cu^{2+}$ both requirements are hardly fulfilled with a nonmagnetic substitute. Thus, the nuclear contribution of the total intensity will be deduced using an incoherent approach for phonon scattering. Ideally, the total measured scattering intensity $S(\mathbf{Q},\omega)$ consists of a magnetic and a phonon term [75]

$$S(\mathbf{Q},\omega) \propto |f(\mathbf{Q})|^2 S_{mag}(\mathbf{Q},\omega) + Q^2 S_{phon}(\mathbf{Q},\omega)\,. \tag{4.22}$$

The magnetic contribution $S_{mag}(\mathbf{Q},\omega)$ scales with the form factor $f(\mathbf{Q})$, while the phonon part $S_{phon}(\mathbf{Q},\omega)$ increases with the squared wavevector. This assumption neglects multiple scattering. The nuclear intensity is estimated from the measured data, where the form factor equals zero. This corresponds in $Ca_{0.83}CuO_2$ to a $Q$ value of $\sim 8\,\text{Å}^{-1}$.
Figure 4.26 shows the scattering intensity $S(\omega)$ for $Q$ values from $1.4\,\text{Å}^{-1}$ to $7.9\,\text{Å}^{-1}$.

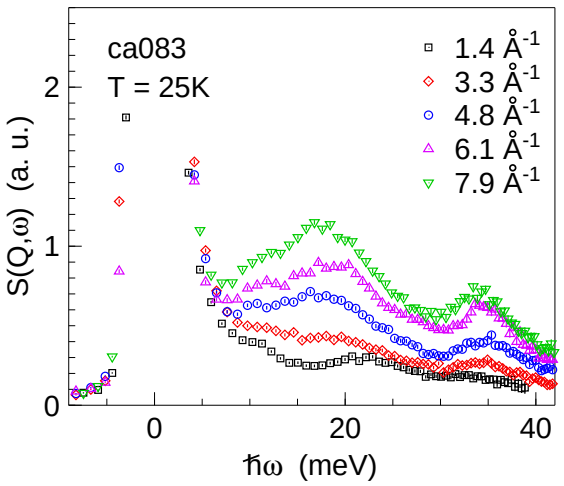


Figure 4.26: Scattering intensity of $Ca_{0.83}CuO_2$ (ca083), measured on IN4 ($E = 67.5$ meV, $T = 25$ K). The data are summed over $\Delta Q \sim 0.8\,\text{Å}^{-1}$, where $Q$ value represents the average value of these ranges. Around $Q = 7.9\,\text{Å}^{-1}$ the magnetic form factor is decreased to zero. The observed intensity originates from coherent and incoherent phonon scattering. Owing to the dominant coherent cross section and the large monoclinic unit cell of this sample a complex $Q$ dependent phonon dispersion is observed with significant peaks around 10 meV, 18 meV and 35 meV. The quasielastic resolution of 3.4 meV leads to a broad tail up to 8 meV for $\hbar\omega > 0$ meV.

We observe at high $Q$ only phonon scattering that scales between $6\,\text{Å}^{-1}$ and $8\,\text{Å}^{-1}$ proportional to $Q^2$. However, the shown spectra show a $Q$ dependent phonon dispersion with major peaks around $\sim 10\,\text{meV}$, $\sim 18\,\text{meV}$ and $\sim 38\,\text{meV}$. Owing to the large monoclinic unit cell of this sample we expect a complex phonon dispersion that has to be taken into account for the phonon part of the scattering cross section. $Ca_{0.83}CuO_2$ represents a mixed coherent-incoherent scatterer with a dominant coherent cross section (18.3 barn versus 0.6 barn per formula unit, respectively). The incoherent approach, i.e. a simple $Q^2$ rescaling of the high $Q$ data, cannot be valid for the phonon term in the scattering law. In addition, the quasielastic energy resolution of 3.4 meV FWHM prevents from resolving any features of the expected scattering function of the 1D chain with $J \simeq 5.1\,\text{meV}$ and $\alpha \simeq 0.98$ behavior that appears from 2 meV on.

Although the nonmagnetic background cannot be reduced, we try to quantitatively match the expected scattering intensity $S(\omega)$ to data with a higher energy resolution than the measurement on IN4 with the incident energy of 67.5 meV. Figure 4.27 displays the energy dependence of the intensity that is obtained by the IN3 experiment at 20 K. The data are summed between $0.5\,\text{Å}^{-1} \leq Q \leq 1.5\,\text{Å}^{-1}$ and corrected for the empty aluminum can and the magnetic form factor. The quasielastic peak at zero energy transfer that is fitted by a Voigt function is subtracted. This function accounts best for the observed lineshape of the peak. For illustration purposes, the residual points and their error bars around $\hbar\omega = 0\,\text{meV}$ are removed.

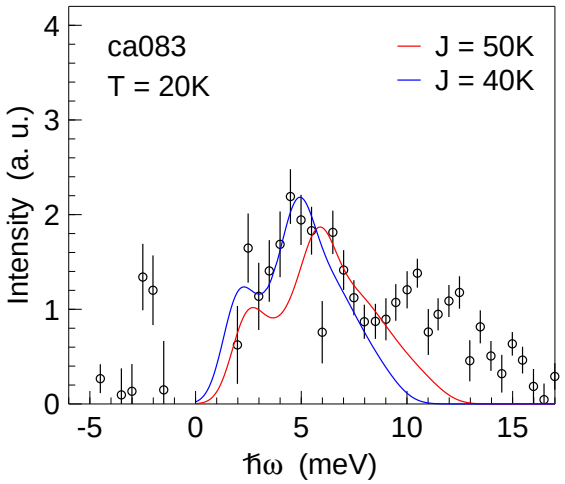


Figure 4.27: Excitation spectrum of $Ca_{0.83}CuO_2$ (ca083), obtained on IN3 at 20 K. The data are summed within $0.5\,\text{Å}^{-1} \leq Q \leq 1.5\,\text{Å}^{-1}$ and corrected for the form factor. Both the empty aluminum can and the quasielastic peak at zero energy transfer in terms of a Voigt function are subtracted. The red and the blue line indicate the expected $S(\omega)$ that arises from the alternating Heisenberg chain for the exchange parameters of 50 K and 40 K, respectively. The scattering function is convoluted with the energy resolution of the spectrometer.

We observe a broad scattering contribution within $2\,\text{meV} \lesssim \hbar\omega \lesssim 7\,\text{meV}$ and around 10 meV. In agreement with the IN4 measurement we at least partially identify the latter one with the phonon contribution to the scattering intensity. Assuming that the first peak of the data only corresponds to the magnetic intensity, we conclude that the major contribution of $S(\omega)$ should account for this. Modeling the scattering intensity with $J = 60\,\text{K}$ and $\alpha = 0.98$ does not describe the shown spectrum. Here, the $Q$ integration of the scattering law $S(Q,\omega)$ was performed with respect to the experimental $Q$ range of the data. The red and the blue curve represent the calculated scattering function $S(\omega)$ for $J = 4.2\,\text{meV} = 50\,\text{K}$ and $J = 3.4\,\text{meV} = 40\,\text{K}$, respectively. Both curves are scaled in such a way that the experimental data are well described. In case of a pure magnetic origin of this peak the better agreement between the data and the model is given for the magnetic exchange equal to 40 K. Respecting both curves the exchange differs from that of

susceptibility and specific heat by 14 % and 31 %, respectively. We admit, this calculation should only serve as qualitative comparison between the model for dimerized chains and the shown data.

In summery, experimental results of inelastic neutron scattering experiments for undoped $Ca_2Y_2Cu_5O_{10}$, medium doped $Ca_{3.5}Y_{0.5}Cu_5O_{10}$ and the highly doped compound $Ca_{0.83}CuO_2$ are presented. The 3D antiferromagnetic parent compound shows below $T_N$ a magnon dispersion that is compatible with that of a single crystal sample. Upon doping, the long range ordered phase diminishes and a spin glass behavior occurs in $Ca_{3.5}Y_{0.5}Cu_5O_{10}$. Further doping leads to a dynamical behavior that arises from the dimerized $CuO_2$ chains. We have found the singlet extension to be equal to the next nearest copper distance in the chain.

## 4.6 Discussion

This section summarizes the experimental results of $Ca_{2+x}Y_{2-x}Cu_5O_{10}$ samples and compares them to literature. In this sense, a generic phase diagram is presented that reflects the long range order (see chapter 4.6.1). We further discuss in the frame of the $J_1$-$J_2$ model how far the approach of the 1D Heisenberg chain applies to the compound series (see chapter 4.6.2).

### 4.6.1 Generic phase diagram

Figure 4.28 illustrates the obtained phase diagram of $Ca_{2+x}Y_{2-x}Cu_5O_{10}$ samples. Both bulk measurements and neutron spectroscopy provide evidence of a long range ordered state at low temperatures that depends on the doping concentration $x$. It arises from the coupling of adjacent $CuO_2$ chains. Compounds with $0 \leq x \leq 1.5$ show a collinear antiferromagnetic structure. The disorder of the $CuO_2$ chains leads to a spin glass-like phase in $Ca_{3.5}Y_{0.5}Cu_5O_{10}$ and the highly doped compound $Ca_{0.83}CuO_2$ exhibits again a Néel state. In this sample the exchange measured along the chain changes from ferromagnetic to antiferromagnetic interaction. The shown phase transition temperatures are obtained by heat capacity measurements (hc) and neutron diffraction (neutron) of the magnetic reflection (0 0 1).

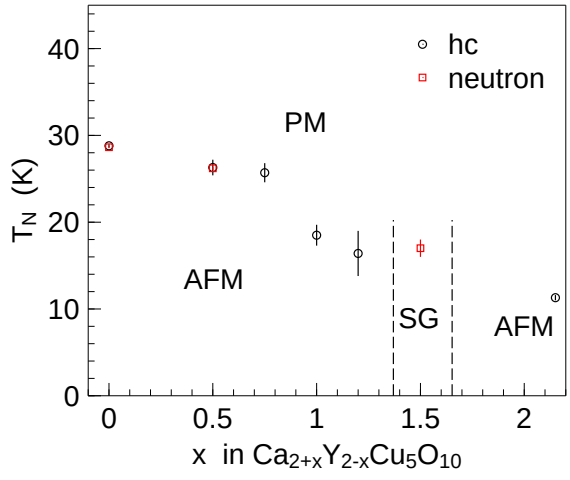


Figure 4.28: Phase diagram of edge sharing $Ca_{2+x}Y_{2-x}Cu_5O_{10}$ compounds. Samples with $0 \leq x \leq 1.5$ and $Ca_{0.83}CuO_2$ are characterized as 3D antiferromagnets, $Ca_{3.5}Y_{0.5}Cu_5O_{10}$ features a spin glass-like phase. The order temperatures $T_N$ are obtained by heat capacity measurements (hc) and by neutron spectroscopy (neutron).

In best agreement with known literature [63, 64] the magnetic unit cell of the parent compound belongs to the face centered orthorhombic space group with the lattice constants $a \simeq 2.8\,\text{Å}$, $b \simeq 6.3\,\text{Å}$ and $c \simeq 10.6\,\text{Å}$. The Cu-O-Cu bond angle within one $CuO_4$ unit was found to be about 92°. Spins are confined to the *ab* plane, where the spin orientation is parallel to the *b* axis. Moreover the magnetic propagation vector [0 0 1] yields ferromagnetic interaction within the *ab* plane and antiferromagnetic correlations perpendicular to this plane. The observed spin wave dispersion of single crystal $Ca_2Y_2Cu_5O_{10}$ [65, 66] coincides with the results of the magnetic structure analysis with respect to the sign of the exchange integrals. The investigation of the polycrystalline parent compound supports these results by resolving a spin gap in the dispersion of the order of the gap predicted by the dispersion relation of the single crystal.
Upon doping, the magnetic structure remains unchanged until the doping concentration $x = 1.5$. Both the Néel temperature and the magnetic moment decrease from $\sim 29\,\text{K}$ to $\sim 16\,\text{K}$ and $\sim 0.92\mu_B$ and $\sim 0.22\mu_B$, respectively. $Ca_{0.83}CuO_2$ shows antiferromagnetic correlations along the chain axis. This result agrees with Meijer and coworkers [82].

Below $T_N$ the change in the magnetic correlations along the chain direction can be explained by the change in the Cu-O-Cu bonding angle. Figure 4.29 displays the concentration dependence of the Cu-O-Cu angles $\theta$ that were derived by means of neutron diffraction (see chapter 4.4.2). The values increase from $\sim 92°$ to $\sim 95.5°$ for $Ca_2Y_2Cu_5O_{10}$ and $Ca_{0.83}CuO_2$, respectively. The $J_1$-$J_2$ model of $CuO_2$ chains describes the magnetic exchange between nearest ($J_1$) and next nearest neighbor spins ($J_2$) [51]. We remind that $J_2$ is angle independent, while both the sign and the magnitude of the exchange $J_1$ depends on $\theta$. As depicted in the figure the nearest neighbor exchange changes from ferromagnetic to antiferromagnetic correlations for $\theta_c \simeq 95°$ in case of $Ca_{2+x}Y_{2-x}Cu_5O_{10}$. The precise value of the critical angle $\theta_c$ strongly depends on the Cu-O distance along the Cu-O-Cu bond. These theoretical predictions coincide with the observed ferromagnetic nearest neighbor interactions of $Ca_{2+x}Y_{2-x}Cu_5O_{10}$ samples up to $x = 1.5$. In agreement, $Ca_{3.5}Y_{0.5}Cu_5O_{10}$ does not show the magnetic Bragg reflection $(\frac{1}{2}\,0\,1)$. A bond angle of $\sim 95.5°$ that was observed for $Ca_{0.83}CuO_2$ anticipates antiferromagnetic nearest neighbor interaction, where $J_1 < J_2$ applies.

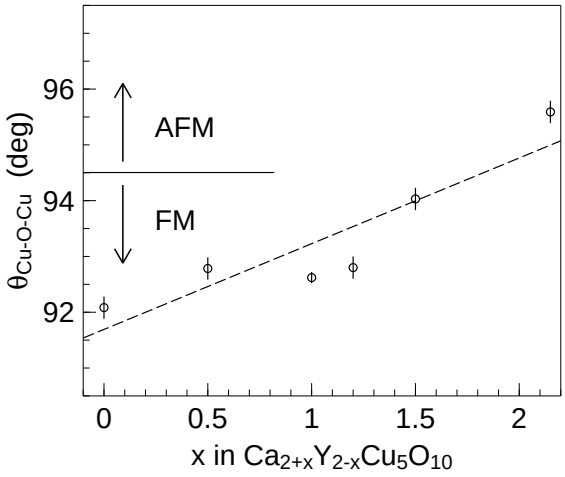


Figure 4.29: Cu-O-Cu bonding angle $\theta$ of $Ca_{2+x}Y_{2-x}Cu_5O_{10}$ samples. The values are obtained by means of neutron diffraction. Increasing Ca/Y ratio yields an increase in $\theta$ from $\sim 92°$ to 95.5° for the parent compound and highly doped $Ca_{0.83}CuO_2$, respectively. Within the frame of the $J_1$-$J_2$ model [51] the magnetic correlations of the chain change from ferromagnetic to antiferromagnetic nearest neighbor interaction around 95°.

Increasing $x$ leads to a decrease of the 3D antiferromagnetic phase. Owing to hole doping into the $CuO_2$ chains, these chains become diluted. One expects that the coupling of

neighboring spin chains is reduced. This effect is visible when considering the decrease of the order temperature and the magnetic moment with doping. In the spin glass phase of $Ca_{3.5}Y_{0.5}Cu_2O_{10}$ the chains are still loosely assembled to each other. Amazingly, the compound series $Ca_{2+x}Y_{2-x}Cu_5O_{10}$ still exhibits a long range order for the highly doped compound $Ca_{0.83}CuO_2$. Even the isomorphic cuprate system $Sr_{0.73}CuO_2$ exhibits an antiferromagnetic state below 12 K, although its $CuO_2$ chains are doped with 0.6 holes/Cu [82].

### 4.6.2 1D Heisenberg behavior

In $Ca_{2+x}Y_{2-x}Cu_5O_{10}$ compounds hole doping leads to the dilution of the $CuO_2$ chains in terms of a spin/charge order. As nonmagnetic Zhang-Rice singlets are known to repel each other [60], $Cu^{2+}$ ions are homogeneously distributed in the chains. We further observe a change in the Cu-O-Cu bonding angle. These two parameters, the number of magnetic spins in the chain and $\theta$, decisively influence the properties of the $CuO_2$ chains.

We first consider the undoped compound $Ca_2Y_2Cu_5O_{10}$ in the idealized situation of the assembly of planar $CuO_4$ units. Effects of a strong interchain coupling of adjacent spin chains as it was found in edge sharing $Li_2CuO_2$ [116] are neglected. In the chains of undoped $Ca_2Y_2Cu_5O_{10}$ every copper ion is magnetic. The observed value for $\theta$ leads to ferromagnetic and antiferromagnetic nearest neighbor and next nearest exchange along the chains, where $|J_1|$ and $J_2$ are of the order of 200 K and 75 K [51]. Owing to the ratio $J_2/|J_1|$ the chains are frustrated and show zero magnetization [55]. Figure 4.30 (a) displays the corresponding spin chain. We observe that half of the nearest neighbor bonds are frustrated. The strong ferromagnetic nearest neighbor interaction might explain the ferromagnetic Curie Weiss temperature that was observed in the paramagnetic temperature range for susceptibility (see chapter 4.2.2).

While doping and leaving $\theta$ constant, spins are removed from the chain. The nonmagnetic holes equally distribute over the chain and lift the frustration of nearest neighbor bonds. When reaching a doping concentration of 0.5 holes/Cu, half of the spins are canceled out in the chain. Only antiferromagnetic next nearest neighbor interaction holds. Such a chain resembles the antiferromagnetic uniform chain that was introduced in chapter 2.1. Figure 4.30 (b) to (d) illustrates this effect. Further increase in the number of holes leads to dimerization of adjacent spins, as the exchange paths with respect to the left and right neighboring spins $2i-1$ and $2i+1$ differ. For instance, the spin chain compound $Sr_{0.73}CuO_2$ shows a Cu-O-Cu angle of 92.5(1)° and 0.6 holes/Cu. It was found by means of neutron scattering that dimers are formed between next nearest neighboring copper ions [117]. Similarly, $Sr_{14}Cu_{24}O_{41}$ reveals for an equivalent number of holes in the chain and a bonding angle of $\sim 91°$ a dimer coupling between next nearest neighboring spins [14, 15, 16, 17].

Doped samples of $Ca_{2+x}Y_{2-x}Cu_5O_{10}$ exhibit an increase in the bonding angle $\theta$. The ferromagnetic interaction $|J_1|$ decreases from $\sim 200$ K to $\sim 100$ K for $x = 0$ and 1.5, respectively. In contrast, the next nearest interaction $J_2 \sim 75$ K remains angle independent. The chains are frustrated [51, 55]. Upon doping, the dilution of the chains remove frustrated bonds. Figure 4.30 (b) and (c) sketch possible spin arrangements for $Ca_3Y_1Cu_5O_{10}$ and $Ca_{3.5}Y_{0.5}Cu_5O_{10}$. The number of holes are chosen according to the

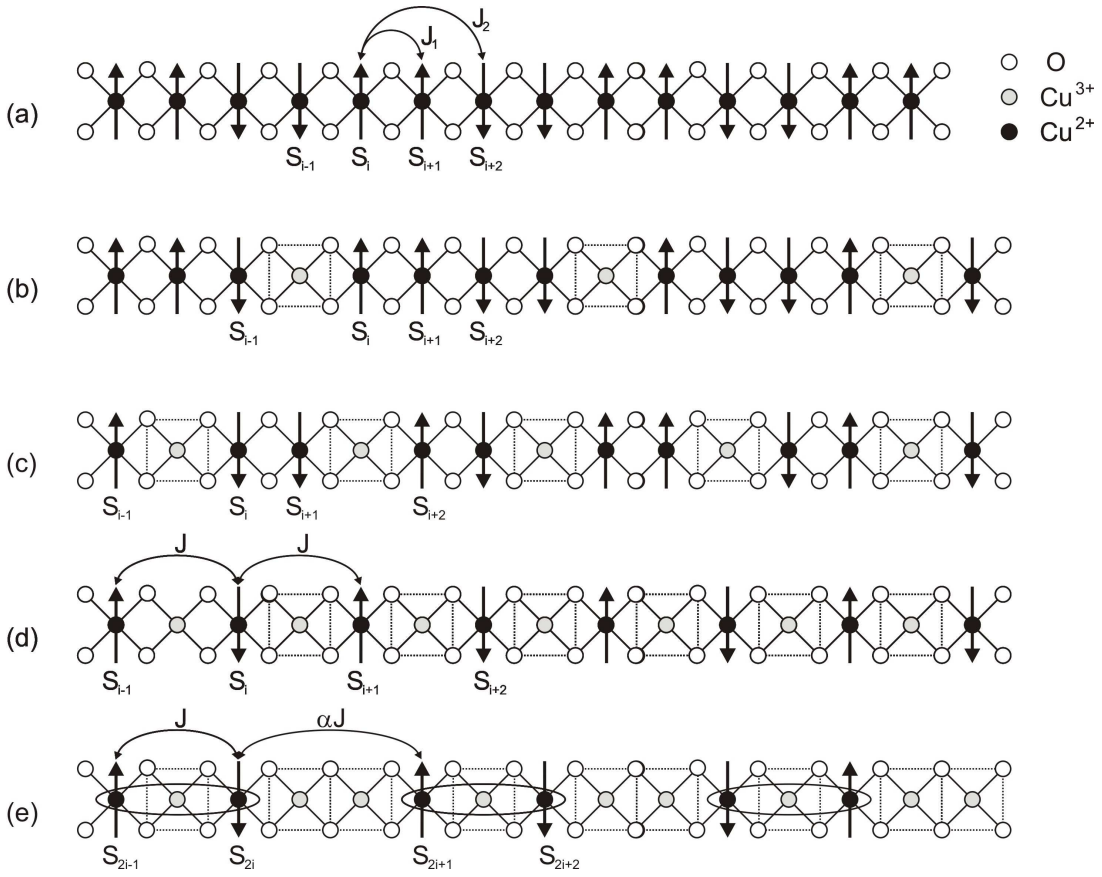


Figure 4.30: $CuO_2$ spin chains with a Cu-O-Cu bonding angle $\theta < 94°$. Oxygen, $Cu^{3+}$ and $Cu^{2+}$ ions are sketched in white, gray and black color. Zhang-Rice singlets (units of $Cu^{3+}$ and four oxygen ions) are illustrated by dashed squares. (a) Uniform chain with ferromagnetic and antiferromagnetic nearest and next nearest neighbor interaction $J_1$ and $J_2$, respectively. Half of the nearest neighbor interactions are frustrated. This situation is found in $Ca_2Y_2Cu_5O_{10}$. (b) and (c) Spin chain with 0.2 and approximately 0.3 holes/Cu. The dilution of the chains with nonmagnetic ions removes frustrated bonds as it can be found in $Ca_3Y_1Cu_5O_{10}$ and $Ca_{3.5}Y_{0.5}Cu_5O_{10}$, respectively. (d) Spin chain with 0.5 holes/Cu. Owing to the equivalent ratio of magnetic and nonmagnetic $CuO_4$ units the frustration of the nearest neighbor interactions in the chain is lifted. Such a spin chain resembles the ideal case of the antiferromagnetic uniform spin chain. (e) Spin chain with 0.6 holes/Cu. This picture corresponds to $Sr_{0.73}CuO_2$ [88, 117] and $Sr_{14}Cu_{24}O_{41}$ [14, 15, 16, 17], where $\theta < 94°$ and an intradimer distance of two copper ions along the chain were found.

copper valence. In the case of $Ca_{3.5}Y_{0.5}Cu_5O_{10}$ a hole density of 0.33 holes/Cu instead of 0.3 holes/Cu is displayed for illustration purposes. A closer look at the diluted frustrated chains in this sample reveals disorder in terms of ferromagnetic nearest neighbor and both antiferromagnetic nearest and next nearest neighbor spins. In this way, susceptibility and specific was interpreted within the model of 1D antiferromagnetic spin chains.

The highly doped compound features a spin density of $\sim 2/3$ that is experimentally ascertained by susceptibility measurements (see chapter 4.2). In this sense approximately every third ion is nonmagnetic. Owing to a bonding angle of 95.5(2)° we expect both antiferromagnetic correlations for $J_1$ and $J_2$. Here, $J_2 > J_1 \gtrsim 0$ applies that leads to almost negligible nearest neighbor interactions. Although the susceptibility characterizes the chain exchange to be almost spatially uniform, we expect from the number of holes/Cu different exchange paths of magnetic ions along the chain. Figure 4.31 displays the two possible types of dimerization. One might expect that dimers are either formed between next nearest neighboring spins (Figure 4.31 (a)) or between nearest neighboring spins (Figure 4.31 (b)). Considering the relative magnitudes of $J_1$ and $J_2$ obviously the first possibility is preferred. We identified the dimer extent by measuring the structure factor. It corresponds to two times the distance of copper ions along the chain. In this way, dimerization in this samples occurs between next nearest neighboring spins.
Another cuprate with an Cu-O-Cu bond $\theta > 95°$ is the spin-Peierls compound $GeCuO_2$. However, dimerization between neighboring $Cu^{2+}$ takes place owing to a lattice distortion that shift the ions closer together.

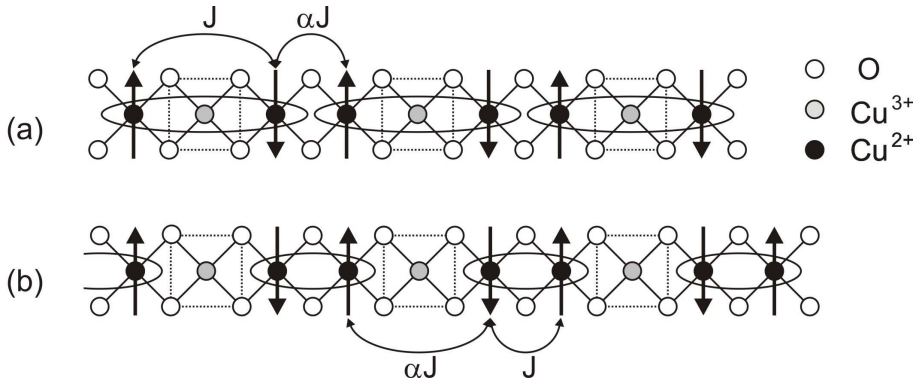


Figure 4.31: Spin chains of $Ca_{0.83}CuO_2$ with 1/3 holes/Cu. Dimerization in the chains takes place along the (a) Cu-O-Cu or the (b) Cu-O-O-Cu path. The picture (a) depicts the experimentally observed situation in this sample.

In conclusion, we have shown that in $Ca_{2+x}Y_{2-x}Cu_5O_{10}$ low dimensional order is evoked by substituting calcium for yttrium ions. However, the coexisting long range order does not vanish upon doping. Due to a lower ion radius of calcium compared to yttrium the increase of the Ca/Y ratio leads to smaller lattice constants $a$ and $c$ of the magnetic unit cell. Accordingly, the increase in the Cu-O-Cu bond angle provokes a transition from ferromagnetic to antiferromagnetic nearest neighbor exchange along the chain. Frustration in these chains is lifted by means of hole doping. The dilution of the magnetic ions in the $CuO_2$ chains further evokes the properties of the antiferromagnetic 1D Heisenberg chain

in terms of dimers with an extent of two times the copper distance along the chain at the doping concentration of $x = 2.15$.

# Chapter 5

# Paramagnetic excitations in $CsVBr_3$

*This chapter summarizes the investigation of the triangular antiferromagnet $CsVBr_3$, whose spin dynamics in the paramagnetic phase is supposed to be dominated by one dimensional behavior. We performed inelastic neutron scattering to elucidate this with respect to its temperature dependence crossing $T_N$. The outline of this chapter is as follows: static and dynamic properties of $CsVBr_3$ are briefly presented in chapter 5.1 and 5.2, respectively. Afterwards, the results obtained by inelastic neutron scattering are shown (see chapter 5.3). Finally, the obtained results are discussed within different theoretical approaches and compared to other members of the $ABX_3$ family (see chapter 5.4).*

## 5.1 Crystal and magnetic structure

The triangular antiferromagnet $CsVBr_3$ belongs to the hexagonal space group $Pm_3/mmc$, in which most of the related $ABX_3$ compounds such as $CsNiCl_3$ and $CsMnBr_3$ crystallize [69]. Vanadium, cesium and bromine ions are located on the crystallographic 2a, 2d and 6h position, where the corresponding fractional coordinates are $(0, 0, 0)$, $(0.33, 0.66, 0.75)$ and $(0.16, 0.32, 0.25)$, respectively. The lattice constants at room temperature are $a \simeq b \simeq 7.57\,\text{Å}$ and $c \simeq 6.32\,\text{Å}$. Upon lowering the temperature to 6 K they isotropically decrease by $\sim 1\,\%$ compared to those at 300 K. The angle of the basal plane $ab$ is 120°. Two $CsVBr_3$ molecules are comprised in one chemical unit cell with the magnetic $V^{2+}$ ions located at the corners of the unit cell. This kind of structure is well known for showing face sharing $BX_6$ octahedra along the $c$ direction that are separated by the alkali ions. The angle between the vanadium-bromine direction and the $c$ axis is given by 53° (300 K). Figure 5.1 displays the on-site view of the nuclear structure of $CsVBr_3$, where vanadium, cesium and bromide ions are sketched in red, blue and yellow color.

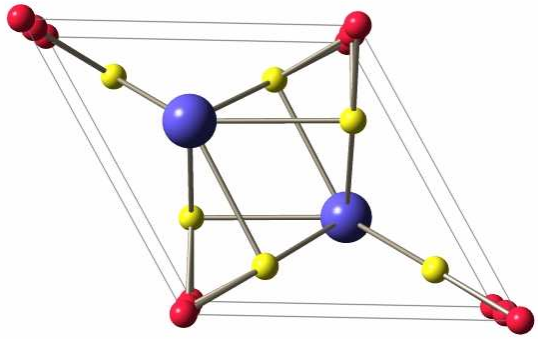

Figure 5.1: Hexagonal unit cell of $CsVBr_3$ with $a \simeq b \simeq 7.57\,\text{Å}$ and $c \simeq 6.32\,\text{Å}$ [69]. View parallel to the [0 0 1] direction. It is a 120° structure, where the unit cell contains two molecules of $CsVBr_3$, i.e. two vanadium(II) ions (sketched red) are each bound to one cesium ion (blue) and three bromide ions (yellow).

The spin configuration of vanadium ([Ar]3d$^3$) yields a spin quantum number $S$ of 3/2. Magnetic neutron diffraction exhibits a second order phase transition to an antiferromagnetically ordered phase below the Néel temperature of 20.4°. Analyzing the magnetic structure Hauser and coworkers [69] determined the magnetic propagation vector to be $[\frac{1}{3}\,\frac{1}{3}\,1]$ with the magnetic unit cell dimensions $\sqrt{3}a$, $\sqrt{3}a$ and $c$ (see Figure 5.2). With respect to the nuclear one the magnetic unit cell is rotated by 30° along the crystallographic $c$ axis and contains 6 $V^{2+}$ ions. The interchain exchange mediated via one bromide and one cesium ion as well as the intrachain exchange along the $c$ direction is antiferromagnetic. Dipolar interaction leads to a confinement of the spins into the basal plane resulting in an easy-plane (XY-like) anisotropy [118]. The opening angle of the hexagonal plane of 120° forces the $V^{2+}$ spins on a triangular lattice. Vanadium spins are thus geometrically frustrated owing to an equal distribution of the magnetic moment per vanadium ion. The actual magnetic moment of 1.87(7) $\mu_B$ is reduced by one half compared to the magnetic moment of a free vanadium ion (3 $\mu_B$). The discrepancy of both values is assigned to zero point fluctuations as well as the covalency of the bromide ions.

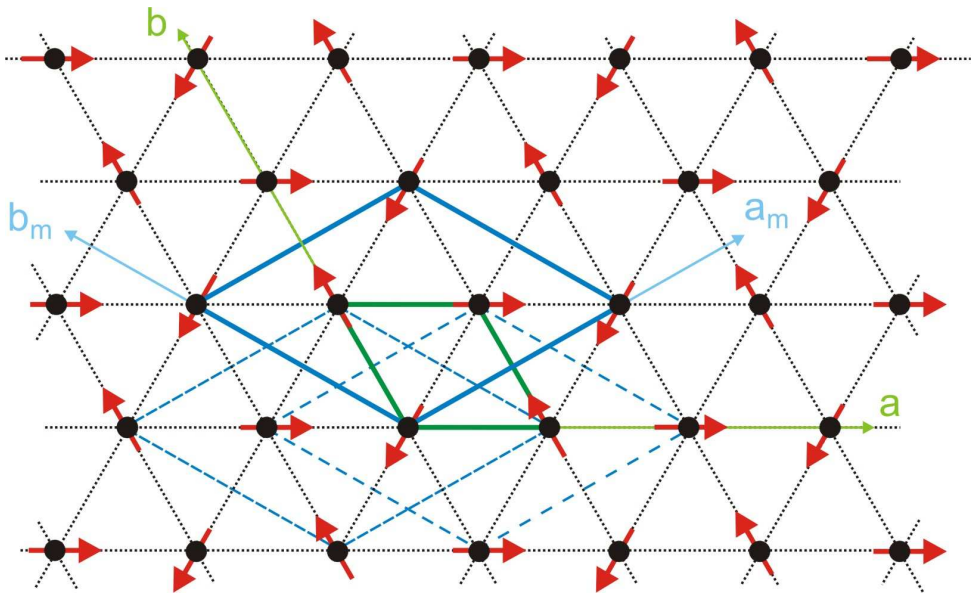


Figure 5.2: Magnetic structure of $CsVBr_3$. View parallel to [0 0 1]. $V^{2+}$ spins are confined in the basal plane $ab$. Superexchange within the plane is mediated via one bromine and one cesium ion, whereas perpendicular to the basal plane superexchange arises via one bromine ion. Adjacent spins located on the triangular lattice are frustrated by 120°, in order to compromise for the antiferromagnetic exchange within the plane. Antiferromagnetic chains run along the crystallographic $c$ axis. The magnetic unit cell consists of three sublattices sketched in blue color. The nuclear unit cell (green color) is rotated by 30° with respect to the magnetic one.

## 5.2 Spin wave dispersion in the ordered state

Based on the presented magnetic structure model Kadowaki and coworkers [119] introduced a procedure for determining the spin wave dispersion of $CsVBr_3$. Taking into account the intrachain and interchain exchange $J$ and $J'$ as well as an XY-like anisotropy $D$ that forces the $V^{2+}$ spins into the basal plane perpendicular to the chain direction

$(D>0)$, the appropriate Hamiltonian of the system reads[1]

$$H = 2J\sum_{i,j}\hat{\mathbf{S}}_i\hat{\mathbf{S}}_j + 2J'\sum_{i,j}\hat{\mathbf{S}}_i\hat{\mathbf{S}}_j + D\sum_i\left(\hat{S}_i^z\right)^2 . \tag{5.1}$$

Linear spin wave theory leads to the dispersion relation $\hbar\omega(\mathbf{q})$ of the system that describes the time dependent propagation of the spin $\hat{\mathbf{S}}$. Here, it is presumed that only the mean value of the $z$-component of the spin direction ($\hat{S}^z$) is time independent, while the much smaller perpendicular components ($\hat{S}^x$, $\hat{S}^y \ll \hat{S}^z$) follow a time-oscillatory behavior. This kind of motion is referred to as a spin wave with magnons as its quantized quasi particles.

Using the spin quantum number $S=3/2$ and the magnetic propagation vector $\mathbf{k}_0=[\frac{1}{3}\ \frac{1}{3}\ 1]$ the dispersion of $CsVBr_3$ reads

$$\hbar\omega_q = \hbar\omega\left(\mathbf{q}\right) = 2S\sqrt{u(\mathbf{q})v(\mathbf{q})} \tag{5.2}$$

with

$$\begin{aligned} u\left(\mathbf{q}\right) &= 4J\sin^2\left(\frac{\pi}{2}\xi_z\right) + J'\left[3 - f\left(\xi_x,\xi_y\right)\right] , \\ v\left(\mathbf{q}\right) &= 4J\cos^2\left(\frac{\pi}{2}\xi_z\right) + J'\left[3 + 2f\left(\xi_x,\xi_y\right)\right] + D , \\ f\left(\xi_x,\xi_y\right) &= \cos\left(2\pi\xi_x\right) + \cos\left(2\pi\xi_y\right) + \cos\left[2\pi(\xi_x+\xi_y)\right] . \end{aligned}$$

The energy $\omega_q$ denotes the excitation energy and $\mathbf{q}$ the reduced wave vector. The quantities $\xi_i$ are coordinates of the scattering vector $\mathbf{q}$ and are defined in reciprocal lattice units (r. l. u.). Following Eq. (5.2) three different dispersion branches can be observed that are degenerate at particular points in reciprocal lattice. $\hbar\omega(\mathbf{q})$ describes the optic out-of-plane mode (perpendicular to the basal plane), whereas $\hbar\omega(\mathbf{q}\pm\mathbf{k}_0)$ refer to the two in-plane branches. When considering the reciprocal lattice point $(\frac{1}{3}\ \frac{1}{3}\ 1)$ these two modes correspond to the acoustic excitation for $\mathbf{q}-\mathbf{k}_0$ and to the optic branch for $\mathbf{q}+\mathbf{k}_0$.

Feile and coworkers determined the exchange values and the anisotropy parameter by means of inelastic neutron scattering to be $J=7.1\,\mathrm{meV}$, $J'=0.0018\,\mathrm{meV}$ and $D=0.002\,\mathrm{meV}$ [120]. A later study by Nagler and coworkers extracted the parameters somewhat different to $J=10.4(9)\,\mathrm{meV}$, $J'=0.010(1)\,\mathrm{meV}$ and $D=0.045(4)\,\mathrm{meV}$ [121]. In the following we will refer to the exchange values of Nagler and coworkers, as these are obtained with a crystal of a smaller mosaicity compared to the earlier study.

Figure 5.3 illustrates the calculated dispersion in different directions in reciprocal space using the interaction parameters of Feile and Nagler, respectively. Notice the increased excitation maximum for the dispersion relation given by Nagler and coworkers that is evoked by the higher intrachain exchange. Moreover, the impact of the anisotropy parameter can be observed by the out-of-plane mode along the $[0\,\xi\,1]$ direction. The lower $D$, the more tends the dispersion to zero energy at the zone center. Along this direction the two in-plane branches are degenerate, while in other crystallographic directions the energy degeneracy is lifted.

[1] In literature of $ABX_3$ compounds the convention $J<0$ is usually used for antiferromagnetic interaction [68]. However, we will adhere to the used denotation $J>0$ and $J<0$ for antiferromagnetic and ferromagnetic exchange, respectively.

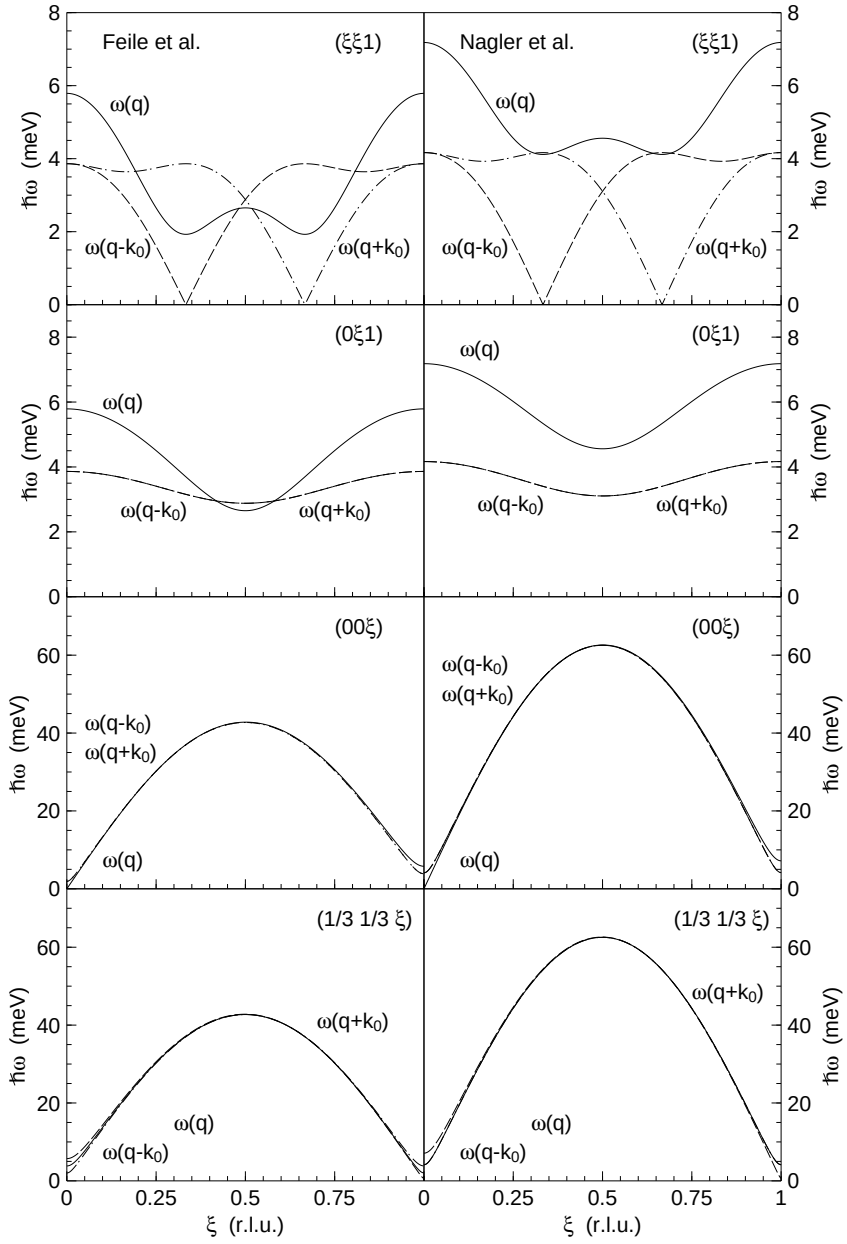


Figure 5.3: Dispersion relation of $CsVBr_3$ along the $[\xi\,\xi\,1]$, $[0\,\xi\,1]$, $[0\,0\,\xi]$ and $[\frac{1}{3}\,\frac{1}{3}\,\xi]$ direction using the exchange couplings by Feile and coworkers [120] (left figures) and Nagler and coworkers [121] (right figures). Respecting $(\frac{1}{3}\,\frac{1}{3}\,1)$ the acoustic and optic in-plane and the optic out-of-plane modes are indicated by the dashed, the dot-dashed and the solid line, respectively.

## 5.3 Spin dynamics in the disordered phase

When approaching the Néel temperature, thermal fluctuations destroy the 3D long range order. While the anisotropy and the interchain exchange turn negligible in the paramagnetic phase, spins are still magnetically coupled along the chain direction within domains of a finite extension $\xi(T)$. However, owing to strong fluctuations the crystal is macroscopically considered as paramagnetic.
Scattering around the ordering temperature is dominated by the spin dynamics of the antiferromagnetic exchange along the $c$ axis. In first approximation the dispersion relation of the 1D spin system around the magnetic zone center is directly proportional to the momentum transfer $q$ with $\hbar\omega_q = \hbar cq$ with $c$ denoting the stiffness of the excitation.

### 5.3.1 Experimental details and data analysis

In order to investigate the spin dynamics of $CsVBr_3$, we used a cylindric single crystal with the dimensions 22 mm × 8 mm (height × diameter). The crystal was grown by K. Krämer, University Bern, Switzerland, and mounted into a cylindric aluminum sample holder. The inelastic neutron scattering experiment was performed on the cold triple axis spectrometer TASP (Paul Scherrer Institut, Switzerland). The set-up was chosen using a fixed final energy $E' = 8$ meV, a focusing monochromator and analyzer and the collimation open-80'-open-open. The single crystal was aligned within the $(h\,h\,l)$ scattering plane.
Measurements were performed in the temperature range of 10 K to 200 K around the magnetic Bragg reflection (0 0 3), where the magnon dispersion features an excitation gap of 4 meV and 8 meV (see Fig. 5.3). In particular, the temperature and the wavevector dependence of the dispersion was investigated by means of constant-**Q** scans. Furthermore, the origin of the gap was proved by constant energy scans for different energy transfers and temperatures at (0 0 3).

Data analysis for both constant-**Q** and constant energy scans includes a deconvolution of the measured intensity $I(\mathbf{Q},\omega)$ with the four dimensional resolution function $R(\mathbf{Q}-\mathbf{Q}_0, \omega-\omega_0)$. The latter was chosen using the approach of Popovici [79] that includes the neutron source and guides, the spectrometer configuration and the sample properties. The obtained quantity, the double differential cross section, is proportional to the scattering function that we derive for constant-**Q** and constant energy scans as presented in the following paragraphs. In order to compare data that are measured in different experimental conditions we normalized the counting time with respect to the monitor.

Constant-**Q** scans are analyzed based on the model of the damped harmonic oscillator that has been successfully used for describing the lineshape of one-phonen excitations [122]. We refer to appendix C for presenting the time and frequency dependence of damped harmonic oscillator and evaluating the corresponding scattering law. The lineshape of $S(\mathbf{Q},\omega)$ corresponds to a double Lorentzian function accounting for the Stokes and the Antistokes line of the excitation. Within this approach the scattering function is given by

$$S(\mathbf{Q},\omega) = (n(\omega)+1)\cdot\chi_q\cdot\frac{\Omega_q^2}{\omega_q}\cdot\frac{1}{2\pi}\left[\frac{\Gamma_q}{(\omega-\omega_q)^2+\Gamma_q^2}-\frac{\Gamma_q}{(\omega+\omega_q)^2+\Gamma_q^2}\right], \qquad (5.3)$$

where $\Omega_q = \sqrt{\omega_q^2 + \Gamma^2}$ is the eigenfrequency, $\omega_q$ the frequency of the damped oscillation and $\Gamma_q$ the linewidth of the Lorentzian function[2]. $\chi_q$ denotes the $q$-dependent susceptibility. For convenience the mathematically identical expression

$$S(\mathbf{Q},\omega) = (n(\omega)+1)\cdot\chi_q\cdot\frac{\Omega_q^2}{\pi}\cdot\frac{2\omega\Gamma_q}{(\omega^2-\Omega_q^2)^2+4\omega^2\Gamma_q^2} \tag{5.4}$$

is used as fitting function.

While fitting, the $q$-dependent frequency of the damped oscillator $\omega_q$, the linewidth $\Gamma_q$ and an overall scaling factor $A = \frac{1}{2}\chi_q\Omega_q^2$ are extracted as fitting parameters. Owing to the increased counting time at the neutron energy loss side compared to energies at neutron energy gain the background increased with time ($\approx 0.5$ cts/min). In the first step of data analyzing the background parameter was kept free yielding results with an error bar of the order of the value itself for the linewidth $\Gamma_q$ and the $q$-dependent susceptibility $\chi_q$. In a second approach the background was kept constant as an average over all temperature scans. Its value was estimated from measured points near $\omega = 0$, where the quasi elastic contribution decreases and the magnetic one is still not dominating the signal ($\approx 20$ cts/mon) as well as by the most far measured point at neutron energy loss ($\approx 19$ cts/mon). These fits yielded compatible results compared to fits with free parameters, the error bar for the $\Gamma_q$ and $\chi_q$ significantly decreased. Notice, the frequency $\omega_q$ of the damped oscillation as well as its error is independent of any assumption for the background. Figure 5.4 (a) shows representative examples of constant-$\mathbf{Q}$ scans at the magnetic Bragg reflection (0 0 3) for the temperatures 40 K and 100 K. The solid lines indicate the fit based on the model of the damped harmonic oscillator, where Eq. (5.4) is convoluted with the resolution function.

Besides constant-$\mathbf{Q}$ scans additional constant-energy scans at (0 0 3) were performed in the disordered phase for two purposes. First, the existence of the gaped dispersion was traced by changing the energy transfer at constant temperature. Furthermore, the temperature dependence of the gap energy was studied by keeping the energy transfer constant and increasing the temperature. For convenient parametrization the spectral weight was assumed to be of Lorentzian type

$$S(\mathbf{Q},\omega) \propto \frac{A\cdot\Gamma^2}{\Gamma^2+(\mathbf{q}-\mathbf{q}_0)^2}\,. \tag{5.5}$$

Here, $\mathbf{Q}$ denotes the scattering vector and $\mathbf{q}$ the reduced scattering vector within the first Brillouin zone, respectively. $\mathbf{q}_0$ defines the center position of the excitation in reciprocal space. As fitting parameters the Lorentzian amplitude $A$, the center position $\mathbf{q}_0$ in units of r. l. u. as well the Lorentzian full width half maximum $\Gamma$ are derived. The integrated area $F$ of the Lorentzian function is defined by the relation $F = \pi A\Gamma$. Figure 5.4 (b) shows typical constant energy scans around (0 0 3) for different temperatures. The solid lines are fits based on Eq. (5.5) convoluted with the resolution function.

[2]The frequency of the damped oscillator $\omega_q$ represents the maximum of an excitation peak. The eigenfrequency $\Omega_q$ is increased compared to $\omega_q$ via $\Omega_q = \sqrt{\omega_q^2+\Gamma_q^2}$. Upon raising temperature the magnetic excitations shift to zero energy transfer, as the anisotropy of a system decreases. In case of $D = 0$ the excitation energy $\omega_q$ corresponds to zero energy, while the eigenfrequency of the damped oscillator yields $\Omega_q \simeq \Gamma_a > 0$. In this sense $\omega_q$ represents the physical quantity that describes the excitation energy.

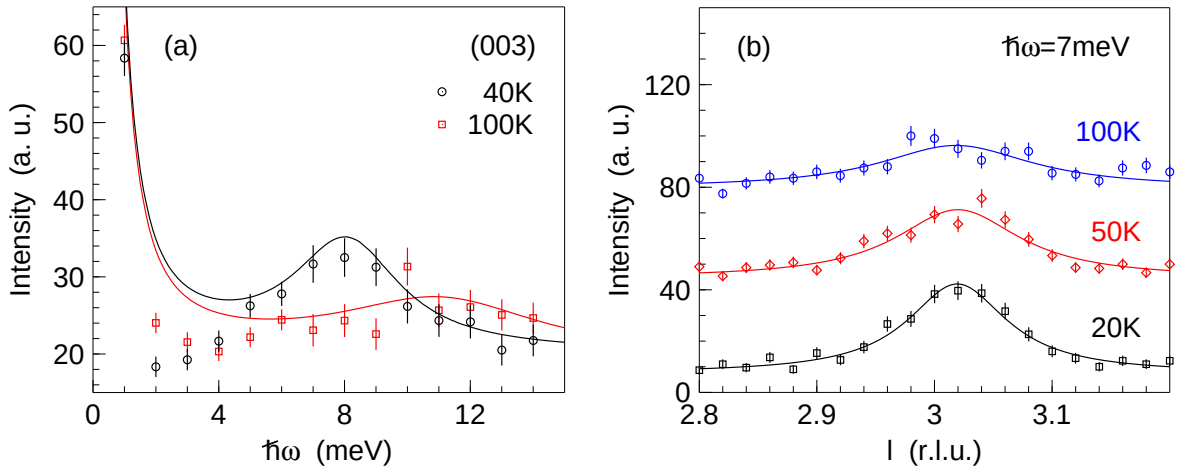


Figure 5.4: Examples of (a) constant-**Q** and (b) constant energy scans around the (0 0 3) reflection. The measurement temperature is indicated in each plot. The solid lines display the fit to the experimental data based on the model of the damped harmonic oscillator and a Lorentzian type function, respectively. For clarity, both the data and the fit curves at 50 K and 100 K in plot (b) are offset by 35 a. u. and 70 a. u., respectively.

### 5.3.2 Upward renormalization with $T$

The first data set of constant-**Q** scans is obtained at the (0 0 3) reflection with a scattering vector **Q** along the [001] direction. The selection rule of the double differential scattering cross section (see chapter 3.2.1, Eq. (3.11)) yields only in-plane fluctuations as origin of the scattering. The temperature dependence of the excitation gap was investigated above the Néel temperature up to 110 K.

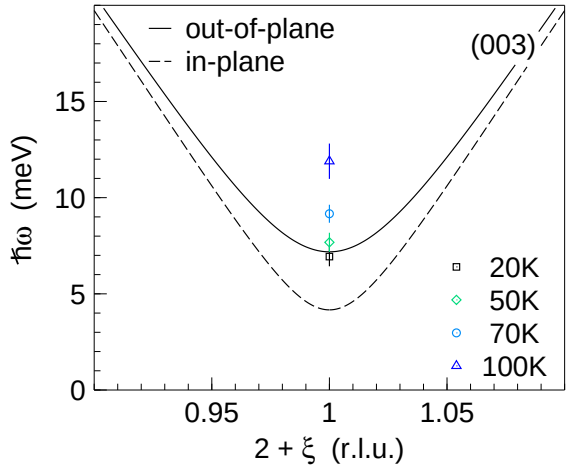


Figure 5.5: Energy gap at the magnetic zone center (0 0 3). The solid and the dashed line indicate the out-of-plane and the degenerate in-plane dispersion branches that are observed below $T_N$. Raising temperature leads to an increase in the frequency $\omega_q$ of the damped oscillator at (0 0 3). This quantity corresponds to the energy gap at the zone center.

Figure 5.4 (a) displays two constant-**Q** scans at 40 K and 100 K. The solid lines indicate the fit to the data convoluted with the resolution function. The data show a shift of the excitation peaks upon raising temperature. In addition, the linewidth of the peaks increase with temperature. Figure 5.5 shows the temperature dependence of the frequency $\omega_q$ of the damped oscillator that corresponds to the excitation energy at the zone center. The values of $\omega_q$ are obtained by fitting the data within the model of the damped harmonic oscillator. For comparison, the degenerate in-plane and the out-of-plane modes of the magnon dispersion are indicated by the dashed and the solid line, respectively.

Analyzing the temperature dependence of the frequency of the damped oscillator $\omega_q$ and the eigenfrequency $\Omega_q$ resolve a linear upward renormalization of both quantities between $\sim 25\,\mathrm{K}$ and $110\,\mathrm{K}$ with

$$\omega_q = (0.05 \pm 0.02)\frac{\mathrm{meV}}{\mathrm{K}} \cdot T + (5.81 \pm 1.08)\ \mathrm{meV}\,, \tag{5.6}$$

$$\Omega_q = (0.053 \pm 0.021)\frac{\mathrm{meV}}{\mathrm{K}} \cdot T + (5.76 \pm 1.02)\ \mathrm{meV}\,. \tag{5.7}$$

Furthermore, we observe an increase in the excitation linewidth $\Gamma_q$ upon increasing temperature. In agreement with $\omega_q$ and $\Omega_q$ this behavior is linear with temperature

$$\Gamma_q = (0.037 \pm 0.002)\frac{\mathrm{meV}}{\mathrm{K}} \cdot T + (0.35 \pm 0.08)\ \mathrm{meV}\,. \tag{5.8}$$

The excitation peaks become broader at higher temperature. However, they are still well defined at 100 K, as $\Gamma_q < \omega_q$ applies.
Figure 5.6 shows the temperature dependence of the eigenfrequency $\Omega_q$, the frequency of the damped oscillator $\omega_q$ and the linewidth $\Gamma_q$ between 15 K and 110 K. The solid lines represent linear fits to the data points.

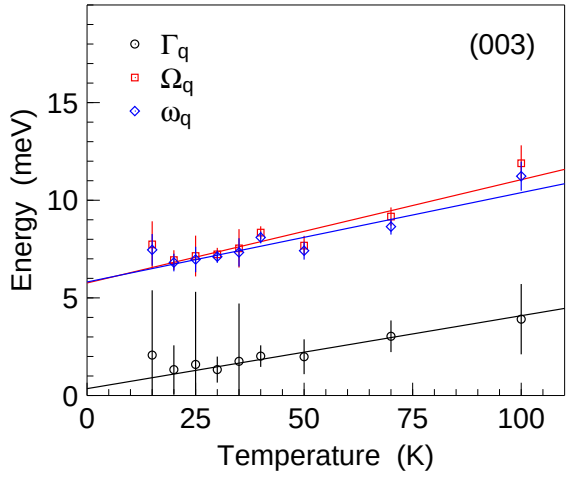


Figure 5.6: Temperature dependence of the fit parameters $\omega_q$ and $\Gamma_q$ within the damped harmonic oscillator model and the eigenfrequency $\Omega_q$ for constant-**Q** scans at (0 0 3). The solid lines indicate linear fits to $\Omega_q$, $\omega_q$ and $\Gamma_q$ between 25 K and 100 K. The linewidth $\Gamma_q$ remains almost constant up to 50 K yielding equivalent values for eigenfrequency $\Omega_q$ and the frequency $\omega_q$ of the damped oscillation.

Furthermore, the wavevector dependence of the excitation energy for points $(h\,0\,3)$ was investigated by means of constant-**Q** scans. With respect to the scattering vector $[\xi\,0\,1]$ both in-plane and out-of-plane fluctuations contribute to the cross section for coherent scattering.
Figure 5.7 displays the wavevector dependence of the frequency $\omega_q$ of the damped oscillator. The data are obtained at $T = 40\,\mathrm{K}$. In addition, the optic out-of-plane and the degenerate in-plane branches of the spin wave dispersion are shown as solid and dashed line. Within the error bars we observe a general increase of the excitation energy, when comparing the data to the spin wave dispersion. This result is compatible with the observed upward renormalization of the gap energy at (0 0 3). Furthermore, no distinct $q$ dependence of the excitation energy is revealed by the measurements, as the dispersion is almost flat along this direction in reciprocal space. Consequently, the eigenfrequency $\Omega_q$ and the linewidth $\Gamma_q$ show no visible $q$ dependence.

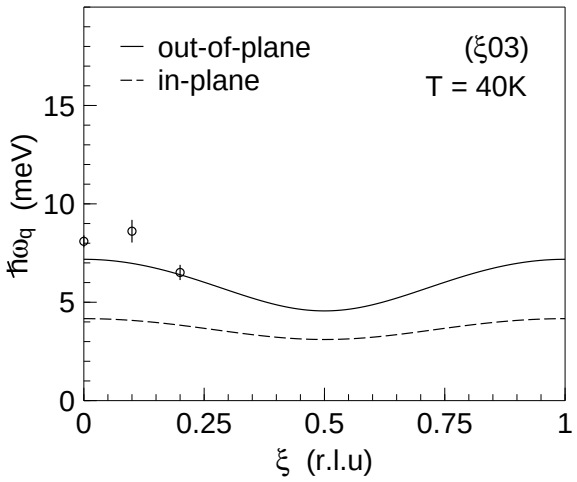


Figure 5.7: Wavevector dependence of the frequency $\omega_q$ at 40 K along the ($\xi$ 0 3) direction. The solid and the dashed line indicate the out-of-plane and the degenerate in-plane spin wave branches of $CsVBr_3$. No distinct $q$ dependence is observed within the investigated $q$ range. This behavior is expected from the flat dispersion modes along this particular direction in reciprocal space.

In order to prove the unusual temperature dependence of the gap energy at (0 0 3), constant-energy scans were performed for numerous energy transfers and temperatures. Figure 5.8 (a) presents an overview of the performed constant-energy scans. Selected data points of the frequency $\omega_q$ are included for comparison. In addition, the degenerate in-plane modes, the out-of-plane branch and the temperature induced renormalization of the in-plane dispersion branch are indicated.
We probed the evolution of the excitation at (0 0 3) for $2\,\text{meV} \leq \hbar\omega \leq 9\,\text{meV}$ at $T = 100\,\text{K}$. The excitation energy $\omega_q$ is equal to $\sim 11$ meV for this particular temperature and the peak width is not supposed to vary much with increasing energy transfer. Thus, the amplitude $A$ and the peak area $F$ of the excitations are expected to increase with raising energy transfer. Furthermore, the temperature dependence of the excitation was investigated for $\hbar\omega = 7\,\text{meV}$ between 20 K and 100 K. As the peak width $\Gamma$ might slightly increase with temperature, the temperature induced upward renormalization of $\omega_q$ yields a decrease of both quantities $A$ and $F$.

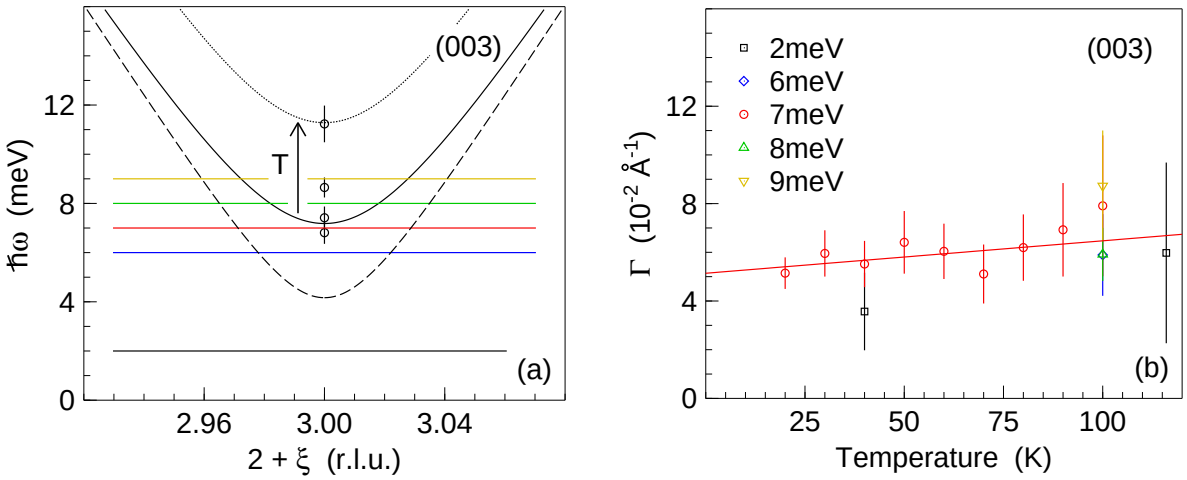


Figure 5.8: (a) Overview of constant energy scans at (0 0 3). The solid, the dashed and the dotted line indicate the out-of-plane mode, the degenerate in-plane dispersion branches and their temperature renormalized counterpart, respectively. (b) Fitting parameter Lorentzian linewidth $\Gamma$. Although raising temperature leads to a slight increase in the linewidth, the excitations remain well defined in the disordered phase up to 100 K. The dashed line is a fit to the 7 meV data points.

Figure 5.8 (b) displays the Lorentzian full width half maximum Γ of the excitation peaks. It slightly increases with raising energy transfer and temperature. The dashed line indicates a linear fit to the 7 meV data for $20\,\mathrm{K} \leq T \leq 100\,\mathrm{K}$. In agreement with the performed constant-**Q** scans all excitation peaks are well defined in the paramagnetic phase. The 3D dispersion persists above the ordering temperature without a peak broadening that is usually observed for conventional 3D compounds such as $LiCuO_2$ [123] and $RbMnF_3$ [124].

We first discuss the opening of the gap with respect to an increasing energy transfer at a constant temperature. Data were obtained for $\hbar\omega = 2\,\mathrm{meV}$, 6 meV, 7 meV, 8 meV and 9 meV in the disordered phase. Figure 5.9 (a) shows the amplitude $A$ and the integrated intensity $F$ of the Lorentzian peak. Data point at 2 meV are linear interpolated values of the two investigated temperatures at 40 K and 116 K. Within the error bars data analysis reveals no temperature dependence of Γ and $A$.
Both the amplitude $A$ and the peak area $F$ follow an upward trend with raising energy transfer. The slight increase of Γ does not influence the overall behavior of the integrated intensity of the excitation peaks, although $F \propto \Gamma$. This behavior agrees well with the upward renormalization of the gap energy with temperature.

The temperature dependence of the gap was elucidated using a constant energy transfer of 7 meV in the temperature range of $20\,\mathrm{K} \leq T \leq 100\,\mathrm{K}$. Obtained raw data at 20 K, 50 K and 100 K are presented in Figure 5.4 (see chapter 5.3.1). The solid lines indicate the fit curves with respect to Eq. (5.5). At first sight we observe that the peak amplitude is decreasing with increasing temperature. Figure 5.9 (b) shows the temperature dependence of the amplitude $A$ and the peak area $F$. Both quantities decrease with higher temperature, what is compatible with the upward renormalization of the gap energy.

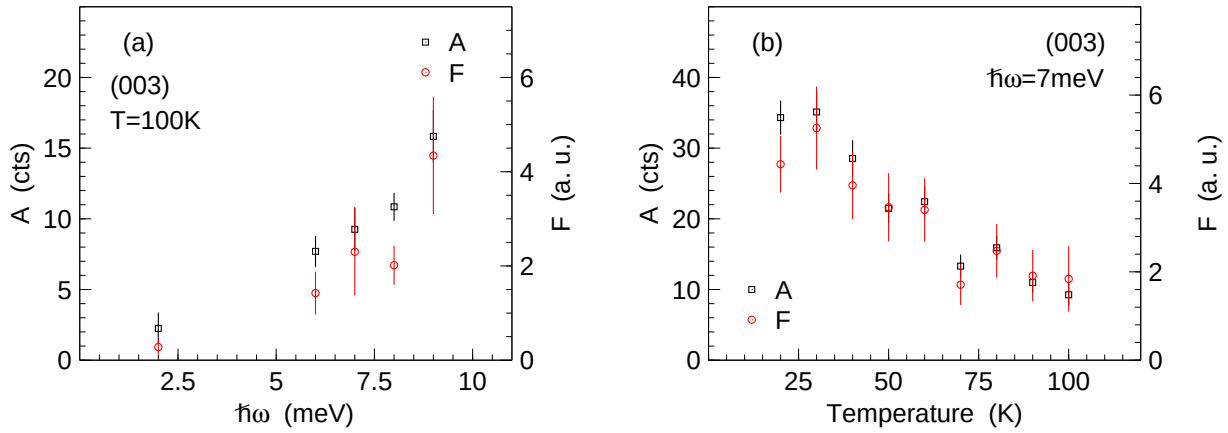


Figure 5.9: Amplitude $A$ and peak area $F$ of constant energy scans at (0 0 3) for (a) different energy transfers ($T = 100\,\mathrm{K}$) and (b) changing the temperature ($\hbar\omega = 7\,\mathrm{meV}$). Higher energy transfers lead to an increase in both the amplitude and the integrated intensity of the Lorentzian peak, while increasing temperature yields a decrease in both quantities.

In summary, we have presented inelastic neutron scattering data of $CsVBr_3$. Both constant-**Q** and constant-energy scans are consistently explained by a linear upward renormalization of the gap energy of the degenerate in-plane modes at the magnetic zone center (0 0 3) upon increasing temperature.

## 5.4 Discussion

In the following, we present different theoretical approaches to describe the unusual upward renormalization of the energy gap at (0 0 3) in $CsVBr_3$. Moreover, we compare the experimental findings of $CsVBr_3$, $CsMnBr_3$ and $CsNiCl_3$ to a hexagonal Heisenberg model with strong intrachain and weak interchain exchange.

### 5.4.1 Theoretical approaches for $ABX_3$ systems

Competing interactions lead to curious magnetic properties of $ABX_3$ compounds. The hexagonal lattice structure with magnetic ions located at the corner sites leads to frustration of adjacent spins [68]. In order to explain the complex spin dynamics that arises from these magnetic structure, various theoretical approaches can be considered.

Linear spin wave theory describes the collective spin dynamics of a magnetic system far below its ordering temperature [30]. A mathematical introduction to this approach it presented in appendix A.1. Within the frame of this theory Kadowaki and coworkers determine the magnon dispersion of $ABX_3$ compounds in the ordered phase [119]. The gaped dispersion arises from the XY-like anisotropy $D$. Upon increasing temperature thermal fluctuations destroy 3D magnetic correlations that dominate in the ordered phase. Furthermore, the anisotropy vanishes at the order temperature. Near the critical temperature the decrease of the magnetic order parameter follows the universal scaling law $M(T) \propto (T - T_c)^{\beta}$ [4]. It is expected that only the strong intrachain exchange holds above $T_N$ in $CsVBr_3$. In this way, neither a gaped dispersion nor its upward renormalization is understood.

Hummel and coworkers showed that dipolar exchange plays an important role for the spin dynamics of $ABX_3$ compounds [118]. This long range order interaction follows an inverse power law of the distance of the particular spin ($\propto r^{-3}$) and it is several orders of magnitude smaller than the inter- and intrachain exchange. The assumption that dipolar forces are the most important source of the XY-like anisotropy in particular $ABX_3$ compounds such as $CsVBr_3$ and $CsMnBr_3$ is justified, as their orbital angular momentum is almost zero and crystal field anisotropy only contributes by 20 % to the total anisotropy energy [125]. Considering this interaction as source of anisotropy in $CsVBr_3$ the gaped dispersion in the ordered phase is understood. However, both the existence of the energy gap at (0 0 3) and the upward renormalization of the gap energy cannot be explained from a theoretical point of view. In the disordered phase only magnetic exchange along the chain holds. Thermal fluctuations evoked by increasing temperature lead to a softening[3] of the magnon dispersion.

In the paramagnetic phase the dynamical behavior of $ABX_3$ systems is considered to originate from their quasi 1D properties. Haldane conjectured for antiferromagnetic spin systems with an integer spin value that the dispersion features a spin gap. Based on the theoretical findings for the antiferromagnetic $S = 1/2$ chain [7, 22, 24] it is generally assumed for spin systems with half odd integer $S$ that the dispersion is gapless.

[3] In analogy to phonons softening of a magnon dispersion is explained by a decreasing energy of the dispersion energy at the zone center. A dispersion becomes harder, when the excitation energy increases.

Only recently, Rastelli and coworkers developed a theoretical approach for hexagonal $ABX_3$ materials with half odd integer $S$ [126]. The results are restricted to the disordered phase, since the model represents an extension of calculations for antiferromagnetic Heisenberg spin chains [127]. It considers 3D magnetic correlations without anisotropy, where the interchain exchange is weak compared to the strong intrachain interaction.
This approach gives two predictions for the evolution of the magnon dispersion with temperature. First, the excitation energy minimizes at $(\frac{1}{3}\,\frac{1}{3}\,1)$. Furthermore, the in-plane modes are observable above $T_N$ and exhibit a wavevector dependent downward and upward renormalization, when the temperature increases. For points $(0\,0\,\xi)$ with $\xi < 2/3$ r.l.u. the dispersion softens, whereas for $\xi > 2/3$ r.l.u. the dispersion renormalizes upwards. Figure 5.10 (a) and (b) shows the calculated out-of-plane and in-plane dispersion branches of $CsMnBr_3$ at different temperatures above $T_N$.

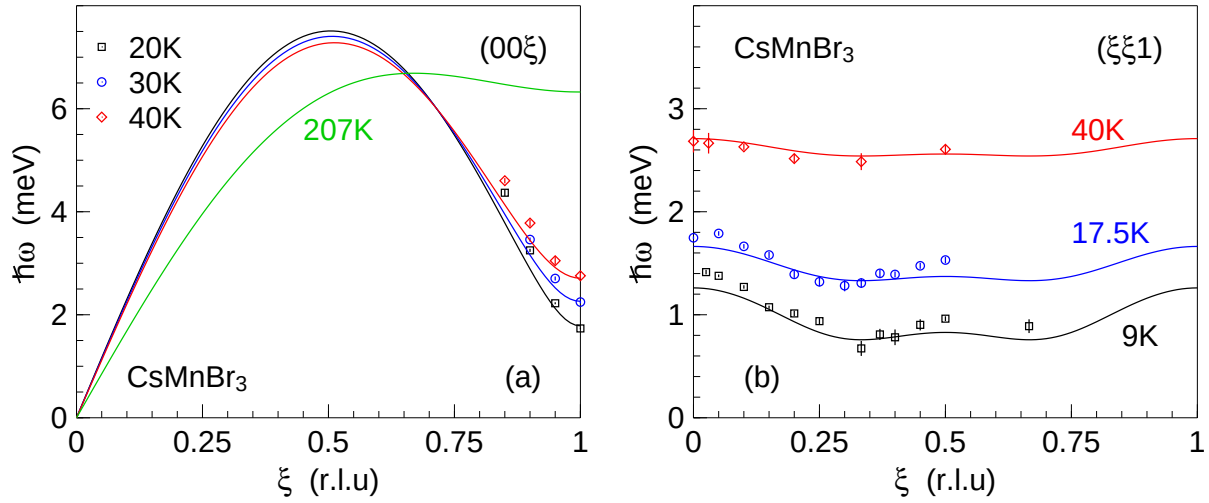


Figure 5.10: Dispersion relation of $CsMnBr_3$ along the (a) [0 0 1] and (b) [1 1 0] direction for different temperatures in the disordered phase. Data points are taken from [131]. The lines indicate the calculated dispersion by Rastelli and coworkers [126].

### 5.4.2 Comparison to $CsVBr_3$, $CsMnBr_3$ and $CsNiCl_3$

We discuss experimental observations for the $S = 5/2$ compound $CsMnBr_3$, $CsVBr_3$ and the Haldane material $CsNiCl_3$ ($S = 1$) within the frame of the approach by Rastelli and coworkers and the predictions for antiferromagnetic spin chains. We focus on these representatives of the $ABX_3$ class, as they exhibit different kinds of anisotropy and spin quantum numbers. Table 5.1 collect the spin value $S$, the order temperature $T_N$, the intrachain and interchain exchange and the anisotropy parameter of these compounds [68]. In addition, the ratio $J/J'$ is given that is a measure for the quasi 1D character in the disordered phase.

All samples crystallize in the $P6_3/mmc$ space group. XY-like anisotropy in $CsMnBr_3$ and $CsVBr_3$ forces spins into a frustrated 120° structure, where they are oriented in the the basal place. Antiferromagnetic spin chains run perpendicular to the basal plane. The magnetic ground state is degenerate, since rotational invariance yields equivalent spin

configurations (for comparison see Figure 5.2). $CsMnBr_3$ and $CsVBr_3$ show a Néel temperature of 8.3 K and 20.4 K, respectively.

| | $S$ | $T_N$ (K) | $J$ (meV) | $J'$ ($\mu$eV) | $D$ ($\mu$eV) | $J/J'$ |
|---|---|---|---|---|---|---|
| $CsMnBr_3$ | 5/2 | 8.3 | 0.89 | 1.7 | 12 | 524 |
| $CsVBr_3$ | 3/2 | 20.4 | 10.4 | 10.28 | 45.19 | 1012 |
| $CsNiCl_3$ | 1 | 4.4/4.84 | 2.28 | 44 | -4.0 | 52 |

Table 5.1: Spin quantum number $S$, order temperature $T_N$, exchange parameters $J$ and $J'$ measured along the chain and in the basal plane, anisotropy $D$ and the ratio $J/J'$ for $CsMnBr_3$, $CsVBr_3$ and $CsNiCl_3$ [68]. $D>0$ and $D<0$ leads to XY-like and single-ion anisotropy, respectively. The compounds are good realizations of quasi 1D spin systems. Owing to its spin value $CsNiCl_3$ is a representative of a Haldane material and $CsMnBr_3$ is assumed to be classically treated.

Owing to a small easy-axis anisotropy the low temperature magnetic structure of $CsNiCl_3$ is characterized by frustrated spins that point out of the basal plane (see Figure 5.11). The spins lie on a triangle that contains the $c$ axis and is perpendicular to the hexagonal basal plane. One magnetic moment is oriented parallel to the crystallographic $c$ axis and for two spins the canting angle $\theta$ between the $c$ axis and the opposite pointing spins is nearly 60°. Along the $a$ axis spins form a spiral, where the moments rotate by 120°. The large antiferromagnetic intrachain exchange yields antiferromagnetic stacked spin triangles along the $c$ axis. Figure 5.11 shows the magnetic structure of $CsNiCl_3$. Besides a magnetic field dependence the complex phase diagram of $CsNiCl_3$ features two temperature induced phase transitions at $T_{N1}=4.4$ K and $T_{N2}=4.84$ K ending up with paramagnetic order above $T_{N2}$. Between $T_{N1}$ and $T_{N2}$ the magnetic order of spins is collinear with all spins pointing parallel to the chain axis.

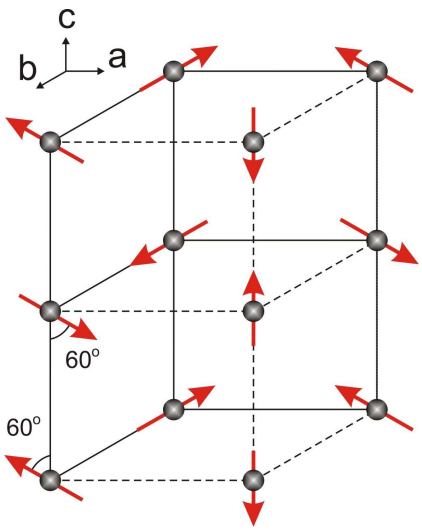


Figure 5.11: Magnetic structure of $CsNiCl_3$ below 4.4 K [128]. The spins form a triangle and lie in the $ac$ plane. One spin is parallel to the $c$ axis. The angle between the two other spins and the $c$ axis is almost 60°. Along the $a$ axis the magnetic moments form a spiral with spins rotating by 120°. Spin chains are antiferromagnetically stacked along $c$.

The compound $CsMnBr_3$ was extensively investigated by means of inelastic neutron spectroscopy above $T_N$. In summary, it was found that the optic in-plane and optic out-of-plane mode exhibit a temperature induced upward renormalization, whereas the acoustic in-plane branch becomes softer upon increasing temperature [129, 130, 131].
Collins and Gaulin [129, 130] investigated in-plane fluctuations between $15\,\mathrm{K} \leq T \leq 40\,\mathrm{K}$

along the [0 0 1] direction and observed an upward renormalization of the excitation energy with temperature. Reich and coworkers investigated the spin dynamics in the temperature range of $20\,\mathrm{K} \leq T \leq 40\,\mathrm{K}$ for points around (0 0 1), ($\frac{1}{3}$ $\frac{1}{3}$ 1) and ($\frac{1}{3}$ 0 1) [131]. Similarly to $CsVBr_3$, the dispersion energy as well as the linewidth $\Gamma_q$ linearly increase with temperature at the zone center (0 0 1) and along [$\xi$ 0 1]. Furthermore, no $Q$ dependence of the linewidth was revealed. Surprisingly, it was found that along [$\xi$ 0 1] the acoustic in-plane mode becomes softer with increasing $T$ and the optic in-plane mode renormalizes upwards.
Figure 5.10 (a) and (b) displays the experimentally observed dispersion relation along the [0 0 1] and [1 1 0] for different temperatures above $T_N$, respectively. Data points are taken from [131]. Upon increasing temperature the dispersion renormalizes upwards. The solid lines represent the calculated curves using the approach of Rastelli and coworkers [126]. The calculations reproduce the measured data well over a large temperature and $Q$ range. We note that within this theoretical approach no explanation of the unusual behavior of the in-plane dispersion branches is provided. Describing the dispersion of $CsMnBr_3$ in the paramagnetic phase within the frame of the theoretical calculations by Rastelli and coworkers resolves the importance of 3D correlations above $T_N$. Obviously, this compound is not capable of serving as model system for the antiferromagnetic half odd integer spin chain. The observed dynamical behavior might be ascribed to its large spin value 5/2.

Paramagnetic spin dynamics of $CsVBr_3$ are also expected to originate from 1D Heisenberg behavior of antiferromagnetic half odd integer spin chains. Owing to its spin value 3/2 the dynamical behavior above $T_N$ shall be closer to the spin 1/2 chain compared to $CsMnBr_3$. Respecting the predictions for antiferromagnetic half odd integer spin chains the dispersion should not exhibit a gap at the magnetic zone center.

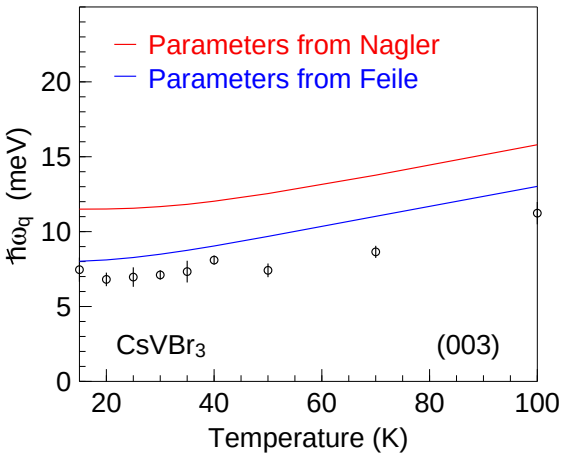


Figure 5.12: Temperature dependence of the frequency $\omega_q$ at (0 0 3). The blue and the red solid line indicate the theoretical calculations of Rastelli [132] using the exchange constants of Feile and coworkers [120] and Nagler and coworkers [121], respectively. In the latter case $J = 10.4\,\mathrm{meV}$ and $J/J' = 0.001$ are used, while the blue curve is based on the parameters $J = 7.1\,\mathrm{meV}$ and $J/J' = 0.0013$. The increase in the excitation energy at the zone center is reproduced by the theoretical prediction for this compound. The deviation of the absolute value of the excitation energy from the the data results from the not well defined exchange constants of the spin wave dispersion.

In order to prove the adaptability of these predictions, we recall the obtained results of our neutron scattering study. Figure 5.12 shows the temperature dependence of the gap energy at (0 0 3) up to 100 K. We observe a gaped dispersion at (0 0 3) in the disordered phase, where the energy gap linearly increases with temperature within the investigated temperature range of $T_N < T < 5T_N$. Both the existence of the spin gap and the temperature induced upward renormalization of the gap energy at (0 0 3) can be explained by Rastelli [132]. The blue and the red solid line in this figure display the theoretical

predicted upward renormalization of the gap energy in $CsVBr_3$ using the exchange parameters of Feile and coworkers [120] and Nagler and coworkers [121]. The slope of both curves compare well with the measured data. We attribute the deviation of the absolute value of the calculated excitation energies from the data to the not precisely measured spin wave dispersion in the ordered phase. The exchange parameters and the anisotropy significantly differs in these studies. Respecting the measured data, the exchange constants obtained by the earlier work of Feile and coworkers reproduce the upward renormalization of the excitation energy better. The applicability of the hexagonal Heisenberg model with strong intrachain and weak interchain exchange demonstrates the 3D character of the magnetic exchange in $CsVBr_3$. We do not observe short range behavior in terms of the antiferromagnetic spin chain.

Spin dynamics of the Haldane material $CsNiCl_3$ was investigated by means of neutron spectroscopy. It is reported that the energy gap of the spin wave dispersion decreases when approaching $T_{N2}$ [133]. This softening of the magnon dispersion at $(\frac{1}{3}\,\frac{1}{3}\,1)$ is compatible with a decrease of the easy-axis anisotropy upon raising temperature. In agreement with the Haldane conjecture an excitation gap for all modes was observed above $T_{N2}$ by Buyers and coworkers [134] and Kenzelmann and coworkers [135]. In addition, an upward renormalization of the energy at $(\frac{1}{3}\,\frac{1}{3}\,1)$ [133, 136] and $(0.81\,0.81\,1)$ [135] was found in the disordered phase. Moreover, measurements of the dispersion branch along the $(\xi\,\xi\,1)$ direction showed the energy minimum at $(\frac{1}{3}\,\frac{1}{3}\,1)$ [134]. The observation of the gaped dispersion supports the quasi 1D behavior of $CsNiCl_3$ in the disordered phase. However, the unusual upward renormalization of the dispersion is also compatible with the theoretical model of Rastelli and coworkers.

The three $ABX_3$ representatives $CsVBr_3$, $CsMnBr_3$ and $CsNiCl_3$ differ in their anisotropy parameter and their inherent spin value, however, the observed spin dynamics in the paramagnetic phase exhibit a similar behavior. All systems show an upward renormalization of the excitation energy with increasing temperature. The temperature dependence of the dispersion in the disordered regime can be understood using the theoretical approach given by Rastelli and coworkers. This model emphasis 3D magnetic correlations that dominates the paramagnetic spin dynamics of the $ABX_3$ compounds mentioned above. This result appears to generally question the model character of $ABX_3$ for antiferromagnetic 1D Heisenberg behavior. Even the $S = 3/2$ compound $CsVBr_3$ that is expected to similarly behave compared to the $S = 1/2$ chain demonstrate that the general belief of the adaptability of 1D magnetism in these compounds does not hold.

# Chapter 6

# Conclusion and outlook

*This chapter summarizes the results of this thesis work. In addition, we discuss central aspects for continuing research.*

This thesis is devoted to two model systems for 1D Heisenberg behavior that originates from antiferromagnetic half odd integer spin chains. We have investigated the complex magnetic properties of the cuprates $Ca_{2+x}Y_{2-x}Cu_5O_{10}$ and the $ABX_3$ compound $CsVBr_3$. The crystal structure of both systems favors one dimensional spin chains.

## 6.1 $Ca_{2+x}Y_{2-x}Cu_5O_{10}$

We first investigated the magnetic behavior of the compound series $Ca_{2+x}Y_{2-x}Cu_5O_{10}$. The crystal structure shows edge sharing $CuO_2$ chains along the $a$ direction of the magnetic relevant CuO-sublattice, where both the magnitude and the sign of the nearest neighbor interaction crucially depend of the Cu-O-Cu bond angle.

Macroscopic measurements such as susceptibility and specific heat resolve antiferromagnetic long range order that is superimposed to 1D Heisenberg behavior (see chapter 4.2 and 4.3). The evident characteristics of the Néel state, the order temperature $T_N$, decreases from 29 K to 12 K upon hole doping into the $CuO_2$ chains from $x = 0$ to 2.15. In contrast to the general belief, no evidence of a dimensional crossover in magnetic correlations from 3D to 1D is observed within this doping regime. The antiferromagnetic Néel state persists even in $Ca_{0.83}CuO_2$ that exhibits 0.33 holes/Cu. Furthermore, susceptibility and specific heat of the the higher doped compounds $Ca_{3.5}Y_{0.5}Cu_5O_{10}$ and $Ca_{0.83}CuO_2$ are interpreted in terms of antiferromagnetic 1D Heisenberg chain behavior. A large Curie Weiss like contribution at low temperatures turned data analyzing difficult for the medium doped compound $Ca_{3.5}Y_{0.5}Cu_5O_{10}$, as this contribution masks the 1D properties. On average, we found for both systems an exchange value $J$ of $\sim 60$ K. The alternating parameter $\alpha$ that measures the spatial isotropy of the exchange along the chain was found to be close to the uniform chain for $Ca_{0.83}CuO_2$. Above 30 K susceptibility of $Ca_{3.5}Y_{0.5}Cu_5O_{10}$ is equally well described for $\alpha$ equal to 0, 0.5 and 1, while specific heat shows an almost isotropic exchange. Analyzing $Ca_{0.83}CuO_2$ in terms of weakly 3D coupled chains predicts an ordered moment of $0.28\,\mu_B$. Besides these two phases, a Curie Weiss like term below $\sim 10$ K is observed whose strength increases with raising the Ca/Y ratio. However, no experimental evidence of this feature was found in $Ca_{0.83}CuO_2$. This finding anticipates

that a change within the magnetic structure occurs between the doping concentrations $x = 1.5$ and 2.15.

Chapter 4.4 describes the investigation of the microscopic magnetic structure of the compound series by means of neutron diffraction. This study represents a central issue in understanding the adaptability of the 1D Heisenberg model to the cuprate compounds. We observe an increase in the Cu-O-Cu bond angle from 92° to 95.5° for $Ca_2Y_2Cu_5O_{10}$ and $Ca_{0.83}CuO_2$, respectively. The average lattice constants are extracted to be $a \simeq 2.8$ Å, $b \simeq 6.28$ Å and $c \simeq 10.5$ Å. The lattice constants along the $a$ and $c$ direction decrease with a raising Ca/Y ratio, while $b$ increases. In agreement with theoretical predictions for planar $CuO_2$ chains with $\theta < 95°$ magnetic correlations along the chain are ferromagnetic for samples with the doping concentration $0 \leq x \leq 1.5$. The magnetic unit cell corresponds to the $CuO_2$ sublattice, where the $ab$ planes show ferromagnetic interaction. Furthermore, an easy-axis anisotropy forces spins parallel to the $b$ direction. The $ab$ planes are antiferromagnetically stacked along $c$. We observe a doubling of the magnetic unit cell along $a$ for the highly doped sample, i.e. the magnetic correlations along the $CuO_2$ chains are of antiferromagnetic type. This was already expected from the Cu-O-Cu angle of 95.5°. In agreement with bulk measurements the order parameters of undoped $Ca_2Y_2Cu_5O_{10}$ and slightly doped $Ca_{2.5}Y_{1.5}Cu_5O_{10}$ exhibit a critical order temperature of 29 K and 26 K. We further observe a decrease in the magnetic moment upon doping from $0.92\mu_B$ to $0.22\mu_B$ for $x = 0$ and 1.5, respectively.

To get further insight into the unusual magnetic properties of the compounds, we investigated the dynamical behavior of the three magnetic phases by means of inelastic neutron spectroscopy on triple axis and time of flight spectrometers. It is worth noting that triple axis spectrometers with a multi detector or time of flight spectrometers are versatile tools for probing the excitation spectrum of powder samples. Both types of instruments offer the advantage to instantaneously reach a broad $(\mathbf{Q}, \omega)$ space.
The spin wave dispersion of the parent compound is consistently understood based on the observed magnetic structure. Resolving the most prominent features of the magnon dispersion, a spin gap of $\sim 1.8$ meV, confirms the three dimensional nature of the magnetic order. Studying the energy resolution dependent integrated intensity of the (0 0 1) reflection with increasing temperature in $Ca_{3.5}Y_{0.5}Cu_5O_{10}$ provides evidence of a spin glass like state. This result confirms the proposed explanation for the low $T$ upturn in susceptibility and the relatively high value of specific heat $C(T \to 0)$ in terms of disordered chains. This effects might originate from a random distribution of $Cu^{2+}$ or $Cu^{3+}$ ions along the chains. We further characterized the structure factor $S(Q)$ and the scattering law $S(Q, \omega)$ of highly doped $Ca_{0.83}CuO_2$ in terms of the 1D Heisenberg behavior. Data are analyzed for $S(Q)$ and reveal an intradimer distance of $\sim 5.7$ Å. This value corresponds to two times the copper distance along the chain, i.e. dimers are formed between next nearest neighbor spins. We found an approximate agreement between the exchange value $J$ extracted from $\chi(T)$ and the scattering law.

Although the results describing the complex magnetic order in $Ca_{2+x}Y_{2-x}Cu_5O_{10}$ can be consistently understood for different measurement techniques, this work still leaves questions not satisfactorily answered. For instance, the long range order of the highly doped sample $Ca_{0.83}CuO_2$ is still not confirmed by a complete magnetic structure analy-

sis. Based on the $CuO_2$ subcell the indexation $(\frac{1}{2}\,0\,1)$ of the observed Bragg reflection at $Q = 1.27\,\text{Å}^{-1}$ supports antiferromagnetic exchange along the chain. In addition, adjacent spin chains are antiferromagnetically coupled along $c$. From an academic point of view it is indispensable to compare the magnetic structure of this sample to lower doped compounds. Owing to the low magnetic moment $0.29\,\mu_B$ this task will be difficult.
We note that the moderate neutron data quality of $Ca_{0.83}CuO_2$ limits the extraction of the chain parameters $J$ and $\alpha$ from the scattering law. A further inelastic neutron scattering study might resolve the approximate agreement between these values for susceptibility and neutron spectroscopy data. Despite the consistent description of the structure factor for IN3 and IN4 data in terms of next nearest neighboring spin coupling, the distance of two dimers along the chain is still not experimentally proved. As already mentioned, theory predicts for the nominal number of holes in the chains that this value corresponds to three times the copper distance along the chain. We note that this distance is independent of nearest and next nearest neighboring dimer coupling.

In analogy to previous studies of $Ca_{2+x}Y_{2-x}Cu_5O_{10}$ samples and related edge sharing $CuO_2$ chain materials such as $Ca_{1-x}CuO_2$, $Sr_{0.73}CuO_2$ or $Sr_{14}Cu_{41}O_{24}$, we dismissed the aspect of a distorted structure for the spin/charge ordering. It is proposed that spatially tilted $CuO_2$ chains represents the origin of the antiferromagnetic long range order in cuprate compounds [137]. In addition, dimerization is preferred, as the distance of adjacent spins depends on the deformation of the chains from their ideal planar structure. The coexistence of both phenomena is reported for the cuprates $CuGe_{1-x}Sr_xO_3$, where Sr ions act as magnetic impurity and locally induce disorder in the chains [138, 139]. The possibility of systematic calcium doping into $Ca_{2+x}Y_{2-x}Cu_5O_{10}$ presents a promising starting point for continuing work on this effect.

## 6.2 $CsVBr_3$

The $ABX_3$ compound $CsVBr_3$ was studied by means of inelastic neutron spectroscopy. Its hexagonal crystal structure favors spin chains along the $c$ axis, that are formed by vanadium ions ($S = 3/2$). Below the Néel temperature of 20.4 K the spin wave excitations results from a 120° spin structure, where magnetic moments are confined to the hexagonal basal plane. In contrast to weaker interchain exchange and XY-like anisotropy, the strong intrachain exchange is expected to persist upon increasing temperature and to dominate the dynamical behavior in the paramagnetic phase. Within the frame of linear spin wave theory or a theoretical approach using dipolar exchange, the spin wave dispersion should soften upon approaching $T_N$. In this way, this compound is expected to be a model system for 1D Heisenberg behavior that originates from the antiferromagnetic half odd integer spin chains. Theory predicts a gapless dispersion in the disordered phase.

We investigated the temperature evolution of the gap energy at the magnetic zone center (003) above $T_N$ by means of constant-$\mathbf{Q}$ and constant energy scans. Owing to the scattering vector $[0\,0\,1]$ only in-plane fluctuations contribute to the magnetic excitations. The dispersion is still gaped above the order temperature. In addition, the gap energy shows a linear upward renormalization between $20\,\text{K} \leq T \leq 100\,\text{K}$. This finding shows that this compound does not serve as model system for quasi 1D behavior. A recent theoret-

ical approach explains the unusual observation using 3D magnetic interactions without anisotropy. Owing to similar experimental results for the in-plane modes of the isomorphic samples $CsMnBr_3$ ($S = 5/2$) and $CsNiCl_3$ ($S = 1$), this might be a general feature of these $ABX_3$ compounds.

Time limitation does not allow for a detailed study of the temperature dependence of the in-plane and out-of-plane modes. In particular, it is reported for $CsMnBr_3$ that at $(\frac{1}{3}\,\frac{1}{3}\,1)$ the acoustic in-plane branch softens above $T_N$, whereas the optic branch shows an upward renormalization with temperature [131]. It is evident to test this finding for $CsVBr_3$ by means of polarized neutron scattering. Resolving this behavior as general feature, further theoretical progress is required to understand the 3D character of magnetic correlations in the paramagnetic phase.
As theoretical calculations strongly depend on the correct value of the exchange parameters, the spin wave dispersion has to be reinvestigated in the ordered phase.

# Appendix A

# Spin wave dispersion of $Ca_2Y_2Cu_5O_{10}$

*This appendix provides an introduction to the calculation of the dispersion relation of undoped $Ca_2Y_2Cu_5O_{10}$ by means of linear spin wave theory.*

## A.1 Linear spin wave theory

Basic equations of classical linear spin wave theory are repeated in order to derive the dispersion relation $\hbar\omega(q)$ of a long range ordered system.

For this purpose the equation of motion for this system

$$\frac{d\hat{\mathbf{S}}_j}{dt} = \frac{1}{i\hbar}\left[\hat{\mathbf{S}}_j, H\right] \tag{A.1}$$

has to be solved. The Hamiltonian

$$H = \sum_{i,j} J_{ij}\hat{\mathbf{S}}_i\hat{\mathbf{S}}_j \tag{A.2}$$

comprises specific magnetic interactions of the spins $\hat{\mathbf{S}}_i$, $\hat{\mathbf{S}}_j$ based on the preferred exchange paths of the crystallographic structure. $\hat{\mathbf{S}} = (\hat{S}^x, \hat{S}^y, \hat{S}^z)^T$ is the spin operator defined by the spin Pauli matrices with $\hat{\mathbf{S}} = \frac{\hbar}{2}\boldsymbol{\sigma}$. Notice that the spin is a physical observable, thus $\hat{S}^z$ is an hermitian operator. $\hat{S}_i^l$ follows the relations $\left[\hat{S}_i^l, \hat{S}_i^m\right] = i\epsilon_{lmn}\hat{S}_i^n$ and $\left[\hat{S}_i^l, \hat{S}_i^l\right] = 0$ for $l, m, n \in \{x, y, z\}$.

For simplicity, first assume a Heisenberg spin system with only nearest neighbor interaction in one dimension. Moreover, single ion anisotropy is neglected. The corresponding Hamiltonian $H$ is given by nearest neighbor exchange between two spins $j$ and $j+1$

$$H = \sum_{i<j} J_{ij}\hat{\mathbf{S}}_i\hat{\mathbf{S}}_j = mJ\sum_j \hat{\mathbf{S}}_j\hat{\mathbf{S}}_{j+1} \tag{A.3}$$

with $J < 0$ for ferromagnetic and $J > 0$ for antiferromagnetic interaction. It is assumed that the magnetic correlations $J_{jj\pm1}$ along both directions of the chain are equal. $m$ denotes the coordination of the spin $\hat{\mathbf{S}}_j$ to its nearest neighboring spins. For an one

dimensional spin chain $m$ is equal to two. The equation of motion reduces to

$$\begin{aligned}\frac{d\hat{\mathbf{S}}_j}{dt} &= \frac{2J}{i\hbar}\left[\hat{\mathbf{S}}_j, .. + \hat{\mathbf{S}}_{j-1}\hat{\mathbf{S}}_j + \hat{\mathbf{S}}_j\hat{\mathbf{S}}_{j+1} + ..\right] \\ &= \frac{2J}{i\hbar}\left(\left[\hat{\mathbf{S}}_j, \hat{\mathbf{S}}_{j-1}\hat{\mathbf{S}}_j\right] + \left[\hat{\mathbf{S}}_j, \hat{\mathbf{S}}_j\hat{\mathbf{S}}_{j+1}\right]\right) \\ &= \frac{-2J}{\hbar}\left(\hat{\mathbf{S}}_j \times \left(\hat{\mathbf{S}}_{j-1} + \hat{\mathbf{S}}_{j+1}\right)\right).\end{aligned}$$

The ground state is classically treated with spins arbitrarily oriented along the $z$-axis, i.e. $\hat{S}_j^z = S$, $\hat{S}_j^x = \hat{S}_j^y = 0$. Linearizion of these equations follows the assumption that only small deviations of the ground state shall occur. Thus $\hat{S}_j^z = S$ and $\hat{S}_j^x, \hat{S}_j^y \ll S$ apply. When solving the equation of motion one has to distinguish between ferromagnetic and antiferromagnetic correlations in the spin system.
Respecting ferromagnetic exchange the equation of motion in Cartesian coordinates reads

$$\frac{d\hat{S}_j^x}{dt} = \frac{-2JS}{\hbar}\left(2\hat{S}_j^y - \hat{S}_{j-1}^y - \hat{S}_{j+1}^y\right) \tag{A.4}$$

$$\frac{d\hat{S}_j^y}{dt} = \frac{2JS}{\hbar}\left(2\hat{S}_j^x - \hat{S}_{j-1}^x - \hat{S}_{j+1}^x\right) \tag{A.5}$$

$$\frac{d\hat{S}_j^z}{dt} = 0\,. \tag{A.6}$$

Solving Eq. (A.4)-(A.6) employs the ansatz for normal modes

$$\hat{S}_j^x(t) = ue^{i(jq_x x - \omega t)} \tag{A.7}$$

$$\hat{S}_j^y(t) = ve^{i(jq_x x - \omega t)}\,, \tag{A.8}$$

where $q_x$ denotes a wavevector in reciprocal space along the chain axis (here chosen along the $x$ axis) and $u$ and $v$ arbitrary amplitudes of the plane waves. Inserting the ansatz into the equation of motion yields

$$\hbar\omega = 4JS(\cos(q_x x) - 1) \qquad (J < 0)\,. \tag{A.9}$$

Note the relation $v = -iu$ for the amplitudes of the $x$ and $y$ coordinate of the spin operator $\hat{\mathbf{S}}$. At the zone center (small $q_x$) the dispersion relation can be linearized resulting in $\hbar\omega \propto q_x^2$.

Considering antiferromagnetic exchange two sublattices with spins $2j$ and $2j+1$ have to be chosen. Each of them exhibits ferromagnetic exchange between the sublattice spins, whereas the $z$ component of the spin operator $\hat{\mathbf{S}}$ changes its sign for one sublattice compared to the other one. The equation of motion for one sublattice is given by

$$\frac{d\hat{S}_k^x}{dt} = \frac{-2JS}{\hbar}\left(-2\hat{S}_k^y - \hat{S}_{k-1}^y - \hat{S}_{k+1}^y\right) \tag{A.10}$$

$$\frac{d\hat{S}_k^y}{dt} = \frac{2JS}{\hbar}\left(-2\hat{S}_k^x - \hat{S}_{k-1}^x - \hat{S}_{k+1}^x\right) \tag{A.11}$$

$$\frac{d\hat{S}_k^z}{dt} = 0 \tag{A.12}$$

with $k$ equals to $2j$ or $2j+1$. The normal modes

$$\hat{S}^x_{2j}(t) = u e^{i(2q_x j x - \omega t)} \qquad \hat{S}^y_{2j}(t) = -iu e^{i(2q_x j x - \omega t)} \tag{A.13}$$

$$\hat{S}^x_{2j+1}(t) = v e^{i(q_x(2j+1)x - \omega t)} \qquad \hat{S}^y_{2j+1}(t) = -iv e^{i(q_x(2j+1)x - \omega t)} \tag{A.14}$$

solve the equation of motion yielding the antiferromagnetic magnon dispersion relation

$$\hbar\omega = 4JS \sin(q_x x) \qquad (J > 0)\,. \tag{A.15}$$

This result can be linearized at the zone center yielding $\hbar\omega \propto q_x$.

In case of an one dimensional chain with single-ion anisotropy that forces spins along a particular direction the corresponding Hamiltonian reads

$$H = \sum_{i<j} \tilde{J}_{ij} \hat{S}^z_j \hat{S}^z_{j+1} = 2\tilde{J} \sum_j \hat{S}^z_j \hat{S}^z_{j+1}\,. \tag{A.16}$$

This expression is equivalent to the often used convention $H = D\sum_i (\hat{S}^z_i)^2$ that leads to the energy shift $\Delta$ of the $\mathbf{q}$ dependent dispersion. For $D>0$ spins are forced within the $XY$-plane (easy-plane anisotropy), whereas $D<0$ describes an easy-axis anisotropy. Accounting for ferromagnetic ($k=j$) and antiferromagnetic ($k=2j\,,\ 2j+1$) interaction Eq. (A.1) is given in the most general form by

$$\frac{d\hat{\mathbf{S}}_k}{dt} = \frac{2J}{\hbar} \begin{pmatrix} -\hat{S}^z_{k-1}\hat{S}^y_k - \hat{S}^z_{k+1}\hat{S}^y_k \\ \hat{S}^z_{k-1}\hat{S}^x_k + \hat{S}^z_{k+1}\hat{S}^x_k \\ 0 \end{pmatrix}. \tag{A.17}$$

Using Eq. (A.7)/(A.8) and (A.13)/(A.14) for normal modes the magnon dispersion relations reads

$$\hbar\omega = 4SJ \qquad (J<0) \tag{A.18}$$

$$\hbar\omega = -4SJ \qquad (J>0) \tag{A.19}$$

for the ferromagnetic and antiferromagnetic case, respectively. No $\mathbf{q}$ dependence of the excitation energy is found and the dispersion is only shifted by a constant energy term.

## A.2 Spin wave dispersion of undoped $Ca_2Y_2Cu_5O_{10}$

Based on the nuclear structure of the magnetic relevant $CuO_2$ sublattice Matsuda and coworkers [65] suggested for undoped $Ca_2Y_2Cu_5O_{10}$ a 3D model Hamiltonian with uniaxial anisotropy

$$H = \sum_{ij} J_{ij} \hat{\mathbf{S}}_i \hat{\mathbf{S}}_j + \sum_{ij} \tilde{J}_{ij} \hat{S}^z_i \hat{S}^z_j\,. \tag{A.20}$$

$J_{ij}$ and $\tilde{J}_{ij}$ denote the Heisenberg exchange and the anisotropy parameter between spins $i$ and $j$, respectively. The summation is carried out over nearest and next nearest neighboring spins in all crystallographic directions respecting the probability of magnetic exchange according to the spin distances in real space.

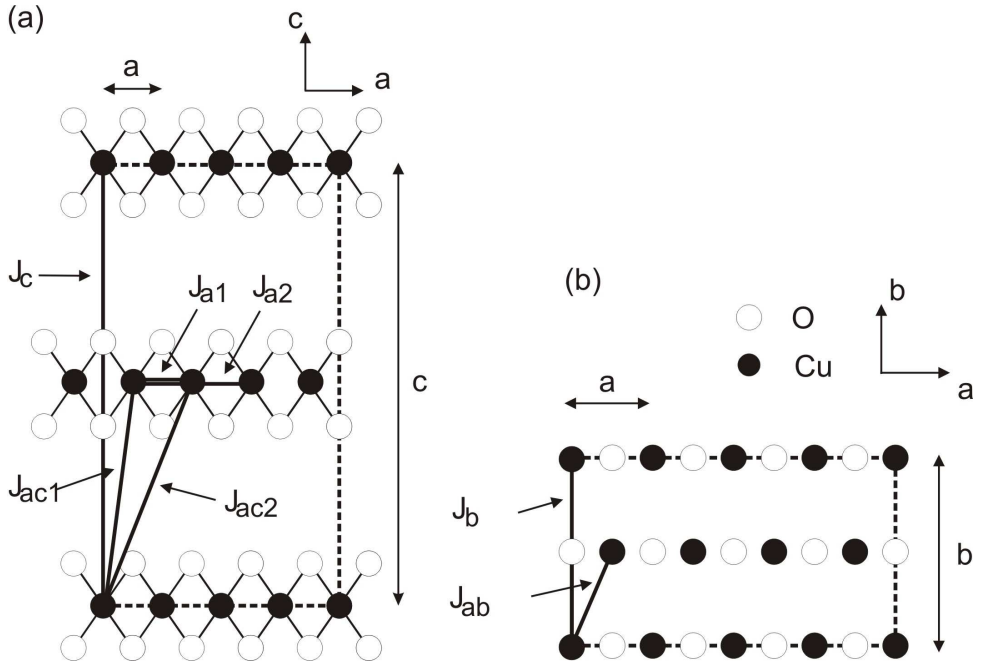


Figure A.1: Structure of edge sharing $CuO_2$ squares in the (a) *ac*- and (b) *ab*-plane [65]. Ferromagnetic interaction is given along the crystallographic $a$ and $b$ axis of the face centered orthorhombic $CuO_2$ sublattice ($J_{a1}$ and $J_{a2}$ along $[1\,0\,0]$, $J_b$ along $[0\,1\,0]$ and $J_{ab}$ along $[\frac{1}{2}\frac{1}{2}0]$). Antiferromagnetic exchange is found along the $c$ direction with $J_{ac1}$ and $J_{ac2}$ along $[\frac{1}{2}\,0\,\frac{1}{2}]$ and $[\frac{3}{2}\,0\,\frac{1}{2}]$. The next nearest interaction along $[0\,0\,1]$ is ferromagnetic ($J_c$).

Figure A.1 (a) and (b) show the top view of the face centered orthorhombic $CuO_2$ sublattice along the $[0\,1\,0]$ and the $[0\,0\,1]$ direction, respectively. The lattice constants of the magnetic relevant unit cell are $a \simeq 2.8\,\text{Å}$, $b \simeq 6.3\,\text{Å}$ and $c \simeq 10.6\,\text{Å}$.

Recall the findings of the 3D magnetic structure for undoped $Ca_2Y_2Cu_5O_{10}$ (see chapter 4.4). Data analysis yields ferromagnetic exchange in the *ab*-plane and antiferromagnetic correlations along the $c$ direction. Easy-axis anisotropy forces the spins parallel to the $b$ axis.
Applying this model to Eq. (A.20) ferromagnetic interaction is found along the $a$ axis between nearest ($J_{a1}$) and next nearest neighbor spins ($J_{a2}$). $J_{a2}$ is considered as the lattice constant $a$ and thus the spin distance is reasonable small in real space. The exchange integral $J_b$ along the $b$ axis is ferromagnetic. Since an easy-axis anisotropy forces spins parallel to $b$, the magnetic exchange within the *ab*-plane ($J_{ab}$) along the side diagonal $[\frac{1}{2}\,\frac{1}{2}\,0]$ of the unit cell is also ferromagnetic. Antiferromagnetic exchange along the $c$ axis yields $J_{ac1} > 0$ and $J_{ac2} > 0$ along the $[\frac{1}{2}\,0\,\frac{1}{2}]$ and $[\frac{3}{2}\,0\,\frac{1}{2}]$ directions, respectively. Ferromagnetic exchange is thus realized between next nearest neighboring spins along the $c$ direction ($J_c$).

This model yields the Hamiltonian $H$ summed over all interactions

$$H = H_{a1} + H_{a2} + H_b + H_{ab} + H_c + H_{ac1} + H_{ac2} + H_{aniso}\,, \tag{A.21}$$

where ferromagnetic and antiferromagnetic interactions are accounted for by a Hamiltonian $\propto J \sum_j \hat{\mathbf{S}}_j \hat{\mathbf{S}}_{j+1}$ with $J < 0$ and $J > 0$, respectively. The Hamiltonian $H_{aniso}$ describes the easy-axis anisotropy in the system and is given according to Eq. (A.16).

The linearity of the Hamiltonian $H$ allows a separation of the equation of motion for each part $H_s = \sum_{i<j} J_{ij}\hat{\mathbf{S}}_i\hat{\mathbf{S}}_j$ $(1 \leq s \leq N)$ by

$$\left[\hat{\mathbf{S}}_j, \sum_{s=1}^{N} H_s\right] = \left[\hat{\mathbf{S}}_j, H_1\right] + ... + \left[\hat{\mathbf{S}}_j, H_N\right] . \tag{A.22}$$

For convenience the coordination system is chosen in such a way that the $a$, $b$ and $c$ axis are parallel to the Cartesian axis $x$, $y$ and $z$. Consider an exchange path that is along the crystallographic axis $a$, $b$ or $c$. The solution of the equation of motion for ferromagnetic and antiferromagnetic interaction as well as for easy-axis anisotropy are presented in the last section A.1 of this appendix. Magnetic correlations that are arbitrarily oriented in the unit cell require a space dependent ansatz for the normal modes in terms of plane waves

$$\hat{S}_k^l(t) = Ae^{i(\mathbf{q}\mathbf{r}k-\omega t)} , \tag{A.23}$$

where $\mathbf{q}$ denotes the wave vector and $\mathbf{r}$ the position of the particular copper atom $k$ in reciprocal space. $l$ defines the Cartesian coordinates $x$, $y$, $z$. The convention of the amplitude $A$ for ferromagnetic and antiferromagnetic interaction is explained in appendix A.1.

Taken into account all exchange integrals with its multiple occurrence in reciprocal space (coordination $m$, $n$) the 3D dispersion of undoped $Ca_2Y_2Cu_5O_{10}$ reads

$$\begin{aligned}
\hbar\omega(\mathbf{q}) \;=\; & \Bigg[\Big( \sum_{m\in\{-1,1\}} 2SJ_{a1}(\cos(mq_a a) - 1) + \sum_{m\in\{-1,1\}} 2SJ_{a2}(\cos(2mq_a a) - 1) \\
& + \sum_{m\in\{-1,1\}} 2SJ_b(\cos(mq_b b) - 1) + \sum_{m\in\{-1,1\}} 2SJ_c(\cos(mq_c c) - 1) \\
& + \sum_{m,n\in\{-1,1\}} 2SJ_{ab}(\cos(\frac{mq_a a}{2} - \frac{nq_b b}{2}) - 1) \\
& + \sum_{m,n\in\{-1,1\}} 2SJ_{ac1}(1 + \cos(\frac{mq_a a}{2} + \frac{nq_c c}{2})) \\
& + \sum_{m,n\in\{-1,1\}} 2SJ_{ac2}(1 + \cos(\frac{3mq_a a}{2} + \frac{nq_c c}{2})) + \tilde{D}\Big) \cdot \\
& \Big( \sum_{m\in\{-1,1\}} 2SJ_{a1}(\cos(mq_a a) - 1) + \sum_{m\in\{-1,1\}} 2SJ_{a2}(\cos(2mq_a a) - 1) \\
& + \sum_{m\in\{-1,1\}} 2SJ_b(\cos(mq_b b) - 1) + \sum_{m\in\{-1,1\}} 2SJ_c(\cos(mq_c c) - 1) \\
& + \sum_{n,m\in\{-1,1\}} 2SJ_{ab}(\cos(\frac{mq_a a}{2} - \frac{nq_b b}{2}) - 1) \\
& + \sum_{m,n\in\{-1,1\}} 2SJ_{ac1}(1 - \cos(\frac{mq_a a}{2} + \frac{nq_c c}{2})) \\
& + \sum_{m,n\in\{-1,1\}} 2SJ_{ac2}(1 - \cos(\frac{3mq_a a}{2} + \frac{nq_c c}{2})) + \tilde{D}\Big)\Bigg]^{\frac{1}{2}}
\end{aligned} \tag{A.24}$$

with the anisotropy parameter $\tilde{D} = 4S\tilde{J}_{a1}+4S\tilde{J}_{a2}+4S\tilde{J}_b+4S\tilde{J}_c+8S\tilde{J}_{ab}-8S\tilde{J}_{ac1}-8S\tilde{J}_{ac2}$. For $Cu^{2+}$ the spin quantum number $S$ is equal to 1/2.

Mathematical calculations[1] yield the dispersion

$$\begin{aligned}\hbar\omega(\mathbf{q}) &= \Big[\Big(2J_{a1}(\cos(q_a a)-1)+2J_{a2}(\cos(2q_a a)-1)+2J_b(\cos(q_b b)-1)\\ &\quad +2J_c(\cos(q_c c)-1)+4J_{ab}(\cos(\frac{q_a a}{2})cos(\frac{q_b b}{2})-1)+4J_{ac1}+4J_{ac2}\\ &\quad -D\Big)^2-\Big(4J_{ac1}\cos(\frac{q_a a}{2})\cos(\frac{q_c c}{2})+4J_{ac2}\cos(\frac{3q_a a}{2})\cos(\frac{q_c c}{2})\Big)^2\Big]^{\frac{1}{2}} \quad \text{(A.25)}\end{aligned}$$

where the anisotropy $D$ is defined by $D = -2\tilde{J}_{a1}-2\tilde{J}_{a2}-2\tilde{J}_b-2\tilde{J}_c-4\tilde{J}_{ab}+4\tilde{J}_{ac1}+4\tilde{J}_{ac2}$.

This result was used by Matsuda and coworkers [65] as basis for data analysis. Note a factor of two between the above given exchange interaction $J$ and that obtained by Matsuda owing to the different convention of the exchange interaction $J$. An iteratively fitting procedure yielded the exchange constants along the $c$-direction $J_{ac1} = 2J_{ac2} = 1.494(3)\,\text{meV}$, $J_c = 0$ and $D_{ac} = -0.262(3)\,\text{meV}$. The dispersion along $b$ is characterized by $J_b = -0.061(6)\,\text{meV}$, $J_{ab} = -0.030(3)\,\text{meV}$ and $D_{ab} = -0.399(1)\,\text{meV}$ and the exchange integrals along the chain direction are given by $J_{a1} = -6.9(1)\,\text{meV}$ and $J_{a2} = 0$ or $J_{a1} = -8(1)\,\text{meV}$ and $J_{a2} = 0.4(3)$, respectively (see Figure A.2).

[1] Here, the symmetry of cosines ($\cos(-x) = \cos x$) and the theorem $\cos\alpha\cos\beta = [\cos(\alpha+\beta)+\cos(\alpha-\beta)]/2$ for trigonometrical functions are used.

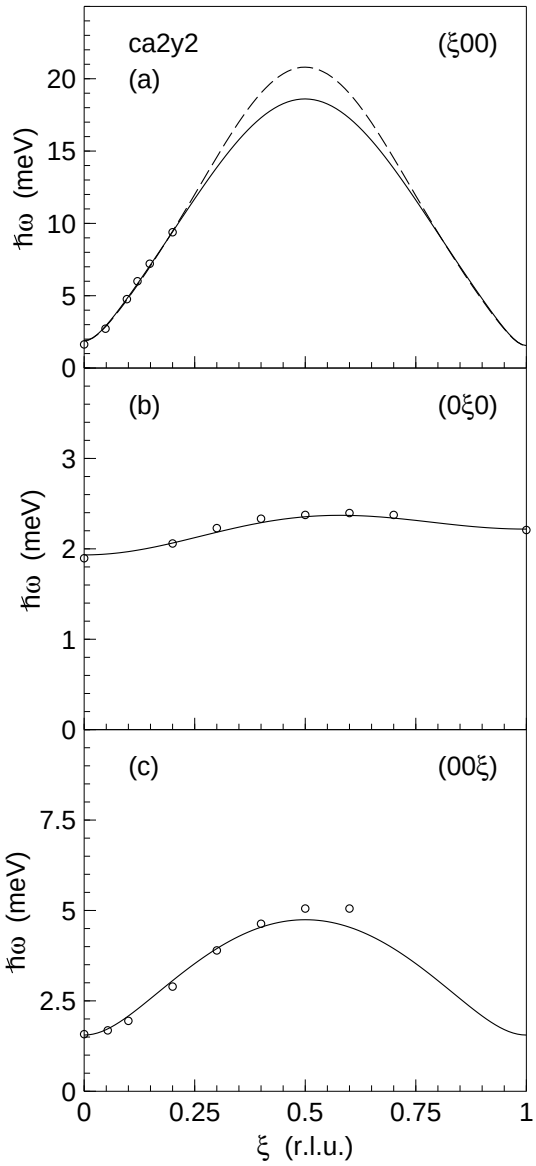


Figure A.2: Theoretical predicted 3D magnon dispersion relation along the (a) $a$, (b) $b$ and (c) $c$ axis of edge sharing $Ca_2Y_2Cu_5O_{10}$. The solid and the dashed line in (a) indicate the dispersion without and with $J_{a2}$. Data points are taken from [65]. The excitation gap at the magnetic zone center originates from an easy-axis anisotropy along the $b$ axis.

# Appendix B

# Structure factor and scattering law of $Ca_{0.83}CuO_2$

*In the following we present the powder averaged structure factor and the scattering law of dimerized chains that apply to $Ca_{0.83}CuO_2$.*

## B.1 Powder averaged structure factor

Dimerization in a spin chain occurs owing to not equivalent interactions with respect to the left and right neighboring spin. In the simple case of isolated dimers the magnetic exchange is interrupted by nonmagnetic ions reducing superexchange between those ions. No coupling between single dimers (space extension $d$) is thus possible. However, the model of an alternating chain allows for the formation of dimers that are coupled between themselves. The center of two dimers are located at the distance $b$ (see Figure B.1).

The excitation spectrum of both approaches is dominated by transitions from the singlet ground state $|0,0\rangle$ of a single dimer with its spin quantum number $S=0$ and $z$-projection $m_z=0$ to the triplet states $|1,1\rangle$, $|1,0\rangle$ and $|1,-1\rangle$ corresponding to $S=1$ and $m_z=1$, 0 and -1.

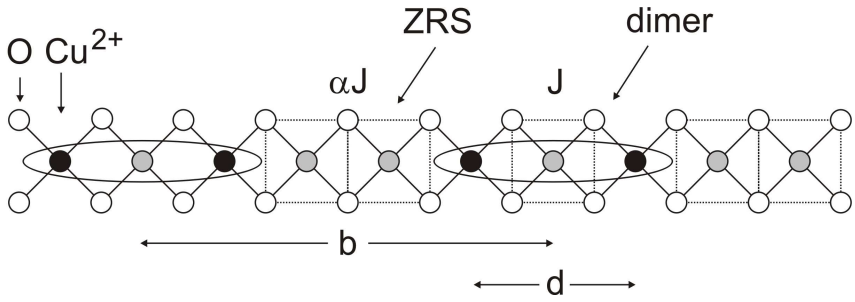


Figure B.1: Scheme of the alternating chain model for an edge sharing $CuO_2$ chain. Hole doping leads to the existence of nonmagnetic $CuO_4$ units called Zhang-Rice singlets (ZRS). Dimers of the extent $d$ are formed due to the magnetic interaction $J \geq \alpha J$ between magnetic $Cu^{2+}$ ions. The interdimer distance is called $b$.

The **Q** dependence of the scattering law of an isolated dimer results from the evaluation of Fermi's Golden Rule (see Chapter 3, Eq. (3.1)) by means of tensor operator methods

[111]. It results in $S(\mathbf{Q},\omega) \propto \frac{1}{2}\sin^2(\frac{1}{2}\mathbf{Qd}) \cdot \delta(\omega - \Delta)$, where $\Delta$ denotes the energy gap to the triplet state. To obtain the powder average scattering law, the relative orientation between the chain axis and the reduced scattering vector $\mathbf{q}$ has to be taken into account via

$$S(\mathbf{Q},\omega) = |f(\mathbf{Q})|^2 \frac{1}{4\pi Q^2} \int\limits_{\substack{\mathbf{q}=\mathbf{q}_\parallel+\mathbf{q}_\perp \\ q=Q}} S(\mathbf{q}_\parallel,\omega) d\mathbf{q} \tag{B.1}$$

The quantities $\mathbf{q}_\parallel$ and $\mathbf{q}_\perp$ denote the the projections of the reduced scattering vector parallel and perpendicular to the chain axis, respectively. Spherical integration results in [112, 113]

$$\begin{aligned} S(\mathbf{Q},\omega) &= |f(\mathbf{Q})|^2 \frac{1}{4\pi Q^2} \int_{\theta=0}^{2\pi} d\theta \int_{\phi=0}^{\pi} d\phi 2Q^2 \sin\phi \sin^2(\frac{1}{2}Qd\cos\phi) \\ &= |f(\mathbf{Q})|^2 (1 - \frac{\sin(Qd)}{Qd}) \,. \end{aligned} \tag{B.2}$$

Based on the $Q$ dependence of the scattering function the intradimer distance $d$ can be derived. In leading order it is defined by the first maximum in the structure factor still decreasing with the form factor.

To obtain the $\mathbf{Q}$ dependence of the structure factor for an alternating chain, we refer to the analytical expression of Barnes and coworkers [32]

$$\begin{aligned} S(\mathbf{Q}) &= |f(\mathbf{Q})|^2 \Big(1 - \cos(\mathbf{Q}\cdot\mathbf{d})\Big) \\ &\quad \cdot \Big[1 - \frac{5}{16}\alpha^2 - \frac{3}{32}\alpha^3 + \Big(\frac{1}{2}\alpha - \frac{1}{8}\alpha^2 - \frac{5}{192}\alpha^3\Big)\cos(\mathbf{Q}\cdot\mathbf{b}) \\ &\quad + \Big(\frac{3}{16}\alpha^2 + \frac{7}{48}\alpha^3\Big)\cos(2\mathbf{Q}\cdot\mathbf{b}) + \frac{5}{64}\alpha^3\cos(3\mathbf{Q}\cdot\mathbf{b})\Big] \,. \end{aligned} \tag{B.3}$$

For powder averaging the structure factor we also spherical integrate $S(\mathbf{Q},\omega)$. This results in first order of $\alpha$ in

$$\begin{aligned} S(Q) &= |f(\mathbf{Q})|^2 \frac{1}{4\pi Q^2} \int_{\theta=0}^{2\pi} d\theta \int_{\phi=0}^{\pi} d\phi \sin\phi \Big(1 - \cos(Qd\cos\phi)\Big) \\ &\quad \cdot \Big(1 + \frac{1}{2}\alpha\cos(Qb\cos\phi)\Big) \\ &= |f(\mathbf{Q})|^2 \Big(1 - \frac{\sin(Qd)}{Qd} + \frac{\alpha}{2}\Big(\frac{\sin(Qb)}{Qb} - \frac{\sin(Q(d-b))}{2Q(d-b)} - \frac{\sin(2Q(b+d))}{2Q(d+b)}\Big)\Big) \,. \end{aligned} \tag{B.4}$$

For $\alpha = 0$ this result coincides with the structure factor for the isolated dimer chain. The position of the first maximum in $S(Q)$ resolves the intradimer distance $d$.

Figure B.2 (a) shows $S(Q)/|f(\mathbf{Q})|^2$ for different values of $\alpha$, where $b = 1.5d$ is chosen. A change of $\alpha$ yields almost equivalent positions of the structure factor maxima. Figure B.2 (b) displays the structure factor for different values of the interdimer distance $b$ in units of $d$. Here, $\alpha$ was set equal to one. We observe a modulation of the amplitude of $S(Q)$, however, the overall lineshape does not vary much.

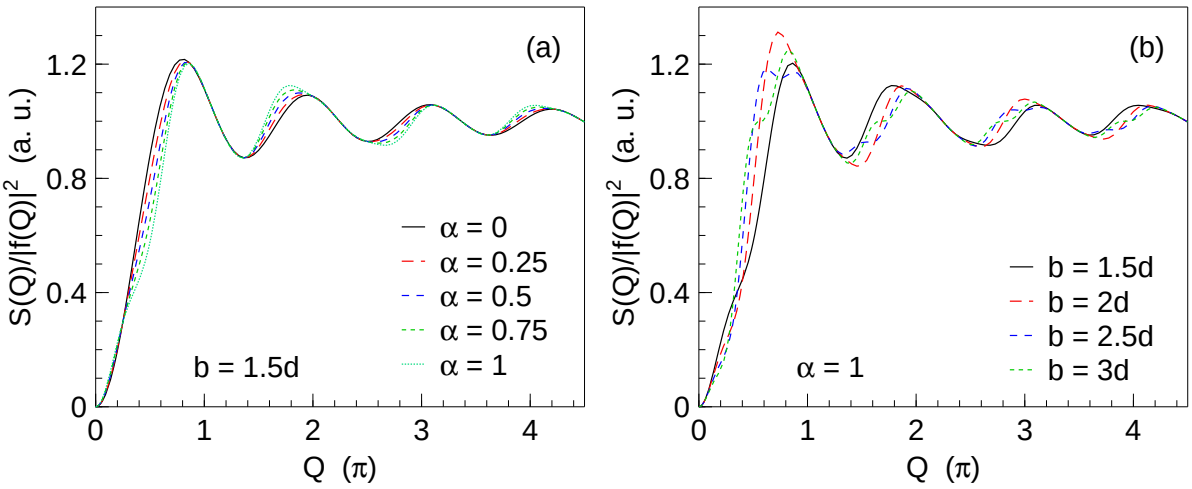


Figure B.2: Powder averaged structure factor of the dimerized chain model for different values of (a) $\alpha$ and (b) the interdimer distance $b$. In plot (a) $b = 1.5d$ and in plot (b) $\alpha = 1$ was chosen, respectively. Within the purely dimerized chain approach the intradimer distance $d$ is given by the first maximum of $S(Q)$. Increase in $\alpha$ and $b$ yield a modulation of the absolute amplitude of the structure factor.

## B.2 Powder averaged scattering law

We remind the excitation spectrum of the antiferromagnetic alternating spin 1/2 chain that is presented in chapter 2. Besides threefold degenerate triplet excitations the 2-magnon continuum is observed.

The scattering function $S(Q,\omega)$ of dimerized chains is composed of two parts that account for the density of states of the magnon branch ($S_{mag}(Q,\omega)$) as well as the continuum ($S_{cont}(Q,\omega)$)

$$S(Q,\omega) = S_{mag}(Q,\omega) + S_{cont}(Q,\omega)\,. \tag{B.5}$$

To estimate the scattering law of the magnon branch, we use the approach $S_{mag}(Q,\omega) \propto S(q)\cdot g(\omega)$, where the $g(\omega) = |d(\hbar\omega(q))/dq|^{-1}$ represents the density of states function [114]. The amplitude $S(q)$ is given by Uhrig and Schulz [35]. Harris and coworkers [34] analytically derived the dispersion relation to order $\mathcal{O}(\alpha^3)$ by means of perturbation theory

$$\begin{aligned}\hbar\omega(q)/\tilde{J} \;=\; &\left(1-\frac{1}{16}\alpha^2+\frac{3}{64}\alpha^3\right)-\left(\frac{1}{2}\alpha+\frac{1}{4}\alpha^2-\frac{1}{32}\alpha^3\right)\cos(2q)\\ &-\left(\frac{1}{16}\alpha^2+\frac{1}{32}\alpha^3\right)\cos(4q)-\frac{1}{64}\alpha^3\cos(2q)\,.\end{aligned} \tag{B.6}$$

Barnes and coworkers [32] extended this result to the order $\mathcal{O}(\alpha^5)$, Uhrig and Schulz [35] used a $\mathcal{O}(\alpha)$ first order approach to determine the scattering law. To obtain $S_{mag}(Q,\omega)$ the wavevector dependence can be explicitly substituted by the inverted dispersion relation. In $\mathcal{O}(\alpha)$ a non zero contribution to the density of states will appear within the energy interval $1-\alpha/2 \lesssim \hbar\omega/\tilde{J} \lesssim 1+\alpha/2$ with the two Van Hove singularities at $\hbar\omega/\tilde{J} \simeq 1\pm\alpha/2$. Figure B.3 displays the magnon term in the scattering law of coupled dimers. The calculation of

$S(Q,\omega)_{mag}$ are performed using the first order $\mathcal{O}(\alpha)$ approach for the dispersion relation.

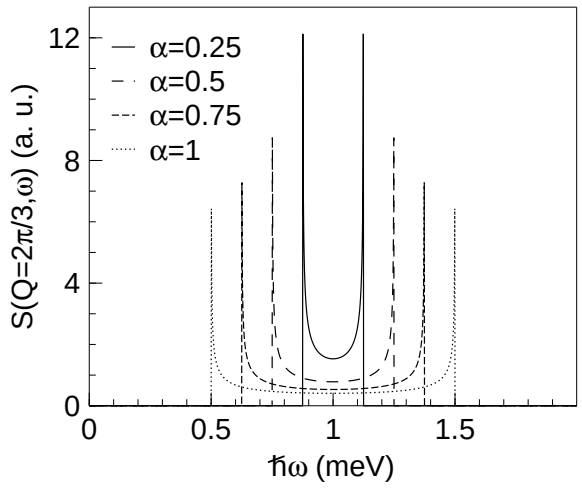


Figure B.3: Cut through the scattering law $S_{mag}(Q,\omega)$ at $Q=2\pi/3$ for the alternating parameter $\alpha=0.25$, 0.5, 0.75 and 1. We note that intensity appears within the interval $1-\alpha/2 \lesssim \hbar\omega/\tilde{J} \lesssim 1+\alpha/2$.

Uhrig and Schulz determined in leading order an analytical solution of the spectral density of the continuum states

$$R_{cont}(Q,\omega) = \frac{\alpha}{4} \cdot \frac{1-\cos(q)}{\frac{\tilde{\omega}-2}{\alpha} + 0.5 + \mathrm{sgn}\left(\frac{\tilde{\omega}-2}{\alpha}\right)\sqrt{\left(\frac{\tilde{\omega}-2}{2}\right)^2 - \cos(q)^2}} \tag{B.7}$$

with the reduced energy $\tilde{\omega} = \omega/\tilde{J}$. The scattering law is proportional to the imaginary part of the spectral density via $S(Q,\omega) = \omega \cdot \Im(R_{cont}(Q,\omega))$. The maximum in the density of states for the continuum is expected to occur at $\hbar\omega/\tilde{J} \simeq 2-\alpha/2$ with a non zero scattering contribution within the interval $2-\alpha \lesssim \hbar\omega/\tilde{J} \lesssim 2+\alpha$.

Figure B.4 displays a simulation of $S_{cont}(Q,\omega)$ for the magnon continuum. For illustration purposes, $\alpha=0.5$ was chosen.

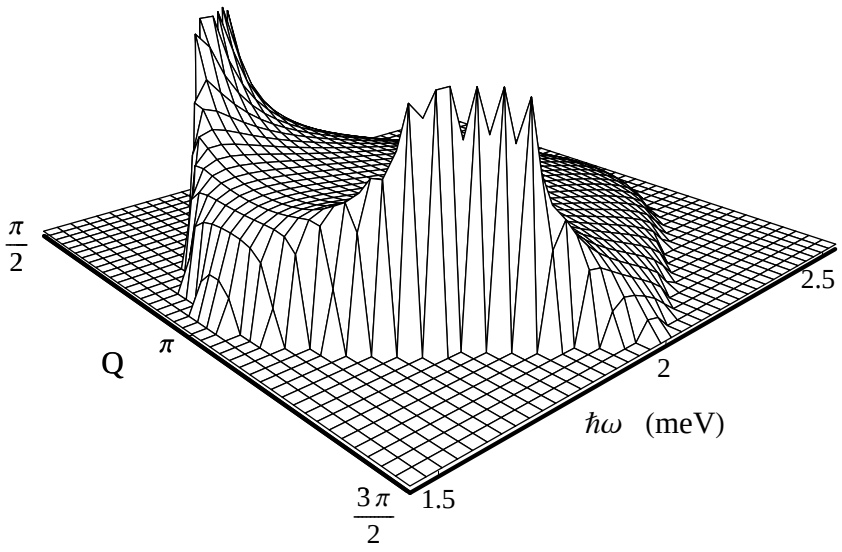


Figure B.4: Illustration of $S_{cont}(Q,\omega)$ for the continuum states. Here, the exchange $\tilde{J}$ and the alternation parameter $\alpha$ equals to 1 meV and 0.5, respectively.

# Appendix C

# Damped harmonic oscillator

*Here, we calculate the scattering law of $CsVBr_3$ that can be probed by inelastic neutron scattering. We use the model of the damped harmonic oscillator that has been successfully used for describing one-phonon processes. Introducing this approach the time and frequency dependent motion is presented (see appendix C.1). Afterwards, the line shape of $S(\mathbf{Q},\omega)$ is derived from the spin pair correlation function.*

## C.1 Motion in the time and frequency domain

The model of a damped harmonic oscillator can be applied for describing the line shape of the scattering function $S(\mathbf{Q},\omega)$ in the frequency domain. Thermal fluctuations that occur with raising temperature and influence the time response of an excitation are included via a temperature independent damping constant.

In the time domain any harmonic excitation is described by the model of an undamped harmonic oscillator. The time behavior of its amplitude $z(t) = Ae^{i\lambda t}$ follows the equation of motion

$$\ddot{z} + \Omega_q^2 z = 0 \tag{C.1}$$

with its eigenfrequency $\lambda = \Omega_q$. Only excitations at zero temperature can be described within this model, since thermal fluctuations are neglected that yield a time dependent decrease of the excitation amplitude.

In contrast, the damped harmonic oscillator includes a damping term $\propto \dot{z}$ (damping constant $\Gamma_q$) that results in a decreasing amplitude with time. With respect to the corresponding equation of motion

$$\ddot{z} + 2\Gamma_q \dot{z} + \Omega_q^2 z = 0 \tag{C.2}$$

its solution employing the standard ansatz $z(t) = e^{\lambda t}$ leads to the eigenvalues $\lambda_{1,2}$ of the damped harmonic oscillator

$$\lambda_{1,2} = -\Gamma_q \pm \sqrt{\Gamma_q^2 - \Omega_q^2} \tag{C.3}$$

and the time dependent motion $z(t) = A_1 e^{\lambda_1 t} + A_2 e^{\lambda_2 t}$. Depending on the damping constant $\Gamma_q$ three different time dependences of the amplitude can be observed (see Fig. C.1).

- Assuming a small damping ($\Gamma_q < \Omega_q$) the eigenvalues of Eq. (C.3) turn to be equal to $-\Gamma_q \pm i\omega_q$. The general solution is found to be $z(t) = e^{-\Gamma_q t} \cdot (A_1 e^{i\omega_q t} + A_2 e^{-i\omega_q t})$. $\omega_q = \sqrt{\Omega_q^2 - \Gamma_q^2}$ denotes the frequency of the damped harmonic oscillation. This case applies for evaluating the scattering function of the magnetic excitations in $CsVBr_3$ for a constant value of $\Gamma_q$.

- The critically damped regime of the damped harmonic oscillator corresponds to a damping constant approximately equivalent to the eigenfrequency of the undamped harmonic oscillator ($\Gamma_q \approx \Omega_q$). Since the eigenvalues are degenerate ($\lambda_1 = \lambda_2$), the time dependent solution is given by $z(t) = e^{-\Gamma_q t} \cdot (A_1 t + A_2)$. Exciting the system will lead to decrease of the amplitude with time without any oscillatory behavior.

- In the overdamped limit ($\Gamma_q > \Omega_q$) the amplitude shows an exponential decay with time according to $z(t) = e^{-\Gamma_q t} \cdot \left(A_1 e^{\sqrt{\Gamma_q^2 - \Omega_q^2} t} + A_2 e^{-\sqrt{\Gamma_q^2 - \Omega_q^2} t}\right)$.

Figure C.1 illustrate the time behavior of the damped oscillation with respect to the underdamped, critically damped and the overdamped case.

## C.2 Scattering Law

In order to calculate the scattering law, we remind the partial differential cross section for inelastic magnetic scattering that is presented in chapter 3. The scattering law is proportional to the spin pair correlation function $\left\langle S^\alpha(0) S^\beta(t) \right\rangle$. Describing the dynamical behavior of $CsVBr_3$ in the disordered phase we use the Heisenberg approach that accounts for isotropically orientated spins. Only elements with $\alpha = \beta$ thus retain in the spin pair correlation function leading to $\langle S^x(0) S^x(t) \rangle = \langle S^y(0) S^y(t) \rangle$. The spin pair correlation function reads

$$\langle S_l^x(0) S_{l'}^x(t) \rangle \propto \left[ \sum_q \left(n(\omega) + 1\right) \cdot e^{-i\mathbf{q}(\mathbf{r}_l - \mathbf{r}_{l'})} \cdot e^{i\Omega_q t} + \sum_q n(\omega) \cdot e^{i\mathbf{q}(\mathbf{r}_l - \mathbf{r}_{l'})} \cdot e^{-i\Omega_q t} \right] , \quad \text{(C.4)}$$

with $n(\omega) = \left(e^{\hbar\omega\beta} - 1\right)^{-1}$ denoting the Bose function and $\beta = k_B T$ the inverse temperature. The first term on the right side of Eq. (C.4) represents the magnon creation process, whereas the second term denotes the magnon annihilation. Consequently, the inelastic part of the scattering function results in

$$S(\mathbf{Q}, \omega) \propto \frac{1}{\omega_q} \sum_{\mathbf{q}, \mathbf{G}_m} \left( n(\omega) + \frac{1}{2} \pm \frac{1}{2} \right) \cdot \delta\left(\omega \mp \Omega_q\right) \cdot \delta(\mathbf{Q} \mp \mathbf{q} - \mathbf{G}_m) \,. \quad \text{(C.5)}$$

The factor $1/\omega_q$ explains the decreasing spin wave intensity with increasing energy $\omega_q$. We express the spectral weight functions with respect to the model of the damped harmonic oscillator that corresponds to a double Lorentzian function accounting for the Stokes and the Antistokes line of the excitation.

The line shape of the $S(\mathbf{Q}, \omega)$ is proportional the time Fourier transformation of the time motion

$$z(\omega) = \frac{1}{2\pi} \int_{-\infty}^{\infty} z(t) e^{-i\omega t} dt = \frac{1}{2\pi} \int_{-\infty}^{\infty} A \cdot \sin(\omega_q t + \Phi) e^{-i\omega t} dt \quad \text{(C.6)}$$

that was earlier presented. Here, boundary conditions are chosen in such a way that $A$ and $\Phi$ are set to unity and zero, respectively. Using the relation

$$\sin(\omega_q T) = \frac{1}{2i}\left(e^{\imath\omega_q t} - e^{-i\omega_q t}\right) \tag{C.7}$$

mathematical calculations yields $z(\omega)$ in terms of two Lorentzian functions

$$z(\omega) = \frac{-i}{2\pi}\left(\frac{\Gamma_q}{(\omega-\omega_q)^2+\Gamma_q^2} - \frac{\Gamma_q}{(\omega+\omega_q)^2+\Gamma_q^2}\right) = \frac{-i}{\pi}\left(\frac{2\omega\omega_q\Gamma_q}{(\omega^2-\omega_q^2)^2+4\omega_q^2\Gamma_q^2}\right). \tag{C.8}$$

This result is equivalent to the known expression for the damped harmonic oscillator. The scattering function $S(\mathbf{Q},\omega)$ is deduced as the imaginary part of $z(\omega)$ multiplied with the Bose factor $n(\omega)+1$. In the high temperature limit ($n(\omega)+1 \to T/\omega$) the energy integration of the unnormalized scattering function yields the normalization constant $C$ by

$$C = \int_{-\infty}^{\infty} (n(\omega)+1)\, z(\omega) d\omega = \frac{\omega_q T}{\Omega_q^2}. \tag{C.9}$$

Analytical calculation of Eq. (C.9) employs the standard integral

$$\int \frac{dx}{xQ} = \frac{1}{2c}\ln\frac{x^2}{Q} - \frac{2b}{\sqrt{D}}\arctan\frac{2ax+b}{\sqrt{D}} \tag{C.10}$$

where the relations $Q = ax^2+bx+c$ and $D = 4ac-b^2$ are used. The inverse temperature dependence of the normalized scattering function is accounted for by the $q$-dependent susceptibility

$$\chi_q = \frac{\chi_0}{q^2+\kappa^2} \tag{C.11}$$

with the static susceptibility at the zone center $\chi_0 \propto 1/T$. The correlation length $\kappa(T)$

$$\kappa(T) \propto \left(\frac{T-T_N}{T_N}\right)^{\nu} \tag{C.12}$$

describes the size expansion of the spin waves in reciprocal space within the paramagnetic phase. Its counterpart in real space $\xi(T) = 1/\kappa(T)$ explains the size expansion in which the relaxation process takes place.

Within the approach of the damped harmonic oscillator the normalized scattering function is written

$$\begin{aligned} S(\mathbf{Q},\omega) &= (n(\omega)+1)\cdot\chi_q\cdot\frac{\Omega_q^2}{\omega_q}\cdot\frac{1}{2\pi}\left(\frac{\Gamma_q}{(\omega-\omega_q)^2+\Gamma_q^2} - \frac{\Gamma_q}{(\omega+\omega_q)^2+\Gamma_q^2}\right) \\ &= (n(\omega)+1)\cdot\chi_q\cdot\frac{\Omega_q^2}{\pi}\cdot\frac{2\omega\Gamma_q}{(\omega^2-\Omega_q^2)^2+4\omega^2\Gamma_q^2}. \end{aligned} \tag{C.13}$$

Figure C.1 illustrates the scattering law $S(\mathbf{Q},\omega)$ for a small damping constant $\Gamma_q$, the critically damped case and the aperiodic limit.

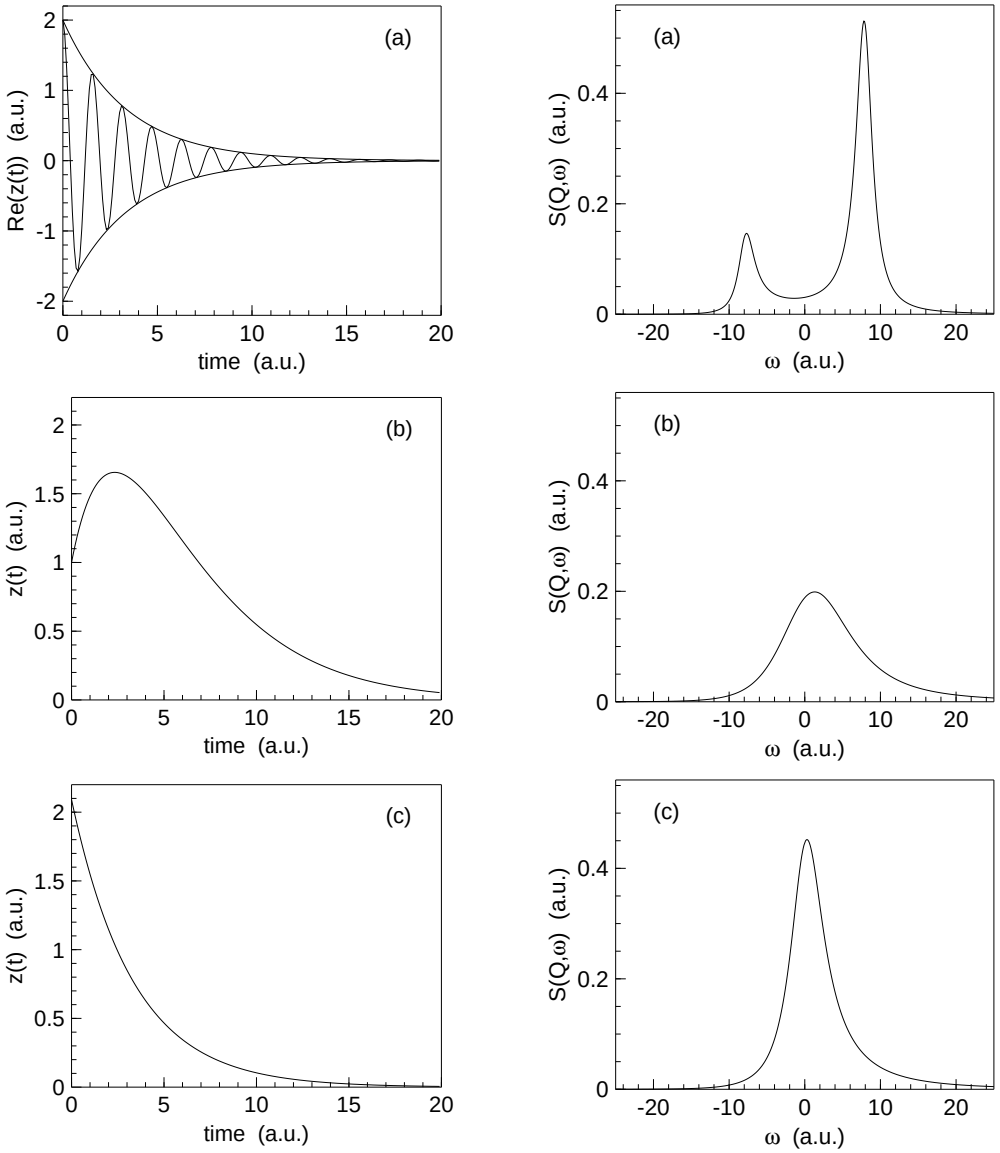


Figure C.1: Model of the damped harmonic oscillator. (a), (b) and (c) illustrate the underdamped, critically damped and overdamped case, respectively. Left figures: In the time domain the amplitude of the harmonic motion decreases with time according to the damping constant $\Gamma_q$. Right figures: The corresponding scattering function $S(Q, \omega)$ in the frequency domain.

# Acknowledgments

I wish to thank many people who joined my life in the last years and contributed to this thesis work. In this sense, I thank Prof. P. Böni who offered me the possibility to pursue my doctoral thesis at his institute and personally supervised me during the three years of my thesis work. He was helpful and encouraged me to gain skills in neutron spectroscopy at other neutron research centers such as the Paul Scherrer Institut, the Institut Laue Langevin and the NIST Center for Neutron Research. In addition, I wish to thank him for his trustful support, to let me independently work during my PhD-time.
Furthermore, I wish to thank Dr. A. Mirmelstein for supervising my work in the first year and introducing me to the susceptibility and specific heat measurement technique.
In addition, I am obliged to Dr. S. Kazakov (ETH Zürich) and Dr. K. Krämer (Universität Bern) for synthesizing various polycrystalline $Ca_{2+x}Y_{2-x}Cu_5O_{10}$ samples and the single crystal of $CsVBr_3$, respectively. I wish to thank Dr. A. Erb of the Walter Meissner Institut for low temperature physics who generously offered his laboratory equipment to synthesize $Ca_2Y_2Cu_5O_{10}$ samples. Although unsuccessfully, I thank Dr. K. Conder and Dr. E. Pomjakushina (PSI) for their efforts to grow a single crystal of $Ca_{0.83}CuO_2$.
I am indebted to several persons of various neutron research institutes who introduced me to practical things of neutron spectroscopy and offered their profound knowledge during the data analysis process. Here, I thank for the support given by Dr. B. Roessli and Dr. V. Pomjakushin of the Paul Scherrer Institut and Dr. M. M. Koza and Dr. H. Mutka of the Institut Laue Langevin. I further thank Dr. H. Mutka and Dr. M. M. Koza who enabled my two months stay at the ILL, read a preliminary version of this manuscript and made useful comments on it. I further thank Dr. D. Neumann and Dr. J. Lynn of the NCNR for offering me the possibility to stay at their institute.
I am grateful to Dr. T. Barnes and Dr. E. Rastelli for their friendly help to theoretically understand properties of antiferromagnetic chains respecting $Ca_{2+x}Y_{2-x}Cu_5O_{10}$ and $CsVBr_3$.
Moreover, I thank S. Stüber, M. Janoschek, Dr. S. Valloppilly and Dr. R. Hildebrandt for useful discussions in the field of physics and mathematics during my work. I am very obliged to S. Stüber for continuously reading my thesis.
I further thank everybody of my home institute E21 who contributed to a pleasant and agreeable work atmosphere during my three years stay.
I am deeply indebted to my family and my husband for their permanent support that enabled my education and scientific working experience.

# Bibliography


[1] J. Rossat-Mignod, in *Neutron and synchrotron radiation for condensed matter studies*, edited by J. Baruchel, J. L. Hodeau, M. S. Lehmann, J. R. Regnard, and C. Schlenker (Springer Verlag, Berlin, 1994)

[2] J. G. Bednorz, and K. A. Müller, Z. Phys. B **64**, 189 (1986)

[3] H. J. Müller-Buschbaum, Angew. Chem. Int. Ed. Engl. **30**, 723 (1991)

[4] S. Blundell, *Magnetism in condensed matter* (Oxford University Press Inc., New York, 2001)

[5] T. M. Rice, Z. Phys. B **103**,165 (1997), and references therein

[6] E. Dagotto, and T. M. Rice, Science **271**, 618 (1996), and references therein

[7] H. Bethe, Z. Phys. **71**, 205 (1931)

[8] F. D. M. Haldane, Phys. Lett. A **93**, 464 (1983); Phys. Rev. Lett. **50**, 1153 (1983)

[9] D. A. Tennant, T. G. Perring, R. A. Cowley, and S. E. Nagler, Phys. Rev. Lett. **70**, 4003 (1993)

[10] R. Eccleston, T. Barnes, J. Brody, and J. W. Johnson, Phys. Rev. Lett. **73**, 2626 (1994)

[11] Z. Hiroi, M. Azuma, M. Takano, and Y. Bando, J. Solid State Chem. **95**, 230 (1991)

[12] M. Azuma, Z. Hiroi, M. Takano, K. Ishida, and Y. Kitaoka, Phys. Rev. Lett. **73**, 3463 (1994)

[13] K. Kojima, A. Keren, G. M. Luke, B. Nachumi, W. D. Wu, Y. J. Uemura, M. Azuma, and M. Takano, Phys. Rev. Lett. **74**, 2812 (1995)

[14] M. Matsuda, K. Katsumata, H. Eisaki, N. Motoyama, S. Uchida, S. M. Shapiro, and G. Shirane, Phys. Rev. B **54**, 12199 (1996)

[15] R. S. Eccleston, M. Uehara, J. Akimitsu, H. Eisai, N. Motoyama, and S. I. Uchida, Phys. Rev. Lett. **81**, 1702 (1998)

[16] M. Matsuda, T. Yoshihama, K. Kakurai, and G. Shirane, Phys. Rev. B **59**,1060 (1999)

[17] L. P. Regnault, J. P. Boucher, H. Moudden, J. E. Lorenzo, A. Hiess, U. Ammerahl, G. Dhalenne, and A. Revcolovschi, Phys. Rev. B **59**, 1055 (1999)

[18] M. Uehara, T. Nagata, J. Akimitsu, H. Takahashi, N. Mori, and K. Kinoshita, J. Phys. Soc. Jpn. **65**, 2765 (1996)

[19] J. P. Boucher, and L. P. Regnault, J. Phys. I **6**, 1939 (1996)

[20] S. Blundell, F. L. Pratt, P. A. Pattenden, M. Kurmoo, K. H. Chow, S. Takagi, Th. Jestädt, and W. Hayes, J. Phys.: Cond. Matt. **9**, L119 (1997)

[21] M. Isobe, and Y. Ueda, J. Phys. Soc. Jpn. **65**, 1178 (1996)

[22] J. des Cloiseaux, and J. J. Pearson, Phys. Rev. **128**, 2131 (1962)

[23] L. D. Faddeev, and L. A. Takhtajan, Phys. Rev. Lett. **85A**, 375 (1981)

[24] G. Müller, H. Beck, and J. C. Bonner, Phys. Rev. Lett. **43**, 75 (1979)

[25] J. M. Kosterlitz, and D. Thouless, J. Phys. C: Solid State Phys. **6**, 1181 (1973); J. M. Kosterlitz, J. Phys. C: Solid State Phys. **7**, 1046 (1974)

[26] I. Affleck, J. Phys. A: Math. Gen. **31**, 4573 (1998)

[27] G. Fáth, and J. Sólyom, J. Phys: Cond. Matt. **5**, 8983 (1993)

[28] I. Affleck, J. Phys.: Cond. Matt. **1**, 3047 (1989)

[29] P. Fazekas, *Lecture notes on electron correlation and magnetism* (World Scientific Publishing Co. Pte. Ltd., Singapore, 1999)

[30] P. W. Anderson, Phys. Rev. B **52**, 694 (1952); Solid State Phys. **14**, 99 (1963); *Basic notions of condensed matter physics*, (The Benjamin/Cummings Publishing Company, Inc., Advanced Book Program, Menlo Park, 1984)

[31] A. H. Bougourzi, M. Karbach, and G. Müller, Phys. Rev. B **57**, 11429 (1998)

[32] T. Barnes, J. Riera, and D. A. Tennant, Phys. Rev. B **59**, 11384 (1999)

[33] T. Barnes, Physical Review B **67**, 024412 (2003)

[34] A. B. Harris, Phys. Rev. B **7**, 3166 (1973)

[35] G. S. Uhrig, and H. J. Schulz, Phys. Rev. B **54**, R9624 (1996); Phys. Rev. B **58**, 2900(E) (1998)

[36] J. C. Bonner, and M. E. Fisher, Phys. Rev. **135**, A640 (1964)

[37] L. J. Jongh, and A. R. Miedema, Adv. Phys. **23**, 1 (1974)

[38] S. Eggert, I. Affleck, and M. Takahashi, Phys. Rev. Lett. **73**, 32 (1994)

[39] B. Frischmuth, B. Ammon, and M. Troyer, Phys. Rev. B **54**, R3714 (1996)

[40] L. N. Bulaevskiĭ, Soviet Phys. JETP **17**, 684 (1963)

[41] J. C. Bonner, H. W. J. Blöte, J. W. Bray, and I. S. Jacobs, J. Appl. Phys. **50**, 1810 (1979)

[42] T. Barnes, and J. Riera, Phys. Rev. B **50**, 6817 (1994)

[43] W. E. Estes, D. P. Gavel, W. E. Hatfield, and D. J. Hodgson, Inorg. Chem. **17**, 1415 (1978)

[44] J. W. Hall, W. E. Marsh, R. R. Weller, and W. E. Hatfield, Inorg. Chem. **20**, 1033 (1980)

[45] M. Matsuda, K. Katsumata, Phys. Rev. B **53**, 12201 (1996)

[46] S. A. Carter, B. Batlogg, R. J. Cava, J. J. Krajewski, W. F. Peck Jr. , and T. Rice, Phys. Rev. Lett. **77**, 1378 (1996)

[47] K. Takeda, S. Matsukawa, and T. Haseda, J. Phys. Soc. Jpn. **30**, 1330 (1971), and references therein

[48] N. E. Brese, and M. O'Keeffe, J. Solid State Chem. **83**, 1 (1989)

[49] P. K. Davies, J. Solid State Chem. **95**, 365 (1991)

[50] P. K. Davies, E. Caignol, and T. King, J. Am. Ceram. Soc. **74**, 569 (1991)

[51] Y. Mizuno, T. Tohyama, S. Maekawa, T. Osafune, N. Motoyama, H. Eisaki, and S. Uchida, Phys. Rev. B **57**, 5326 (1998)

[52] P. W. Anderson, in *Magnetism, Vol. 1*, edited by G. T. Rado and H. Suhl (Academic Press, 1963)

[53] J. Kanamori, J. Phys. Chem. Solids **10**, 87 (1959)

[54] J. B. Goodenough , Phys. Rev. **100**, 564 (1955)

[55] T. Tonegawa, I. Harada, and M. Kaburagi, J. Phys. Soc. Jpn. **61**, 4665 (1992)

[56] C. K. Majumdar, and D. K. Ghosh, J. Mat. Phys. **10**, 1388 (1969)

[57] K. Okamoto, and K. Nomura, Phys. Rev. A **169**, 433 (1992)

[58] S. White, and I. Affleck, Phys. Rev. B **54**, 9862 (1996)

[59] T. Hamada, J. Kane, S. Kakagawa, and Y. Natsume, J. Phys. Soc. Jpn. **57**, 1891 (1988)

[60] F. C. Zhang, and T. M. Rice, Phys. Rev. B **37**, 3759 (1988)

[61] A. Hayashi, B. Batlogg, and R. J. Cava, Phys. Rev. B **58**, 2678 (1996)

[62] M. D. Chabot, and J. T. Markert, Phys. Rev. Lett. **86**, 163 (2001)

[63] H. F. Fong, B. Keimer, J. W. Lynn, A. Hayashi, and R. J. Cava, Phys. Rev. B **59**, 6873 (1999)

[64] M. Matsuda, K. Ohayama, M. Ohashi, J. Phys. Soc. Jpn. **68**, 269 (1999)

[65] M. Matsuda, H. Yamaguchi, T. Ito, C. H. Lee, K. Oka, and K. Kakurai, Phys. Rev. B **63**, 180403(R) (2001)

[66] M. Matsuda, K. Kakurai, S. Kurogi, K. Kudo, Y. Koike, H. Yamaguchi, T. Ito, and K. Oka, Phys. Rev. B **71**, 104414 (2005)

[67] G. I. Meijer, C. Rossel, W. Henggeler, L. Keller, F. Fauth, J. Karpinski, H. Schwer, E. M. Kopnin, P. Wachter, R. C. Black, and J. Diederichs, Phys. Rev. B **58**, 11452 (1998)

[68] M. F. Collins, and O. A. Petrenko, Canad. J. Phys. **75**, 605 (1997).

[69] A. Hauser, U. Falk, P. Fischer, and H. U. Güdel, J. Solid State Chem. **65**, 343 (1985)

[70] N. Niel, C. Cros, G. Le Flem, M. Pouchard, and P. Hagenmuller, Physica B **86**, 702 (1977)

[71] *Physical Property Measurement System, Hardware Manual* (Quantum Design, Inc., San Diego, 2000)

[72] J. S. Hwang, K. J. Lin, and C. Tien, Rev. Sci. Instr. **87**, 94 (1997)

[73] G. L. Squires, *Introduction to the theory of thermal neutron scattering* (Cambridge University Press, Cambridge, 1978)

[74] G. E. Bacon, *Neutron diffraction* (Oxford University Press, 1975)

[75] S. W. Lovesey, *Theory of neutron scattering from condensed matter* (Oxford University Press, Oxford, 1984)

[76] G. Shirane, S. M. Shapiro, and J. M. Tranquada, *Neutron scattering with a triple-axis spectrometer - basic techniques* (Cambridge University Press, Cambridge, 2002)

[77] M. J. Cooper, and R. Nathans, Act. Cryst. **23**, 357 (1967)

[78] B. Dorner, Act. Cryst. A **28**, 319 (1972)

[79] M Popovici, Act. Cryst. A **31**, 507 (1974)

[80] J. Wuttke, *Data reduction for quasielastic neutron scattering* (ILL report No. 91WU08T, 1991)

[81] H. H. Paalman, and C. J. Prings, J. Appl. Phys. **33**, 2635 (1962)

[82] G. I. Meijer, C. Rossel, E. M. Kopnin, M. Willemin, J. Karpinski, H. Schwer, K. Conder, and P. Wachter, Europhys. Lett. **42**, 339 (1998)

[83] K. Conder, S. Rusiecki, and E. Kaldis, Mat. Res. Bull. **24**, 581 (1989)

[84] N. E. Breese, M. O'Keeffe, R. B. Von Dreele, and V. G. Young, J. Solid State Chem. **83**, 1 (1989)

[85] T. Siegrist, R. S. Roth, C. J. Rawn, and J. J. Ritter, Chem. Mat. **2**, 192 (1990)

[86] A. Abragam, and B. Bleaney, *Electron Paramagnetic Resonance of Transitions Ions* (Oxford University Press, Dover, 1984)

[87] J. Dolinsek, D. Arcon, and P. Cevec, Phys. Rev. B **57**, 7798 (1998)

[88] A. Shengelaya, G. I. Meijer, J. Karpinski, G.M. Zhao, H. Schwer, E. M. Kopnin, C. Rossel, and H. Keller, Phys. Rev. Lett. **80**, 3626 (1998)

[89] C. A. M. Mulder, A. J. van Duyneveldt, and J. A. Mydosh, Physical Review B **23**, 1384 (1981)

[90] C. Kittel, *Einführung in die Festkörperphysik* (R. Oldenburg Verlag, München, 1999)

[91] K. Kudo, S. Kurogi, Y. Koike, T. Nishizaki, and N. Kobayashi, Phys. Rev. B **71**, 104413 (2005)

[92] H. J. Schulz, Phys. Rev. Lett. **77**, 2790 (1996)

[93] A. J. Bevolo, Cryogenics **14**, 661 (1974)

[94] J. S. Payson, and L. E. Wenger, Cryogenics **22**, 44 (1982)

[95] B. Cort, and D. G. Naugle, Cryogenics **21**, 313 (1981)

[96] G. T. Furukawa, W. G. Saba, and M. L. Reilly, Nat. Bur. Stand. Ref. Data Ser. (National Bureau of Standards, Washington, DC, USA) No 18, 1 (1968)

[97] D. L. Martin, Canad. J. Phys. 65, 1104 (1987)

[98] A. Mirmelstein, A. Junod, K.-Q. Wang, E. Janod, and J. Muller, Physica C **241**, 301 (1995)

[99] V. Pomjakushin, private communication

[100] R. Jenkins, and R. L. Snyder, *Introduction to X-ray powder diffractometry* (John Wiley and Sons, New York 1996)

[101] K. D. Rouse, and M. J. Cooper, Act. Cryst. **A26**, 682 (1970)

[102] *International Tables for Crystallography Vol. C*, edited by A. J. C. Wilson and E. Prince, Alden Press, Oxford (1999)

[103] G. Shirane, Act. Cryst. **12**, 282 (1959)

[104] J. Rodriguez-Carvajal, *Fullprof*, http://www-llb.cea.fr/fullweb/

[105] W. Sikora, F. Bialas, L. Pytlik, and J. Malnowski, *Mody*, http://novell.ftj.agh.edu.pl/ sikora/modyopis.htm

[106] J. Rodriguez-Carvajal, *Supercell*, http://www-llb.cea.fr/fullweb/

[107] S. J. Kang, and T. C. Ozawa, *Balls & Sticks*, http://www.softbug.com/toycrate/bs

[108] Y. Miyazaki, I. Gameson, and P. P. Edwards, J. Solid State Chem. **145**, 511 (1999)

[109] W. Opechowski, and R. Guccione, *Magnetic Symmetry*, in *Magnetism, Vol. 2a*, edited by G. T. Rado and H. Suhl, (Academic Press, New York, 1965)

[110] J. C. Le Guillou, and J. Zinn-Justin, Phys. Rev. B **21**, 3976 (1980)

[111] H. U. Güdel, and A. Furrer, Mol. Phys. **33**, 1335 (1977)

[112] A. Furrer, and H. U. Güdel, Phys. Rev. Lett. **39**, 657 (1977)

[113] H. U. Güdel, A. Stebler, and A. Furrer, Inorg. Chem. **18**, 1021 (1979)

[114] H. Mutka, C. Payen, P. Molinié, J. L. Soubeyroux, P. Colombet, and A. D. Taylor, Phys. Rev. Lett. **67**, 497 (1991)

[115] A. P. Murani, Phys. Rev. B **50**, 9882 (1994)

[116] Y. Mizuno, T. Tohyama, and S. Maekawa, Phys. Rev. B **60**, 6230 (1999)

[117] G. I. Meijer, R. S. Eccleston, H. Mutka, C. Rossel, J. Karpinski, S. Kazakov, and P. Wachter, Phys. Rev. B **60**, 9260 (1999)

[118] M. Hummel, F. Schwabl, and C. Pich, Phys. Rev. B **63**, 094425 (2001)

[119] H. Kadowaki, K. Hiarakawa, and H. Ubukoshi, J. Phys. Soc. Jpn. **52**, 1799 (1983)

[120] R. Feile, J. K. Kjems, A. Hauser, H. U. Güdel, U. Falk, and A. Furrer, Solid State Comm. **50**, 435 (1984)

[121] S. E. Nagler, D. G. Mandrus, and D. A. Tennant, Physica B **241-243**,561 (1998)

[122] B. Fåk, and B. Dorner, Physica B **234-236**, 1107 (1997)

[123] M. Boehm, S. Coad, B. Roessli, A. Zheludev, M. Zolliker, P. Böni, D. McK. Paul, H. Eisaki, N. Motoyama, and U. Uchida, Europhys. Lett. **43**, 77 (1998)

[124] C. G. Windsor, and R. W. H. Stevenson, Proc. Phys. Soc. **87**, 501 (1966)

[125] G. McPherson, T. Kistenmacher, and G. Stucky, J. Chem. Phys. **52**, 815 (1970)

[126] E. Rastelli, and A. Tassi, Phys. Rev. B **70**, 214407 (2004)

[127] J. Kondo, and K. Yamaji, Prog. Theor. Phys. **47**, 807 (1972)

[128] V. J. Minkiewicz, D. E. Fox, and G. Shirane, Solid State Comm. **8**, 1001 (1970)

[129] M. F. Collins, and D. B. Gaulin, J. Appl. Phys. **55**, 1869 (1984)

[130] D. B. Gaulin, and M. F. Collins, Can. J. Phys. **62**, 1132 (1984)

[131] C. Reich, P. Böni, and B. Roessli, Phys. Rev. Lett. **91**, 157203 (2003)

[132] E. Rastelli, private communication

[133] M. Steiner, K. Kakurai, J. K. Kjems, D. Petitgrand, and P. Pynn, J. Appl. Phys. **61**, 3953 (1987)

[134] W. J. L. Buyers, R. M. Morra, R. L. Amstrong, M. J. Hogan, P. Gerlach, and K. Hirakawa, Phys. Rev. Lett. **56**, 371 (1986)

[135] M. Kenzelmann, R. A. Cowley, W. J. L. Buyers, R. Coldea, M. Enderle, and D. F. McMorrow, Phys. Rev. B **66**, 174412 (2002)

[136] I. A. Zaliznyak, L. P. Regnault, and D. Petitgrand, Phys. Rev. B **50**, 15824 (1994)

[137] H. Fukuyama, T. Tanimoto, and M. Saito, J. Phys. Soc. Jpn. **65**, 1182 (1996)

[138] J. P. Renard, K. Le Dang, P. Veillet, G. Dhalenne, A. Revcolevschi, and L. P. Regnault, Europhys. Lett. **30**, 475 (1995)

[139] L. P. Regnault, J. P. Renard, G. Dhalenne, and A. Revcolevschi, Europhys. Lett. **32**, 579 (1995)